

**“QUANTUM” MOLECULAR DYNAMICS  
A DYNAMICAL MICROSCOPIC  $n$ -BODY  
APPROACH TO INVESTIGATE FRAGMENT  
FORMATION AND THE NUCLEAR EQUATION  
OF STATE IN HEAVY ION COLLISIONS**

**Jörg AICHELIN**

*Institut für Theoretische Physik der Universität Heidelberg, D-6900 Heidelberg, Fed. Rep. Germany*



**NORTH-HOLLAND**

**“QUANTUM” MOLECULAR DYNAMICS—A DYNAMICAL MICROSCOPIC  
*n*-BODY APPROACH TO INVESTIGATE FRAGMENT FORMATION  
AND THE NUCLEAR EQUATION OF STATE IN  
HEAVY ION COLLISIONS**

Jörg AICHELIN

*Institut für Theoretische Physik der Universität Heidelberg, D-6900 Heidelberg, Fed. Rep. Germany*

Editor: G.E. Brown

Received June 1990

*Contents:*

1. Introduction	235	5. The model	297
2. The nuclear equation of state	241	5.1. Initialization	298
2.1. The nuclear equation of state	242	5.2. Propagation in the effective potential	299
2.2. Nonrelativistic nuclear matter calculations	243	5.3. Collisions	305
2.3. Relativistic nuclear matter calculations	245	5.4. Pauli blocking	306
2.4. Momentum dependent versus density dependent interactions	249	5.5. Numerical tests	307
3. Kinetic equations	250	6. Multifragmentation	315
3.1. Classical molecular dynamics approach	252	6.1. Experimental facts and review of the theories	316
3.2. Density matrix, reduced density matrix and their time evolution	253	6.2. Confrontation of the model with data	317
3.3. Different truncation schemes	255	6.3. Predictions and results of the calculation	325
4. On the derivation of the quantum molecular dynamics approach	263	6.4. What causes fragmentation?	333
4.1. Scattering on a bound particle	264	6.5. Fragments and the nuclear equation of state	337
4.2. Wigner densities	269	7. Probing the nuclear equation of state	340
4.3. Scattering in the Wigner density formalism	273	7.1. Velocity dependence versus compressibility	341
4.4. Scattering on a system of bound particles	280	7.2. Particle production and the equation of state	344
4.5. Initial Wigner density	284	7.3. Can we extract the nuclear equation of state from present data?	346
4.6. Interference between subsequent collisions	285	8. Conclusions	354
4.7. Attempts to treat nucleons as fermions	293	References	357
		Note added in proof	360

*Single orders for this issue*

PHYSICS REPORTS (Review Section of Physics Letters) 202, Nos. 5 & 6 (1991) 233–361.

Copies of this issue may be obtained at the price given below. All orders should be sent directly to the Publisher. Orders must be accompanied by check.

Single issue price Dfl. 96.00, postage included.

*Abstract:*

The quantum molecular dynamics approach, an  $n$ -body theory to describe heavy ion reactions between 100 MeV/n and 2 GeV/n, is reviewed. We start out with a survey of the present status of nuclear matter calculations and of kinetic theories as far as they are of importance for our approach. We then present a detailed derivation of the quantum molecular dynamics equation, discuss the various approximations necessary to derive this equation and to make actual calculations feasible. The calculations presented aim at the solution of two of the most interesting questions of contemporary heavy ion physics: What causes a nucleus to fragment into many heavy pieces, and can we determine the nuclear equation of state from heavy ion reactions? We first make detailed comparisons with a multitude of experimental data, which yield unexpectedly good agreement. We then proceed to detailed investigations of these questions. We find that fragmentation at these energies is triggered by the density wave caused by the projectile while travelling through the target. We reproduce the "squeeze out" and the "bounce off" predicted by hydrodynamical calculations and recently seen in experiment. Thus there is hope that the nuclear equation of state can be extracted from heavy ion experiments. However, very careful multiparameter experiments are necessary before one can achieve this goal.

**1. Introduction**

One of the most challenging questions which presently are addressed in nuclear physics is the behaviour of nuclear matter under extreme conditions. The correct answer has consequences which reach far beyond the scope of nuclear physics. The explosion mechanism of supernovae, the interior structure of neutron stars and the formation of matter during the evolution of the early universe strongly depend on the properties of hadron matter over a wide range of densities and temperatures.

Unfortunately these astrophysical objects are remote in space and time so that their use for studies of the nuclear matter equation of state under extreme conditions is quite difficult and the conclusions drawn depend on a rather limited set of observations of these rare natural events. The only possible candidates for a systematic study of the nuclear matter properties in the laboratory are high energy heavy ion experiments. Here the system may be dominated by the surface and the influence of the short reaction time must be addressed. Furthermore it has to be investigated whether equilibrium is reached in these reactions.

These experiments became possible at the beginning of the seventies. At that time the BEVALAC at the Lawrence Berkeley Laboratory in Berkeley and the Synchrotron in Dubna started to deliver highly accelerated heavy ions.

Previously heavy ions with energies larger than 20 MeV/n were only available as part of cosmic rays. The technical complications to measure reactions of these natural beams and their rareness set strong limits to the number of events recorded. From accelerator experiments one could expect an increase in the number of events of several orders of magnitude as well as a clear set up for multiparameter events.

The previously available proton beams neither compress the system substantially nor do they deposit a large amount of energy in the target. The interaction of protons with heavy ions was successfully described in the framework of the Glauber theory [1], which assumes that the incoming proton crosses the target on a straight line and deposits around 400 MeV/c momentum in the transverse direction per collision with a target nucleon. Thus the target does not receive a substantial excitation energy.

Heavy ion projectiles were expected to allow one to explore large regions of the density-temperature ( $\rho, T$ ) plane. Theoretical calculations predicted this plane to be full of structure. A pictorial view of the different speculations is shown in fig. 1. It also contains trajectories of heavy ion reactions and supernova explosions. At moderate temperatures ( $T \approx 15$  MeV) a liquid-gas phase transition is predicted. Speculations about density isomers at  $\rho = 3\rho_0$  and the occurrence of pion condensation at about the same density were advanced. Finally, for very high densities and temperatures one expects the transition to the quark-gluon plasma. Testing these speculations seemed to be possible in the now available experiments.

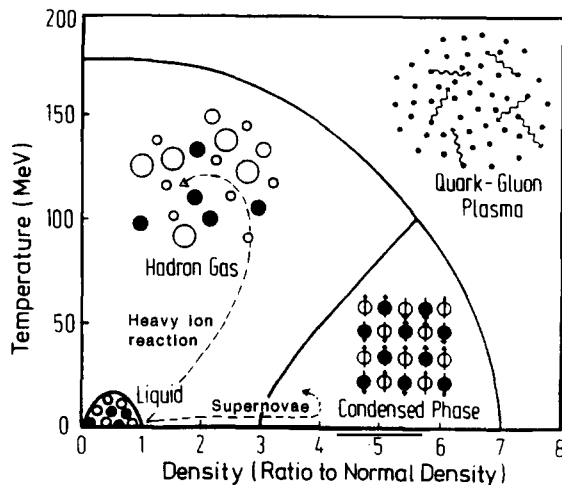


Fig. 1. Phase diagram of nuclear matter. We see the theoretical predictions of what may occur at high densities and high temperatures. The only experimentally known point is  $\rho = \rho_0$ ,  $T = 0$ . Also displayed are the trajectories of a supernova explosion and of a heavy ion reaction.

The first – inclusive – experimental results were rather disappointing. It seems that heavy ion experiments between 250 MeV/n and 1 GeV/n could be well described by the participant spectator model. In this model nucleons in the geometrical overlap of projectile and target form a globally equilibrated source of particle emission whereas the rest of the matter – the spectators – remains cold and undetected, being either at rest in the laboratory system (target spectators) or at  $\theta = 0^\circ$  (projectile spectators). Hence all observables are determined by the expansion of a thermalized nuclear gas. Even the formation of light composite particles was obtained in these models applying a coalescence formula to the single particle spectra. For a discussion of these thermal models we refer to a recent review of Csernai and Kapusta [2].

The more exclusive experiments were performed, the more it became obvious that this was a highly idealized picture of the collision. Determining the centrality of the collision with a multiplicity trigger, it turned out that only central collisions of a heavy projectile–target combination lead to an almost complete stopping and thermalization. The lighter the projectile and the more peripheral the reaction was, the stronger non-equilibrium components appeared. This general behaviour was confirmed when some years later the experimental gap between low energy heavy ion accelerators ( $E_{\text{lab}} < 20$  MeV/n) and BEVALAC energies ( $E_{\text{lab}} > 250$  MeV/n) was closed by the new machines at CERN, Michigan State University and GANIL.

The general feature which emerged from the analysis of these reactions shows that equilibrium situations can only be found at very low and very high energies. In between we see a wide range of energies where projectile and target do not equilibrate and thus the measured quantities reflect directly the dynamics of the heavy ion reactions. At low energies we find compound nuclear reactions where collisions are almost absent and hence the mean field keeps the nucleons together long enough to equilibrate. At high beam energies, on the contrary, frequent nucleon–nucleon collisions cause the thermalization whereas effects of the mean field are small. Results of kinetic theory indicate that about three collisions per nucleon are sufficient to produce a Maxwellian spectrum. Since Pauli blocking is no longer severe at very high energies, the mean free path  $\lambda$  is roughly given by  $\lambda = 1/\sigma\rho \approx 2$  fm, where  $\sigma$  denotes the free nucleon–nucleon cross section. Hence we should expect equilibration at central collisions of heavy projectile–target combinations. Indeed, an almost complete equilibration is seen

experimentally. Between these two extremes the Pauli blocking of the collisions is neither strong enough to avoid emission during the mean field equilibration time, nor is it weak enough to allow a sufficient number of nucleon–nucleon collisions before the system disperses.

Hence intermediate and high energy heavy ion reactions offer a unique possibility to study the evolution of nuclear systems towards equilibrium, the details of the reaction mechanism and how nuclear forces act in the dense nuclear environment. Two observables emerged as the most exciting ones from the present experiments: multifragmentation and the collective flow of nuclear matter.

Multifragmentation, i.e. the production of low and medium mass fragments  $5 < A < 30$ , has first been observed in proton induced collisions with heavy targets and beam energies well beyond 5 GeV. These fragments have received the name "deep spallation products" but their production was never explained in physical terms. They are much more copiously produced than expected from compound evaporation models and hence they point to a new reaction mechanism which is absent at low beam energies. When heavy ion projectiles were available for the first time the experiments indicated that these fragments cannot come from an equilibrated source. Emulsion data revealed [3] that several of these fragments were produced simultaneously in central collisions. The form of the mass yield curve triggered the suggestion that these fragments present evidence for a liquid–gas phase transition and that their yield is directly connected with the critical exponent. This conjecture caused a lot of interest although it was never substantiated by a detailed theoretical analysis of all measured quantities.

The flow of nuclear matter in heavy ion collisions has been predicted by hydrodynamical calculations [4]. It is caused in nearly central collisions where nuclear matter is first compressed and the compressional energy is released afterwards. The compressional energy stems from the longitudinal motion but the release is isotropic thus accelerating particles also transversely. Experimentally it has been first observed by the Plastic Ball Group [5–8]. This observation of flow demonstrates clearly that the mean field still plays an important role for the dynamics of the reaction at beam energies around 1 GeV/n and that nuclear matter is compressed in the course of the reaction. More exciting, however, is the relation between the flow and the nuclear equation of state. Thus measurements seem to offer an experimental handle on the equation of state, i.e., on the compressibility of nuclear matter.

Flow of nuclear matter is a collective phenomenon. Nucleon–nucleon collisions tend to destroy the alignment of the momentum of the collision partners and hence weaken the collective flow. On the one hand, nucleons which suffer violent two-body collisions usually end up at different regions of phase space compared to those nucleons which go with the flow and are unscattered. On the other hand, nucleons which suffer violent two-body collisions are less likely to end up as part of a fragment. Combining both observations we can expect that complex fragments provide an even better tool to study the collective flow than emitted protons.

To pin down the nuclear equation of state from relativistic heavy ion collision data several reliable independent models should be employed to follow the evolution of the system. The predicted observables from such time dependent theories must then be compared with data by adjusting the equation of state.

Theoretical investigations of heavy ion collisions can have two starting points. Either one can invent simple phenomenological models which describe one or another aspect of the reaction, or one has to find reasonable approximations to the time dependent  $n$ -body Schrödinger equation

$$i\hbar \partial \psi^{(n)} / \partial t = H^{(n)} \psi^{(n)}. \quad (1.1)$$

Here  $\psi^{(n)}$  is the  $n$ -body wave function and  $H^{(n)}$  the  $n$ -body Hamiltonian. The first approach has the

advantage of being clearly defined and quite simple. Indeed, many of the gross features of heavy ion reactions have been understood by such models. The above mentioned participant–spectator model is an excellent example. It has the disadvantage that the complex reaction dynamics cannot be studied in such simple models. Consequently, the results may strongly depend on the particular choice of the input and the assumed reaction dynamics. An example of these problems are the models which try to understand multifragmentation. Starting from quite different, almost opposite, assumptions (which range from global equilibrium to processes like shattering of glass, from a liquid–gas phase transition to percolation of a lattice) almost all models produce the same form of mass yield curve. Conversely, it is hard to make sure that the agreement between model and experiment really reveals the underlying physics. For a discussion of these models see ref. [9].

The second approach suffers from the complexity of the equation, which cannot be solved in a straightforward manner. Hence reasonable approximations are required. Before starting to solve the time dependent equation a close inspection of the solutions of the time independent equation

$$E\psi^{(n)} = H^{(n)}\psi^{(n)} \quad (1.2)$$

is advised. This equation was widely used to study the nuclear matter properties as well as binding energies and root mean square radii of finite nuclei. One has to keep in mind, however, that this equation is only valid as long as the mesons do not have to be treated as particles themselves but only appear as potentials.

One of the most surprising results was, that in spite of the strength of the nucleon–nucleon interaction, nucleons at low energies can be described in the Hartree–Fock approach. Here the nucleons move in an average potential

$$\langle a|V^{\text{MF}}|a\rangle = \sum_{E(b) < E_{\text{Fermi}}} (\langle a, b|v^{(2)}|a, b\rangle - \langle a, b|v^{(2)}|b, a\rangle), \quad (1.3)$$

which is generated by all other nucleons and no explicit two-body interaction is required.  $v^{(2)}$  refers here to the two-body interaction. The single particle wave functions are then solutions of the one-body Schrödinger equation with the potential  $V^{\text{MF}}$  and the  $n$ -particle wave function is just the Slater determinant of the single particle wave functions. Attempts to use potentials fitted to nucleon–nucleon scattering data failed because the two-body term diverges. By employing effective potentials obtained by summing the one-hole graphs, i.e., by solving the Bethe–Goldstone equation, this problem can be resolved [10]. Even better agreement with nuclear matter properties is obtained employing a density dependent local interaction  $V^{\text{MF}} = U(\rho)$ . The validity of such an approximation can be verified by comparing these results with the original results based on two-body interactions. For actual calculations a renormalized form of the density dependent potential is used which gives proper binding energies and saturation density. Both quantities could not be reproduced simultaneously by a nonrelativistic potential based on scattering data. Nevertheless, density dependent potentials seem to be a good starting choice to describe the dynamics of nucleus–nucleus collisions.

In the energy regime  $E_{\text{lab}} > 25 \text{ MeV}/n$ , which we are interested in, the two colliding ions usually do not come to global equilibrium in the course of the reaction. This complicates the problem tremendously. If equilibrium is reached, the details of the dynamics on the way towards it are not reflected in the final observables. Here we have to follow the details of the dynamics from the initial separation of projectile and target up to the final distribution of the remnants in phase space.

The calculation of the time evolution of two colliding nuclei in phase space has first been performed successfully in hydrodynamical calculations. Later also the Time Dependent Hartree–Fock (TDHF) and the Boltzmann–Uehling–Uhlenbeck (BUU) equations were solved. The validity of each of these approaches is limited to a certain energy regime. However, these equations have in common that they are one-body equations; hence all predictions are limited to one-body observables like the double differential cross section for protons or  $(n - 1)$ -body observables like the linear momentum transfer. (Here the terms one-body and  $(n - 1)$ -body have to be taken with a grain of salt.) The formation of fragments is beyond the scope of these models. The results obtained with these approaches have recently been reviewed [4].

Here we present a microscopic dynamical  $n$ -body theory tailored to describe the formation of fragments in heavy ion collisions [11–19]. It is dubbed "quantum molecular dynamics" (QMD), since it is essentially a quantal extension of the classical molecular dynamics approach widely used in chemistry and astrophysics. We will see, however, that this extension is not straightforward although the formal structure of the equations is quite similar. Starting from the  $n$ -body Schrödinger equation we will derive the time evolution equation for the Wigner transform of the  $n$ -body density matrix. This will show that the time evolution is determined by the real and imaginary parts of the transition matrix (or – if the blocking of the intermediate states becomes important – the Brückner  $g$ -matrix). We discuss the approximations which are necessary to solve the final equation with present day computers. These approximations include:

- (a) the assumption that the scattering of the nucleons can be treated as if they were free, thus allowing us to use measured nucleon–nucleon cross sections;
- (b) the assumption that interference between two different sequences of collisions vanishes;
- (c) the assumption that collisions are independent;
- (d) the replacement of the real part of the transition matrix by an effective potential, which is easier to handle and can be directly compared with the results of nuclear matter calculations and with the effective potentials used in one-body theories;
- (e) the assumption that the fermionic nature of the nucleons can be mimicked and that calculations with antisymmetrized wave functions, which require an order of magnitude more computer time and have not even been tried so far, do not give substantially different results.

To establish the validity of our approach we present extensive comparisons with the results of one-body theories. The differences we find are rather small and are expected from statistical fluctuations.

The emphasis of the QMD approach resides in actual calculations, which allow a detailed comparison with experimental data. Here our interests are concentrated on two topics: the understanding of multifragmentation and the extraction of the nuclear equation of state.

For the first topic we performed calculations for almost all high energy fragmentation data. We find remarkable agreement not only with single particle observables but also with fragmentation data. These include the total cross section for fragment production, the multiplicity of fragments in a single event and the transverse momentum the fragments gain as a consequence of the bounce off. This agreement gives us confidence that we can use our approach to investigate the central question, namely what causes a heavy target to break up into fragments? We find that at the energies considered the multifragmentation is caused by a high density zone due to the traversing projectile. We could not find any evidence for a liquid–gas phase transition. On the contrary, the investigated systems never reached complete local or global equilibrium.

Although in principle the nuclear equation of state should be obtained by nuclear matter calcula-

tions, it turns out that the uncertainties due to higher order terms and to the largely unknown behaviour of mesons and resonances in nuclear matter are so large that reliable predictions are not presently within reach. It is therefore a challenging possibility to infer the nuclear equation of state from heavy ion reactions. For this purpose one follows the strategy of employing various potentials, which yield different equations of state in nuclear matter, and investigating their influence on observables. Unfortunately it turns out that the effects are of the same order of magnitude as those caused by small variations in other input quantities, such as a change in the nucleon–nucleon cross section due to in-medium effects, or a slight change of the momentum dependences of the nucleon–nucleon potentials without changing the equation of state. Therefore many observables have to be measured simultaneously in order to disentangle these different effects. We will report on the present status of this project.

Although in principle the dependence of the equation of state on the input parameters can also be investigated in one-body theories, this approach has a large drawback. Experimentally single particles and fragments are measured. Both react differently to changes of the input parameters and have a different probability to be detected even for the same energy/nucleon. In one-body theories there exist only single particles. Hence a direct comparison with experiment is not possible and unfortunately the effects observed by varying the parameters are of the same size as the uncertainties in relating experiments to the one-body theories. Thus in this case a theory which is able to describe the formation of fragments is again superior to one-body approaches.

This paper is organized as follows.

In chapter 2 we start with a review of the nuclear equation of state obtained in nonrelativistic and relativistic nuclear matter calculations. We discuss why it is essential to disentangle the density and momentum dependent parts of the nucleon–nucleon potentials, which determine the equation of state. We give the present status of different nuclear matter approaches and discuss the current results for the optical potential at high densities and temperatures.

In chapter 3 we review the kinetic equations which are or which can be employed to describe the dynamics of heavy ion collisions on the one-body level. The quantal one-body equations can be derived from the  $n$ -body von Neumann equation in analogy to the BBGKY hierarchy in classical transport theory. We will show which approximations are made to obtain the TDHF, the intranuclear cascade and the BUU equations.

In chapter 4 we discuss the derivation of the QMD equation from the  $n$ -body Schrödinger equation. We investigate in detail the approximations which are necessary and the range of validity of the QMD approach. We motivate the choice of the initial distribution, and finally discuss the independent scattering approximation and the present status of the attempts to solve the time evolution equation for fermionic systems.

Chapter 5 is devoted to the description of the numerical realization of the QMD model. We discuss the inputs from nuclear matter calculations and present in detail how the equations are solved. We report on the tests performed and compare our results with those of one-body theories.

In chapter 6 we present calculations of fragment production and confront them with experimental data. We take advantage of the additional information available in the calculation, i.e., we study the coordinate space distribution as a function of time to investigate the impact parameter dependence of the reactions and to study correlations between the initial and final distribution of the nucleons.

In chapter 7 we present a detailed comparison of our proton data with experiments and with the results of one-body theories. We investigate different suggestions of observables being sensitive to the nuclear equation of state and discuss the influence of the equation of state on particle production and the collective flow. We also investigate how variations of the cross section and the momentum

dependence of the interaction influence the observables and whether this may spoil the information on the equation of state.

Finally, in chapter 8 we summarize the results and present the conclusions.

## 2. The nuclear equation of state

One can think of three different sources to obtain information about the nuclear equation of state (EOS):

- (1) astrophysical measurements, in particular the explosion of supernovae and the stability of neutron stars;
- (2) giant monopole vibrations;
- (3) high energy heavy ion collisions.

Up to now the key quantity "compressibility" extracted in these three different approaches still differs by a factor of two. Some authors claim that their models for supernovae need a soft equation of state (EOS) with a compressibility of  $K \approx 140$  MeV in order to make them explode [20]. A stiffer EOS, i.e. a larger value of  $K$ , does not allow sufficient energy to be stored during the collapse phase and hence the subsequent explosion dies out on the way to the surface.

Early analyses of giant monopole resonances seemed to yield a compressibility of  $K \approx 200$  MeV [21]. Recent more refined experiments, however, lead to much larger values ( $K \approx 300$  MeV) [22]. A still higher compressibility,  $K \approx 380$  MeV, has been deduced from  $4\pi$  data [23, 24].

The discrepancy between the results obtained in these different fields may be less surprising if one keeps in mind the quite strong assumptions made in the calculations of heavy ion reactions and astrophysical phenomena as well as the different time scales and/or momentum space distributions involved:

(1) The iron core of the progenitor star could be smaller [25] than estimated previously [26]. Then prompt supernovae explosions would occur even with a stiff EOS [27].

(2) The supernova explosions could be due to mechanisms other than the prompt bounce, e.g. by late shock revival due to neutrino heating [28].

(3) The time scales involved in the two processes are quite different ( $10^{-3}$  s versus  $10^{-22}$  s), so that a softening of the neutron matter equation of state due to processes in  $\beta$ -equilibrium could be important [29].

(4) The angular momentum of the progenitor, which should play an important role in the prompt collapse, has been ignored in most calculations. Up to now almost all conclusions are based upon one-dimensional hydrodynamical calculations [30]. Recent calculations present evidence that the collapse of a rotating star can yield a quite different scenario compared to a static collapse [31].

(5) The momentum dependence of the interactions could provide an additional repulsion in heavy ion collisions, which could help to produce the large observed transverse momentum transfer [13, 32–35].

(6) The in-medium scattering cross section could be smaller or larger than the free cross section. Up to recently nuclear matter calculations predicted a reduced in-medium cross section [36, 37] for momenta larger than the Fermi momentum. Now it seems that a better description of the pion polarization may enhance the cross section [38, 39].

(7) In monopole vibrations [21, 22] the nucleons oscillate around their equilibrium density. However, the change in density is less than a tenth of a percent, whereas in heavy ion collisions we expect to

obtain more than twice nuclear matter density. So it seems quite unrealistic to extrapolate the EOS from these small density variations to very high densities.

All information beyond the sparse astrophysical observations on rare events like, e.g., SN1987A has ultimately to be obtained from nuclear collisions simply because there is no other reliable source of experimental information. This situation makes it not only worthwhile but compulsory to try to extract information on the nuclear equation of state (EOS) from heavy ion experiments. This, however, is a very complicated task and hence only about the first steps towards this ultimate goal can be reported. The main complications are:

(1) The properties of finite nuclei are quite different from those of nuclear matter. Even in the heaviest nuclei most nucleons "feel" the surface. This makes it difficult to relate results of nuclear experiments to properties of nuclear matter.

(2) High densities can be obtained in heavy ion collisions only for very short times (of the order of 10 fm/c). Such a time span may be too short to allow possible phase transitions, which may occur at the same density but on a longer time scale.

(3) Nuclear matter calculations are not able to reproduce the known nuclear properties. Even the most sophisticated nuclear matter calculations with potentials adjusted to nucleon–nucleon phase shifts are not able to describe the experimental facts on the binding energy at saturation density and the optical model potentials measured in proton–nucleus collisions. Modelling high energy heavy ion collisions requires knowledge of these potentials not only at nuclear matter density and zero temperature but also at high densities and high temperatures. Even calculations which agree on ground state properties and optical potentials at normal nuclear matter densities give vastly different results at high densities and temperatures.

(4) Only in extreme cases (central collisions in heavy projectile–target combinations) [17] do the light particles reach a global equilibrium. Usually we face situations far from equilibrium. This complicates the theoretical calculations tremendously; e.g., relatively simple equilibrium Pauli blocking in the  $g$ -matrix calculation cannot be applied. Furthermore, dynamical models which require local equilibrium like fluid dynamics or hydrodynamics can only be applied with caution. They do not allow one to investigate whether a discrepancy between theory and experiment is due to the assumptions of equilibrium kinematics or due to a wrong parametrization of the potentials.

So the determination of the properties of nuclear matter under extreme conditions requires not only a detailed calculation of the dynamics of the system but also further progress in calculating the static properties of finite nuclei under extreme densities and temperatures. Ultimately only a combined effort can lead to success.

### 2.1. The nuclear equation of state

The properties of nuclear matter in equilibrium can be described by two variables, the density  $\rho$  and the temperature  $T$ . The pressure  $P$ , i.e. the equation of state, can be obtained from these variables via the thermodynamical relations. In nuclear physics one usually defines the energy/baryon  $E$ , which is a function of  $\rho$  and  $T$ .  $E$  is connected to the pressure by the relation  $P = \rho^2 \partial E / \partial \rho |_{S=\text{const}}$ . Here  $S$  denotes the entropy. The compressibility  $K$  is defined as  $K = 9\rho \partial P / \partial \rho |_{S=\text{const}}$ . In order to disentangle the change of the static energy/baryon due to cold ( $T = 0$ ) compression from the energy due to an increase of the temperature, we define [4, 40]

$$E(\rho, T) = E_T(\rho, T) + E_C(\rho, T = 0) + E_0, \quad (2.1)$$

where  $E_C$  is the compressional energy and  $E_T$  is the thermal energy.  $E_T$  consists of the kinetic energy above the degenerate Fermi gas and possibly of a potential energy (if momentum dependent potentials are used). Only a single point of this two-dimensional surface  $E(\rho, T)$  is known experimentally: At normal nuclear matter density  $k_{\text{Fermi}} \approx 1.36 \text{ fm}^{-1}$ , the binding energy per baryon is  $E_0 = -15.75 \text{ MeV}$  and the pressure equals zero.

## 2.2. Nonrelativistic nuclear matter calculations

The energy per nucleon in nuclear matter and ultimately the equation of state, i.e. the dependence of the binding energy on the density  $\rho$  and the temperature  $T$ , should in principle be calculated from the underlying nucleon–nucleon interactions. This has been attempted using the Brückner  $g$ -matrix [10, 41] approach, but was not completely successful, as we will see. The same is true for the optical potential, which describes how an incoming proton reacts with the target nucleus, which is considered as a one-body object, thus reducing the  $(n + 1)$ -body problem to a two-body problem.

The retarded Green's function, which describes at the same time the propagation of a particle added to the medium and of a hole punched into the medium (of momentum  $k$  and energy  $E$ ), is given by

$$G^+(k, E) = \frac{1}{E - k^2/2m - M(k, E) + i\epsilon}, \quad (2.2)$$

where the mass operator  $M(k, E)$  is a function of the Brückner  $g$ -matrix. The  $g$ -matrix is defined via the Bethe–Goldstone equation,

$$g(E) = V + V \frac{\sum_{a,b} |a, b\rangle \langle a, b|}{E - e(a) - e(b) + i\epsilon} g(E). \quad (2.3)$$

If  $E$  is less than twice the Fermi energy the imaginary part of the propagator can be omitted because it does not have a pole. We will discuss the consequences in chapter 3. Here  $V$  is the elementary nucleon–nucleon interaction; usually a multiparameter fit to nucleon–nucleon scattering data such as the Reid soft core potential [42] is used in these approaches. The sum runs over all unoccupied states  $|a, b\rangle$  and  $e(a)$  is the single particle energy of the state  $a$ ,

$$e(a) = a^2/2m + \text{Re } M(a, e(a)). \quad (2.4)$$

The mass operator  $M(a, e(a))$  can be expanded in  $g$  [41]. The second-order approximation reads as

$$M(a, E) = M_1(a, E) + M_2(a, E), \quad (2.5)$$

$$M_1(a, E) = \sum_j n(j) \langle a, j | g(E + e(j)) | a, j \rangle + \langle a, j | g(E + e(j)) | j, a \rangle, \quad (2.6)$$

$$M_2(a, E) = \frac{1}{2} \sum_{j,l,k} n(j)n(l)[1 - n(k)] \frac{[\langle l, j | g(e(l) + e(j)) | a, k \rangle + \langle l, j | g(e(l) + e(j)) | k, a \rangle]^2}{E + e(k) - e(j) - e(l) - i\epsilon}. \quad (2.7)$$

Here  $n(j)$  is the occupation probability of the single particle state  $j$ . The single particle energy  $e(a)$

depends on  $M(a, e(a))$ .  $M(a, e(a))$  in turn depends on the single particle energy  $e(a)$ , so that we have to determine  $M(a, e(a))$  self-consistently. The mass operator  $M(a, e(a))$  can be identified with the complex optical model potential,

$$M(a, e(a)) = V(a) + iW(a), \quad (2.8)$$

which is the potential felt by a particle that enters nuclear matter. This potential can be measured in proton–nucleus reactions. This allows us to check the validity of the approximations necessary to calculate an optical potential from the nucleon–nucleon interaction. Actual calculations show [41] that for particle energies between 0 and 200 MeV the real part of the optical potential can be quite well approximated by

$$V(k, \rho) = V_0(\rho) + (\alpha k^2/2m)\rho/\rho_0, \quad (2.9)$$

with  $\alpha = 0.3$ .  $k$  is the proton momentum and  $m$  the proton mass. Comparing now eq. (2.9) with the result of eq. (2.2) we find that the main influence of the surrounding nuclear matter on a particle is the change of its mass from  $m$  to

$$m^* = \frac{k^2}{2[k^2/2m + (\alpha k^2/2m)\rho/\rho_0]} \approx \frac{m}{1 + 0.3\rho/\rho_0}. \quad (2.10)$$

The momentum dependence of the optical potential contains a generic momentum dependence of the potential as well as the nonlocality of the potential. By inspecting the Schrödinger equation, one can see that the latter can also be expressed as a momentum dependence.

The extraction of the nuclear matter properties from nucleon–nucleon potentials adjusted to nucleon–nucleon scattering data [42], however, failed in nonrelativistic calculations. They yield a saturation density of nuclear matter about twice as high as experimentally observed. Also, when applied to finite nuclei, these forces do not reproduce experimental facts [43]. For different potentials which are adjusted to nuclear scattering data the extracted binding energies and root mean square radii fall on a line, the Coester line, which does not match the experimental point. Even the inclusion of three-body correlations [44] does not cure this problem, which seems to be intrinsic in nonrelativistic nuclear matter calculations. The most probable reason for this will be discussed in the next section.

In order to enforce saturation at normal nuclear matter density a phenomenological force has to be invoked. Friedman and Pandharipande [45] introduced a repulsive interaction in a form which can also be expressed as the density dependence of the two-body potential  $v_1$ . For densities close to nuclear matter density

$$\Delta E/A = -v_1 a \rho = 3.6(\rho/\rho_0)^2 [\text{MeV}] \quad (2.11)$$

yields the correct binding energy of  $-15.75$  MeV/n of nuclear matter. Calculating the energy/nucleon, i.e. the equation of state

$$\frac{E}{A} = \frac{3}{5} E_F + \frac{1}{\rho} \int d\rho V(\rho) = \frac{3}{5} E_F + \frac{1}{\rho} \beta \int d\rho \rho \left(1 - \frac{3.6}{\beta} \rho\right), \quad (2.12)$$

we obtain a quite low compressibility as can be seen by inspecting fig. 2.

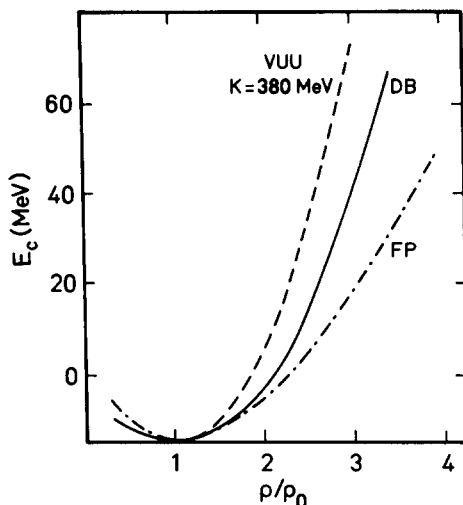


Fig. 2. Nuclear equation of state as predicted by different theories. We display the compressional energy obtained in the phenomenological approach of Friedman and Pandharipande [45], which is very close to that of Horowitz and Serot [47], as well as Dirac-Brückner calculations by ter Haar and Malfliet [36]. For the sake of comparison we also display the hard equation of state used in VUU and QMD calculations [64].

The phenomenological introduction of such a term excludes, however, the approach for high energy heavy ion collisions. In the ground state the equation of state is a function of the density only, because the Fermi motion yields terms proportional to  $(\rho/\rho_0)^{2/3}$ . Thus from comparison at the single point (at zero temperature and normal nuclear matter density) where one knows the binding energy one cannot disentangle the static from the kinetic part of the equation of state [see eq. (2.1)], i.e. momentum and density dependent potentials. To have both these parts separated is essential for the description of heavy ion collisions. Here we have initially a large relative momentum between projectile and target nucleons and hence a momentum dependent potential would act quite differently than a density dependent potential. This will be discussed in section 2.4.

### 2.3. Relativistic nuclear matter calculations

Relativistic nuclear matter calculations [36, 46–48] usually start out from a Lagrangian density which describes baryons  $\psi$ , scalar mesons  $\phi$  and vector mesons  $V_\mu$ ,

$$L = \bar{\psi}[\gamma_\mu(i\partial^\mu - g_v V^\mu) - (m - g_s \phi)]\psi + \frac{1}{2}(\partial_\mu \phi \partial^\mu \phi - m_s^2 \phi^2) - \frac{1}{4}(\partial_\mu V_\nu - \partial_\nu V_\mu)^2 + \frac{1}{2}m_v^2 V_\mu V^\mu - \frac{1}{4}F_{\mu\nu} F^{\mu\nu}. \quad (2.13)$$

Mesons with pseudoscalar and pseudovector coupling are neglected because they do not contribute in the mean field approximation in spin saturated nuclear matter. The motivation for this approach comes from the experimental observation that nucleon–nucleon potentials, fitted to nucleon–nucleon scattering data, exhibit a strong attraction due to the exchange of a scalar particle at medium range and strong repulsion at short range due to the exchange of a vector particle. The parameters of this theory, i.e. the masses and the coupling constants, can be determined from experiments.

The equations of motion of these interacting fields have not been solved so far. Further approximations have been made. The most commonly used approximation is the mean field approach of Serot and

Walecka [46]. They assume that the time and space evolution of the mesons can be neglected and the actual meson fields can be replaced by their mean values,

$$\phi_0 = (g_s/m_s^2)\langle\bar{\psi}\psi\rangle = (g_s/m_s^2)\rho_s, \quad (2.14)$$

$$V_0 = (g_v/m_v^2)\langle\psi^\dagger\psi\rangle = (g_v/m_v^2)\rho. \quad (2.15)$$

Here  $\rho_s$  is the scalar density and  $\rho$  is the baryon density. With these approximations we calculate the energy density

$$\frac{E}{A} = \frac{g_v^2}{2m_v^2}\rho + \frac{m_s^2}{2g_s^2}(m - m^*)^2 \frac{1}{\rho} + \frac{g_v^2}{2m_v^2} \frac{1}{\rho} B^2 + \frac{\gamma}{(2\pi)^3\rho} \int_0^{k_F} d^3k \sqrt{k^2 + m^{*2}}, \quad (2.16)$$

where the density  $\rho$ , the scalar density  $\rho_s$ , the baryon current  $\mathbf{B}$  and the effective mass  $m^*$  are given by

$$\rho = \frac{\gamma}{(2\pi)^3} \int_0^{k_F} d^3k, \quad (2.17)$$

$$\rho_s = \frac{\gamma}{(2\pi)^3} \int_0^{k_F} d^3k \frac{m^*}{\sqrt{k^2 + m^{*2}}}, \quad (2.18)$$

$$\mathbf{B} = \frac{\gamma}{(2\pi)^3} \int_0^{k_F} d^3k \frac{\mathbf{k}}{\sqrt{k^2 + m^{*2}}}, \quad (2.19)$$

$$m^* = m - (g_s^2/m_s^2)\rho_s. \quad (2.20)$$

For later use we define  $U = g_s^2/m_s^2$  and  $V = g_v^2/m_v^2$ , with couplings chosen in order to reproduce the binding energy at normal nuclear matter density. For nuclear matter (degeneracy factor  $\gamma = 4$ ) this mean field ansatz yields a very stiff equation of state ( $K = 500$  MeV). This approach can be extended to finite temperatures and to terms proportional to  $\phi^3$  and  $\phi^4$  [49]. The higher order terms allow a softening of the equation of state in agreement with the known nuclear matter properties. They introduce two new parameters, which can be fixed by optical model experiments [49] and by the compressibility extracted from monopole vibrations.

Recently it was pointed out by Brown et al. [50] that the failure of the nonrelativistic nuclear matter calculations is most probably due to a process which is embedded neither in a nonrelativistic theory nor in a relativistic mean field approach. A strongly repulsive density dependent contribution to the particle potential is caused by the virtual production of a nucleon-antinucleon pair via a scalar interaction. For  $p^2 < M$  this term contributes to the single particle energy by [51]

$$\Delta E = (U^2/M)p^2/2m. \quad (2.21)$$

Assuming that  $U = -400$  MeV  $\cdot \rho/\rho_0$  the energy per nucleon is changed by [51]

$$\Delta E = 2.4(\rho/\rho_0)^2 p^2 / \langle p^2 \rangle, \quad (2.22)$$

where  $\langle p^2 \rangle = 0.6 p_{\text{Fermi}}^2$  is the average Fermi momentum squared at normal nuclear matter density. This term reveals a quadratic density dependence and hence the same form – and even the same numerical values – as the phenomenological term of Friedman and Pandharipande (eq. 2.11). A comparison with the experimental values of the optical potential clearly demonstrates that the virtual pair creation accounts for almost the entire energy dependence. However, this should be verified by more elaborate calculations since it would imply that all the other contributions to the momentum dependence of the potential have to cancel.

The other contributions can best be discussed using the [51, 52] "Schrödinger equivalent" potential of the Walecka mean field theory. The Dirac equation of a particle with energy  $E$  interacting with the medium via a mean scalar field  $U$  and vector field  $V$  is

$$(E - V\rho)\gamma_0 - \boldsymbol{\gamma} \cdot \mathbf{p} - m - U\rho_s = 0. \quad (2.23)$$

We multiply the equation with

$$(E - V\rho)\gamma_0 - \boldsymbol{\gamma} \cdot \mathbf{p} + m + U\rho_s \quad (2.24)$$

and we obtain the quadratic equation

$$(E - V\rho)^2 - p^2 = (m + U\rho_s)^2. \quad (2.25)$$

Replacing  $E$  by  $\varepsilon + m$  and identifying the asymptotic momentum  $k_{r \rightarrow -\infty}^2 = \varepsilon^2 + 2m\varepsilon$  with  $p^2 + 2mV(\varepsilon)$ , we finally arrive at

$$V(\varepsilon) = V\rho + U\rho_s + \frac{(U\rho_s)^2 - (V\rho)^2}{2m} + V\rho \frac{\varepsilon}{m}, \quad (2.26)$$

with  $\rho_s = (E/m)\rho$ . The energy/nucleon is then given by

$$\frac{E}{A} = \frac{3}{5} \frac{p_{\text{F}}^2}{2m} + \frac{1}{\rho} \int V(\rho, \varepsilon) d\rho \approx \frac{3}{5} \frac{p_{\text{F}}^2}{2m} + \frac{1}{2} V(\varepsilon), \quad (2.27)$$

where the factor 1/2 comes from the conversion of the potential to the potential energy for a two-body potential.

We see also that relativistic calculations yield a repulsive potential which is proportional to the kinetic energy of the particles and proportional to the density. Taking the values of the original mean field theory  $U = -420$  MeV and  $V = 330$  MeV we even end up quantitatively with the nonrelativistic dependence of eq. (2.9),  $V(k, \rho) = V_0(\rho) + 0.3 T\rho/\rho_0$ , where  $T$  is the kinetic energy of the particle. The value of the coefficient of proportionality  $\alpha$  as well as the linear dependence of the second term on the density have been confirmed recently by more involved Brückner–Dirac [36, 47] calculations.

Horowitz and Serot [47] advanced a renormalized theory where the one nucleon loop corrections were taken into account. These loops are very repulsive thus lowering the value of the attractive scalar

potential to roughly half of the original mean field value. A smaller scalar potential increases the value of the effective mass, which was too low at high densities ( $m^*/m = 0.2$  at  $\rho = 4\rho_0$ ). The repulsive vector potential is lowered in magnitude as well. Both together reproduce the binding energy at normal nuclear matter density quite well. This calculation yields a quite soft equation of state (compressibility  $K = 200$  MeV), a value which is almost identical to the one obtained by Friedman and Pandharipande [45] in their phenomenological nonrelativistic calculation. Ter Haar and Malfliet [36] published results of a Brückner–Dirac calculation which include the production of the  $\Delta(3, 3)$  resonance but they do not renormalize the one nucleon loop. Their results agree almost completely with the original mean field values, in the quantitative values as well as in their dependences. Thus they obtain a very hard equation of state with a compressibility of 500 MeV. Both calculations, however, do not agree with experiment. In a recently published analysis of  $\text{Ca}(p, p')$  data Cooper and al. [53] found a quite strong energy dependence of both the scalar as well as the vector potential. Both lose strength almost linearly with increasing energies. In mean field calculations, where the mesonic degrees of freedom are not treated dynamically, both fields have to be constant. So obviously one has to go beyond the mean field approach to explain the data. First successful attempts to include the dynamics of the meson field were reported by Cusson et al. [54] and more recently by Feldmaier et al. [55], who solved the Euler–Lagrange equations derived from the Lagrangian (2.13). However, a detailed comparison between data and theory has not been made up to now.

Applying the mean field concept to relativistic heavy ion collisions several additional difficulties arise [51]:

(1) Projectile and target are moving in the centre of mass system. In a moving system the scalar density is decoupled from the vector density because  $\rho_s$  equals  $\rho/\gamma$ . In heavy ion collisions projectile nucleons “feel” the potential not only from the other projectile nucleons – where  $\rho \approx \rho_s$  – but also from the target nucleons – where  $\rho > \rho_s$  – and vice versa. The resulting repulsion adds to the energy dependence already present as one can see from eq. (2.26).

(2) The vector potential, which has only a fourth component in the rest system, now gets other components. The vector field carries a sizeable fraction of the total momentum and hence the momentum of the nucleons is lowered.

(3) We explore densities much higher than normal nuclear matter densities. During equilibration the density increases and the energy is stored in mesonic degrees of freedom. None of these problems is satisfactorily solved so far.

Due to these circumstances it is premature to use the result of one specific relativistic or nonrelativistic nuclear matter calculation as input of a dynamical calculation. Considering the mentioned difficulties we cannot expect to relate the specific form of the nucleon–nucleon interaction with the results of a dynamical calculation. Rather than aiming at deriving the nucleon–nucleon potential from heavy ion experiments, we have the more moderate goal of obtaining information on the equation of state in nuclear matter. We start with a parametrization of the nuclear equation of state with as few parameters as possible and adjust the experimental energy dependence. This operational point of view ensures that we get the correct infinite matter properties. The dependence on the parameters chosen is easy to handle. If we reduce our  $n$ -body theory to a one-body theory, the average potential coincides with a nonrelativistic local density approximation to the  $g$ -matrix. This approximation has been successfully used in time dependent Hartree–Fock calculations. Recently it has been shown that this approach remains reasonable also at high beam energies [56].

Since we want to solve an  $n$ -body theory we have to employ nucleon–nucleon potentials and not a mean field. There are an infinite number of effective nucleon–nucleon potentials which yield a given

equation of state. We take one which is easy to handle numerically, i.e. a local interaction in coordinate space supplemented by a Yukawa and a Coulomb part. Hence the total interaction reads as

$$V^{\text{tot}} = \alpha\delta^3(\mathbf{r}_1 - \mathbf{r}_2) + \beta\delta^3(\mathbf{r}_1 - \mathbf{r}_2)\delta^3(\mathbf{r}_1 - \mathbf{r}_3) + V_{\text{Coul}}(\mathbf{r}_1 - \mathbf{r}_2) + V_{\text{Yuk}}(\mathbf{r}_1 - \mathbf{r}_2) + V_{\text{mdi}}(\mathbf{p}_1 - \mathbf{p}_2)\delta^3(\mathbf{r}_1 - \mathbf{r}_2). \quad (2.28)$$

$V_{\text{mdi}}$  stands for the momentum dependent interaction. The parameters are varied to allow the study of different equations of state without changing the ground state properties.

This procedure results in the following strategy: Rather than performing straightforward calculations with nucleon–nucleon interactions adjusted to scattering data and making predictions, we have to perform the calculation with a variety of reasonable sets of parameters which all give the correct ground state properties. We first have to search for observables which are sensitive to different interactions and investigate then whether one set of parameters can satisfy all the experimental observations. Furthermore this can help to determine which additional observables should be measured. One of the major obstacles towards this goal is the observation that momentum dependent interactions and density dependent interactions can produce, at least qualitatively, the same phenomena.

#### 2.4. Momentum dependent versus density dependent interactions

In this section we will explain why momentum dependent and density dependent interactions can produce similar effects for some observables.

As long as the projectile and target do not overlap, the relative momentum between the interacting nucleons is rather small. Therefore momentum dependent interactions do not play an essential role. Now let us assume that projectile and target hit at a semi-central impact parameter. As soon as the nuclei overlap, particles of very large relative momenta are positioned closely in configuration space (fig. 3a).

Here projectile nucleons "feel" a very strong repulsive potential due to the neighbouring target nucleons and vice versa (fig. 3b). Outside the overlap region we find either projectile or target

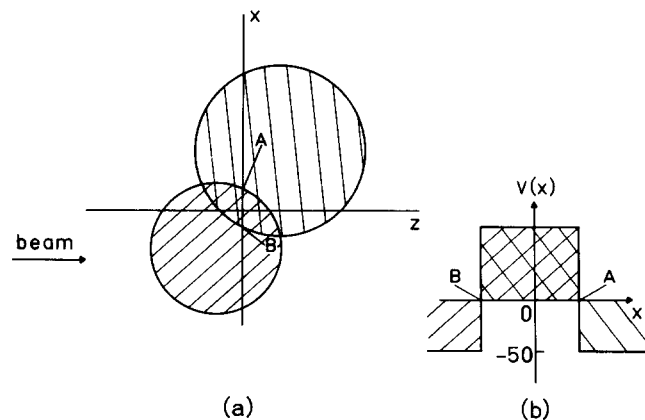


Fig. 3. Transverse momentum caused by momentum dependent forces. (a) The reaction in the beam–impact parameter plane. (b) The potential along the  $x$  axis. We see in the overlap region a strong repulsive and outside it an attractive potential. Hence the particles want to leave the overlap zone by gaining transverse momentum.

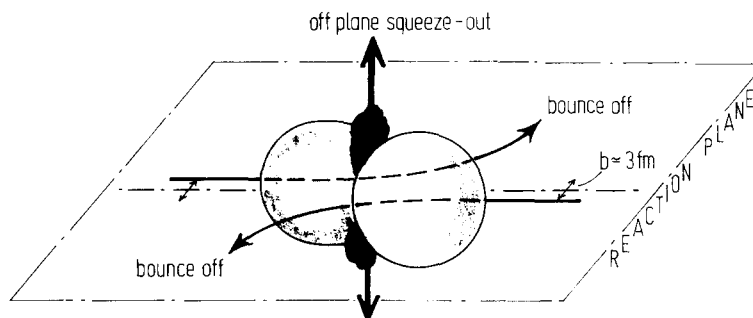


Fig. 4. Pictorial display in the in-plane bounce off caused by compression. We see that the forward moving particles have opposite transverse momentum to the backward moving particles. Also displayed is the squeeze out, the enhanced emission of light particles perpendicular to the reaction plane close to mid-rapidity. Both effects are caused by compression and have been predicted in hydrodynamical calculations [4].

nucleons, and therefore the potential is still attractive. Consequently there is a strong potential gradient perpendicular to the beam direction, i.e. in the direction of the impact parameter. This causes a strong force which tries to sweep particles out of the overlap zone quite early during the reaction. This force transfers an appreciable amount of transverse momentum to the particles. So we expect a finite transverse momentum transfer. This transverse momentum causes the system to expand radially, thus decreasing the density. Hence we obtain a lower maximal compression. In this more dilute system fewer collisions can occur since the mean free path has increased. Observables which are connected to the number of nucleon–nucleon collisions should reflect this lower number. Also we should see a strong beam energy dependence of the observables.

If we employ a static interaction only, we have a density of about twice nuclear matter density in the overlap region when the nuclei start to overlap. For realistic potentials the difference between normal and twice nuclear matter density is small as compared to the additional difference due to the momentum dependent interactions. Therefore we do not have large transverse momenta at the beginning of the interaction. We rather expect more equilibration and a higher central density. Hence more energy is stored in compressional energy. During the expansion this energy is released. Consequently particles from the compression zone pick up their transverse velocity later than in the case of momentum dependent interactions. A pictorial view of this process is displayed in fig. 4.

Since the mean free path is shorter in this case, all observables connected with the number of collisions should be different from the values calculated for a momentum dependent potential.

Hence finite transverse momentum transfer is obtained in both cases. However, it remains to be checked, and this is one of the goals of the detailed calculation, whether the two different assumptions can quantitatively produce the same result. This question will be investigated in chapter 7.

### 3. Kinetic equations

All information about a quantal  $n$ -body system such as two colliding nuclei with  $A_p$  projectile and  $n - A_p$  target nucleons – if we neglect particle production – is contained in the  $n$ -body density matrix, whose time evolution is given by the von Neumann equation. As a boundary condition the solution of this equation requires the knowledge of the unknown initial correlations among all nucleons and therefore only a formal solution is possible. This formidable task has not been tackled so far. Furthermore, a complete solution probably is so complicated that it does not help to understand the

physics which governs the nucleus–nucleus reaction. So it is not only compulsory but also for the benefit of understanding if one concentrates on reasonable approximations to the quantal  $n$ -body equation.

A variety of approximations have been suggested and applied so far to investigate heavy ion reactions. Their validity depends on the energy range and the desired information. One can start out from the intuitive picture that a nucleus which interpenetrates another nucleus can be described as a superposition of quasi-particles. They move in an average field generated by all the other nucleons and undergo hard stochastic scattering, which changes the quantum state of the considered nucleon. This picture emerges from the structure of potentials fitted to nucleon–nucleon scattering data and their action in nuclear matter. They show a strong repulsive core and a long range attraction. In nuclear matter the long range attraction of all the fellow nucleons can be described as a mean field. The short range repulsion is highly suppressed due to the Pauli principle and can be understood as a scattering of the particles into unoccupied states. Low momentum scattering and hence long range correlations are forbidden since the states which can be reached with low momentum transfer are already occupied and hence Pauli blocked. So between subsequent collisions the particles move on mean field orbitals.

The classical equation of motion approach [33, 57, 58] lacks stochastic collisions. It is assumed that classical potentials act among the nucleons which are considered as classical particles. This approach will be discussed in section 3.1.

The validity of the different approximations made can best be judged if one introduces different length scales. For this purpose we define:

mean free path:  $\lambda = 2\text{--}10$  fm,

length of the system:  $L = 5\text{--}15$  fm,

range of the hard core interaction:  $a = 0.4$  fm,

length of the de Broglie wavelength:  $\Lambda \approx 1$  fm at the Fermi energy.

Unfortunately in nuclei all ratios of these length scales are of the order of unity. So any approximation which is based on the ratio of two lengths being small is close to the limit of its validity if applied to nuclear physics.

If  $\Lambda \ll \lambda$  we are in the classical regime (although this is not quite true since we have diffractive scattering). This approximation is best for  $E_{\text{lab}} \geq 200$  MeV/n, where the energy per nucleon in the centre of mass system is large as compared to the Fermi energy. This is the energy regime where the classical molecular dynamics approach [33, 57, 58] has been applied to heavy ion collisions.

If  $\lambda \ll L$  we are in the domain where fluid or hydrodynamical equations can be applied [4, 59]. However, these equations are derived under the assumption of local equilibrium and small deviations from local equilibrium, respectively. Therefore they rely completely on the assumption that in heavy ion collisions the time for local equilibration is short. Since  $\lambda$  is decreasing with energy due to the less effective Pauli blocking, this approach is best suited to high energy collisions of very heavy nuclei.

If  $a \ll \lambda$  and  $\Lambda \ll \lambda$  we are in the dilute limit. This is the domain of the Boltzmann equation, the Boltzmann–Uehling–Uhlenbeck equation [60–65] and the cascade calculations [66, 67]. All assume that subsequent nucleon–nucleon collisions are independent. Between collisions the particles move on straight line trajectories (in cascade calculations) or on curved trajectories (in Boltzmann-type calculations) under the influence of a mean field.

Finally, at very low energies we find  $\lambda > L$ ; due to the Pauli principle most of the states into which the particles may scatter are already occupied and hence the effective cross section is quite small. At beam energies of a few MeV/n we can expect a mean free path of  $\approx 10$  fm [68]. In this extreme limit one may neglect collisions completely and then arrives at the time dependent Hartree–Fock theory [69–71] (TDHF).

Formally the Boltzmann–Uehling–Uhlenbeck equation, TDHF, cascade calculations and hydrodynamics represent just different truncation schemes to the  $n$ -body density matrix. This will be discussed in sections 3.2 and 3.3. Some of the results obtained with these approaches have recently been reviewed [4].

### 3.1. Classical molecular dynamics approach

A classical  $n$ -body system is described completely by the  $n$ -body phase space density  $f^{(n)}(\mathbf{p}_1, \dots, \mathbf{p}_n, \mathbf{r}_1, \dots, \mathbf{r}_n, t)$ , whose time evolution is given by the Liouville equation

$$(\partial/\partial t)f^{(n)}(t) = \{H, f^{(n)}(t)\} = -\sum_{i=1}^n (\dot{\mathbf{r}}_i \cdot \nabla_{\mathbf{r}_i} f^{(n)} + \dot{\mathbf{p}}_i \cdot \nabla_{\mathbf{p}_i} f^{(n)}). \quad (3.1)$$

Here  $\{a, b\}$  denotes the Poisson bracket and we have made use of Hamilton's equations.

The classical molecular dynamics approach is directly modelled to solve the Liouville equation numerically, using a Monte Carlo sampling procedure. For heavy ion collisions the calculations [33, 57, 58] are performed as follows: Initially the positions and momenta of all  $n$  nucleons are chosen randomly in a sphere of radius  $R = r_0 A_T^{1/3}$  and  $R = r_0 A_P^{1/3}$ , respectively. Hence the  $n$ -body phase space density is the product of delta functions in phase space. During the nuclear collision the nucleons are propagated using Hamilton's equations,

$$\dot{\mathbf{r}}_i = \nabla_{\mathbf{p}_i} H = \mathbf{p}_i/m + \nabla_{\mathbf{p}_i} V(\mathbf{p}_1, \dots, \mathbf{p}_n), \quad (3.2)$$

$$\dot{\mathbf{p}}_i = -\nabla_{\mathbf{r}_i} H = \mathbf{F}_i, \quad (3.3)$$

where the force  $\mathbf{F}_i$  is given by  $\mathbf{F}_i = -\nabla_{\mathbf{r}_i} U_i$  with  $U_i = \sum_{i \neq j} V_{ij}$ . Finally, physically meaningful observables are obtained by averaging over many runs of different initial configurations.

Hence, the Classical Molecular Dynamics approach is a true  $n$ -body theory, which keeps track of all correlations among the particles. It is also able to treat nonequilibrium situations, which appear at the early stage of a heavy ion collision.

In this approach all essential quantum effects have to be mimicked by the proper choice of the potential. In order to give the calculations a predictive power, the classical nucleon–nucleon potential  $V_{ij}$ , simultaneously has to take care of

- (1) the proper binding energy/nucleon,
- (2) the measured scattering cross section,
- (3) the stability of the nucleus for a time span required for a nucleus–nucleus collision.

Especially the second point is hard to mimic in classical theories because it reflects typical quantum features like Pauli blocking and diffractive scattering.

In practice [33, 57, 58] the potential is chosen as a sum of an attractive and a repulsive Yukawa interaction. Hence four parameters have to be adjusted (two ranges and two strengths). The cross section is calculated with the weight factor appearing in the calculation of the viscosity coefficient from the Boltzmann equation. This weight factor emphasizes the transverse momentum transfer more strongly than the total cross section.

Actual calculations have shown that the potential cannot fulfill the above-mentioned requirements to

a degree which allows quantitative comparison with experiments. There is not enough room to accommodate the Pauli principle, and probably more important, for strong gradients of the potentials Hamilton's equations are a poor approximation to the evolution of the quantum system. Here the quantal features must be implemented via short range stochastic scattering [72], as we will see in chapter 4. Usually the stability leaves much to be desired because due to the huge fluctuation of the potential it is almost impossible to initialize the nucleus close to its ground state. So the particles are emitted rapidly. Hence the classical molecular dynamics approach was mainly used for schematic studies and never allowed detailed comparison with experiments. The only recent use of this model was an investigation of the possibility of a liquid-gas phase transition in expanding nuclei [73].

### 3.2. Density matrix, reduced density matrix and their time evolution

In this section we will review the definition of the  $n$ -body density matrix and the reduced density matrices. We will start out from the quantum von Neumann equation, which is equivalent to the  $n$ -body Schrödinger equation. It describes the complete time evolution of a quantal system. We proceed by defining reduced density matrices which act in a subspace only. Their time evolution can be defined in very close analogy to the classical BBGKY hierarchy equations [74]. We derive the equation for the time evolution of the one-body density matrix, which depends on the two-body density matrix. This general feature that the equation for the  $m$ -body density depends on the  $(m + 1)$ -body density, which is true for all reduced density matrices, requires for actual calculations a truncation of the  $(m + 1)$ -body density into products of at most  $m$ -body densities. This will be discussed in section 3.3.

*N-body density matrix.* Let  $|\Phi_k\rangle$  being a  $n$ -body state vector of an isolated  $n$ -body system with the quantum number  $k$ . Then the complete information about the  $n$ -particle system is contained in the  $n$ -body density operator

$$\rho^{(n)} = |\Phi_k\rangle\langle\Phi_k|, \quad (3.4)$$

which reads in coordinate space as

$$\rho^{(n)}(\mathbf{r}_1, \dots, \mathbf{r}_n, \mathbf{r}'_1, \dots, \mathbf{r}'_n) = \Phi_k(\mathbf{r}_1, \dots, \mathbf{r}_n) \Phi_k^*(\mathbf{r}'_1, \dots, \mathbf{r}'_n). \quad (3.5)$$

The expectation value of an operator  $A$  can be defined as

$$\begin{aligned} \langle A \rangle &= \langle \Phi_k | A | \Phi_k \rangle \\ &= \int \Phi_k^*(\mathbf{r}'_1, \dots, \mathbf{r}'_n) A(\mathbf{r}_1, \dots, \mathbf{r}_n, \mathbf{r}'_1, \dots, \mathbf{r}'_n) \Phi_k(\mathbf{r}_1, \dots, \mathbf{r}_n) d^3r_1 \cdots d^3r_n d^3r'_1 \cdots d^3r'_n \\ &= \text{tr}[A\rho]. \end{aligned} \quad (3.6)$$

For an isolated system the density operator is a projection operator,

$$(\rho^{(n)})^2 = \rho^{(n)}, \quad (3.7)$$

with  $\text{Tr}[\rho^2] = 1$ . A system whose density matrix satisfies this condition is said to be in a pure state.

If the system is not isolated but, for example, in contact with a heat bath it is useful to extend the above definition and define the density matrix of a system in a mixed state as

$$\rho^{(n)} = \sum_k |\Phi_k\rangle w_k \langle \Phi_k|, \quad (3.8)$$

where  $k$  runs over the complete set of basis states  $|\Phi_k\rangle$  and  $w_k$  describes the probability that the system is in the state  $|\Phi_k\rangle$ . We normalize  $w_k$  by requiring  $\sum_k w_k = 1$ .

*Reduced density matrix.* We define reduced density matrices by

$$\rho^{(k)} = \frac{n!}{(n-k)!} \text{tr}_{(k+1, \dots, n)} \rho^{(n)}. \quad (3.9)$$

If we normalize  $\text{tr}_{(1, \dots, n)} \rho^{(n)} = 1$ , we obtain for the expectation value of the  $k$ -body operator  $A^{(k)}$ ,

$$\langle A^{(k)} \rangle = \frac{1}{k!} \text{tr}_{(1, \dots, k)} A^{(k)} \rho^{(k)}. \quad (3.10)$$

However, other definitions can also be found in the literature.

*Time evolution of density matrices.* The time evolution of the  $n$ -body density operator is given by the von Neumann equation

$$i(\partial/\partial t)\rho^{(n)}(t) = [H, \rho^{(n)}(t)]. \quad (3.11)$$

Here  $H$  is the Hamiltonian, which is assumed to consist of the kinetic energy and two-body interactions only,

$$H = \sum_i T_i + \frac{1}{2} \sum_{\substack{i,j \\ i \neq j}} V_{ij}. \quad (3.12)$$

One defines the Liouville operators  $L_i = [T_i, ]$  and  $L_{ij} = [\frac{1}{2}V_{ij}, ]$  and expresses the von Neumann equation by

$$\frac{\partial}{\partial t} \rho^{(n)}(t) = -i \left( \sum_{i=1}^n L_i + \sum_{\substack{i,j=1 \\ j \neq i}}^n L_{ij} \right) \rho^{(n)}(t). \quad (3.13)$$

To obtain the time evolution for the  $k$ -body density matrix we integrate over  $(n-k)$  particles and, due to the cyclic invariance of the trace, arrive at

$$\begin{aligned} \frac{\partial}{\partial t} \rho^{(k)}(t) &= -i \frac{n!}{(n-k)!} \text{tr}_{(k+1, \dots, n)} \left( \sum_{i=1}^n L_i + \sum_{\substack{i,j=1 \\ j \neq i}}^n L_{ij} \right) \rho^{(n)}(t) \\ &= -i \frac{n!}{(n-k)!} \text{tr}_{(k+1, \dots, n)} \left( \sum_{i=1}^k L_i + \sum_{\substack{i,j=1 \\ j \neq i}}^k L_{ij} + \sum_i \sum_{j=k+1}^n L_{ij} \right) \rho^{(n)}(t). \end{aligned} \quad (3.14)$$

Since by definition the density operator is symmetric in its variables we can simplify this expression further,

$$\frac{\partial}{\partial t} \rho^{(k)}(t) = -i \frac{n!}{(n-k)!} \text{tr}_{(k+1, \dots, n)} \left( \sum_{i=1}^k L_i + \sum_{\substack{i,j=1 \\ j \neq i}}^k L_{ij} + (n-k) \sum_{i=1}^k L_{i,k+1} \right) \rho^{(n)}(t). \quad (3.15)$$

This is the general form of the evolution equation of a reduced density matrix. We observe that for two-body interactions the time evolution of the reduced  $m$ -body density matrix depends on the  $(m+1)$ -body density matrix. The same feature is observed in classical physics for the BBGKY hierarchy equations [74], i.e., the equations for the time evolution of the reduced phase space densities. In order to obtain a solution one has to truncate the  $(m+1)$ -body density matrix to products of at most  $m$ -body density matrices.

The first two equations of this hierarchy read as follows:

$$\frac{\partial}{\partial t} \rho^{(1)}(t) = -i [L_1 \rho^{(1)}(t) + \text{tr}_{(2)} L_{12} \rho^{(2)}(t)], \quad (3.16)$$

$$\frac{\partial}{\partial t} \rho^{(2)}(t) = -i [(L_1 + L_2 + L_{12}) \rho^{(2)}(t) + \text{tr}_{(3)} (L_{13} + L_{23}) \rho^{(3)}(t)]. \quad (3.17)$$

The sum over all particles  $i+1, \dots, n$  cancels just the different factors in front of the traces  $\text{tr}_{(i, \dots, n)}$  and  $\text{tr}_{(i+1, \dots, n)}$ .

### 3.3. Different truncation schemes

In order to solve the time evolution equation of the  $m$ -body density one has to truncate the  $(m+1)$ -body density matrix. In this section we will review three different truncation schemes of the two- and three-body density matrices, which lead to different one-body quantum kinetic equations. The first approach reduces the time evolution of the one-body density matrix to the TDHF equation written in the density matrix formalism. The second approach describes the time evolution of the one-body density if the range of the interaction potential is small compared to the mean free path, i.e. the dilute limit. In contrast to the TDHF equation the potential does not have to be smooth. We introduce two different time scales,  $t_{\text{coll}}$ , the time between two subsequent collisions, and  $t_{\text{int}}$ , the duration of the interaction. If  $t_{\text{coll}} \gg t_{\text{int}}$ , we can assume that between the individual nucleon–nucleon interactions the density matrix is diagonal in momentum space; then the  $n$ -body density matrix is just the product of one-body density matrices. With this approximation the equation turns out to be formally very similar to that of the classical Boltzmann equation with vanishing potential.

The third approach makes a specific ansatz for the three-body density matrix and describes the time evolution of the one-body density in a smoothly varying self-consistent mean field with short range hard core interactions. This reduction scheme was widely used in the so called Boltzmann–Uehling–Uhlenbeck (BUU) or Vlasov–Uehling–Uhlenbeck (VUU) calculations. In the further derivation we will set  $\hbar = 1$ .

*Time dependent Hartree–Fock equation.* In the time dependent Hartree–Fock approach [69, 70] (TDHF) the two-body density matrix is approximated by the antisymmetrized product of the one-body density matrices,

$$\rho_{\text{TDHF}}^{(2)} = \rho_1^{(1)} \rho_2^{(1)} - \rho_2^{(1)} \rho_1^{(1)} = A_{12} \rho_1^{(1)} \rho_2^{(1)}. \quad (3.18)$$

This method to approximate two-body densities by the product of one-body densities is called the Stosszahlansatz and goes back to Boltzmann, who via this method obtained the classical Boltzmann equation. With this ansatz for eq. (3.16) we can perform the trace over particle 2 and arrive at the familiar TDHF equation,

$$(\partial/\partial t)\rho_1^{(1)}(t) = -i[T + U, \rho_1^{(1)}(t)], \quad (3.19)$$

where  $U$  is obtained by performing

$$\text{tr}_{(2)}[V_{12}, \rho_{\text{TDHF}}^{(2)}] = [U_{\text{dir}} + U_{\text{exch}}, \rho_1^{(1)}(t)] = [U, \rho_1^{(1)}(t)].$$

This approximation is valid, as we will see, if  $V_{12} \ll V_{12} G^{+\text{med}} V_{12}$ , i.e., if the Born approximation is valid.  $G^{+\text{med}}$  is the in-medium Green's function, which we will discuss later. These requirements are quite reasonably fulfilled in low energy heavy ion collisions provided one uses effective interactions and not the Hartree–Fock (HF) terms with a potential adjusted to nucleon–nucleon scattering data. Due to the hard core the HF matrix elements diverge. The remedy is to replace the bare nucleon–nucleon interaction by an effective interaction, usually the Brückner  $g$ -matrix [10]. It is an infinite sum of scatterings of two nucleons in a nuclear medium, i.e. a sum over all ladder diagrams. In chapter 4 we will see that this approximation scheme gives indeed the right low density limit. The contribution of the different diagrams is proportional to  $(ak_F)^n$ , where  $a$  is the range of the interaction,  $k_F$  is the Fermi momentum and  $n$  is the number of hole lines. Hence at low densities the  $g$ -matrix can be obtained systematically employing  $(ak_F)$  as the expansion parameter. The  $g$ -matrix obeys the Bethe–Goldstone equation, which we met already in the nuclear matter discussion (eq. 2.3),

$$\langle ab|g(E)|cd\rangle = \langle ab|V|cd\rangle + \sum_{mn} \langle ab|V|mn\rangle G^{+\text{med}} \langle mn|g(E)|cd\rangle, \quad (3.20)$$

where the in-medium propagator  $G^{+\text{med}}$  is defined as

$$G^{+\text{med}} = \frac{Q_{12}}{E - e(m) - e(n) + i\varepsilon}. \quad (3.21)$$

$e(n)$  is the single particle energy of the state  $n$  and  $V$  includes direct and exchange terms.  $Q_{12}$  is the Pauli projection operator, which allows scattering into the unoccupied states only. It is taken as

$$Q_{12} = (1 - \rho_1^{(1)})(1 - \rho_2^{(1)}). \quad (3.22)$$

If the starting energy  $E$  is smaller than  $2\varepsilon_F$  we cannot have a singularity in the propagator and can ignore the  $i\varepsilon$  in the denominator. The solution can be obtained in analogy to that of the Lippmann–Schwinger equation. For the wave function we find

$$|\Psi_{cd}\rangle = |cd\rangle + \frac{Q}{E - H_0} g(E)|cd\rangle, \quad H_0|ab\rangle = (E_a + E_b)|ab\rangle. \quad (3.23)$$

In contrast to the solution of the Lippmann–Schwinger equation the second term disappears for larger distances,

$$\lim_{|r_1 - r_2| \rightarrow \infty} \langle r_1, r_2 | \Psi_{cd} \rangle = \langle r_1, r_2 | cd \rangle, \quad (3.24)$$

if  $E < 2\varepsilon_F$ .

The solution shows that at large distances the particles do not feel the hard core interaction. Hence the correlations induced by the hard core potential are short ranged. For  $\lim_{|r_1 - r_2| \rightarrow 0} \langle r_1, r_2 | \Psi_{cd} \rangle$  vanishes, and hence the matrix elements remain finite despite the hard core. The  $g$ -matrix turns out to be a smooth function, which for practical purposes can be expressed as a function of the local density.

Actual calculations usually start from the Schrödinger equation, with a mean field  $U_i$  in which the nucleon–nucleon potential is replaced by the real part of the  $g$ -matrix,

$$U_i = \sum_{E(b) < E_{\text{Fermi}}} (\langle i, b | \text{Re } g | i, b \rangle + \langle i, b | \text{Re } g | b, i \rangle). \quad (3.25)$$

$U_i$  has to be calculated self-consistently. The time evolution of the single particle orbital  $\phi_\alpha$  with the quantum numbers  $\alpha$  in the self-consistent mean field  $U_i$  is given by the one-body Schrödinger equation

$$(T_i + U_i)\phi_\alpha(i) = i d\phi_\alpha(i)/dt. \quad (3.26)$$

Here  $T_i$  is the kinetic energy. The  $n$ -body wave function is just the Slater determinant of the one-body wave functions.

The first TDHF calculations for heavy ion collisions were performed in the seventies [69]. Later also axial symmetric and full three-dimensional calculations were advanced [70]. In these calculations a local density approximation to the  $g$ -matrix is used which has been proven to be quite accurate even for light nuclei, and which simplifies calculations tremendously. In this approximation  $U_i$  is given (in nuclear matter) by

$$U_i(\rho) = \frac{3}{4}t_0\rho + \frac{3}{16}t_3\rho^2 + \frac{3}{80}(3t_1 + 5t_2)\rho k_{\text{Fermi}}^2, \quad (3.27)$$

with parameters  $t_0$  to  $t_3$  adjusted to reproduce nuclear matter properties [70]. For finite nuclei the energy density is supplemented by terms proportional to the gradient of the density and the spin density [4, 70]. We observe that the parametrization of the potential has terms proportional to  $\rho$  and  $\rho^2$  as well as a momentum dependence which is proportional to the kinetic energy. The same structure of the potential will be recovered below when the Boltzmann–Uehling–Uhlenbeck theory and the quantum molecular dynamics approach are discussed.

These TDHF calculations were quite successful in describing fusion cross sections, scattering angles, deep inelastic collisions and momentum transfer at  $E_{\text{lab}} \leq 5$  MeV/n. Due to the lack of two-body collisions this approach fails as the energy increases and hard core two-body collisions can occur.

Many attempts have been made to extend the TDHF approach by including a collision term [75, 76]. However, already in first-order perturbation one has to evaluate octupole Fock space operators. Hence these attempts have never succeeded in producing calculations which allow detailed comparison with experiments.

*Cascade calculations.* The second approximation, which describes almost the opposite situation, was developed by Snider [77]. He considers the situations where long range interactions among particles can

be neglected and collisions (i.e. rapidly changing short range correlations) play the dominant role for the time evolution of the density matrix. The average number of particles in the phase space volume  $h^3$  is assumed to be small so that the Pauli blocking of the collisions can be neglected.

Following Snider, we introduce two different time scales, the time between two subsequent collisions,  $t_{\text{coll}}$ , and the duration of the interaction,  $t_{\text{int}}$ . This implies two length scales, the mean free path  $\lambda$  and the range of the potential  $a$ . We expand the Green's function, which describes the propagation of the particle between both scatterings, in a power series in  $a/\lambda$  and keep only the first term. This is equivalent to assuming that the particle moves on shell between the scattering events and that the cross section for double scattering is proportional to the square of that for single scattering.

We transform the two-body density matrix into the interaction representation. Then it does not change due to the kinetic motion of the particles. Then formal scattering theory is applied with an adiabatic switching of the interaction. In the above mentioned approximation outside the interaction radius the density matrix is that of free moving particles. Hence the  $n$ -body density matrix is just the product of one-body density matrices. Møller operators transform the density matrix from outside to inside the scattering range, so the two-body density matrix at the interaction time  $t$  is approximated by

$$\rho^{(2)}(t) = \Omega^+(t-t')\rho_1^{(1)}(t')\rho_2^{(1)}(t')\Omega^{+\dagger}(t-t'). \quad (3.28)$$

We choose the zero of our time scale in which we measure  $t_{\text{int}}$  as the macroscopic time  $t$  where the collision occurs. The Møller operator  $\Omega^+$  is defined as

$$\begin{aligned} \Omega^+ &= \lim_{\varepsilon \rightarrow 0} \lim_{t' \rightarrow -\infty} -\varepsilon \int_0^{t'} e^{\varepsilon t''} e^{iHt''} e^{-iH_0 t''} dt'' \\ &= \sum_{\alpha} \lim_{\varepsilon \rightarrow 0} \lim_{t' \rightarrow -\infty} -\varepsilon \int_0^{t'} e^{\varepsilon t''} e^{iHt''} |\phi_{\alpha}\rangle \langle \phi_{\alpha}| e^{-iE_{\alpha} t''} dt'' = 1 + G_0^+(E_{\alpha})V\Omega^+. \end{aligned} \quad (3.29)$$

For the last step we have introduced a complete set of asymptotic basis states. The Green's function  $G$  is given by

$$G_0^{\pm}(E_{\alpha}) = \lim_{\varepsilon \rightarrow 0} \frac{1}{E_{\alpha} - H_0 \pm i\varepsilon}. \quad (3.30)$$

If  $t_{\text{coll}} \gg t_{\text{int}}$ , we can perform the limit  $t' \rightarrow -\infty$  in eq. (3.29), although on the macroscopic time scale  $t_{\text{coll}}$  this is a small time span during which the one-body density matrix does not vary substantially. Hence we can neglect retardation effects and replace  $\rho(t-t')$  by  $\rho(t)$ .

The transition matrix is connected with the Møller operator by the relation

$$T = V\Omega^+. \quad (3.31)$$

We apply this relation to our eq. (3.28) and obtain

$$\begin{aligned} (\partial/\partial t)\rho^{(1)}(t) &= -i \text{tr}_{(2)} [T_{12}\rho_1^{(1)}(t)\rho_2^{(1)}(t) - \rho_1^{(1)}(t)\rho_2^{(1)}(t)T_{12}^{\dagger} \\ &\quad + T_{12}\rho_1^{(1)}(t)\rho_2^{(1)}(t)T_{12}^{\dagger}G_0^- - G_0^+T_{12}\rho_1^{(1)}(t)\rho_2^{(1)}(t)T_{12}^{\dagger}]. \end{aligned} \quad (3.32)$$

We recall that

$$G_0^+(E) - G_0^-(E) = -2\pi i \delta(E - H_0). \quad (3.33)$$

We normalize the plane wave states by  $\delta^3(\mathbf{p} - \mathbf{p}')$  and give some results of the scattering theory,

$$v_{\text{rel}} \sigma_{\text{tot}}(\mathbf{p}) = -2(2\pi)^3 \text{Im} \langle \mathbf{p} | T | \mathbf{p} \rangle, \quad (3.34)$$

$$d\sigma(\mathbf{p}, \mathbf{p}')/d\Omega = (2\pi)^4 \mu^2 |\langle \mathbf{p}' | T | \mathbf{p} \rangle|^2. \quad (3.35)$$

$v_{\text{rel}}$  is the relative velocity between the scattering partners,  $\mu$  is the reduced mass and  $\sigma_{\text{tot}}$  is the total cross section for particles with the relative momentum  $\mathbf{p}$ . Since  $\rho$  is diagonal in momentum space, we can easily perform the trace over the second particle and arrive finally at

$$\begin{aligned} \frac{\partial}{\partial t} \rho^{(1)}(\mathbf{P}_1, t) &= \frac{C}{(2\pi)^3} \int d^3p \, d^3q \, v_{\text{rel}} \rho^{(1)}(\mathbf{P}_1 - \mathbf{q} + \mathbf{p}, t) \rho^{(1)}(\mathbf{P}_1 - \mathbf{q} - \mathbf{p}, t) \\ &\quad \times \left( \delta^3(\mathbf{p} - \mathbf{q}) \sigma^{\text{tot}}(\mathbf{p}) - \delta(\mathbf{p} - \mathbf{q}) \frac{1}{p^2} \frac{d\sigma(\mathbf{q} \rightarrow \mathbf{p})}{d\Omega} \right). \end{aligned} \quad (3.36)$$

The right hand side of this equation is, up to a normalization factor, exactly the collision term of the Boltzmann equation integrated over coordinate space. The time evolution of the one-body density matrix of a system of particles which interact by short range interactions has the formal structure of a collision integral. The system described by this equation behaves like a quantum billiard system, quantum in the sense that we do not have a unique relation between scattering angle and impact parameter as in classical physics. The cross section can be taken from experiment and one may include also inelastic processes.

In practice [66, 67] the form of the scattering term is just taken as a guideline and implemented in a classical environment. Particles are initialized with sharp momenta and definite positions and are randomly distributed over a sphere of nuclear radius as in the classical molecular dynamics approach. They are boosted and then move on straight line trajectories until a nucleon–nucleon collision occurs. Whenever two particles come closer than  $r = \sqrt{\sigma_{\text{exp}}/\pi}$ , the nucleons collide with a scattering angle  $\theta$ , which is chosen randomly under the constraint that the average over many equivalent collisions reproduces the experimentally measured cross section  $d\sigma_{\text{exp}}/d\theta$ . Thus the stochasticity of the scattering and the production of particles are the only quantum features in this approach.

This approach describes successfully inclusive proton spectra at high beam energies ( $E_{\text{lab}} > 500$  MeV/n), predicts the observed pion yield to within a factor of two [78] and makes possible the study of reaction dynamics in detail. The average number of collisions [66] and the production of entropy [79] were among those questions which were investigated in this approach. The limit of this approach is the lack of any mean field. So particles cannot form fragments. This rules out a straightforward application to peripheral or low energy reactions where clusters are observed in the final state. Furthermore, due to the lack of any repulsive potential, the average density obtained in these calculations for high beam energies is much larger than that obtained in more realistic approaches. Pauli blocking can only approximately be included by forbidding scattering into phase space regions which were initially occupied by target or projectile.

*Boltzmann–Uehling–Uhlenbeck approach.* The cascade reduction of the density matrix is certainly not appropriate for intermediate energy nuclear physics, where the nucleons outside the hard core interaction radius are not free but move in the slowly varying field generated by all the other nucleons. For particles moving in an external potential this approach was first considered by Nordheim [60] and Uehling and Uhlenbeck [61]. If we want to treat the mean field as generated by all the other nucleons and not by an external source we have to start from the three-body density matrix. Besides the particle under consideration, we need a second particle as a scattering partner and a third particle which generates the field in which the first two particles move outside their hard core interaction radius. This situation is similar to that of the scattering of a deuteron, which also requires a three-body density matrix approach. For the latter case Remler [80, 81] has introduced the following approximation to the density matrix:

$$\rho^{(3)} = \Omega_{13}^+ A_{13} \rho_{12}^{(2)} \rho_3^{(1)} \Omega_{13}^{++} + \Omega_{23}^+ A_{23} \rho_{12}^{(2)} \rho_3^{(1)} \Omega_{23}^{++}. \quad (3.37)$$

$A$  is the exchange operator. This is the first-order approximation to the full three-particle Møller operator  $\Omega_{123}^+$  for  $\rho_{123}^{(3)}$  [82]. Recently Botermans and Malfliet [83] have proposed the same approximation to describe the hard scattering of two particles which move in a slowly varying field. The potential between the pairs (1, 3) and (2, 3) is assumed to be sufficiently smooth to approximate the Møller operators  $\Omega_{13}^+$  and  $\Omega_{23}^+$  by 1, i.e., to apply the Born approximation, whereas that between 1 and 2 is considered as strong. In chapter 4 it will be shown that such a splitting of the nucleon–nucleon potential in a weak long range and a strong short range part is not necessary, even somehow misleading. Pursuing this approach we see that as in the TDHF approach the trace over particle 3 produces just a mean field  $U_i$  in which the particle  $i$  moves,

$$\text{tr}_{(3)}[V_{13} + V_{23}, \rho_{123}^{(3)}] = [U_1 + U_2, \rho_{12}^{(2)}], \quad (3.38)$$

where  $U_i$  is given by ( $i = 1, 2$ )

$$U_i = \text{tr}_{(3)} V_{i3} A_{i3} \rho_3^{(1)}. \quad (3.39)$$

Recalling now our evolution equation (3.17) for the two-body density matrix,

$$(\partial/\partial t)\rho^{(2)}(t) = -i[(L_1 + L_2 + L_{12})\rho^{(2)}(t) + \text{tr}_{(3)}(L_{13} + L_{23})\rho^{(3)}(t)], \quad (3.40)$$

we see that the approximation (3.37) closes this equation on the two-body level,

$$(\partial/\partial t)\rho^{(2)}(t) = -i[T_1 + T_2 + V_{12} + U_1 + U_2, \rho^{(2)}(t)]. \quad (3.41)$$

Performing the trace over particle 2 and neglecting retardation effects (as discussed in the above derivation of the cascade equations) we obtain

$$(\partial/\partial t)\rho^{(1)}(t) = -i\{[T_1 + U_1, \rho^{(1)}(t)] + \text{tr}_{(2)}[V_{12}, \rho^{(2)}(t)]\}. \quad (3.42)$$

Comparing eqs. (3.19), (3.36) and (3.42) we see that the last equation describes a particle which moves in a self-consistent mean field and undergoes hard core two-body scattering. To evaluate the collision

term we proceed as above but now take into account the fact that the nucleons move in a mean field between subsequent collisions.

If we want to take into account the Pauli blocking we have to replace the transition matrix by the Brückner  $g$ -matrix, the solution of the Bethe–Goldstone equation (eq. 3.20). Then one can write the time evolution of the one-body density in a completely equivalent form to eq. (3.32) [83],

$$\begin{aligned} i(\partial/\partial t)\rho^{(1)}(t) = & [T_1 + U_1, \rho^{(1)}(t)] + \text{tr}_{(2)}[g\rho_1^{(1)}(t)\rho_2^{(1)}(t) - \rho_1^{(1)}(t)\rho_2^{(1)}(t)g^\dagger] \\ & + \text{tr}_{(2)}[g\rho_1^{(1)}(t)\rho_2^{(1)}(t)g^\dagger G_0^{-\text{med}} - G_0^{+\text{med}} g\rho_1^{(1)}(t)\rho_2^{(1)}(t)g^\dagger]. \end{aligned} \quad (3.43)$$

The exchange operator is absorbed in the  $g$ -matrix. As in the cascade approach we assume two different time scales. Because we approximated  $\Omega$  by 1 in the derivation, we can apply this approach only to slowly varying potentials, i.e., where the Born approximation is valid. The propagators then can be approximated by a delta function for energy conservation as is the case for free scattering. With these approximations we now obtain an equation which describes the time evolution of the one-body density matrix in a smooth mean field, generated by all the other particles, and a short range interaction, which is described by an effective cross section. It differs from the free cross section in the Pauli blocking of the final and intermediate states. Furthermore, the energy denominators of the Green's function contain now also the potential energy. For a different approximation scheme we refer to chapter 4.

In practice [62–65] eq. (3.43) is solved with the test particle method. This was developed by Wong [71] in order to calculate time dependent Hartree–Fock equations. In this approach the particles are initially placed at random in a sphere of the projectile or the target radius, as is done in the cascade or the classical molecular dynamics calculations. They have sharp momenta and positions. Then projectile and target are boosted towards each other. Applying a fixed time step the positions and momenta of all particles are updated via Hamilton's equations,

$$\dot{\mathbf{r}}_i = \nabla_{\mathbf{p}_i} H \rightarrow \mathbf{r}_i(n+1) = \mathbf{r}_i(n) + \frac{\mathbf{p}_i(n + \frac{1}{2})}{m} \Delta t, \quad (3.44)$$

$$\dot{\mathbf{p}}_i = -\nabla_{\mathbf{r}_i} H \rightarrow \mathbf{p}_i(n + \frac{1}{2}) = \mathbf{p}_i(n - \frac{1}{2}) - \nabla_{\mathbf{r}_i} U_i(n) \Delta t, \quad (3.45)$$

where the potential is calculated self-consistently.

In principle, potential and cross section should be obtained from the real and the imaginary part of the  $g$ -matrix calculation with realistic nucleon–nucleon interactions. However, the nonrelativistic approaches do not give the right saturation density of finite nuclei, as shown in chapter 2. At relativistic energies, where nuclear matter is compressed substantially, the real parts of the different approaches to the  $g$ -matrix have differences in the compressional energy of the order of 100 MeV for the same density.

Therefore a reliable input for the Boltzmann–Uehling–Uhlenbeck equation is not at hand. For the imaginary part of the  $g$ -matrix the situation is even worse at these energies. An actual calculation of the  $g$ -matrix suited for the calculation of heavy ion collisions has to take into account the highly nonthermal environment at the beginning of a heavy ion collision. Here the Pauli blocking of the intermediate states cannot be calculated with an average occupation probability as for a gas at a temperature  $T$ . Rather one has to take into account that initially there are two well separated Fermi spheres, out of which particles are scattered. Gradually the momentum space around mid-rapidity gets filled, which influences the blocking probability. Only very late in the course of central collisions of heavy nuclei can

the distribution of nucleons approximately be described by a single thermal distribution centred around mid-rapidity.

Due to these difficulties one takes an operational point of view: it is assumed that eq. (3.43) has the proper form. One takes for the mean field a Skyrme-type potential, which was already employed in the TDHF calculations (eq. 3.27),

$$U = U(\rho) = \alpha\rho/\rho_0 + \beta(\rho/\rho_0)^\gamma . \quad (3.46)$$

The density is calculated via a space fixed grid with cells of size  $1 \text{ fm}^3$  [63] or via a comoving sphere around the test particles [64].

Beyond the pion threshold the experimentally measured (elastic or inelastic) scattering cross section is employed,

$$d\sigma/d\Omega = d\sigma_{\text{exp}}/d\Omega . \quad (3.47)$$

Scattering does not take place if the final state of the scattering partners is already occupied by other nucleons.

At lower energies, where the experimental cross section is several hundred millibarns, an isotropic 40 mb cross section [63, 64] or a density dependent suppression factor  $\kappa$  with  $\sigma = \kappa(\rho)\sigma_{\text{exp}}$  [65] is employed.

This operational point of view has the advantage of a very controlled equation of state, since two out of the three parameters of eq. (3.46) are fixed by the requirement that in nuclear matter the total energy has a minimum at  $\rho = \rho_0$  with a binding energy of 15.75 MeV/n. The only free parameter is hence determined by requiring a specific compressibility. Rather than extracting the equation of state from the highly involved  $g$ -matrix calculation, this approach offers the opportunity to test how stiff the EOS has to be in order to reproduce the experimental data. Hence effectively the compressibility is treated as a free parameter of the theory.

All actual calculations suffer from huge density fluctuations occurring during the simulation of the individual nucleus–nucleus collisions. In order to dampen these fluctuations one typically solves 100 collisions in parallel and averages the potential over all these simulations. This reduces statistical density fluctuations to a tolerable 15%.

The BUU model was first developed at Michigan State University by Bertsch, Kruse and Stöcker in order to test the conjecture that in relativistic heavy ion collisions the pions can serve as a measure for the compressional energy and hence of the nuclear equation of state [62, 64]. Later improved versions were used to investigate heavy ion reactions at energies as low as 25 MeV/n [63]. In this energy regime, where single particle spectra show that no equilibrium is achieved, the model offered for the first time the possibility to investigate the space–time evolution of the reaction. The remarkable agreement of the results with experiments was taken as evidence that the essential physics is contained in the BUU equation despite the many approximations. These calculations helped to understand the proton spectra, the origin of the Fermi jets, the linear momentum transfer and out of plane correlations. In recent years this model has also turned out to be a successful tool to study the creation of particles like pions [84], photons [85], kaons [86], deuterons [87], and etas [88], especially its dependence on the nuclear equation of state. For reviews we refer to refs. [4, 89].

Recently it has been verified that the solution of the classical Boltzmann equation employing the test particle method is indeed equivalent to the analytical solution as far as the single particle distribution is

concerned [90]. It was never investigated, however, how far the success of the BUU model in heavy ion physics depends on the fact that the test particle method induces many body correlations. In the limit of vanishing potentials the test particle method is equivalent to the cascade calculations if one chooses one test particle for each nucleon. In this case the test particle method solves the  $n$ -body and not a one-body equation. The mean field, as calculated in the BUU approach, reduces these correlations in an uncontrolled way. It is not strong enough, however, to wash out the correlations completely. Suppose we change the momenta of all particles of *one* simulation of a cold nucleus at  $t_0$ . Then most of these particles which had scattered at  $t_1$  will scatter again at  $2(t_0 - t_1)$  due to an only moderate change of the mean field generated by all the other simulations whose momenta have not been changed at  $t_1$ . Hence these particles are correlated, which should not happen in a one-body theory. The procedure to make a real one-body theory out of the BUU model is easily seen: At each time step the one-particle distribution function  $f^{(1)}$  has to be generated from the test particles. Then one chooses again randomly test particles according to the distribution  $f^{(1)}$ . This method destroys all correlations in each time step.

For practical purposes one would like to keep these correlations because they are physical. The price one has to pay, however, is that the BUU approach cannot be compared in detail with systematic approximations to the von Neumann equation in the framework of the BBGKY hierarchy [91].

Although some correlations are present in the BUU approach, its predictive power is limited to one-body observables. Many of the most challenging problems such as correlations between emitted particles and the formation of clusters in the exit channel cannot be addressed and even for the one-body observables there remains always the problem of how to deal with the measured composite particles.

*Fluid dynamics and hydrodynamics.* The BUU/VUU calculations can be used to calculate the time evolution of mean values like the density  $\rho(\mathbf{r}, t)$ , the average velocity  $u(\mathbf{r}, t)$  and the temperature  $T(\mathbf{r}, t)$ . Under the assumption of local thermal equilibrium, i.e., when the collision term has established a locally stationary momentum distribution, the time evolution of the mean values  $\rho$ ,  $u$ ,  $T$  is given by the Euler equations. Certainly these are highly idealized assumptions for a heavy ion collision. A more realistic description can be expected from the Navier–Stokes equations, which treat small deviations from equilibrium. The transport coefficients, i.e. the viscosity and the heat conductivity, which appear as an input in the Navier–Stokes equations, as well as a judgement about the validity of this equation at certain impact parameters, can be obtained from the Boltzmann–Uehling–Uhlenbeck calculation.

Hydrodynamical calculations are widely used. In these calculations viscosity and thermal conductivity are just treated as parameters. A detailed description of this approach to heavy ion collisions is given in ref. [4].

#### 4. On the derivation of the quantum molecular dynamics approach

In chapter 3 we have seen that a quantum system of distinguishable particles obeys the cascade equations if the mean free path is large compared to the range of the nucleon–nucleon potential. Then the particles move on shell between subsequent collisions and the scattering amplitudes coincide with those of free particles. The pure fact that nuclei are bound shows that these conditions are not fulfilled in heavy ion reactions.

In a denser system we observe that during a collision the collision partners are interacting with other nucleons, and hence are not in momentum eigenstates before, during and after the interaction.

Furthermore, the amplitudes of different collisions may interfere, and the on shell approximation for the propagation between the collisions may not be valid.

In this chapter we investigate the above-mentioned topics. We start in section 4.1 with the investigation of the most simple situation where the particles are not in plane wave states prior to scattering: the collision of a projectile on a bound target particle. We find that under certain conditions the collision can be treated as a collision between two free particles, and verify that one of these conditions is met in heavy ion collisions.

We want to formulate our approach in phase space coordinates. This amplifies the understanding of the highly complicated heavy ion collisions. How quantum mechanics can be transformed into phase space coordinates has been shown by Wigner [92]. In section 4.2 we present the basic definitions for this transformation and show how the Schrödinger equation is formulated in this approach. We display the close connection between time dependent perturbation theory, formulated with wave functions, and the solution of the time evolution equation of the Wigner transform of the density matrix. In section 4.3 we discuss scattering in the Wigner density formalism. We will derive the equations for potential scattering and two-body collisions. In this section we will present our basic equation. In section 4.4 we extend the work presented in section 4.1 and investigate the interaction between systems of bound particles. We discuss which approximations can be justified, and present the equations that are approximately solved in the quantum molecular dynamics approach. Finally we outline the method of solution and the approximations required to make calculations feasible. In section 4.5 we give reasons for our choice of the initial phase space distribution of the nucleons.

Section 4.6 is devoted to the second of the above-mentioned topics. We calculate the total cross section for a sequence of scatterings and find that there exists a "formation time" and a "formation distance" below which a scattered particle does not interact with the next one as it should in the independent collision approach. This also sheds light on the recent controversy about the existence of a formation time in nuclear reactions at much higher energies. Furthermore we show that in the quasi-free limit the interference terms vanish because two different sequences of scatterings lead to different final states. With increasing width of the final state in momentum space we observe the occurrence of interference. However, due to kinematical constraints the interference term does not play a decisive role in heavy ion collisions at the energies of interest.

To treat nucleons as fermions is beyond the limits of all available kinetic theories, which are suited to describe medium and high energy heavy ion collisions. The quantum molecular dynamics approach is no exception to this. As in all the other approaches, it assumes that the essential quantum features can be mimicked and do not require the calculation of the time evolution of antisymmetrized wave functions. Recently this common belief was questioned. It is argued that a fermionic system does not obey Hamilton's equations. In section 4.6 we will discuss this topic and show that the non-Hamiltonian dynamics is due to the method applied and is not a consequence of the fermionic nature of the particles.

Much of the material presented in this chapter has been discussed by various authors. Many detailed calculations of in-medium effects of an interacting many body system can be found in ref. [93]. The application of the Wigner transforms to – usually high energy – heavy ion collisions was developed in the seventies. Details, especially concerning the high energy limit (eikonal approximation), may be found in refs. [80, 94–97].

#### 4.1. Scattering on a bound particle

In this section we start with the simplest situation in which the free particle transition matrix has to be modified: the scattering of a projectile particle on a particle that is bound in a fixed potential centred

at the origin. We will call this bound particle the target particle and refer to it with the index T. The quantities connected with the beam particle we will denote by P. We will show in this section that under certain conditions the scattering on a bound particle can be described by the free particle transition matrix, and will also demonstrate that one of these conditions is met in medium and high energy heavy ion collisions. We will assume that we can apply nonrelativistic kinematics.

*Description of the scattering.* The target particle is bound by the potential  $U(\mathbf{r}_1)$ . Its Hamiltonian  $H_T$  is therefore

$$H_T = -\frac{1}{2m} \nabla_{\mathbf{r}_1}^2 + U(\mathbf{r}_1) = T_T + U. \quad (4.1)$$

Initially the target particle is in its ground state  $\chi_0(\mathbf{r}_1)$ , which is the solution of the Schrödinger equation,

$$H_T \chi_0(\mathbf{r}_1) = W_0 \chi_0(\mathbf{r}_1). \quad (4.2)$$

$W_0$  is the binding energy of the target particle. After the scattering the target particle may be free or in an excited state  $\chi_n$ , which is an eigenstate of the same Schrödinger equation with the energy eigenvalue  $W_n$ . The projectile particle is initially ( $t \rightarrow -\infty$ ) free. It is described by a plane wave

$$\varphi_p(\mathbf{r}_2) = (2\pi)^{-3/2} e^{i\mathbf{p}\cdot\mathbf{r}_2}, \quad (4.3)$$

which is the solution of the projectile Schrödinger equation,

$$H_p \varphi_p(\mathbf{r}_2) = T_p \varphi_p(\mathbf{r}_2) = -\frac{1}{2m} \nabla_{\mathbf{r}_2}^2 \varphi_p(\mathbf{r}_2) = \frac{p^2}{2m} \varphi_p(\mathbf{r}_2). \quad (4.4)$$

For simplicity we assume the masses of target and projectile particle to be the same. The initial state of the combined target–projectile system is the direct product of the projectile and target states,

$$\phi_{0p} = \varphi_p \chi_0 = (2\pi)^{-3/2} e^{i\mathbf{p}\cdot\mathbf{r}_2} \chi_0(\mathbf{r}_1), \quad (4.5)$$

and satisfies the Schrödinger equation

$$(H_T + H_p) \phi_{0p} = (T_p + T_T + U) \phi_{0p} = (p^2/2m + W_0) \phi_{0p}. \quad (4.6)$$

The interaction between the projectile and the target particle is given by  $V(\mathbf{r}_1 - \mathbf{r}_2)$ . For simplicity, but without losing the generality of the derivation, we neglect any interaction between the projectile and the binding potential. The asymptotic scattering state  $\Psi_{0p}$  can be obtained by solving the Lippmann–Schwinger equation,

$$\Psi_{0p} = \phi_{0p} + \frac{1}{W_0 + p^2/2m - H_T - H_p + i\epsilon} T_b \phi_{0p}, \quad (4.7)$$

$$T_b = V + V \frac{1}{W_0 + p^2/2m - H_T - H_p + i\epsilon} T_b. \quad (4.8)$$

$T_b = \langle p'n | T_b | p0 \rangle$  represents the transition matrix from the initial state  $(p, 0)$  to the final state  $(p', n)$ . If the target particle were initially free (with momentum  $p_T$ ), the scattering would be described by the free particle transition matrix,

$$T = V + V \frac{1}{p_T^2/2m + p^2/2m - T_T - T_P + i\varepsilon} T. \quad (4.9)$$

Thus the fact that the target nucleon is bound is manifested by the appearance of the potential energy operator in the denominator and by the appearance of  $W_0$  instead of the kinetic energy term. In more complicated situations this term encapsulates the full complexity of the  $n$ -body system.

In order to reduce the complexity of the many body system contained in eqs. (4.7) and (4.8), Chew [98] introduced the so-called impulse approximation, in which the bound state transition operator  $T_b$  is approximated by the free scattering transition operator  $T$ . This approximation is valid if one of two quite different criteria are met:

– the binding energy of the bound particle is small compared to the beam energy (weak binding limit),  
or

– the potential is smooth (quasi-classical limit).

In the extreme case of a constant potential  $T_b$  and  $T$  coincide.

The first criterion has frequently been used to justify the calculation of proton–heavy ion collisions at high beam energies in the impulse approximation. For our purpose the second condition is more important because in cold or moderately excited nuclei the gradient of the potential is such that this condition is fulfilled.

*Impulse approximation.* We will now derive the limits of validity of the impulse approximation. For this purpose it is useful to define

$$\begin{aligned} \tilde{K} &= p_T^2/2m \equiv \langle \chi_0 | T_T | \chi_0 \rangle = - \int \chi_0(\mathbf{r}_1) \frac{\nabla^2}{2m} \chi_0(\mathbf{r}_1) d^3r_1, \\ \tilde{U} &= \langle \chi_0 | U | \chi_0 \rangle, \quad R = W_0 - p_T^2/2m. \end{aligned} \quad (4.10)$$

With these definitions we can write the bound state transition operator as

$$T_b = V + V \frac{1}{p_T^2/2m + p^2/2m - T_T - T_P + R - U + i\varepsilon} T_b. \quad (4.11)$$

$T_b$  differs from the free scattering transition matrix of particles with momentum  $p$  and  $p_T$  by the presence of the term  $R - U$ . Under the aforementioned conditions this term is small as we will demonstrate now. Employing the operator identity

$$\frac{1}{A+B} = \frac{1}{A} - \frac{1}{A} B \frac{1}{A} + \dots, \quad (4.12)$$

we can expand the propagator and obtain

$$T_b = T + T G_0^+ (U - R) G_0^+ T + O(U - R)^2. \quad (4.13)$$

$G_0^+$  is defined as

$$G_0^+ = \frac{1}{p_T^2/2m + p^2/2m - T_T - T_p + i\varepsilon} . \quad (4.14)$$

In order to justify the impulse approximation, i.e. the approximation of  $T_b$  by  $T$ , we have to show that the correction term

$$\Delta = TG_0^+(U - R)G_0^+T \quad (4.15)$$

is small compared to  $T$ . There may be two situations in which this happens: either both  $U$  and  $R$  are small quantities, or  $(U - R)$  is small. In the first case – the weak binding limit – we can assume  $U$  to be zero because a finite  $U$  lowers the correction. If we assume that the particles move on shell between collisions, one finds for the correction term [93]

$$\Delta_{U=0} \approx T \left( \frac{2m}{\hbar p} f \cdot R \right) , \quad (4.16)$$

where  $f$  is the scattering amplitude. Aiming at corrections of the order of 10% for  $R = 10$  MeV, we need projectile momenta of the order of 2 GeV/ $c$ .

We now investigate the second condition, i.e. the validity of the impulse approximation for smoothly varying potentials. If we take  $U$  as rigorously constant,  $T_b$  coincides with  $T$  because the bound particle is also in a momentum eigenstate, and we obtain  $R = \tilde{U}$ . Thus intuitively it is obvious that for smooth potentials the bound particles have a narrow width in momentum space.

In order to estimate  $\Delta$  for a smoothly varying potential we assume that we can approximate

$$(U - R)G_0T \approx [U, G_0T] , \quad (4.17)$$

which implies

$$\langle \chi_0 | U | \chi_0 \rangle \approx \langle k | U | k' \rangle \quad \text{for } k \approx k' , \quad (4.18)$$

and zero otherwise. If we further assume that the momentum transfer due to the potential is small compared to that due to scattering, and hence

$$[U, T] \approx 0 , \quad (4.19)$$

we obtain

$$(U - R)G_0T \approx [U, G_0]T \approx G_0[T_T, U]G_0T . \quad (4.20)$$

To obtain the right hand side of this expression we have used the identity

$$\frac{1}{A} - \frac{1}{B} = \frac{1}{A} (B - A) \frac{1}{B} . \quad (4.21)$$

The last expression can be easily verified using the matrix representation of the operators. The commutator can now be approximated,

$$[T_{\text{T}}, U] \approx -\frac{1}{2m} [\nabla^2, U] \approx \frac{1}{2m} \frac{\tilde{U}}{a^2}, \quad (4.22)$$

where  $a$  is the range of the potential.

Collecting the terms we obtain

$$T_{\text{b}} \approx T + \frac{1}{2Ma^2} \tilde{U}(TG_0^3T) = T(1 + \Delta), \quad (4.23)$$

with

$$\langle ij|TG_0^3T|mn\rangle = \int \frac{\delta(i+j-k-l)\delta(k+l-m-n)\langle ij|T|kl\rangle\langle kl|T|mn\rangle}{[(1/2m)(m^2+n^2-l^2-k^2)+i\epsilon]^3} d^3l d^3k. \quad (4.24)$$

Employing the residue theorem we can evaluate this integral and obtain [93]

$$\Delta = \frac{f\tilde{U}2m\hbar}{a^2p^3} T. \quad (4.25)$$

For typical values  $f \approx 1$  fm,  $\tilde{U} = 40$  MeV,  $a = 3$  fm and  $p = 300$  MeV/ $c$  we obtain

$$\Delta \approx 1/15.$$

Although the weak binding condition is not fulfilled in this case, we only expect corrections of the order of 10% (due to the smooth potential) if we use  $T$  instead of  $T_{\text{b}}$ . For more energetic particles the corrections decrease as  $p^{-3}$ , hence at  $p = 500$  MeV/ $c$  we have corrections of the order of 1%.

Next we calculate the wave function of the final state in the impulse approximation. It is defined by the Lippmann–Schwinger equation

$$\Psi_{0p} = \phi_{0p} + \frac{1}{W_0 + p^2/2m - T_{\text{P}} - T_{\text{T}} - U + i\epsilon} T\phi_{0p}. \quad (4.26)$$

Similar to the above case of the transition matrix, we can expand the propagator around the free particle propagator,

$$\begin{aligned} & \frac{1}{p_{\text{T}}^2/2m + R + p^2/2m - T_{\text{T}} - T_{\text{P}} - U + i\epsilon} \\ &= \frac{1}{p^2/2m + p_{\text{T}}^2/2m - T_{\text{T}} - T_{\text{P}} + i\epsilon} \left[ \sum_n \left( (U - R) \frac{1}{p^2/2m + p_{\text{T}}^2/2m - T_{\text{T}} - T_{\text{P}} + i\epsilon} \right)^n \right]. \end{aligned} \quad (4.27)$$

If the impulse approximation is valid, we can truncate the expansion after the leading term and obtain finally

$$\Psi_{0p} = \phi_{0p} + \frac{1}{p^2/2m + p_T^2/2m - T_T - T_P + i\varepsilon} T\phi_{0p},$$

or, in matrix representation,

$$\langle \mathbf{k}, \mathbf{k}_T | \Psi \rangle = \langle \mathbf{k}, \mathbf{k}_T | \phi_{0p} \rangle + \int \frac{\langle \mathbf{k} \mathbf{k}_T | T | \mathbf{p}_T \mathbf{p} \rangle \langle \mathbf{p}_T | \chi_0 \rangle}{p_T^2/2m + p^2/2m - k^2/2m - k_T^2/2m + i\varepsilon} \delta(\mathbf{k} + \mathbf{k}_T - \mathbf{p} - \mathbf{p}_T) d^3 p_T. \quad (4.28)$$

Thus in the impulse approximation the particles scatter as if they are free. The only reminder of the fact that the particles are bound is their wave function. The bound particles are not in momentum eigenstates, but have a momentum distribution  $|\chi_0(p)|^2$ . The impulse approximation will be the essential tool when we derive the time evolution equation for nucleus–nucleus collisions. However, before that it is necessary to give an introduction into the Wigner density formalism.

#### 4.2. Wigner densities

*Definitions.* We want to study the time evolution of a nucleus–nucleus collision. This can be achieved by solving the  $n$ -body Schrödinger equation. However, even if we succeed, the result would remain rather unclear. We are used to understanding the motion of particles in the coordinates of the phase space  $(\mathbf{P}, \mathbf{r}, t)$  but the Schrödinger equation would yield observables which depend on coordinate space or momentum space only. One can overcome this lack of intuitive understanding by introducing Wigner densities [92]. They are defined as Fourier transforms of the density operator  $\rho(\mathbf{r}, \mathbf{r}')$  and depend on the phase space coordinates  $\mathbf{P}$  and  $(\mathbf{r} + \mathbf{r}')/2$ . The Wigner densities allow us to formulate quantum mechanics in a language very close to classical transport theory, and therefore give a quite intuitive understanding of the time evolution of the reaction.

The Wigner transform of the Schrödinger equation has the same form as the classical continuity equation. In the classical limit it is formally identical to the Vlasov equation, which describes the time evolution of the single particle phase space density in an external potential. One of the major advantages of this formalism is the possibility of writing the time evolution equations as a Taylor series expansion in  $\hbar$ . Therefore a smooth transition to the classical limit exists. Furthermore, as a full quantum theory formulated in classical phase space, this approach provides much insight into quantum phenomena and how they can be understood in terms of phase space observables.

We start by quoting the basic relations. The Wigner transform  $O^W$  of an operator  $O$  is defined by

$$O^W(\mathbf{P}, \mathbf{R}) = \int \frac{d^3 r}{(2\pi)^3} e^{i\mathbf{P}\cdot\mathbf{r}} \langle \mathbf{R} - \mathbf{r}/2 | O | \mathbf{R} + \mathbf{r}/2 \rangle = \int \frac{d^3 p}{(2\pi)^3} e^{-i\mathbf{p}\cdot\mathbf{R}} \langle \mathbf{P} - \mathbf{p}/2 | O | \mathbf{P} + \mathbf{p}/2 \rangle. \quad (4.29)$$

Consequently, the Wigner transform of a commutator  $[O, R]$  is given by

$$[O, A]^W = \int \frac{d^3 r}{(2\pi)^3} e^{i\mathbf{P}\cdot\mathbf{r}} \langle \mathbf{R} - \mathbf{r}/2 | [O, A] | \mathbf{R} + \mathbf{r}/2 \rangle = -2i O^W(\mathbf{P}, \mathbf{R}) \sin(\Lambda/2) A^W(\mathbf{P}, \mathbf{R}), \quad (4.30)$$

where  $\Lambda B$  is defined as

$$A \Lambda B = \nabla_P A \cdot \nabla_R B - \nabla_P B \cdot \nabla_R A . \quad (4.31)$$

The expectation value of the operator  $O$  is given by

$$\langle \mathbf{R} | O | \mathbf{R} \rangle = \int O^W(\mathbf{P}, \mathbf{R}) d^3 P , \quad (4.32)$$

$$\langle \mathbf{P} | O | \mathbf{P} \rangle = \int O^W(\mathbf{P}, \mathbf{R}) d^3 R . \quad (4.33)$$

This is the connection to measurable quantities. If we identify  $O$  with the density operator, we see that its Wigner density has just the properties of the classical phase space density. Identifying  $O$  with the density operator we obtain for its Wigner transform, usually called the Wigner density,

$$\begin{aligned} f(\mathbf{R}, \mathbf{P}, t) &= \int \frac{d^3 p}{(2\pi)^3} e^{i\mathbf{R} \cdot \mathbf{p}} \langle \mathbf{P} + \mathbf{p}/2 | \psi(t) \rangle \langle \psi(t) | \mathbf{P} - \mathbf{p}/2 \rangle \\ &= \int \frac{d^3 r}{(2\pi)^3} e^{-i\mathbf{P} \cdot \mathbf{r}} \langle \mathbf{R} + \mathbf{r}/2 | \psi(t) \rangle \langle \psi(t) | \mathbf{R} - \mathbf{r}/2 \rangle . \end{aligned} \quad (4.34)$$

For later purposes we define

$$f(\mathbf{P}, \mathbf{p}, t) \equiv \langle \mathbf{P} + \mathbf{p}/2 | \psi(t) \rangle \langle \psi(t) | \mathbf{P} - \mathbf{p}/2 \rangle , \quad (4.35)$$

the density matrix in momentum space representation. By integration over the coordinate and momentum space we obtain the density in momentum and coordinate space, respectively,

$$\int d^3 R f(\mathbf{R}, \mathbf{P}, t) = \langle \mathbf{P} | \psi(t) \rangle \langle \psi(t) | \mathbf{P} \rangle = |\psi(\mathbf{P}, t)|^2 , \quad (4.36)$$

$$\int d^3 P f(\mathbf{R}, \mathbf{P}, t) = \langle \mathbf{R} | \psi(t) \rangle \langle \psi(t) | \mathbf{R} \rangle = |\psi(\mathbf{R}, t)|^2 . \quad (4.37)$$

However, whereas a classical phase space density can never be negative, the Wigner density is not positive definite. For further details we refer to the review article of Carruthers and Zachariasen [99].

The equation for the time evolution of the one-body Wigner density of a particle moving in a potential  $V(\mathbf{r})$  can be obtained by employing the Schrödinger equation,

$$\begin{aligned} \frac{\partial}{\partial t} f(\mathbf{R}, \mathbf{P}, t) &= -i \int \frac{d^3 p}{(2\pi)^3} e^{i\mathbf{R} \cdot \mathbf{p}} \left( \frac{(\mathbf{P} + \mathbf{p}/2)^2}{-2m} - \frac{(\mathbf{P} - \mathbf{p}/2)^2}{-2m} \right) f(\mathbf{P}, \mathbf{p}, t) \\ &\quad - i \int \frac{d^3 r}{(2\pi)^3} e^{-i\mathbf{P} \cdot \mathbf{r}} \langle \mathbf{R} + \mathbf{r}/2 | [V, |\psi(t)\rangle \langle \psi(t)|] | \mathbf{R} - \mathbf{r}/2 \rangle \\ &= -\frac{\mathbf{P}}{m} \cdot \nabla_{\mathbf{R}} f(\mathbf{P}, \mathbf{R}, t) - i \int \frac{d^3 r d^3 P'}{(2\pi)^3} e^{-i(\mathbf{P}-\mathbf{P}') \cdot \mathbf{r}} [V(\mathbf{R} + \mathbf{r}/2) - V(\mathbf{R} - \mathbf{r}/2)] f(\mathbf{P}', \mathbf{R}, t) . \end{aligned} \quad (4.38)$$

Formally we can write the time evolution equation of the Wigner density as

$$\left(\frac{\partial}{\partial t} + \frac{\mathbf{P}}{m} \cdot \nabla_{\mathbf{R}}\right) f(\mathbf{P}, \mathbf{R}, t) = \int d^3 P' K_1(\mathbf{P} - \mathbf{P}', \mathbf{R}) f(\mathbf{P}', \mathbf{R}, t). \quad (4.39)$$

So far we have not gained anything. The solution of this equation is completely equivalent to the solution of the Schrödinger equation.

Before we proceed to scattering processes we take a closer look at the function  $K_1$  defined in eq. (4.39),

$$K_1(\mathbf{P} - \mathbf{P}', \mathbf{R}) = \frac{1}{i\hbar} \int \frac{d^3 r}{(2\pi\hbar)^3} e^{-i(\mathbf{P}-\mathbf{P}') \cdot \mathbf{r}/\hbar} [V(\mathbf{R} + \mathbf{r}/2) - V(\mathbf{R} - \mathbf{r}/2)]. \quad (4.40)$$

We have restored  $\hbar$  here for reasons which will soon become obvious. This function can be evaluated in two different ways. Either we can write it as the Fourier transform of the potential,

$$K_1(\mathbf{P} - \mathbf{P}', \mathbf{R}) = \frac{16}{\hbar^4} \sin(2(\mathbf{P} - \mathbf{P}') \cdot \mathbf{R}/\hbar) V(2(\mathbf{P} - \mathbf{P}')), \quad (4.41)$$

with

$$V(\mathbf{p}) = \frac{1}{(2\pi)^3} \int e^{i\mathbf{p} \cdot \mathbf{r}} V(\mathbf{r}) d^3 r,$$

or one can expand the potential into a Taylor series around  $\mathbf{R}$ ,

$$K_1(\mathbf{P} - \mathbf{P}', \mathbf{R}) = \frac{2}{\hbar} \sin(\hbar \nabla_{\mathbf{R}} \cdot \nabla_{\mathbf{P}}/2) V(\mathbf{R}) \delta(\mathbf{P} - \mathbf{P}'). \quad (4.42)$$

The last form is especially suitable for the semiclassical limit. We see that  $K_1$  can be viewed as a series with the expansion coefficient  $\hbar \nabla_{\mathbf{R}} \cdot \nabla_{\mathbf{P}}$ . Hence the Schrödinger equation is equivalent to the classical Vlasov equation,

$$\left(\frac{\partial}{\partial t} + \frac{\mathbf{P}}{m} \cdot \nabla_{\mathbf{R}}\right) f(\mathbf{P}, \mathbf{R}, t) = [\nabla_{\mathbf{R}} V(\mathbf{R})] \cdot \nabla_{\mathbf{P}} f(\mathbf{P}, \mathbf{R}, t), \quad (4.43)$$

provided  $\hbar \nabla_{\mathbf{R}} \cdot \nabla_{\mathbf{P}}$  is small compared to 1, i.e., if the potential and the momentum distribution are smooth. The Vlasov equation describes the time evolution of the phase space density of particles which move on classical orbits specified by the Hamilton equations  $\partial \mathbf{R}/\partial t = \mathbf{P}/m$  and  $\partial \mathbf{P}/\partial t = -\nabla_{\mathbf{R}} V$ .

We see that in the Wigner formalism the quantum equation is just a Taylor expansion around the classical equation in the parameter  $\hbar$ . The validity of the classical approximation depends on the gradients of the potential and the phase space density, which are correlated. The classical limit is valid when the potential is slowly changing. Hence the range of validity is determined by the same parameter as that of the impulse approximation.

*The relation between Wigner densities and time dependent perturbation theory.* To demonstrate the close connection between the Schrödinger equation and eq. (4.39) and in order to see how the Wigner transformation helps to understand quantum mechanics, we solve both in parallel using the Green's function method. The Green's functions are the solutions of the following equations:

$$\left(\frac{\partial}{\partial t} + \frac{\mathbf{P}}{m} \cdot \nabla_{\mathbf{R}}\right) G^{\text{W}}(\mathbf{P}, \mathbf{R} - \mathbf{R}', t - t') = \delta(\mathbf{R} - \mathbf{R}') \delta(t - t'), \quad (4.44)$$

$$\left(i\hbar \frac{\partial}{\partial t} + \frac{\hbar^2 \nabla_r^2}{2m}\right) G_0^+(\mathbf{r} - \mathbf{r}', t - t') = \delta(\mathbf{r} - \mathbf{r}') \delta(t - t'). \quad (4.45)$$

These equations have the solutions

$$G^W(\mathbf{P}, \mathbf{R} - \mathbf{R}', t - t') = \Theta(t - t') \delta(\mathbf{R} - \mathbf{R}' - (\mathbf{P}/m)(t - t')), \quad (4.46)$$

$$\begin{aligned} G_0^+(\mathbf{r} - \mathbf{r}', t - t') &= \Theta(t - t') \frac{-i}{\hbar} \int \frac{d^3 k}{(2\pi)^3} e^{ik \cdot (\mathbf{r} - \mathbf{r}')} \exp\left[\left(-i \frac{\hbar k^2}{2m} - \varepsilon\right)(t - t')\right] \\ &= \Theta(t - t') \frac{-i}{\hbar} \left(\frac{m}{2\pi i \hbar (t - t')}\right)^{3/2} \exp\left(\frac{im|\mathbf{r} - \mathbf{r}'|^2}{2\hbar(t - t')}\right). \end{aligned} \quad (4.47)$$

The solution of the time evolution equations is given by

$$f(\mathbf{P}, \mathbf{R}, t) = f_0(\mathbf{P}, \mathbf{R}, t) + \int_{-\infty}^t dt' \int d^3 P' K(\mathbf{P} - \mathbf{P}', \mathbf{R} - (\mathbf{P}/m)(t - t')) f(\mathbf{P}', \mathbf{R} - (\mathbf{P}/m)(t - t'), t'), \quad (4.48)$$

$$\psi^+(\mathbf{r}, t) = \phi(\mathbf{r}, t) - \frac{i}{\hbar} \int d\mathbf{r}' \int_{-\infty}^t dt' \int \frac{d^3 k}{(2\pi)^3} e^{ik \cdot (\mathbf{r} - \mathbf{r}')} \exp\left[\left(-i \frac{\hbar k^2}{2m} - \varepsilon\right)(t - t')\right] V(\mathbf{r}') \psi^+(\mathbf{r}', t'). \quad (4.49)$$

Here  $f_0(\mathbf{P}, \mathbf{r}, t)$  and  $\phi(\mathbf{r}, t)$  are the solutions of the homogeneous equations.

If we assume that the potential is time independent but disappears for  $r \rightarrow \infty$  and  $\phi(t)$  and  $\psi(t)$  thus have a trivial time dependence,  $\phi(t) = \phi_E e^{iEt}$  and  $\psi(t) = \psi_E e^{iEt}$ , the time dependence drops out completely and we end up with the Lippmann-Schwinger equation,

$$\psi_E^+ = \phi_E + G_0^+(E) V \psi_E^+ = \phi_E + G_0^+(E) T(E) \phi_E. \quad (4.50)$$

This equation is the quantum description of the scattering of a particle in a potential  $V$  and contains exactly the same information as eq. (4.48).

Of course a similar simplification does not show up in the Wigner density formalism, since this approach describes the space-time structure of the reaction. So scattering does not take place between different quantum states but at different points in phase space. How quantum mechanics works in phase space can best be discussed if we expand to second order:

$$\begin{aligned} f(\mathbf{P}, \mathbf{R}, t) &= f_0(\mathbf{P}, \mathbf{R}, t) + \int_{-\infty}^t dt' \int d^3 P' K(\mathbf{P} - \mathbf{P}', \mathbf{R} - (\mathbf{P}/m)(t - t')) f_0(\mathbf{P}', \mathbf{R} - (\mathbf{P}/m)(t - t'), t') \\ &\quad + \int_{-\infty}^t dt' \int_{-\infty}^{t'} dt'' \int d^3 P'' \int d^3 P' K(\mathbf{P} - \mathbf{P}', \mathbf{R} - (\mathbf{P}/m)(t - t')) \\ &\quad \times K(\mathbf{P}' - \mathbf{P}'', \mathbf{R} - (\mathbf{P}/m)(t - t') - (\mathbf{P}'/m)(t' - t'')) \\ &\quad \times f_0(\mathbf{P}'', \mathbf{R} - (\mathbf{P}/m)(t - t') - (\mathbf{P}'/m)(t' - t''), t''). \end{aligned} \quad (4.51)$$

Now the Wigner density approach allows a very intuitive interpretation [72, 99]: The time evolution of the quantum particle interacting with a potential proceeds by alternating quantum and classical steps. In the classical step the particle moves on the classical trajectory determined by Hamilton's equations. The quantum step  $K(\mathbf{P}, \mathbf{R})$  makes the particle jump in momentum space at a given space-time point. This jump transfers a point in momentum space into a momentum space distribution, i.e., it acts as a random force. Thus the higher order terms neglected in eq. (4.43) act as a random force. Since they are proportional to  $\hbar$  we see that the Wigner formalism displays quite nicely the quantum fluctuations around the classical path, which cannot be neglected if the gradients of the potential are strong, as they are for the nucleon potentials which have a hard or soft core. Thus stronger gradients not only yield stronger forces but also larger fluctuations around the mean trajectories. This is one of the reasons why classical molecular dynamics fails in describing heavy ion collisions. We will see in the next section that there also exists a closed solution of the time evolution equation of the Wigner density. This equation will have exactly the structure discussed above.

### 4.3. Scattering in the Wigner density formalism

*General discussion.* We are now prepared to calculate the scattering of particles in the Wigner formalism. Being interested in the time evolution of the scattering event, we would like to be able to define the beginning and the end of the scattering. Hence we have to give up the plane wave approximation, which we used for simplicity in section 4.1, and have to return to the formulation of the scattering in terms of wave packets. These we define for the scattered and the incoming waves as

$$\psi(\mathbf{r}, t) = \int \frac{d^3 p}{(2\pi)^{3/2}} g(\mathbf{p}) e^{-iE_p t} \psi_p(\mathbf{r}) = \int \frac{d^3 p}{(2\pi)^{3/2}} g(\mathbf{p}) \psi_p(\mathbf{r}, t), \quad (4.52)$$

$$\phi(\mathbf{r}, t) = \int \frac{d^3 p}{(2\pi)^{3/2}} g(\mathbf{p}) e^{i\mathbf{p}\cdot\mathbf{r} - iE_p t},$$

where  $E_p$  equals  $p^2/2m$ . A very convenient choice, which we will use later, are the Gaussian wave packets known under the name coherent states,

$$g(\mathbf{P}) = (2L/\pi)^{3/4} e^{-(\mathbf{P}-\mathbf{P}_0)^2 L} e^{-i\mathbf{P}\cdot\mathbf{R}_0}. \quad (4.53)$$

The Wigner density of coherent states can easily be calculated,

$$\begin{aligned} f(\mathbf{P}, \mathbf{R}, t) &= \int \frac{d^3 q}{(2\pi)^3} e^{i\mathbf{q}\cdot(\mathbf{R}-\mathbf{v}_p t)} g(\mathbf{P} + \mathbf{q}/2) g^*(\mathbf{P} - \mathbf{q}/2) \\ &= \frac{1}{\pi^3} e^{-(\mathbf{P}-\mathbf{P}_0)^2 2L} e^{-(\mathbf{R}-\mathbf{R}_0-\mathbf{v}_p t)^2 2L}. \end{aligned} \quad (4.54)$$

$\mathbf{v}_p$  is defined as  $\mathbf{P}/m$ . We start now to derive the time evolution equation of the Wigner density for potential scattering. We begin by recalling the solution of the Schrödinger equation in the Wigner formalism (eq. 4.38),

$$\begin{aligned} \left( \frac{\partial}{\partial t} + \frac{\mathbf{P}}{m} \cdot \nabla_{\mathbf{R}} \right) f(\mathbf{P}, \mathbf{R}, t) = & \frac{1}{i} \int \frac{d^3 q}{(2\pi)^3} e^{i\mathbf{q} \cdot \mathbf{R}} \{ \langle \mathbf{P} + \mathbf{q}/2 | V | \psi(t) \rangle \langle \psi(t) | \mathbf{P} - \mathbf{q}/2 \rangle \\ & - \langle \mathbf{P} + \mathbf{q}/2 | \psi(t) \rangle \langle \psi(t) | V | \mathbf{P} - \mathbf{q}/2 \rangle \}. \end{aligned} \quad (4.55)$$

$f(\mathbf{P}, \mathbf{R}, t)$  denotes the Wigner transform of  $|\psi(t)\rangle \langle \psi(t)|$ .

*Potential scattering.* We now discuss how to apply the Wigner density formalism to scattering events. Due to causality the wavefunction  $|\psi_k\rangle$  obeys the well known relation

$$\psi_k^+ = \phi_k + \frac{1}{E_k - H_0 + i\varepsilon} V \psi_k^+. \quad (4.56)$$

We now insert this relation in the above eq. (4.55) and replace  $\psi(t)$  by eq. (4.56) whenever  $V$  is not acting directly on  $\psi$ . Performing the time integration over  $dt'$  we obtain

$$\begin{aligned} \left( \frac{\partial}{\partial t} + \frac{\mathbf{P}}{m} \cdot \nabla_{\mathbf{R}} \right) f(\mathbf{P}, \mathbf{R}, t) = & \frac{1}{i} \int \frac{d^3 p \, d^3 k \, d^3 k'}{(2\pi)^3} g(\mathbf{k}) g^*(\mathbf{k}') e^{i\mathbf{p} \cdot \mathbf{R}} e^{-i(E_k - E_{k'})t} \\ & \times \left[ \langle \mathbf{P} + \mathbf{p}/2 | V | \psi_k \rangle \langle \psi_{k'} | \mathbf{P} - \mathbf{p}/2 \rangle - \langle \mathbf{P} + \mathbf{p}/2 | \psi_k \rangle \langle \psi_{k'} | V | \mathbf{P} - \mathbf{p}/2 \rangle \right. \\ & \left. + \langle \mathbf{P} + \mathbf{p}/2 | V | \psi_k \rangle \langle \psi_{k'} | V | \mathbf{P} - \mathbf{p}/2 \rangle \left( \frac{1}{E_k - E_{\mathbf{P}+\mathbf{p}/2} + i\varepsilon} - \frac{1}{E_{k'} - E_{\mathbf{P}-\mathbf{p}/2} - i\varepsilon} \right) \right]. \end{aligned} \quad (4.57)$$

We now make use of the relation between the potential and the transition matrix  $T|\phi\rangle = V|\psi\rangle$  and define

$$g(\mathbf{k}) g^*(\mathbf{k}') = f_0(\mathbf{k} + \mathbf{k}', (\mathbf{k} - \mathbf{k}')/2) = \int e^{-i(\mathbf{k} - \mathbf{k}') \cdot \mathbf{R}} f_0(\mathbf{R}, \mathbf{k} + \mathbf{k}') d^3 R, \quad (4.58)$$

and obtain finally

$$\begin{aligned} \left( \frac{\partial}{\partial t} + \frac{\mathbf{P}}{m} \cdot \nabla_{\mathbf{R}} \right) f(\mathbf{R}, \mathbf{P}, t) = & \frac{1}{i} \int \frac{d^3 p \, d^3 Q \, d^3 q}{(2\pi)^3} e^{i\mathbf{R} \cdot \mathbf{p}} f_0(\mathbf{Q}, \mathbf{q}, t) \\ & \times \left[ \langle \mathbf{P} + \mathbf{p}/2 | T | \mathbf{Q} + \mathbf{q}/2 \rangle \delta(\mathbf{P} - \mathbf{p}/2 - \mathbf{Q} + \mathbf{q}/2) - \langle \mathbf{P} - \mathbf{p}/2 | T^\dagger | \mathbf{Q} - \mathbf{q}/2 \rangle \delta(\mathbf{P} + \mathbf{p}/2 - \mathbf{Q} - \mathbf{q}/2) \right. \\ & \left. + \langle \mathbf{P} + \mathbf{p}/2 | T | \mathbf{Q} + \mathbf{q}/2 \rangle \langle \mathbf{Q} - \mathbf{q}/2 | T^\dagger | \mathbf{P} - \mathbf{p}/2 \rangle \right. \\ & \left. \times \left( \frac{1}{(\mathbf{Q} + \mathbf{q}/2)^2/2m - (\mathbf{P} + \mathbf{p}/2)^2/2m + i\varepsilon} - \frac{1}{(\mathbf{Q} - \mathbf{q}/2)^2/2m - (\mathbf{P} - \mathbf{p}/2)^2/2m - i\varepsilon} \right) \right]. \end{aligned} \quad (4.59)$$

$f_0$  is the time evolved free wave packet, corresponding to  $\Phi$  in the Lippmann-Schwinger equation (4.50).

This is our seminal equation. Its structure will not change when we proceed to two-body scattering of bound scattering partners in the impulse approximation. As we have seen in section 4.1, in the impulse approximation the free particle transition matrix is used, and only the wavefunction contains the information that the particle is bound. For the above equation this means that only the Wigner density  $f_0$  carries this information.

Unfortunately eq. (4.59) is far from being transparent. Therefore we will discuss now the meaning of the different terms. If we set the right hand side equal to zero we have just the time evolution equation for free particles. The right hand side contains the description of the scattering. It consists of two terms linear in  $T$ , and a term which is quadratic in  $T$  ( $I_3$ ). The linear terms are proportional to the real ( $I_1$ ) and the imaginary part ( $I_2$ ) of the transition matrix, respectively. We start with the interpretation of the linear terms. For this purpose we perform the integrations and make use of the relation (4.58). For  $I_1$  we arrive at

$$I_1(\mathbf{P}, \mathbf{R}, t) = 16 \int d^3P' \sin(2(\mathbf{P} - \mathbf{P}') \cdot \mathbf{R}) \operatorname{Re} T(2(\mathbf{P} - \mathbf{P}')) f_0(\mathbf{P}', \mathbf{R}, t). \quad (4.60)$$

The physics of the first term is revealed by comparing (4.60) with eq. (4.42). Both expressions have exactly the same structure. In our case the potential is replaced by the real part of the transition matrix, which acts on the Wigner transform of the freely propagated wave packet  $f_0$  and not on that of the full  $f$ . Thus the real part of the transition matrix acts as an effective potential. If the effective potential is sufficiently smooth, we can expand the expression in terms of  $\hbar$  analogously to the discussion following eq. (4.42), and obtain

$$I_1(\mathbf{P}, \mathbf{R}, t) = [\nabla_{\mathbf{R}} T(\mathbf{R})] \cdot \nabla_{\mathbf{P}} f_0(\mathbf{P}, \mathbf{R}, t). \quad (4.61)$$

Thus in the quasiclassical limit, which is also the limit where the impulse approximation is valid, the real part of the transition matrix acts as a force.

To discuss the term which is proportional to the imaginary part of the transition matrix it is best to assume a specific form of the transition matrix. Since we ultimately want to deal with nucleon–nucleon collisions we choose a Gaussian form,

$$\langle \mathbf{p} | T | \mathbf{q} \rangle = (A + iB) c^{-a(\mathbf{q} - \mathbf{p})^2}, \quad (4.62)$$

which fits nuclear scattering data for beam energies larger than 100 MeV [100]. Using eq. (4.62) the second term can now be cast into the form

$$I_2(\mathbf{P}, \mathbf{R}, t) = -\frac{8v_{\text{rel}}}{(2\pi)^3} \int d^3P' \cos(2(\mathbf{P} - \mathbf{P}') \cdot \mathbf{R}) e^{-4(\mathbf{P} - \mathbf{P}')^2 a} f_0(\mathbf{P}', \mathbf{R}, t) \sigma_{\text{tot}}. \quad (4.63)$$

Here we have made use of relation (3.34). The meaning of the term becomes even more evident if we perform the integration over  $d^3R$ . Then  $I_2(\mathbf{P}, t)$  is proportional to the product of the total nucleon–nucleon cross section for point particles and the form factor, i.e. the Fourier transform of the spatial distribution of the particle. Having an overall minus sign it describes the scattering of particles out of the phase space cell at  $(\mathbf{P}', \mathbf{R})$ .

Now we come to  $I_3$ . The Gaussian form of the scattering amplitude allows us to express the square of the transition matrix in eq. (4.59) in the form

$$\langle \mathbf{P} + \mathbf{p}/2 | T | \mathbf{Q} + \mathbf{q}/2 \rangle \langle \mathbf{Q} - \mathbf{q}/2 | T^\dagger | \mathbf{P} - \mathbf{p}/2 \rangle = |\langle \mathbf{P} | T | \mathbf{Q} \rangle|^2 e^{-a(\mathbf{p}-\mathbf{q})^2/2} \sim \frac{d\sigma}{d\Omega} (\mathbf{P} \rightarrow \mathbf{Q}) e^{-a(\mathbf{p}-\mathbf{q})^2/2} \quad (4.64)$$

For  $\mathbf{P} \cdot \mathbf{q} < p^2$  and  $\mathbf{Q} \cdot \mathbf{q} < Q^2$  the difference of the propagators is just equivalent to the energy conserving  $\delta$ -function  $\delta(E_Q - E_P)$ . Substituting these expressions in  $I_3$  we find

$$I_3(\mathbf{P}, \mathbf{R}, t) \sim \int \frac{d^3p d^3Q d^3q}{(2\pi)^3} e^{-i\mathbf{R} \cdot \mathbf{p}} f_0(\mathbf{Q}, \mathbf{q}, t) e^{-a(\mathbf{p}-\mathbf{q})^2/2} \delta(E_P - E_Q) \frac{d\sigma}{d\Omega} (\mathbf{Q} \rightarrow \mathbf{P}). \quad (4.65)$$

We see that the term quadratic in  $T$  describes the scattering of particles into the phase space cell at  $(\mathbf{P}, \mathbf{R})$ .

Thus the equation which describes the time evolution of a quantum particle which traverses a potential has the same formal structure as the classical Boltzmann equation. Besides terms which describe the free streaming of particles, we have in the semiclassical limit an effective potential as well as a gain and a loss term, which describe the scattering into and out of the considered phase space cell. This is a remarkable result because in classical physics this situation would be described by the Vlasov equation, which has a quite different structure. This result teaches us two things:

(1) The analogy between the classical Boltzmann equation and the time evolution equation of quantum wave packets can only be formal. Obviously collisions can be quantum features without any classical analogs.

(2) In a quantum equation strong potential gradients, such as those caused by the hard core in nucleon-nucleon potentials, do not cause a strong force as in a classical equation. Rather they show up as a random force or, what amounts to the same, as a cross section. Thus classical molecular dynamics with two-body nucleon-nucleon potentials is conceptually wrong if applied to a system which is dominated by quantum effects.

*Two-body scattering.* To deepen the understanding of our seminal eq. (4.59), we proceed now by treating the scattering of two wave packets in the same formalism. In classical physics this situation is described by the Boltzmann equation with vanishing potential term. Here we start from the two-body Schrödinger equation, which reads after a Wigner transformation

$$\left( \frac{\partial}{\partial t} + \frac{\mathbf{P}_1}{2m} \cdot \nabla_{\mathbf{R}_1} + \frac{\mathbf{P}_2}{2m} \cdot \nabla_{\mathbf{R}_2} \right) f(\mathbf{R}_1, \mathbf{R}_2, \mathbf{P}_1, \mathbf{P}_2, t) \\ = \int d^3\mathbf{P}'_1 d^3\mathbf{P}'_2 K_2(\mathbf{P}_1 - \mathbf{P}'_1, \mathbf{P}_2 - \mathbf{P}'_2, \mathbf{R}_1, \mathbf{R}_2) f(\mathbf{R}_1, \mathbf{R}_2, \mathbf{P}'_1, \mathbf{P}'_2, t), \quad (4.66)$$

where  $K_2(\mathbf{P}_1 - \mathbf{P}'_1, \mathbf{P}_2 - \mathbf{P}'_2, \mathbf{R}_1, \mathbf{R}_2)$  is completely analogous to  $K_1$ ,

$$iK_2(\mathbf{P}_1 - \mathbf{P}'_1, \mathbf{P}_2 - \mathbf{P}'_2, \mathbf{R}_1, \mathbf{R}_2) = \int \frac{d^3\mathbf{r}_1 d^3\mathbf{r}_2}{(2\pi)^6} e^{i(\mathbf{P}'_1 - \mathbf{P}_1) \cdot \mathbf{r}_1 + i(\mathbf{P}'_2 - \mathbf{P}_2) \cdot \mathbf{r}_2} \\ \times [V(\mathbf{R}_1 + \mathbf{r}_1/2, \mathbf{R}_2 + \mathbf{r}_2/2) - V(\mathbf{R}_1 - \mathbf{r}_1/2, \mathbf{R}_2 - \mathbf{r}_2/2)]. \quad (4.67)$$

Evaluating the transition matrix on the momentum shell, we can integrate over the centre of mass coordinates of the scattering partners and obtain an equation which is formally completely equivalent to eq. (4.59). All phase space variables, however, now refer to the relative coordinates, and  $m$  has to be replaced by the reduced mass. The equation describes the time evolution of the system in these variables. The centre of mass streams freely.

Equation (4.59), with (4.67), describes the time evolution of two colliding quantum particles. If we compare with the classical counterpart, the Boltzmann equation, we see a striking similarity in their formal structure.

Both have a potential term and a gain–loss structure in the collision term, which depend on the differential and the total cross section, respectively. This similarity justifies the use of these classical equations as a starting point to describe heavy ion collisions as has been done in the BUU approach.

More important, however, are the differences: Whereas the Boltzmann equation is an integro–differential equation, the quantum counterpart is only a differential equation, which makes the solution much easier. The  $T$  matrices act on the Wigner density of the freely propagating wavepacket. Both the classical and the quantum equations have a potential term. Its meaning, however, is completely different. Following the derivation of the Boltzmann equation in the framework of the BBGKY hierarchy, one sees that all two-body potentials have to be accommodated in the collision term. The force term contains only gradients of external potentials. In the quantum equations the effective potential is a two-body potential. Of course, one can argue that the two-body potential can be expressed by an average potential and a residual interaction, where the average potential can be treated like an external field. But this argument misses the essential point, namely that without any approximation a potential term is present and uniquely determined in the quantum equation. Furthermore, the effective quantum potential is not the potential which enters the Schrödinger equation, but the real part of the transition matrix. Hence for vanishing collisions (e.g. due to Pauli blocking at low beam energy) the Hartree–Fock equation with nucleon–nucleon potentials (whose Wigner transform is the Vlasov equation) is not the right limit. Rather one has to employ the real part of the transition matrix (or – if one wants to take care of the Pauli blocking of the intermediate states – Brückner's  $g$ -matrix) as is done in TDHF calculations. Besides that, a transition matrix or a scattering amplitude is more easily obtained from experiment than a potential, which requires us to solve an inverse scattering problem. In the nuclear case, the nucleon–nucleon potential has a hard core whereas the transition matrix is rather smooth. Hence solving this equation is feasible.

Finally we want to mention that a straightforward calculation yields the well known form for the optical potential [1]

$$V_{\text{eff}} \propto T(0)\rho(r) . \quad (4.68)$$

In order to obtain this result one has to assume that the target nucleon does not recoil and that the target radius is large compared to the range of the transition matrix.

*Scattering of two Gaussian wave packets.* Before we proceed to investigate how the formalism changes if at least one of the scattering partners is bound, we would like to make the physics contained in eq. (4.59) still more transparent. For this purpose we solve eq. (4.59) for the case that initially the relative motion of the scattering partners is described by the wave packet (4.54). This calculation can be done analytically under the assumption that the increase of the width of the wave packet is small during the collision,

$$L(t) = L(0)\sqrt{1 + (\hbar t/m)^2/L^2(0)} \approx L(0). \quad (4.69)$$

If this is valid we can replace  $\mathbf{v}_p$  by  $\mathbf{v}_{p_0}$  in eq. (4.54). Thus the motion of the centroid of the distribution is approximated by

$$\mathbf{R}_0(t) = \mathbf{R}_0 + \mathbf{v}_{p_0} t. \quad (4.70)$$

By a shift of the time axis we can choose  $\mathbf{R}_0$  to be the minimal distance between the scattering partners  $\mathbf{R}_{0\perp}$ .  $\mathbf{R}_{0\perp}$  is then equivalent to the impact parameter (with respect to the centroids) and is perpendicular to  $\mathbf{P}_0$ . The calculation is lengthy but straightforward, and finally, after integration over  $d^3R$  and  $dt$ , we obtain

$$f(\mathbf{P}, t = \infty) = f(\mathbf{P}, t = -\infty) + I^{\text{lin}}(\mathbf{P}) + I^{\text{quad}}(\mathbf{P}), \quad (4.71)$$

with

$$I^{\text{lin}}(\mathbf{P}) = \frac{2\mu}{P_0} \sqrt{\pi} \frac{L^{3/2}}{2L+a} \exp[-(\mathbf{P} - \mathbf{P}_0)_{\parallel}^2 \cdot 4L] \exp\left(-P_{\perp}^2 \frac{4L(L+a)}{2L+a}\right) \exp\left(-\frac{R_{0\perp}^2}{8L+4a}\right) \\ \times \left[ A \sin\left(\mathbf{P} \cdot \mathbf{R}_{0\perp} \frac{2L}{2L+a}\right) + B \cos\left(\mathbf{P} \cdot \mathbf{R}_{0\perp} \frac{2L}{2L+a}\right) \right], \quad (4.72)$$

$$I^{\text{quad}}(\mathbf{P}) = \frac{4\mu^2 \pi^3 (A^2 + B^2)}{(2L+a)P_0} \left(\frac{4L}{\pi}\right)^{3/2} \exp\left(-P_{\perp}^2 \frac{2La}{2L+a}\right) \exp\left(-\frac{R_{0\perp}^2}{8L+4a}\right) \\ \times \int \frac{d^3m}{m} \delta(m - P) \exp[-2a(\mathbf{P} - \mathbf{m})^2 + a(\mathbf{P} - \mathbf{m})_{\perp}^2] \exp[-4L(\mathbf{m} - \mathbf{P}_0)^2] \\ \times \exp[-(2L+a)m_{\perp}^2] \cos\left(\left(\frac{a}{a+2L} \mathbf{P} - \mathbf{m}\right) \cdot \mathbf{R}_{0\perp}\right). \quad (4.73)$$

$\mu$  is the reduced mass of the scattering partners, and we recall that the  $A$ ,  $B$ ,  $a$  and  $L$  are defined in eqs. (4.62) and (4.54).

This equation displays quite nicely how one can visualize quantum scattering in the familiar phase space coordinates, and we will discuss this in a moment. Before that it is useful to investigate the limit  $L \rightarrow \infty$ .

In this limit the particles are in momentum eigenstates and described by plane waves. We recall

$$(A^2 + B^2) e^{-(\mathbf{P}-\mathbf{m})^2 \cdot 2a} = TT^* = \frac{1}{(2\pi)^4 \mu^2} \frac{d\sigma}{d\Omega}, \quad (4.74)$$

$$B = -\frac{P_0}{2(2\pi)^3 \mu} \sigma_{\text{tot}}. \quad (4.75)$$

We notice that in this limit the sine term of  $I^{\text{lin}}$  does not contribute and the cosine term yields

$$I^{\text{lin}}(\mathbf{P}) = -\frac{1}{4\pi L} \delta(\mathbf{P} - \mathbf{P}_0) \sigma_{\text{tot}}. \quad (4.76)$$

The quadratic part gives

$$I^{\text{quad}}(\mathbf{P}) = \frac{1}{4\pi L P^2} \delta(\mathbf{P} - \mathbf{P}_0) \frac{d\sigma}{d\Omega}. \quad (4.77)$$

Hence as the final result we have, with  $f(\mathbf{P}, t = -\infty) = \delta(\mathbf{P} - \mathbf{P}_0)$ ,

$$f(\mathbf{P}, t = \infty) = \frac{1}{4\pi L P^2} \delta(\mathbf{P} - \mathbf{P}_0) \frac{d\sigma}{d\Omega} + \left(1 - \frac{\sigma_{\text{tot}}}{4\pi L}\right) \delta(\mathbf{P} - \mathbf{P}_0). \quad (4.78)$$

We still have to clarify the meaning of the term  $1/4\pi L$ . It turns out to be the time integrated current,

$$\int \mathbf{j} \cdot \hat{\mathbf{P}}_0 dt = \frac{1}{4\pi L} \exp[-(\mathbf{R} - \mathbf{R}_0)_\perp^2 / 4L], \quad (4.79)$$

where  $\mathbf{j}$  is defined as

$$\mathbf{j} = \left(\frac{1}{4\pi L}\right)^{3/2} \frac{\mathbf{P}_0}{\mu} \exp[(\mathbf{R} - \mathbf{R}_0 - \mathbf{P}_0 t / \mu)^2 / 4L]. \quad (4.80)$$

The last expression is easy to interpret. As  $t \rightarrow \infty$ ,  $f(\mathbf{P})$  is finite at the surface of a sphere with radius  $P_0$ . The value of  $f$  is proportional to  $d\sigma/d\Omega$ , the probability of scattering into a momentum space cell around  $(\mathbf{P}, \Omega)$ . Hence the first term describes the scattering out of the initial state  $\mathbf{P}_0$  into the possible final states. The second term takes care of particle number conservation. Since the integral  $\int f d^3P$  has to be constant, the initial population of  $\delta(\mathbf{P} - \mathbf{P}_0)$  has to be reduced by the number of scattered particles. When we compare our final eq. (4.78) with (4.69) we notice that in the plane wave limit the term proportional to  $\sin((\mathbf{P} - \mathbf{P}_0) \cdot \mathbf{R}_0)$  has completely disappeared. Consequently, only localized particles feel an effective potential, which acts in the semiclassical limit as a force. The scattering of asymptotically free particles is completely described by cross sections as we expect from the solution of the Lippmann–Schwinger equation. The force term will become very important when we investigate the motion of particles in a bound system.

Going back to eqs. (4.69) and (4.73) we now see how a phase space picture of quantum scattering can emerge which fully takes care of the uncertainty relation; for large relative distances between the scattering partners collisions are exponentially suppressed. As one would assume intuitively, particles which are far apart do not scatter. The range in which scattering takes place is given by the sum of the widths of the Gaussian plus the width of the interaction. The exponential suppression is modulated by a cosine term, which can make the terms negative for some values of  $\mathbf{P}$  and  $\mathbf{R}_{0\perp}$ . Integrated over all impact parameters  $\mathbf{R}_{0\perp}$  the result is positive, of course. The energy is conserved because the time integration was performed from  $-\infty$  to  $+\infty$ . If there are many particles present this has to be modified. This topic will be discussed in section 4.6.

*Scattering on a bound particle in impulse approximation.* At the end of section 4.1 we saw that the scattering of a beam particle on a bound particle can be described by

$$\langle \mathbf{k}, \mathbf{k}_T | \Psi \rangle = \langle \mathbf{k}, \mathbf{k}_T | \phi_{0\rho} \rangle + \int \frac{\langle \mathbf{k} \mathbf{k}_T | T | \mathbf{p}_T \mathbf{p} \rangle \langle \mathbf{p}_T | \chi_0 \rangle}{p_T^2/2m + p^2/2m - k^2/2m - k_T^2/2m + i\epsilon} \delta(\mathbf{k} + \mathbf{k}_T - \mathbf{p} - \mathbf{p}_T) d^3p_T, \quad (4.81)$$

provided the impulse approximation is valid.

When we compare this result with  $|\psi(t)\rangle$  obtained for free particle scattering we observe that the only difference is in the term  $|\mathbf{p}\mathbf{p}_T\rangle\langle\mathbf{p}_T|\chi_0\rangle d^3p_T$ , which would be equal to  $|\mathbf{p}\mathbf{p}_T\rangle$  in the case of free particles which asymptotically have the momenta  $\mathbf{p}$ ,  $\mathbf{p}_T$ . Thus for the actual scattering the particles are treated as free in the impulse approximation. The only place where the binding becomes apparent is in the term  $\langle\mathbf{p}_T|\chi_0\rangle$ . We have a distribution of momenta which we have to integrate over. In the Wigner density approach this is especially advantageous. We only have to replace the Gaussian form of the wave packet by the Wigner density of the bound state. The rest of eq. (4.59) remains unaltered.

*Projection onto a definite final target state.* In eq. (4.81) it is not specified into which final state the target particle is scattered. If we are interested in the time evolution of the beam particle under the condition that the target particle is finally in the excited state  $n$ , we have to project onto the phase space of the final state. We quote only the final result here,

$$\left(\frac{\partial}{\partial t} + \frac{\mathbf{P}_1}{m_1} \cdot \nabla_{\mathbf{R}_1}\right) f(\mathbf{P}_1, \mathbf{R}_1, t) = -i \int d^3R_2 d^3P_2 \chi_n(\mathbf{R}_2, \mathbf{P}_2) [V, \rho^{(2)}]_{\text{W}}, \quad (4.82)$$

where  $\rho^{(2)}$  is the two-particle density operator,  $\chi_n$  is the Wigner density of the final state of the target particle and the subscript W stands for the Wigner transform integrated over the initial phase space coordinates of both particles. In deriving this equation we have made use of the fact that

$$\int d^3r d^3p (AB)_{\text{W}} = \int d^3r d^3p A_{\text{W}} B_{\text{W}}. \quad (4.83)$$

The evaluation of this expression follows the same lines as we have discussed in deriving eq. (4.59). Thus, as far as the impulse approximation is valid, the results are close to what one expects from intuition.

#### 4.4. Scattering on a system of bound particles

The scattering of a beam particle on complex bound target systems which consist of many constituents is described by the Lippmann–Schwinger equation,

$$\psi_a^+ = \chi_a + G^+ V \psi_a^+, \quad (4.84)$$

where  $V$  contains the scattering of the incident particle  $i$  with target particles  $m$ ,

$$V = \sum_m V_{im}, \quad (4.85)$$

and  $\chi_a$  is the initial state wave function, i.e., the product of the plane wave of the projectile and the target ground state wave function,

$$g_0 = \frac{e^{i\mathbf{P}\cdot\mathbf{R}}}{(2\pi)^{3/2}} \phi_0(\mathbf{r}_1, \dots, \mathbf{r}_n).$$

The first term describes the centre of mass motion.  $g$  is the solution of the target Schrödinger equation,

$$H_T g_n = \left( \sum_i -\frac{1}{2m} \nabla_{r_i}^2 + U \right) g_n = W_n g_n, \quad (4.86)$$

where  $W_n = P^2/2M_{\text{tot}} + w_n$  is the sum of centre of mass and internal energy and  $U$  is the interaction amongst the target particles. The propagator

$$G^+ = \frac{1}{E_a - T_P - H_T + i\varepsilon} \quad (4.87)$$

contains in the denominator the total target Hamiltonian and the kinetic energy operator of the projectile.  $E_a$  is the initial energy.

We define the transition matrix  $t_{im}^b$ , which describes the scattering of the beam particle on the target particle  $m$ ,

$$t_{im}^b = V_{im} + V_{im} \frac{1}{E_a - T_P - H_T - V_{im} + i\varepsilon} V_{im} = V_{im} + V_{im} G^+ t_{im}^b. \quad (4.88)$$

The superscript b stands for scattering on a bound particle. Watson [101] has shown that eq. (4.84) can be solved by a set of coupled equations,

$$\psi_a^+ = \chi_a + \sum_{m=1}^N G^+ t_{im}^b \psi_m, \quad \psi_m = \chi_a + \sum_{\substack{n=1 \\ m \neq n}}^N G^+ t_{in}^b \psi_n. \quad (4.89)$$

For the purpose of understanding the structure of these equations we display the first terms of the expansion,

$$\psi_a^+ = \chi_a + \sum_m G^+ t_{im}^b \chi_a + \sum_{\substack{m,n \\ m \neq n}} G^+ t_{im}^b G^+ t_{in}^b \chi_a \cdots. \quad (4.90)$$

The scattered wave has contributions from previously unscattered particles, as well as from those which have already undergone collisions with other target particles. Thus this generalized Lippmann–Schwinger equation has for the incoming wave not  $\chi_a$ , but an effective  $\psi_m$ , which describes possible previous scatterings.

If the impulse approximation is valid we can proceed along the same lines as in section 4.1. We can replace the bound transition matrix  $t_{im}^b$  by the free particle transition matrix  $t_{im}$ ,

$$t_{im} = V_{im} + V_{im} \frac{1}{p^2/2m + p_T^2/2m - T_P - T_T + i\varepsilon} t_{im}, \quad (4.91)$$

where  $p^2/2m$  is the kinetic energy of the beam particle,  $p_T^2/2m$  is the expectation value of the kinetic energy of the target particle [see eq. (4.10)]. To adapt our present problem to the discussion in section 4.1 we recall

$$E_a = W_0 + p^2/2m, \quad (4.92)$$

and define

$$\Delta R \equiv E_a - p^2/2m - p_T^2/2m. \quad (4.93)$$

In analogy to eq. (4.13) we can expand the propagator in the transition matrix  $T_b$ ,

$$\frac{1}{p^2/2m + p_T^2/2m - T_P - T_T + \Delta R - U + i\epsilon} = \frac{1}{p^2/2m + p_T^2/2m - T_P - T_T + i\epsilon} \times \left( 1 - (\Delta R - U) \frac{1}{p^2/2m + p_T^2/2m - T_P - T_T + \Delta R - U + i\epsilon} \right). \quad (4.94)$$

$U$  represents the interaction of the target particle  $m$  with the other target nucleons. If this potential is sufficiently smooth [cf. eq. (4.26)] we can terminate the expansion after the first term, which means that we can replace the bound state transition matrix  $t^b$  by the free transition matrix  $t$ .

We proceed now to the evaluation of  $\psi_m$ , which is the wave function of the projectile particle prior to scattering with the target particle  $m$ . We denote the initial momentum of the projectile by  $p_i$ , its final momentum by  $p_f$ , and the momentum it has prior to scattering with the target particle  $m$  by  $p'$ . The wave function of the incoming projectile can be expanded in plane waves,

$$\langle p_f | \psi_a^+ \rangle = \langle p_f | \chi_a \rangle + \int \frac{d^3 p'}{p_i^2/2m - p_f^2/2m - H_T + W_0 + i\epsilon} \langle p_f n | t_{im}^b | p' 0 \rangle \langle p' | \psi_m \rangle. \quad (4.95)$$

0 and  $n$  are the initial and final states of the target. If the wave length is small compared to the mean free path, we can evaluate the propagator by its asymptotic value, on the energy shell, and obtain, if the target nucleon had initially the momentum  $(p_f + p_T - p')$ ,

$$\langle p_f | \psi_a^+ \rangle = \langle p_f | \chi_a \rangle + \int d^3 p' d^3 p_T \frac{\langle p_f p_T | t_{im} | p' p_f + p_T - p' \rangle \langle p' | \psi_m \rangle}{p_i^2/2m - p_f^2/2m - p_T^2/2m + (p_f + p_T - p')^2/2m - \Delta E + i\epsilon}. \quad (4.96)$$

$\Delta E$  is the energy shift of the projectile due to previous scatterings. If the target nucleon initially is not in a momentum eigenstate we have to integrate over its initial momentum distribution. In this limit each scattering is an isolated event, which can be evaluated with the free scattering cross section. The incoming wave has a quite narrow distribution in momentum space around a value  $p_i$  which is specific for a sequence of previous scatterings. In order to come from one to the next scattering centre only momenta in a narrow range around  $r_{rel}$ , the relative vector of the scattering partners, are allowed. Otherwise the particle would miss the potential range of the next collision partner. For details of this approximation and the first-order correction term we refer to ref. [93].

We have seen now that in the short wave length limit  $\lambda > 1/k$  ( $\lambda$  is the mean free path,  $k$  is the wave number of the particle) the scattering of a projectile on a bound system can be approximated by single scatterings between projectile and target constituents. Provided the binding potential is sufficiently smooth we are entitled to use the free scattering  $T$  matrices. However, even in this approach we are still faced with the full complexity of the  $(n+1)$ -body problem. The bound state wave function of the target nucleon, over which we have to integrate in order to obtain  $\langle p_f | \psi_a^+ \rangle$ , is a solution of the  $n$ -body target Schrödinger equation. We will not be able to solve this equation. Rather we have to make an ansatz for the  $n$ -body wave function.

The equation of the quantum molecular dynamics model. We now have all the ingredients to formulate the time evolution equation for proton–nucleus interactions in the impulse approximation. It is straightforward to extend eq. (4.59) from two to  $N + 1$  nucleons. Then the time evolution equation is given as

$$\begin{aligned} & \left( \frac{\partial}{\partial t} + \sum_i \frac{\mathbf{P}_i}{m} \cdot \nabla_{\mathbf{R}_i} \right) f^{(n)}(\mathbf{P}_1, \dots, \mathbf{P}_{N+1}, \mathbf{R}_1, \dots, \mathbf{R}_{N+1}, t) \\ & = \int \prod_i d^3 p_i d^3 Q_i d^3 q_i e^{i\mathbf{R}_i \cdot \mathbf{p}_i} f_0^{(n)}(\mathbf{Q}_1, \dots, \mathbf{Q}_{N+1}, \mathbf{q}_1, \dots, \mathbf{q}_{N+1}, t) [I_1(T) + I_2(T) + I_3(T)]. \end{aligned} \quad (4.97)$$

$T$  is the sum of all possible transition matrix combinations,

$$T = \sum_m t_{im} + \sum_{k \neq m} \sum_m t_{im} G_0^+ t t_{ik} \dots, \quad (4.98)$$

i.e., all possible scattering sequences which may occur when the projectile  $i$  travels through the target. The terms  $I_1$  to  $I_3$  are defined as follows:

$$\begin{aligned} I_1 &= \langle \mathbf{P}_1 + \mathbf{p}_1/2, \dots, \mathbf{P}_{N+1} + \mathbf{p}_{N+1}/2 | T | \mathbf{Q}_1 + \mathbf{q}_1/2, \dots, \mathbf{Q}_{N+1} + \mathbf{q}_{N+1}/2 \rangle \\ & \quad \times \prod_i^{N+1} \delta(\mathbf{P}_i - \mathbf{p}_i/2 - \mathbf{Q}_i + \mathbf{q}_i/2), \\ I_2 &= \langle \mathbf{P}_1 - \mathbf{p}_1/2, \dots, \mathbf{P}_{N+1} - \mathbf{p}_{N+1}/2 | T^\dagger | \mathbf{Q}_1 - \mathbf{q}_1/2, \dots, \mathbf{Q}_{N+1} - \mathbf{q}_{N+1}/2 \rangle \\ & \quad \times \prod_i^{N+1} \delta(\mathbf{P}_i + \mathbf{p}_i/2 - \mathbf{Q}_i - \mathbf{q}_i/2), \\ I_3 &= \langle \mathbf{P}_1 + \mathbf{p}_1/2, \dots, \mathbf{P}_{N+1} + \mathbf{p}_{N+1}/2 | G_0^+ T | \mathbf{Q}_1 + \mathbf{q}_1/2, \dots, \mathbf{Q}_{N+1} + \mathbf{q}_{N+1}/2 \rangle \\ & \quad \times \langle \mathbf{P}_1 - \mathbf{p}_1/2, \dots, \mathbf{P}_{N+1} - \mathbf{p}_{N+1}/2 | G_0^+ T | \mathbf{Q}_1 - \mathbf{q}_1/2, \dots, \mathbf{Q}_{N+1} - \mathbf{q}_{N+1}/2 \rangle^*. \end{aligned}$$

$t_{im}$  are the free scattering transition matrices and  $G_0^+$  are the on shell propagators. If the potential gradients are sufficiently small to employ the impulse approximation for scattering amongst target (or projectile) nucleons as well, the extension to the equation which describes the nucleus–nucleus collision is again straightforward. The index for the momentum and coordinate space variables runs now from 1 to  $N_T + N_p$  instead of  $N + 1$ , and  $T$  has to be replaced by the sum over all possible scattering sequences of all projectile and target nucleons.

In the quantum molecular dynamics approach this equation is solved in an approximate way by means of a Monte Carlo procedure. The details of this procedure will be discussed in the next chapter. Here we only mention the essential approximations. The real part of  $I_1 + I_2$ , which, as we have seen, acts as an effective potential, has been replaced by a much easier to handle two-body potential, which in nuclear matter can be easily related to the nuclear equation of state. It is a parametrization of the  $g$ -matrix (instead of the transition matrix), which additionally takes into account the fact that nucleons are fermions and therefore cannot scatter into phase space regions which are already occupied by other nucleons.

The propagator which describes the time evolution of the particles in between the scattering events is taken on the energy shell. Thus each two-body scattering event conserves energy and momentum.

If the particles are in momentum eigenstates, as is approximately the case for smooth potentials, terms with different sequences of transition matrix elements in  $G_0^+ T$  and  $T^+ G_0^-$  do not contribute to  $I_3$ . These terms describe the interference between different paths. In this limit the paths are distinguishable and therefore do not interfere. Assume a projectile nucleon scatters with quasi-free target nucleons  $1, \dots, N$ . In order to proceed from nucleon  $i$  to nucleon  $i + 1$  it has to have a definite momentum  $\mathbf{K}_1$ , which points in the direction of the relative distance vector between the target particles  $i$  and  $i + 1$ . The absolute value is given by requiring energy conservation for each nucleon–nucleon scattering event. Due to momentum conservation the recoil of the target particle is fixed and unique for this sequence of scatterings. A different sequence means a different momentum transfer to target particle  $i$ . Thus the final state of the  $(N_T + N_p)$ -body system is different and interference cannot take place. We will substantiate this statement in section 4.6. In this limit  $I_3$  reduces to a sum of terms which contains only absolute squares of transition matrices  $|T_{ij} G_0^+ T_{ik}|^2$ . In the actual calculation it is assumed that these terms are proportional to products of the cross sections. The limit of validity of this assumption is also discussed in section 4.6.

The term proportional to the imaginary part of  $I_1 + I_2$  serves to conserve the norm, as we have seen eq. (4.78). Instead of calculating this term explicitly, it is much easier to replace it by norm conservation in a Monte Carlo calculation.

As an initial condition we still have to choose the initial Wigner density  $f_0(\mathbf{R}_1, \dots, \mathbf{R}_{N_T + N_p}, \mathbf{P}_1, \dots, \mathbf{P}_{N_T + N_p})$ . We will discuss our choice in the next section. We initialize the nuclei according to our choice of the initial distribution. Then we follow the space–time evolution of all the particles, and perform the scattering whenever the particles are sufficiently close [cf. eq. (4.69)]. The scattering angle is chosen randomly from a distribution which reproduces the measured free scattering cross section. Thus in each calculation one specific summand of  $T$  (eq. 4.98) is chosen. For the same  $f_0$  but a different sequence of random numbers we obtain a different scattering sequence. Performing very many calculations we obtain a distribution of different paths, where each path is represented with a weight factor which corresponds to the probability that it occurs. Thus the Monte Carlo procedure is a very convenient way of integrating out the  $12^N$  integration variables, where  $N$  is the number of collisions and the 12 is due to the 12 phase space coordinates of the scattering partners.

#### 4.5. Initial Wigner density

In the foregoing sections we have seen that under approximations which can be justified for nucleus–nucleus collisions the time evolution equation for the  $n$ -body Wigner density requires three inputs:

- (a) the free nucleon–nucleon cross section;
- (b) the effective potential between the nucleons given by the real part of the transition matrix;
- (c) the initial  $n$ -body Wigner density.

Whereas the first two inputs can be inferred from experiments, the last input is not at all experimentally accessible. The most we can learn from experiments are one- or, in a few cases, two-body observables. The calculations of the  $n$ -body Wigner density from first principles is also far outside the range of possibilities of present day nuclear matter calculations, as we have seen in chapter 2. Thus one has to start with an educated guess. The most one can do is to make a choice which is in agreement with experimentally measured observables and generally accepted theoretical predictions.

Especially our choice should reproduce:

- (a) a one-body density distribution which coincides with observed density profiles;
- (b) the uncertainty principle;
- (c) the relative wave function between two nucleons as calculated in the  $g$ -matrix approach; this relative wave function approaches zero for small relative distances, as we have discussed in section 3.3; in a cold nucleus this is rather independent of the relative momentum of the nucleons; thus the nucleus is similar to a lattice with wave function located around the sites.

One, but certainly not the only, ansatz which can fulfill these requirements is the assumption that the  $n$ -body Wigner density is a product of  $n$  Gaussians,

$$f_0^{(n)}(\mathbf{r}_1, \dots, \mathbf{r}_n, \mathbf{p}_1, \dots, \mathbf{p}_n, t) = \prod_{i=1}^n \frac{1}{\pi^3} \exp\{-[\mathbf{r}_i - \mathbf{r}_{i0}(t)]^2/2L\} \exp\{-[\mathbf{p}_i - \mathbf{p}_{i0}(t)]^2 \cdot 2L\}. \quad (4.99)$$

For a fixed time  $f_0^{(n)}$  is the Wigner transform of the product of  $n$  coherent states. The possible values of  $L$  are quite limited due to conditions (a) and (b). If we choose  $L$  too large, we cannot reproduce the nuclear surface; if  $L$  is too small, we are faced with unreasonably high momenta due to the uncertainty principle. In this limited range we checked that the calculated observables are robust against a change of  $L$ . As we have seen in section 4.3, the width of a coherent state increases as a function of time if propagated with the free Schrödinger equation. In our approach we keep the width constant, i.e., we do not allow the spreading of the wave function. This is motivated by the observation that otherwise the nucleus as a whole would spread in coordinate space as a function of time. Thus keeping the width constant imitates in a crude way the influence of the potential on the wavefunction.

#### 4.6. Interference between subsequent collisions

*Formation time and formation distance.* We have seen in section 4.4 that the time evolution equation for the  $N$ -body system requires as input only the real part of the transition matrix and the experimentally measured nucleon–nucleon cross sections, provided we are in the short wave length limit  $\lambda K > 1$  ( $\lambda$  is the mean free path and  $K$  is the wave number of the particle). In this section we investigate in detail how large this product has to be in order to justify the approximation of independent collisions. We will derive the exact result, and discuss the correction terms for  $\lambda K$  not being large. We find that the cross section vanishes if the distance between the scattering centres approaches zero, independent of the wave number  $K$ . Hence we can talk about a "formation distance" below which the scattered particle is not able to interact again. In this calculation it is assumed that we can integrate over all possible time differences  $\tau$  between the two subsequent collisions. Then we proceed by allowing only a finite  $\tau$  between the collisions in a manner similar to that of the kinetic theories. For small  $\tau$  we observe a strong suppression of the cross section. Even if  $\tau = R/v_{\text{rel}}$  ( $R$  is the distance between scattering centres,  $v_{\text{rel}}$  is the relative velocity of the particles prior to the first collision), the total cross section has not reached its asymptotic value for parameters suited for a nucleus–nucleus collision. Thus there exists also a "formation time". This is the time a particle needs after a collision before it can collide again with its full (asymptotic) cross section.

We will perform our calculation in the frozen target approximation because it allows for almost analytical results without giving up the essential physics. Extending our calculation to three moving particles described by Wigner densities is straightforward but the results are quite lengthy.

Consider an incoming nucleon approaching two potentials located at  $\mathbf{R}/2$  and  $-\mathbf{R}/2$ . There are two possibilities for double scattering. Either it scatters first with the potential at  $-\mathbf{R}/2$  and then with that at  $\mathbf{R}/2$ . The amplitude for this process we will denote by  $A_{12}$ . Or we have the opposite sequence of scatterings with the amplitude  $A_{21}$ . The incoming nucleon is described by the Fourier transform of the Wigner density, eq. (4.54), with the approximated width (4.69),

$$f_0(\mathbf{Q}, \mathbf{q}, t) = (2L/\pi)^{3/2} e^{-(\mathbf{Q}-\mathbf{Q}_0)^2 \cdot 2L} e^{-q^2 L/2} e^{i\mathbf{q} \cdot (\mathbf{R}_0 - \mathbf{Q}_0 t/m)}. \quad (4.100)$$

We calculate the total cross section with the help of our Wigner density formalism. The total cross section is contained in the terms linear in the transition matrix  $I^{\text{lin}}(T)$  [cf. eq. (4.76)]. In the limit  $L \rightarrow \infty$  the real part of  $I^{\text{lin}}(T)$  vanishes and we obtain

$$f(\mathbf{P}, t = \infty) = f(\mathbf{P}, t = -\infty) - \frac{\Delta\sigma_{\text{tot}}}{2\pi L} \delta(\mathbf{P} - \mathbf{Q}_0) + I^{\text{quad}}(TT^*). \quad (4.101)$$

$I^{\text{quad}}(TT^*)$  refers to the term quadratic in the transition matrix (eq. 4.77) and  $\mathbf{Q}_0$  is the initial momentum. Omitting the terms  $\sim TT^*$  the time evolution equation of the Wigner density of the incoming nucleon reads as [see eq. (4.59)]

$$\begin{aligned} \frac{\partial}{\partial t} f(\mathbf{P}, t) = & -i \int \frac{d^3\mathbf{Q} d^3\mathbf{q} d^3\mathbf{p} d^3\mathbf{R}}{(2\pi)^3} e^{i\mathbf{p} \cdot \mathbf{R}} \\ & \times \{ \langle \mathbf{P} + \mathbf{p}/2 | A_{12} + A_{21} | \mathbf{Q} + \mathbf{q}/2 \rangle \delta(\mathbf{P} - \mathbf{p}/2 - \mathbf{Q} + \mathbf{q}/2) \\ & - \langle \mathbf{P} - \mathbf{p}/2 | A_{12}^\dagger + A_{21}^\dagger | \mathbf{Q} - \mathbf{q}/2 \rangle \delta(\mathbf{P} + \mathbf{p}/2 - \mathbf{Q} - \mathbf{q}/2) \} f_0(\mathbf{Q}, \mathbf{q}, t). \end{aligned} \quad (4.102)$$

The operators for the different scattering sequences is given by

$$A_{12} + A_{21} = 2m \int d^3l T_1 \frac{|l\rangle\langle l|}{(\mathbf{P} + \mathbf{p}/2)^2 - l^2 + i\epsilon} T_2 + T_2 \frac{|l\rangle\langle l|}{(\mathbf{P} + \mathbf{p}/2)^2 - l^2 + i\epsilon} T_1. \quad (4.103)$$

The transition matrix for scattering on a scattering centre located at  $\mathbf{R}/2$  is obtained by a translation from scattering on a particle located at  $\mathbf{r} = 0$ ,

$$\langle \mathbf{m} | T_1 | \mathbf{n} \rangle = e^{i(\mathbf{n}-\mathbf{m}) \cdot \mathbf{R}/2} \langle \mathbf{m} | T | \mathbf{n} \rangle, \quad \langle \mathbf{m} | T_2 | \mathbf{n} \rangle = e^{-i(\mathbf{n}-\mathbf{m}) \cdot \mathbf{R}/2} \langle \mathbf{m} | T | \mathbf{n} \rangle. \quad (4.104)$$

We replace  $T_1$  and  $T_2$  by these expressions and perform the integrations over  $d^3q$ ,  $d^3p$  and  $d^3R$ ,

$$\begin{aligned} \frac{\partial}{\partial t} f(\mathbf{P}, t) = & -i 32m \int d^3\mathbf{Q} d^3l \left( \frac{2L}{\pi} \right)^{3/2} e^{-(\mathbf{Q}-\mathbf{Q}_0)^2 \cdot 2L} e^{-(\mathbf{Q}-\mathbf{P})^2 \cdot 2L} \\ & \times \left( \frac{\langle \mathbf{P} | T | l \rangle \langle l | T | 2\mathbf{Q} - \mathbf{P} \rangle}{P^2 - l^2 + i\epsilon} \cos[(l - \mathbf{Q}) \cdot \mathbf{R}] e^{i2(\mathbf{Q}-\mathbf{P}) \cdot (\mathbf{R}_0 - \mathbf{Q}_0 t/m)} \right. \\ & \left. - \frac{\langle \mathbf{P} | T^\dagger | l \rangle \langle l | T^\dagger | 2\mathbf{Q} - \mathbf{P} \rangle}{P^2 - l^2 - i\epsilon} \cos[(l - \mathbf{Q}) \cdot \mathbf{R}] e^{-i2(\mathbf{Q}-\mathbf{P}) \cdot (\mathbf{R}_0 - \mathbf{Q}_0 t/m)} \right). \end{aligned} \quad (4.105)$$

We proceed by integrating over the time. Then we perform the limit  $L \rightarrow \infty$ , substitute  $\langle m|T|n \rangle = (A + iB) e^{-(m-n)^2 a}$  and obtain

$$\int_{-\infty}^{\infty} dt f(\mathbf{P}, t) = \frac{-i 16m^2 \pi^2}{Q_0} \frac{1}{L} \int d^3l e^{-2a(P-l)^2} \cos[(\mathbf{l} - \mathbf{P}) \cdot \mathbf{R}] \delta(\mathbf{P} - \mathbf{Q}_0) \times \left( \frac{(A + iB)^2}{P^2 - l^2 + i\epsilon} - \frac{(A - iB)^2}{P^2 - l^2 - i\epsilon} \right). \quad (4.106)$$

Comparing this result with eq. (4.78) we see that the total cross section of scattering on two potentials is given by

$$\Delta\sigma_{\text{tot}} = \frac{-i}{\pi P} (m \cdot 4\pi^2)^2 \int d^3l e^{-2a(P-l)^2} 2 \cos[(\mathbf{l} - \mathbf{P}) \cdot \mathbf{R}] \left( \frac{(A + iB)^2}{P^2 - l^2 + i\epsilon} - \frac{(A - iB)^2}{P^2 - l^2 - i\epsilon} \right). \quad (4.107)$$

The term  $2 \cos[(\mathbf{l} - \mathbf{P}) \cdot \mathbf{R}]$  can easily be identified as being proportional to the Fourier transform of the spatial distribution of the two scattering centres. This allows a straightforward generalization of the above expression. Defining

$$F(\mathbf{q}) = \text{Re} \int e^{i\mathbf{q} \cdot \mathbf{R}} \rho(\mathbf{R}) d^3R, \quad (4.108)$$

where  $\text{Re}$  refers to the real part of the complex function, we obtain as the general result

$$\Delta\sigma_{\text{tot}} = \frac{-i}{\pi P} (m \cdot 4\pi^2)^2 \int d^3l e^{-2a(P-l)^2} F(\mathbf{P} - \mathbf{l}) \left( \frac{(A + iB)^2}{P^2 - l^2 + i\epsilon} - \frac{(A - iB)^2}{P^2 - l^2 - i\epsilon} \right). \quad (4.109)$$

In order to appreciate our result, and to make contact with the well known high energy limit, we calculate the cross section in the high energy (Glauber) limit. In this limit the propagator  $G_0^+$  is replaced by

$$G_0^+ = \frac{2m}{P^2 - l^2 + i\epsilon} \rightarrow \frac{2m}{\mathbf{P} \cdot (\mathbf{P} - \mathbf{l}) + i\epsilon}. \quad (4.110)$$

This implies that the projectile does not change its longitudinal momentum.

Backward scattering is impossible in this limit, and therefore only one of the amplitudes  $A_{12}$  and  $A_{21}$  has a finite value. Consequently, we have to replace in our expression

$$2 \cos[(\mathbf{P} - \mathbf{l}) \cdot \mathbf{R}] \rightarrow \text{Re} \left( \int e^{i(\mathbf{P} - \mathbf{l}) \cdot \mathbf{R}} \rho(\mathbf{R}) d^3R \right). \quad (4.111)$$

Furthermore we assume that the imaginary part of the scattering amplitude is large compared to the real part,  $A \ll B$ . We can now perform the integrations. Recalling the definition of the scattering amplitude,

$$f(\mathbf{l} - \mathbf{q}) = 4\pi^2 m \langle \mathbf{l} | T | \mathbf{q} \rangle, \quad (4.112)$$

we obtain

$$\Delta\sigma_{\text{tot}} = -\frac{2B^2}{p^2} \int d^2q f(\mathbf{q})f(-\mathbf{q})F(\mathbf{q}) \approx -\frac{1}{8\pi^2} (\sigma_{\text{tot}}^{\text{NN}})^2 \int d^2q F(\mathbf{q}). \quad (4.113)$$

To derive the last expression we have assumed that we can replace  $f(\mathbf{q})$  by  $f(0)$  under the integral. This is justified if  $\langle R^2 \rangle^{1/2} \gg a$ , where  $R$  is the distance between the scattering centres and  $a$  is the range of the potential. Using  $\int F(\mathbf{q}) d\mathbf{q} = 2\pi \langle R^{-2} \rangle$  we finally arrive at the well known result [1]

$$\Delta\sigma_{\text{tot}} = -(\sigma_{\text{tot}}^{\text{NN}})^2 \langle R^{-2} \rangle / 4\pi. \quad (4.114)$$

We come back now to our question about how the total cross section is modified due to double scattering. To investigate its dependence on the relative distance it is best to assume a Gaussian distribution of the relative distance between the scattering centres in coordinate space,

$$\rho(R) \sim e^{-R^2/4\Delta R}. \quad (4.115)$$

Consequently we have to replace  $2 \cos[(\mathbf{P} - \mathbf{l}) \cdot \mathbf{R}]$  by  $2e^{-(\mathbf{P} - \mathbf{l})^2 \Delta R}$ . Again we assume the imaginary part of the scattering amplitude to be large compared to the real part. Then we can perform the integrations and obtain

$$\Delta\sigma_{\text{tot}} = -\frac{2}{4\pi} \frac{(\sigma_{\text{tot}}^{\text{NN}})^2}{8a + 4\Delta R} [1 - e^{-(4\Delta R + 8a)p^2}]. \quad (4.116)$$

First of all we see that the cross section due to double scattering has a negative sign. Therefore it lowers the value of the cross section obtained from single scattering. This would be different if  $A \gg B$ . Secondly, double scattering does not take place if the scattering centres are close to each other. There exists a formation distance below which the projectile can only react with a reduced cross section. This distance depends on the sum of the range of the effective potential and the distance between the scattering centres. For large  $\Delta R$  the expression approaches a limit which is easy to interpret. Assuming an isotropic cross section ( $a = 0$ ) we have

$$\Delta\sigma_{\text{tot}} = -\frac{\langle R^{-2} \rangle}{4\pi} (\sigma_{\text{tot}}^{\text{NN}})^2. \quad (4.117)$$

$\langle R^2 \rangle^{1/2}$  is the average distance of the scattering centres in the reaction plane and  $\sigma_{\text{tot}} \langle R^{-2} \rangle / 4\pi = \langle R^{-2} \rangle d\sigma/d\Omega$  is just the probability that the scattering angle is such that the projectile hits the second scattering centre.

Still more insight into the quantum mechanics of double scattering can be obtained by inspecting the dependence of the double scattering on the time the projectile travels between the scattering centres. We recall that the propagators in eq. (4.105) are obtained by assuming that the time between the subsequent scatterings can vary between 0 and infinity,

$$\frac{i}{p^2 - t^2 + i\varepsilon} = \int_{-\infty}^t e^{ip^2(t-t')} e^{-it^2(t-t')} e^{-\varepsilon(t-t')} dt'. \quad (4.118)$$

If we allow a finite time difference only, the difference of the propagators in eq. (4.106) has to be replaced by

$$\frac{2m}{P^2 + l^2 + i\epsilon} - \frac{2m}{P^2 + l^2 - i\epsilon} \rightarrow -\frac{4im \sin((P^2 - l^2)\tau/2m)}{P^2 - l^2}, \quad (4.119)$$

where  $\tau$  is the maximal allowed time between the scatterings. For  $\tau \rightarrow \infty$  the left and right hand sides of eq. (4.119) become identical. In order to calculate the dependence of the double scattering term on the temporal distance we replace in eq. (4.106) the difference of the propagators by the right hand side of the above expression. We integrate over the angles and obtain finally

$$\sigma(\tau) = -\frac{(\sigma_{tot}^{NN})^2}{4\pi^2} \frac{2}{\Delta R + 2a} \int_0^\infty e^{-(\Delta R + 2a)(P^2 + l^2)} \sinh(2(\Delta R + 2a)Pl) \frac{2m \sin((P^2 - l^2)\tau/2m)}{P^2 - l^2} l dl. \quad (4.120)$$

In fig. 5 we display  $\sigma(\tau)$  for different values of  $\langle R^2 \rangle$  as a function of time.  $\sigma(\tau)$  is normalized to  $\sigma(\tau \rightarrow \infty)$ . Thus the suppression due to the finite distance between the scattering centres has been divided out. The time is displayed in units of  $\tau_0 = \langle R^2 \rangle^{1/2} m/P$ , the time it would take for a classical particle to travel from the first to the second scattering centre. We see that only for a very large distance ( $R \sim 6$  fm) is the asymptotic value obtained around  $\tau_0$ . At smaller distances the cross section is considerably reduced there. If the distance between the scattering centres decreases further we find an oscillatory form, which only at very large times approaches its asymptotic value.

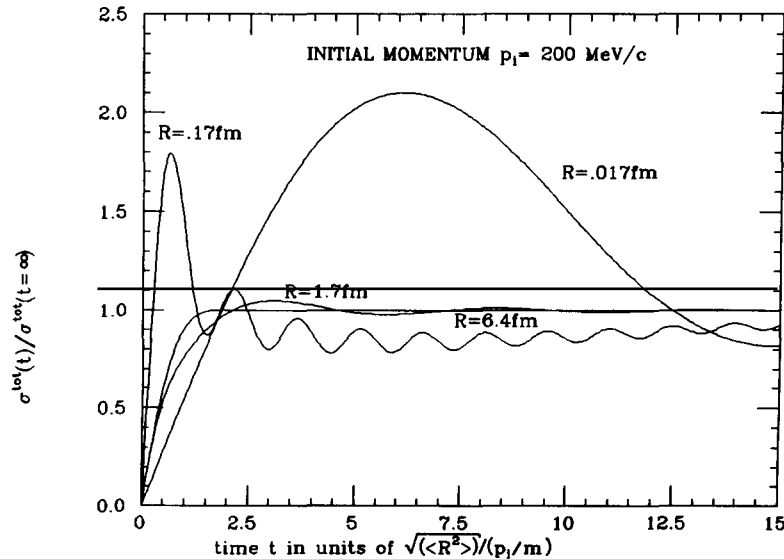


Fig. 5. On the formation time. Allowing only a finite time difference  $\tau$  between subsequent scatterings we observe a reduction of the asymptotic cross section for double scattering  $\sigma(\tau \rightarrow \infty)$ . This reduction  $\sigma(\tau)/\sigma(\tau \rightarrow \infty)$  is displayed as a function of  $\tau$  for different distances between the scattering centres.  $\tau$  is presented in units of the time it would take for a classical particle to travel from one to the other scattering centre.

We can conclude that the double scattering term has a negative sign if the imaginary part of the scattering amplitude is large compared to the real part, and therefore lowers the total cross section, which is a sum of single, double, etc. scattering. The double scattering is strongly reduced if the wave length of the particles is not small compared to the distance  $R$  between the scattering centres. If we furthermore limit the time the particle is allowed to spend between the scatterings, a further reduction occurs for values of  $R$  around the nuclear mean free path.

Hence, for values of  $R$  and  $\tau$  which are typical for nuclear collisions, the independent scattering approximation can hardly be rigorously justified, although the long mean free path at low energies due to the Pauli principle works in our favour. The corrections, however, may be of the order of 50% and yield a decrease in the effective number of collisions. At higher energies the mean free path is large enough compared to the particle's wave length to justify the independent collision approach. The only excuse for using the independent scattering approach for practical calculations lies in the fact that calculation of the correction terms is beyond what is at present numerically feasible, and that careful investigations have shown that the dynamics of the reactions considered here are not influenced by quite different treatments of the collisions of nucleons with a centre of mass energy of around 50 MeV [102].

*Interference in the quasi-free limit.* In section 4.4 we mentioned that in the quasi-free limit the interference term vanishes. In the quasi-free limit the knocked on target nucleon recoils as a free particle. The recoil energy equals  $q^2/2m$ , where  $q$  is the momentum transfer. Although we are not quite in the quasi-free limit, the smoothness of the potential keeps the width of the wave function in momentum space small. Thus the quasi-free limit can be considered as a first-order approach, whose corrections have to be calculated. The disappearance of the interference term is caused by different scattering sequences leading to distinguishable final states. Thus the scattering sequence can be determined by measuring the momenta of all nucleons which are involved in the collisions, and there are no indistinguishable alternatives which could interfere. In this section we will substantiate this finding. We reduce this problem to its easiest version: the scattering of a beam particle at two scattering centres which are located at  $R/2$  and  $-R/2$ , respectively. We take the simplification that the range of the potential is small compared to the mean free path, so that the width of the coordinate and momentum distribution of the scattering centres can be neglected. This is true for a wide range of nuclear reactions. It allows us to approximate the propagator of the projectile between the subsequent scatterings in a way which avoids the otherwise necessary integrations over angles. As we have seen, there are two possible scattering sequences. Either the beam particle scatters first with particle 1 (described by the transition operator  $T_1$ ) and then with particle 2 (described by  $T_2$ ), or vice versa. The amplitude for these processes are denoted by  $A_{12}$  and  $A_{21}$ ,

$$A_{ij} = \int \langle \mathbf{K}_i \mathbf{P}'_i | T_i | \mathbf{K}' \mathbf{P}_i \rangle G_0^+ \langle \mathbf{K}' \mathbf{P}'_j | T_j | \mathbf{K}_i \mathbf{P}_j \rangle d^3 K' . \quad (4.121)$$

$\mathbf{K}_i$ ,  $\mathbf{K}'$  and  $\mathbf{K}_f$  describe the momenta of the beam particles before, in between and at the end of the two collisions, respectively, and  $\mathbf{P}_i$  and  $\mathbf{P}'_i$  are the initial and final momenta of particle  $i$ .  $G_0^+$  is the propagator of the beam particle between the collisions,

$$G_0^+ = \frac{2m}{K_i^2 + P_j^2 - P_j'^2 - K'^2 + i\varepsilon} . \quad (4.122)$$

In order to make use of the above-mentioned approximations we Fourier transform  $A_{ij}$ ,

$$A_{21} = \int d^3 r'' d^3 r' f_2(r'') g(r'' - r') f_1(r'), \quad (4.123)$$

with

$$f_2(r'') = \frac{1}{(2\pi)^{3/2}} \int e^{-i\mathbf{K}' \cdot \mathbf{r}''} \langle \mathbf{K}_i \mathbf{P}'_2 | T_2 | \mathbf{K}' \mathbf{P}_2 \rangle d^3 K', \quad (4.124)$$

$$f_1(r') = \frac{1}{(2\pi)^{3/2}} \int e^{i\mathbf{K}'' \cdot \mathbf{r}'} \langle \mathbf{K}'' \mathbf{P}'_1 | T_1 | \mathbf{K}_i \mathbf{P}_1 \rangle d^3 K'',$$

$$g(\mathbf{r}' - \mathbf{r}'') = -\frac{m}{2\pi} \frac{e^{iK|\mathbf{r}' - \mathbf{r}''|}}{|\mathbf{r}' - \mathbf{r}''|}. \quad (4.125)$$

We denote the range of the potential by  $a$ .  $f_2(r'')$  and  $f_1(r')$  are only different from zero in a region of radius  $a$  around  $\mathbf{R}/2$  and  $-\mathbf{R}/2$ , respectively. If  $a$  is small compared to  $R$ , we can replace  $|\mathbf{r}' - \mathbf{r}''|$  in the denominator by  $R$  and approximate

$$K|\mathbf{r}' - \mathbf{r}''| \approx \frac{K}{|\mathbf{r}' - \mathbf{r}''|} (\mathbf{r}' - \mathbf{r}'') \cdot (\mathbf{r}' - \mathbf{r}'') \approx \frac{K}{R} \mathbf{R} \cdot (\mathbf{r}' - \mathbf{r}'') \equiv \mathbf{K}_{21} \cdot (\mathbf{r}' - \mathbf{r}''). \quad (4.126)$$

Performing the integration over  $r''$  and  $r'$  we obtain

$$A_{21} = -\frac{4\pi^2 m}{R} \langle \mathbf{K}_i \mathbf{P}'_2 | T | \mathbf{K}_{21} \mathbf{P}_2 \rangle \langle \mathbf{K}_{21} \mathbf{P}'_1 | T | \mathbf{K}_i \mathbf{P}_1 \rangle. \quad (4.127)$$

Thus we have replaced the propagator

$$\frac{2m}{K_i^2 + P_1^2 - P_1'^2 + K'^2 + i\epsilon} \approx -\frac{4\pi^2 m}{R} \delta(\mathbf{K}' - \sqrt{K_i^2 + P_1^2 - P_1'^2} \mathbf{R}/R) = -\frac{4\pi^2 m}{R} \delta(\mathbf{K}' - \mathbf{K}_{21}). \quad (4.128)$$

Particles which do not have about this momentum after the first scattering would miss scattering centre 2 and hence  $A_{21}$  would be zero. Thus this result is as expected by intuition. For  $A_{12}$  we can proceed in the same way, but of course we have to replace  $\mathbf{P}_1$  by  $\mathbf{P}_2$  and  $\mathbf{R}$  by  $-\mathbf{R}$  in eq. (4.128). In this case we denote the momentum of the beam particle between the collisions as  $\mathbf{K}_{12}$ .

In our normalization the differential cross section is given by

$$d\sigma/d\Omega = [(2\pi)^4/v_0] |A_{12} + A_{21}|^2 \rho(E). \quad (4.129)$$

$\rho(E)$  is the density of final states for a given energy  $E$  and  $v_0/(2\pi)^3$  is the incoming flux. For evaluation of the cross section we have to take the transition matrix on the momentum shell,

$$\langle \mathbf{K}l | T | mn \rangle = \delta(\mathbf{K} + l - m - n) \langle \mathbf{K}l | \tilde{T} | mn \rangle. \quad (4.130)$$

The square of the delta function which appears when evaluating eq. (4.129) is treated in the standard way,

$$(\delta(\mathbf{m} - \mathbf{n}))^2 = \delta(0)\delta(\mathbf{m} - \mathbf{n}) = \frac{1}{(2\pi)^3} \int e^{i0R} d^3R \delta(\mathbf{m} - \mathbf{n}) = \frac{V}{(2\pi)^3} \delta(\mathbf{m} - \mathbf{n}) = \delta(\mathbf{m} - \mathbf{n}). \quad (4.131)$$

The last relation is due to our normalization.

We begin with the calculation of the cross section for the direct terms  $|A_{12}|^2$  and  $|A_{21}|^2$ ,

$$\begin{aligned} \frac{d\sigma_{\text{QF}}^{\text{dir}}}{d\Omega} &= \frac{(4\pi^2 m)^2}{v_0} |\langle \mathbf{K}_{12} \mathbf{P}'_1 | \tilde{T}_1 | \mathbf{K}_1 \mathbf{P}_1 \rangle|^2 \frac{(2\pi)^4}{R^2} |\langle \mathbf{P}'_2 \mathbf{K}_f | \tilde{T}_2 | \mathbf{K}_{12} \mathbf{P}_2 \rangle|^2 \rho(E) \\ &= |f(\mathbf{K}_1, \mathbf{P}_1 \rightarrow \mathbf{K}_{12}, \mathbf{P}'_1)|^2 \frac{(2\pi)^4}{v_0 R^2} |\langle \mathbf{P}'_2 \mathbf{K}_f | \tilde{T}_2 | \mathbf{K}_{12} \mathbf{P}_2 \rangle|^2 \rho(E). \end{aligned} \quad (4.132)$$

$f$  is the scattering amplitude for elastic scattering and  $\rho(E)$  is given by

$$\begin{aligned} \rho(E) &= 2m\delta(P_1^2 + K_1^2 + P_2^2 - P_2'^2 - K_f^2 - P_1'^2)\delta(\mathbf{P}_1 + \mathbf{K}_1 - \mathbf{K}_{12} - \mathbf{P}'_1) \\ &\quad \times \delta(\mathbf{P}_2 + \mathbf{K}_{12} - \mathbf{K}_f - \mathbf{P}'_2) d^3P_2' d^3P_1' K_f^2 dK_f \\ &= 2m\delta(P_2^2 + K_{12}^2 - K_f^2 - P_2'^2)\delta(\mathbf{K}_{12} + \mathbf{P}_2 - \mathbf{K}_f - \mathbf{P}'_2) K_f^2 dK_f d^3P_2'. \end{aligned} \quad (4.133)$$

Thus  $\rho(E)$  is the phase space for the last two-body collision for a given initial momentum  $\mathbf{K}_{12}$ .

Finally we obtain for the quasi-free cross section, with  $v_f$  as relative velocity between the partners in the second collision,

$$\frac{d\sigma_{\text{QF}}}{d\Omega} = \frac{d\sigma}{d\Omega}(\vartheta_1) \frac{d\sigma}{d\Omega}(\vartheta_2) \frac{v_f}{v_0 R^2}, \quad (4.134)$$

which is the expected result.  $\vartheta_1$  denotes the scattering angle in the first collision, which directs the beam particle to the second scattering centre, and  $\vartheta_2$  is the scattering angle in the second collision in order to be finally observed in  $d\Omega$ . The calculation of the term  $|A_{12}|^2$  is completely analogous.

Now we proceed to the interference term. Performing the same steps as before we obtain

$$\begin{aligned} (A_{12}A_{21}^*)_{\text{QF}} &= \delta(\mathbf{P}_1 + \mathbf{K}_1 - \mathbf{K}_{12} - \mathbf{P}'_1)\delta(\mathbf{P}_2 + \mathbf{K}_{12} - \mathbf{P}'_2 - \mathbf{K}_f)\delta(\mathbf{P}_2 + \mathbf{K}_1 - \mathbf{K}_{21} - \mathbf{P}'_2) \\ &\quad \times \delta(\mathbf{P}_2 + \mathbf{K}_{21} - \mathbf{P}'_2 - \mathbf{K}_f) |\tilde{T}_1 \tilde{T}_2|^2 (m \cdot 4\pi^2)^2 / R^2. \end{aligned} \quad (4.135)$$

This product of  $\delta$ -functions can only be fulfilled if  $\mathbf{K}_{12} = \mathbf{K}_{21}$ . Since  $\mathbf{K}_{12}$  points from target particle 1 to target particle 2, and thus in the opposite direction to  $\mathbf{K}_{21}$ , this requires  $\mathbf{K}_{12} = \mathbf{K}_{21} = 0$ , a condition under which the collisions do not occur.

If we give up the quasi-free limit, but assume that the target particles are represented by wave functions  $\varphi_i$  which have a finite width in momentum space, we can investigate under which conditions the interference term becomes finite. To investigate this point we assume that we are still in the range of validity of the impulse approximation. Then we can continue to use free transition matrices and can neglect the potential energy terms in the propagators.

In section 4.3 we have investigated how to describe the scattering into a specific final target state in

the impulse approximation. Here we make use of these results and calculate the interference term for the case that the target particles 1 and 2 are scattered into final target states  $\varphi_1$  and  $\varphi_2$ . If the target particles initially have the momenta  $P_1$  and  $P_2$ , we obtain for  $A_{21}A_{12}^*$ ,

$$\begin{aligned} A_{21}A_{12}^* &= \langle \varphi_2 | P'_2 \rangle \langle K_f P'_2 | T_2 | K_{12} P_2 \rangle \langle \varphi_1 | P'_1 \rangle \langle K_{12} P'_1 | T_1 | K_i P_1 \rangle \langle K_i P_2 | T_2^\dagger | K_{21} P''_2 \rangle \langle P''_2 | \varphi_2 \rangle \\ &\quad \times \langle K_{21} P_1 | T_1^\dagger | K_f P''_1 \rangle \langle P''_1 | \varphi_1 \rangle d^3 P'_2 d^3 P'_1 d^3 P''_2 d^3 P''_1 (4\pi^2 m)^2 / R^2 \\ &= \varphi_2^*(K_{12} + P_2 - K_f) \varphi_2(K_i + P_2 - K_{21}) \varphi_1^*(K_i + P_1 - K_{12}) \\ &\quad \times \varphi_1(P_1 + K_{21} - K_f) (4\pi^2 m / R)^2 \times \text{product of } \tilde{T} \text{ matrix elements.} \end{aligned} \quad (4.136)$$

Thus the final cross section reads as

$$\begin{aligned} \frac{d\sigma}{d\Omega} &= [(2\pi)^4 / v_0 R^2] f(P_1, K_i \rightarrow P_1 + K_i - K_{12}, K_{12}) f(P_2, K_{12} \rightarrow P_2 + K_{12} - K_f, K_f) \\ &\quad \times f^*(P_2, K_i \rightarrow P_2 + K_i - K_{21}, K_{21}) f^*(P_1, K_{21} \rightarrow K_f, P_1 + K_{21} - K_f) \\ &\quad \times \varphi_1(K_i + P_1 - K_{12}) \varphi_1^*(P_1 + K_{21} - K_f) \varphi_2(K_{12} + P_2 - K_f) \varphi_2^*(K_i + P_2 - K_{21}) \\ &\quad \times 2m\delta(P_1^2 + P_2^2 + K_i^2 - K_f^2 - 2m(E_1 + E_2)) K_f^2 dK_f. \end{aligned} \quad (4.137)$$

$E_1$  and  $E_2$  are the final energies of the bound particles. The contribution of the interference term to the cross section is determined by the products  $\varphi_1 \varphi_1^*$  and  $\varphi_2 \varphi_2^*$ . If the states  $\varphi_1$  and  $\varphi_2$  are sufficiently sharp in momentum space this product approaches zero, as we have seen. If they are broad, i.e., if vastly different arguments of  $\varphi$  and  $\varphi^*$  do not cause the product to disappear, then the interference terms cannot be neglected. Unfortunately, in order to estimate the size of these terms, one has to know the target wave function.

We can conclude that in the quasi-free limit interference terms do not contribute to the cross section. Since all available kinetic models are based on the assumption of quasi-free scattering, they do not offer the possibility of estimating this contribution. A reliable calculation requires the nuclear wave function as an input, and hence is far beyond the present status of kinetic theories. From a practical point of view two arguments can be given in favour of neglecting the interference term in a first approach. First of all, inside the nucleus potential gradients are presumably small, and hence the wave function is narrow in momentum space. Hence the condition for neglecting the interference terms coincides with that for justifying the impulse approximation, which was seminal for deriving any kinetic theory. Secondly, in addition to what we have discussed so far, there are strong kinematical correlations. In the laboratory system the scattering angle of the projectile is smaller than  $\vartheta_{\text{lab}} = 90^\circ$  if the target nucleon is at rest initially. Thus only one of the two possible sequences of scatterings is kinematically possible. The Fermi motion of the nucleons also allows scattering into larger angles. The probability for this is small, however, even for an isotropic cross section in the nucleon–nucleon centre of mass system. Thus one of the sequences always has a much higher probability.

These rather qualitative arguments have not yet been extended to quantitative calculations. This will certainly be one of the future tasks in the development of kinetic theories.

#### 4.7. Attempts to treat nucleons as fermions

Nucleons are fermions. Hence a nucleus behaves quite differently from a system of distinguishable particles, and a reliable description of any nuclear system requires us to take these effects into account.

Nobody, however, has yet succeeded in solving a properly antisymmetrized  $n$ -body system in which the constituents can scatter. This is not only a matter of principle. Due to the  $n$ -body correlations the time evolution equations for a properly antisymmetrized  $n$ -body wave function contain  $n!$  terms as compared to one term for a direct product ansatz. Thus presently, even if the time evolution equations were formally known, an exact calculation would not be feasible. What one can hope, however, is to find a systematic expansion in which higher order correlations are proven to be small. Such an expansion is not available yet although in principle it is known how to proceed [106].

Up to now one had to mimic those fermionic effects which are believed to be essential for a reasonable treatment of the dynamics. These include the Pauli blocking of scatterings into already occupied states, as well as the description of the ground state, which is – for a given Hamiltonian – quite different from that of distinguishable particles. This mimicry has quite a long history. Already in the classical molecular dynamics approach Wilets et al. [57] tried to mimic the Pauli principle by a momentum dependent potential which keeps two particles apart from each other in phase space if their distance becomes smaller than  $\hbar$ . In the meantime Dorso [103] showed that indeed a Fermi distribution can be obtained as the ground state of a system of distinguishable particles which interact by a properly chosen momentum dependent two-body interaction. Also the influence of the Pauli potential on the time evolution of the quantum molecular dynamics approach has been investigated recently [104, 136]. All these approaches have in common that they neglect all higher than two-body correlations and even these are introduced ad hoc, i.e. not derived from antisymmetrization. In principle, on the level of two-body correlations the effect of the antisymmetrization was believed to be expressible as an effective potential.

This common belief that quantal effects can be mimicked, at least in principle, has recently been questioned by Feldmeier [105]. He claimed that the dynamics of fermions cannot be described by Hamilton's equations. This would invalidate of course all the above mentioned approaches, as well as all kinetic theories applied so far to heavy ion reactions. We will therefore present his arguments, and discuss the generality of his approach. His claim is based on the application of a variational principle originally suggested by Kerman and Koonin [106]. This variational principle is applicable to a system whose wave function  $\psi$  depends on time only via parameters. For these systems a generalized Lagrange density can be defined,

$$\mathcal{L}(\mathbf{r}_0(t), \mathbf{p}_0(t), \dot{\mathbf{r}}_0(t), \dot{\mathbf{p}}_0(t)) = \int d^3r \psi(H - i d/dt)\psi, \quad (4.138)$$

where  $\psi$  is a parametrized trial wave function. The true motion will be obtained if the trial wave function has sufficient freedom to reproduce the true solution. The main purpose, however, is to apply this principle to restricted basis states. The time evolution equations for the parameters can be obtained by requiring  $\mathcal{L}$  to be stationary with respect to variations of  $|\psi\rangle$  and  $\langle\psi|$  between fixed end points  $t_1$  and  $t_2$ ,

$$\left(\frac{d}{dt} \frac{\partial}{\partial \dot{\mathbf{p}}_0} - \frac{\partial}{\partial \mathbf{p}_0}\right)\mathcal{L} = 0, \quad (4.139)$$

$$\left(\frac{d}{dt} \frac{\partial}{\partial \dot{\mathbf{r}}_0} - \frac{\partial}{\partial \mathbf{r}_0}\right)\mathcal{L} = 0. \quad (4.140)$$

These equations are quite similar to the Euler–Lagrange equations, and probably this similarity led to eq. (4.138) being called a Lagrange density, although it depends on  $(\mathbf{r}_0, \mathbf{p}_0, \dot{\mathbf{r}}_0, \dot{\mathbf{p}}_0)$  and not on  $(\mathbf{r}_0, \dot{\mathbf{r}}_0)$ .

It has been shown that for a number of nonfermionic systems the correct time evolution of the system can be obtained by applying this variational principle.

Feldmeier now applied this method to two freely moving fermions. As trial wave function he chose an antisymmetrized product of states of the form

$$\psi_i(\mathbf{r}, \mathbf{p}_{i0}, \mathbf{r}_{i0}) = \frac{e^{i[\mathbf{p}_{i0} \cdot (\mathbf{r} - \mathbf{r}_{i0}) - \mathbf{p}_{i0}^2 t / 2m]}}{[\sqrt{\pi/2L} 2L(t)]^{3/2}} e^{-(\mathbf{r} - \mathbf{r}_{i0} - \mathbf{p}_{i0} t / m)^2 / 4L(t)}, \quad (4.141)$$

with a constant width  $L(t) = L$ . With  $L(t)$  defined as  $L + it/2m$ , eq. (4.141) is a solution of the Schrödinger equation for a free particle. The time evolution equation of the parameters are the same for a constant as well as for a time dependent width of the above-mentioned form as long as the total wave function is a direct product of coherent states. This is not true, however, for antisymmetrized coherent states. The calculation of  $\mathcal{L}$  for the product of two antisymmetrized coherent states is quite lengthy but straightforward, and we obtain finally (after separation of the free centre of mass motion)

$$\mathcal{L} = -\left( \frac{3\dot{B}}{2L} + \dot{\mathbf{R}}_0 \cdot \mathbf{P}_0 + \frac{\dot{\mathbf{r}}_0 \cdot \mathbf{p}_0 - [\mathbf{r}_0 \cdot \dot{\mathbf{p}}_0 + 2\dot{B}p_0^2 - 2\dot{B}(\mathbf{r}_0 - 4B\mathbf{p}_0)^2 / 16L^2]Y}{1 - Y} \right), \quad (4.142)$$

$$Y = e^{-p_0^2 4L - (\mathbf{r}_0 - 4B\mathbf{p}_0)^2 / 4L}, \quad (4.143)$$

$$H = \frac{3}{4Lm} + \frac{P^2}{4m} + \frac{p_0^2 + [(\mathbf{r}_0 - 4B\mathbf{p}_0)^2 / 16L^2]Y}{m(1 - Y)}. \quad (4.144)$$

$p_0$  and  $r_0$  refer to  $(\mathbf{p}_{10} - \mathbf{p}_{20})/2$  and  $\mathbf{r}_{10} - \mathbf{r}_{20}$ , respectively. Feldmeier now proved that there exists no Hamilton function  $\tilde{H}$  which satisfies Hamilton's equations, i.e., for which  $\dot{p}_0 = -\partial\tilde{H}/\partial r_0$  and  $\dot{r}_0 = \partial\tilde{H}/\partial p_0$ , with  $\dot{r}_0$  and  $\dot{p}_0$  given by eq. (4.140) and (4.139), respectively.

One can, however, take a different approach to the fermionic motion. Starting from the time evolution equation of the Wigner density for two free particles,

$$\left( \frac{\partial}{\partial t} + \frac{\mathbf{p}_1}{m_1} \cdot \nabla_{\mathbf{r}_1} + \frac{\mathbf{p}_2}{m_2} \cdot \nabla_{\mathbf{r}_2} \right) f(\mathbf{r}_1, \mathbf{p}_1, \mathbf{r}_2, \mathbf{p}_2, t) = 0, \quad (4.145)$$

we obtain immediately the solutions

$$f(\mathbf{r}_1, \mathbf{r}_2, \mathbf{p}_1, \mathbf{p}_2, t) = \frac{1}{\pi^6} \exp[-(\mathbf{r}_1 - \mathbf{r}_{10} - \mathbf{p}_1 t / m_1)^2 / 2L] \exp[-(\mathbf{r}_2 - \mathbf{r}_{20} - \mathbf{p}_2 t / m_2)^2 / 2L] \\ \times \exp[-(\mathbf{p}_1 - \mathbf{p}_{10})^2 \cdot 2L - (\mathbf{p}_2 - \mathbf{p}_{20})^2 \cdot 2L]. \quad (4.146)$$

As can be easily seen,  $f$  is the product of two Wigner transforms of time dependent coherent states,

$$\psi(\mathbf{r}_1, \mathbf{p}_{10}, \mathbf{r}_{10}) = C' \exp[-(\mathbf{r}_1 - \mathbf{r}_{10} - \mathbf{p}_1 t / m)^2 / (4L + 2it/m) + i\mathbf{r}_1 \cdot \mathbf{p}_{10}]. \quad (4.147)$$

After a lengthy calculation we obtain for the antisymmetrized Wigner density of the relative coordinates

$$\begin{aligned}
f(\mathbf{r}, \mathbf{p}, \mathbf{r}_0, \mathbf{p}_0, t) = C \{ & \exp[-(\mathbf{r} - \mathbf{r}_0 - \mathbf{p}t/\mu)^2/4L - (\mathbf{p} - \mathbf{p}_0)^2 \cdot 4L] \\
& + \exp[-(\mathbf{r} + \mathbf{r}_0 - \mathbf{p}t/\mu)^2/4L - (\mathbf{p} + \mathbf{p}_0)^2 \cdot 4L] \\
& - 2\exp[-r^2/4L - p^2 \cdot 4L] \cos(2\mathbf{r} \cdot \mathbf{p}_0 - 2\mathbf{p} \cdot (\mathbf{r}_0 + \mathbf{p}_0t/\mu)) \}. \quad (4.148)
\end{aligned}$$

We have separated out the free motion of the centre of mass.  $p$  and  $r$  refer to the relative coordinates and  $\mu$  is the reduced mass. For discussing the time evolution of the fermionic system, we neglect the time dependence of the width of the coherent states, which corresponds to a replacement of  $pt/\mu$  by  $p_0t/\mu$ . This can always be done by choosing the width at  $t=0$  sufficiently large or the mass sufficiently heavy. This yields

$$\begin{aligned}
f^a(\mathbf{r}, \mathbf{p}, \mathbf{r}_0, \mathbf{p}_0, t) = C \{ & \exp[-(\mathbf{r} - \mathbf{r}_0 - \mathbf{p}_0t/\mu)^2/4L - (\mathbf{p} - \mathbf{p}_0)^2 \cdot 4L] \\
& + \exp[-(\mathbf{r} + \mathbf{r}_0 + \mathbf{p}_0t/\mu)^2/4L - (\mathbf{p} + \mathbf{p}_0)^2 \cdot 4L] \\
& - 2\exp[-r^2/4L - p^2 \cdot 4L] \cos(2\mathbf{r} \cdot \mathbf{p}_0 - 2\mathbf{p} \cdot (\mathbf{r}_0 + \mathbf{p}_0t/\mu)) \}. \quad (4.149)
\end{aligned}$$

The time evolution of the Wigner density in coordinate and momentum space is obtained by integration over the complementary variable, and is displayed for the one-dimensional case in fig. 6. There we have chosen the initial condition  $r_0 = 2(\text{fm})$  and  $p_0 = 0.1(1/\text{fm})$ . We display in this figure the direct term, the exchange term and the sum of both. For large distances ( $t=0$ ) we see two separate Gaussians in coordinate space and the exchange term has little influence there. In momentum space, however, the exchange term acts strongly and generates two Gaussians out of the one peak made by the

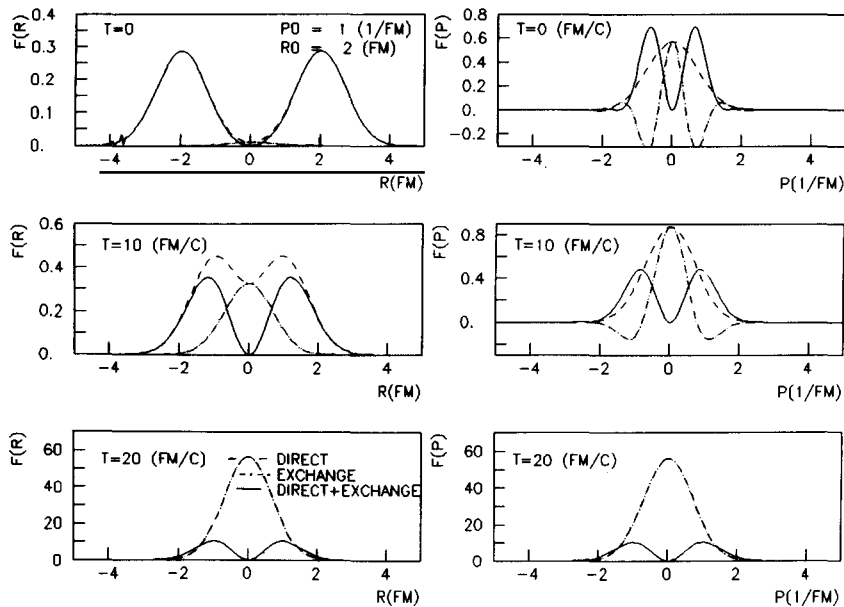


Fig. 6. Time evolution of two approaching antisymmetrized Gaussian wave packets in coordinate and momentum space. We display the density and momentum space density as a function of the relative coordinates at three times: (a) before the wave packets overlap in coordinate space, (b) during an intermediate step and (c) at the point of maximal overlap. In the last row the sum of direct and exchange terms is multiplied by a factor 100 in order to be visible.

direct term. At 10 fm/c the direct term also overlaps strongly in coordinate space. The exchange term separates the peaks in coordinate space. The widths of both peaks have decreased, and the width in momentum space has to compensate for this in order to fulfill the uncertainty relation. Finally, when the direct terms merge into one Gaussian, both the direct and the exchange terms increase in magnitude tremendously. The peaks generated by the exchange term are still quite separated, and the width of the peaks in momentum space has increased once more.

Inspecting eq. (4.149), we see that the centroids of the Gaussians obey Hamilton's equations with  $H = p_0^2/2m$ , obviously in contradiction to Feldmeier's results.

How can this happen? The answer lies in the fact that both the antisymmetrized product of coherent states of the form (4.141) with a constant width  $L$ , as well as its Wigner transform (4.149), are not solutions of the free particle Schrödinger equation. Equation (4.149) was obtained under the assumption  $L(t) \approx L(0)$ . We also see that in the same limit,  $Y$ , defined in (4.143), approaches zero. It is a drawback of the variational approach, however, that a condition for justifying the replacement of  $Y$  by zero cannot be given. One can conclude that, if the trial wave function does not have enough freedom to reproduce the true solution, the variational principle can yield equations of motion for the parameters which cannot be formulated as Hamilton's equations of motion. If one allows sufficient freedom in the parameter space, in this case by allowing also the width to be a function of time, eq. (4.148), one has to recover Hamilton's equations of motion. The non-Hamiltonian dynamics is hence a result of a specific choice of the parameters, and is not due to the fermionic nature of the particles under consideration. As shown, it may yield quite unrealistic equations of motion.

Comparing the time evolution of the approximate solution, eqs. (4.142), (4.139) and (4.140), with that of the full solution, we observe some quite unpleasant features of the former. At large relative distances, when the fermions have passed each other, the interference term approaches zero and we observe two spreading Wigner densities. There is no information that the fermions have passed each other. The momentum distribution is as it was before the encounter. The approximate solution accelerates the approaching fermions, followed by deceleration. There is a net momentum transfer. At finite impact parameters we observe in addition an unphysical transverse momentum transfer [105]. These unpleasant results question the usefulness of the variational principle for fermionic systems if one does not know the full solution beforehand. Thus one has not really made a step forward since the introduction of the effective two-body Pauli potentials. Although they are at least partially successful, they have a lot of drawbacks: they also produce artificial transverse momentum transfer when two fermions pass each other, they yield effective masses which do not agree with nuclear matter calculations, they modify the equation of state, and, last but not least, they convert a nucleus into a lattice if they really aim at a complete hindrance of overoccupation of phase space cells; this is because the motion of one nucleon always leads to an overoccupation if all other nucleons do not give way collectively.

## 5. The model

In this chapter we describe the details of the quantum molecular dynamics model (QMD) and its numerical realization [11–19]. We give an account of the tests performed and show how different potentials change the stability of the nuclei.

The typical time for a heavy ion reaction, as we will see, is around 200 fm/c. For this time noninteracting nuclei have to be stable. Otherwise one cannot be sure that the results really reveal the

physics and are not just numerical artifacts. The stability, and hence the successful simulation of heavy ion collisions, depends on the solution of two critical problems: how the initial configuration is to be made and how one has to evolve the  $A_T + A_P$  system in time. We start with the first topic.

### 5.1. Initialization

When we compared quantal (TDHF) and classical (Vlasov) mean field systems [63, 107] we found an almost identical time evolution of the nuclear density for beam energies larger than 25 MeV/n. This means, first of all, a justification for terminating the  $\hbar$  expansion of the potential term in the time evolution equation (eq. 4.42). Nevertheless, this is surprising because the initializations are quite different. The initial density of the first calculation is given by a Slater determinant whereas the Vlasov equation starts out from point-like particles randomly distributed in a sphere of radius  $r = 1.12A^{1/3}$ . This corresponds to a normal nuclear matter density of 0.17 nucleons/fm<sup>3</sup>. From these results we have concluded that, at the energies considered in this work, the detailed form of the wave functions has only a minor influence on the time evolution of the bulk properties of the system, especially on the single particle observables, if they fulfill the minimal requirements listed in section 4.5. They are determined by the single particle density and rather independent of the way the single particle density is generated by the density distributions of the individual nucleons. We cannot expect to learn from these different theories much about two-nucleon correlations. Therefore, as discussed in section 4.5, one has to start with an educated guess for the  $n$ -body Wigner density. As we have seen there, the description of the nuclear wave function as a product of  $n$  coherent states,

$$\psi_i(\mathbf{r}, \mathbf{p}_{i0}, \mathbf{r}_{i0}, t) = \frac{\exp\{i[\mathbf{p}_{i0} \cdot (\mathbf{r} - \mathbf{r}_{i0}) - p_{i0}^2 t / 2m]\}}{[\sqrt{\pi/2L} 2L(t)]^{3/2}} \exp\{-[\mathbf{r} - \mathbf{r}_{i0} - \mathbf{p}_{i0} t / m]^2 / 4L(t)\}, \quad (5.1)$$

allows one to satisfy most of the experimental and theoretical demands on single particle distributions and two-body correlations.  $L(t)$  is defined as  $L + it/2m$ .

The Wigner transforms of the coherent states are Gaussians in momentum and coordinate space. In the calculation we keep the width constant,  $L(t) = L$ . Then the Wigner density reads

$$\begin{aligned} f(\mathbf{r}, \mathbf{p}, t) &= \frac{1}{(2\pi)^3} \int e^{-i\mathbf{p} \cdot \mathbf{r}_{12}} \psi_i(\mathbf{r} + \mathbf{r}_{12}/2, t) \psi_i^*(\mathbf{r} - \mathbf{r}_{12}/2, t) d^3 r_{12} \\ &= \frac{1}{\pi^3} \exp[-(\mathbf{r} - \mathbf{r}_{i0} - \mathbf{p}_{i0} t / m)^2 / 2L - (\mathbf{p} - \mathbf{p}_{i0})^2 \cdot 2L], \end{aligned} \quad (5.2)$$

where  $L = 1.08 \text{ fm}^2$ , corresponding to a root mean square radius of the nucleons of 1.8 fm. The Wigner representation of our Gaussian wave packets obeys the uncertainty relation  $\Delta r_x \Delta p_x = \hbar/2$ .

As discussed in section 4.5 the  $n$ -body Wigner density is the direct product of the Wigner densities of  $n$  coherent states. As we discussed there we keep the width fixed.

The one-body densities in coordinate and in momentum space are

$$\begin{aligned} \rho(\mathbf{r}, t) &= \sum_{i=1}^N \delta(\mathbf{r} - \mathbf{r}_i) \int f^{(N)}(\mathbf{r}_1, \dots, \mathbf{r}_N, \mathbf{p}_1, \dots, \mathbf{p}_N, t) d^3 p_1 \cdots d^3 p_N d^3 r_1 \cdots d^3 r_N \\ &= \sum_i \frac{1}{(2\pi L)^{3/2}} e^{-(\mathbf{r} - \mathbf{r}_{i0} - \mathbf{p}_{i0} t / m)^2}, \end{aligned} \quad (5.3)$$

and equivalently

$$g(\mathbf{p}, t) = \sum_{i=1}^N \delta(\mathbf{p} - \mathbf{p}_i) \int f^{(N)}(\mathbf{r}_1, \dots, \mathbf{r}_N, \mathbf{p}_1, \dots, \mathbf{p}_N, t) d^3p_1 \cdots d^3p_N d^3r_1 \cdots d^3r_N. \quad (5.4)$$

A random choice of the centres of the  $A_T + A_P$  Gaussians in coordinate and momentum space, where the momentum is chosen between zero and the local Fermi momentum, is not sufficient to maintain the stability of the nuclei for a sufficiently long time span. Due to fluctuations, a limited sequence of random numbers does not create the ground state of a nucleus but rather a metastable excited state, which decays by emission of nucleons. The time span for which the nucleus has to be stable implies an upper limit to the excitation energy which can be tolerated.

Eigenstates of a Hamiltonian have to fulfill the uncertainty relation. The variance  $\Delta r_x \Delta p_x$  of two neighbouring eigenfunctions is separated by  $\hbar$ , i.e., each level fills a volume of  $\hbar^3$  in phase space. If a system is in the ground state, the phase space is densely filled up to a maximum value in coordinate and momentum space. Loosely speaking, there is no hole in the phase space. It is this property of the ground state which we employ to initialize the nuclei.

First we determine the position of the nucleons in a sphere of the radius  $r = 1.12A^{1/3}$ . We draw random numbers but reject those which would position the centres of two nucleons closer than  $r_{\min} = 1.5$  fm. The next step is to determine the local potential  $U(r)$  generated by all the other nucleons at the centres of the Gaussians. The local Fermi momentum is determined by the relation  $p_F(r_{i0}) = \sqrt{2mU(r_{i0})}$ , where  $U(r_{i0})$  is the potential energy of particle  $i$ . Finally the momenta of all particles are chosen randomly between zero and the local Fermi momentum. We then reject all random numbers which yield two particles closer in phase space than  $(r_{i0} - r_{j0})^2 (\mathbf{p}_{i0} - \mathbf{p}_{j0})^2 = d_{\min}^2$ . Typically only 1 out of 50 000 initializations is accepted under the present criteria. The computer time required for the initialization is short compared to the time needed for the propagation.

The accepted configurations are quite stable: usually no nucleon escapes from a heavy nucleus in 300 fm/c, as we will see in section 5.5. This procedure also ensures that the nuclei have the proper root mean square radii in coordinate and momentum space. Light nuclei are somewhat less stable. One or two out of ten nuclei lose a nucleon in the required time span. To avoid the initialization of unstable nuclei the following procedure can be applied: We select a sample of nuclei which have the required stability. We then choose randomly two Euler angles and rotate the positions of all nucleons of one nucleus around its centre of mass. The rotated nuclei are then boosted towards each other along the old z-axis. Each set of Euler angles yields a completely different reaction without changing the stability.

## 5.2. Propagation in the effective potential

Successfully initialized nuclei are boosted towards each other with the proper centre of mass velocity using relativistic kinematics. The centres of projectile and target move along Coulomb trajectories up to a distance of 2 fm between the surface of projectile and target. From then on we employ a generalized version of the Ritz variational principle [106] to determine the further time evolution of the system.

For that purpose we define a generalized Lagrange function,

$$\mathcal{L} = \int \psi \left[ H - i \frac{\partial}{\partial t} - i \sum \left( \dot{\mathbf{r}}_{i0} \cdot \frac{d}{d\mathbf{r}_{i0}} + \dot{\mathbf{p}}_{i0} \cdot \frac{d}{d\mathbf{p}_{i0}} \right) \right] \psi d^3r_1 \cdots d^3r_n. \quad (5.5)$$

$\psi$  is the direct product of  $n$  coherent state wave functions and  $H$  is the total  $n$ -body Hamiltonian

$H = \sum T_i + V_i$  with  $V_i$  and  $T_i$  being the potential and kinetic energy of particle  $i$ . The Lagrange function can depend on all parameters  $\mathbf{p}_{10}, \dots, \mathbf{p}_{n0}, \mathbf{r}_{10}, \dots, \mathbf{r}_{n0}$  and the time derivatives of these parameters. For a direct product of coherent states  $\mathcal{L}$  is given by

$$\mathcal{L} = \sum \left( -\dot{\mathbf{r}}_{i0} \cdot \mathbf{p}_{i0} + \langle V_i \rangle + \frac{3}{8Lm} \right). \quad (5.6)$$

The time evolution of the centroids  $\mathbf{p}_{i0}$  and  $\tilde{\mathbf{r}}_{i0} = \mathbf{r}_{i0} + \mathbf{p}_{i0}t/m$  is given by the Euler–Lagrange equations,

$$\frac{d}{dt} \frac{\partial \mathcal{L}}{\partial \dot{\mathbf{p}}_{i0}} - \frac{\partial \mathcal{L}}{\partial \mathbf{p}_{i0}} = 0 \rightarrow \dot{\tilde{\mathbf{r}}}_{i0} = \frac{\mathbf{p}_{i0}}{m} + \nabla_{\mathbf{p}} U_i, \quad (5.7)$$

$$\frac{d}{dt} \frac{\partial \mathcal{L}}{\partial \dot{\tilde{\mathbf{r}}}_{i0}} - \frac{\partial \mathcal{L}}{\partial \tilde{\mathbf{r}}_{i0}} = 0 \rightarrow \dot{\mathbf{p}}_{i0} = -\nabla U_i. \quad (5.8)$$

Here we have defined the potential  $U_i$  as  $\langle \Sigma V_i \rangle$ . Thus the Ritz variational principle yields the same time evolution of the parameters as one would obtain if one moves the centroids of the wave function (eq. 5.1) according to the classical equations of motion given by the Poisson brackets,

$$\dot{\mathbf{p}}_{i0} = \left\{ \mathbf{p}_{i0}, \sum_j H_j \right\} = \{ \mathbf{p}_{i0}, T_i + U_i \}, \quad (5.9)$$

$$\dot{\tilde{\mathbf{r}}}_{i0} = \left\{ \tilde{\mathbf{r}}_{i0}, \sum_j H_j \right\} = \{ \tilde{\mathbf{r}}_{i0}, T_i + U_i \}. \quad (5.10)$$

This is remarkable because due to the fixed width the underlying wave function is not a solution of the Schrödinger equation for a free particle. These differential equations are solved using an Eulerian integration routine with a fixed timestep  $\Delta t$ ,

$$\mathbf{p}_{i0}(n+1) = \mathbf{p}_{i0}(n) - \nabla_{\mathbf{r}_{i0}} U_i(n+1/2) \Delta t, \quad (5.11)$$

$$\tilde{\mathbf{r}}_{i0}(n+1/2) = \tilde{\mathbf{r}}_{i0}(n-1/2) + \frac{\mathbf{p}_{i0}(n)}{[\mathbf{p}_{i0}^2(n) + m_i^2]^{1/2}} \Delta t + \nabla_{\mathbf{p}_{i0}} U_i(n-1/2) \Delta t. \quad (5.12)$$

*Static interactions.* Following the discussion of chapters 2 and 4 we replace the real part of the transition or the  $g$ -matrix by a local Skyrme-type interaction supplemented by a long range Yukawa interaction, which is necessary to reproduce the surface, and an effective charge Coulomb interaction, where all particles of projectile and target have a charge  $Z_p/A_p$  and  $Z_T/A_T$ , respectively.

Our total static interaction reads

$$V^{\text{tot}} = V^{\text{loc}} + V^{\text{Yuk}} + V^{\text{Coul}}, \quad (5.13)$$

where the different terms are

$$V^{\text{loc}} = t_1 \delta(\mathbf{r}_1 - \mathbf{r}_2) + t_2 \delta(\mathbf{r}_1 - \mathbf{r}_2) \delta(\mathbf{r}_1 - \mathbf{r}_3), \quad (5.14)$$

$$V^{\text{Yuk}} = t_3 e^{-|r_1 - r_2|/m} (|r_1 - r_2|/m), \quad (5.15)$$

with  $m = 1.5$  fm and  $t_3 = -6.66$  MeV. These parameters give the best preservation of the nuclear surface, as we will see in section 5.5.

The total energy  $H_i$  of particle  $i$  is the sum of kinetic and potential energies,

$$H_i = T_i + V_i = T_i + \frac{1}{2} \sum_j U_{ij}^{(2)} + \frac{1}{3} \sum_{jk} U_{ijk}^{(3)}. \quad (5.16)$$

$T_i$  refers to the kinetic energy of particle  $i$  and the potentials are defined as

$$U_{ij}^{(2)} = \int f_i(\mathbf{p}_i, \mathbf{r}_i, t) f_j(\mathbf{p}_j, \mathbf{r}_j, t) V^{(2)}(\mathbf{r}_i - \mathbf{r}_j) d^3 r_i d^3 r_j d^3 p_i d^3 p_j, \quad (5.17)$$

$$U_{ijk}^{(3)} = \int f_i(\mathbf{p}_i, \mathbf{r}_i, t) f_j(\mathbf{p}_j, \mathbf{r}_j, t) f_k(\mathbf{p}_k, \mathbf{r}_k, t) V^{(3)}(\mathbf{r}_i, \mathbf{r}_j, \mathbf{r}_k) d^3 r_i d^3 r_j d^3 r_k d^3 p_i d^3 p_j d^3 p_k. \quad (5.18)$$

$V^{(2)}$  and  $V^{(3)}$  are the two- and three-body parts of the interaction defined in eq. (5.13).

Performing the integration one sees immediately that the local part of  $\Sigma U_{ij}^{(2)}$  can be written as

$$\sum_j U_{ij}^{(2)} = t_1 \tilde{\rho}(\mathbf{r}_{i0}), \quad (5.19)$$

where the interaction density  $\tilde{\rho}(\mathbf{r}_{i0})$  is

$$\tilde{\rho}(\mathbf{r}_{i0}) = \frac{1}{(4\pi L)^{3/2}} \sum_j e^{(\mathbf{r}_{i0} - \mathbf{r}_{j0})^2/4L}. \quad (5.20)$$

The interaction density has twice the width of the single particle density. We can approximate the three-body part of  $V$  as a function of  $\tilde{\rho}(\mathbf{r}_{i0})$ ,

$$\begin{aligned} \sum_{j,k} U_{ijk}^{(3)} &= t_2 \sum_{j,k;j,k \neq i;j \neq k} \int V^{(3)} d^3 R_1 d^3 P_1 d^3 R_2 d^3 P_2 d^3 R_3 d^3 P_3 f_i(\mathbf{R}_1, \mathbf{P}_1, t) f_j(\mathbf{R}_2, \mathbf{P}_2, t) f_k(\mathbf{R}_3, \mathbf{P}_3, t) \\ &= \frac{t_2}{(2\pi L)^3 \cdot 3^{3/2}} \sum_{j,k;j,k \neq i;j \neq k} \exp\{[(\mathbf{r}_{k0} - \mathbf{r}_{i0})^2 + (\mathbf{r}_{k0} - \mathbf{r}_{j0})^2 + (\mathbf{r}_{j0} - \mathbf{r}_{i0})^2]/6L\} \\ &\approx \frac{t_2}{(2\pi L)^3 \cdot 3^{3/2}} \sum_{j,k;j,k \neq i;j \neq k} \exp\{[(\mathbf{r}_{i0} - \mathbf{r}_{j0})^2 + (\mathbf{r}_{i0} - \mathbf{r}_{k0})^2]/4L\} \\ &= \frac{t_2 (4\pi L)^{3\nu/2}}{(2\pi L)^{3(\nu-1)/2} (\nu+1)^{3/2}} \tilde{\rho}_i^\nu(\mathbf{r}_{i0}), \end{aligned} \quad (5.21)$$

with  $\nu = 2$ . In spin saturated nuclear matter the three-body interaction can either be viewed as a genuine three-body interaction or as the density dependence of the two-body interaction due to the hard core, since we find

$$t_2 \delta(\mathbf{r}_1 - \mathbf{r}_2) \delta(\mathbf{r}_1 - \mathbf{r}_3) = \frac{1}{6} t_2 \delta(\mathbf{r}_1 - \mathbf{r}_2) \rho((\mathbf{r}_1 + \mathbf{r}_2)/2). \quad (5.22)$$

Therefore this effective three-body term is not in disagreement with the calculation by Kümmel [44], who found a very small genuine three-body contribution to the binding energy.

The Yukawa part of the potential energy is given by

$$\sum_j U_{ij}^{(2)\text{Yuk}} = t_3 \sum_{i \neq j} \frac{e^{L/m^2}}{r_{ij}/2m} \{e^{-r_{ij}/m} [1 - \Phi(\sqrt{L}/m - r_{ij}/2\sqrt{L})] - e^{r_{ij}/m} [1 - \Phi(\sqrt{L}/m + r_{ij}/2\sqrt{L})]\}, \quad (5.23)$$

where  $\Phi(x)$  is the error function and  $r_{ij}$  is the distance between the centres of the  $i$ th and the  $j$ th particle.

Next we have to determine the parameters  $t_1$  and  $t_2$ . We start from the observation that in nuclear matter, where the density is constant, the interaction density coincides with the single particle density, and  $U_{\text{loc}}^{(2)}$ , as well as  $U_{\text{Yuk}}^{(2)}$ , is directly proportional to  $\rho/\rho_0$ . The three-body part  $U^{(3)}$  of the interaction is proportional to  $(\rho/\rho_0)^2$ . If we adopt for  $U^{(3)}$  the approximation (5.21) we can directly relate our parameters to nuclear matter properties. In nuclear matter our potential has the form

$$U^{\text{loc}} = \alpha(\rho/\rho_0) + \beta(\rho/\rho_0)^2. \quad (5.24)$$

This potential has two free parameters, which can be fixed by the requirement that at normal nuclear matter density the averaging binding energy is  $-15.75$  MeV and the total energy has a minimum at  $\rho_0$ . The adjustment of the two parameters fixes the compressibility as well. In order to investigate the influence of different compressibilities one can generalize the potential to

$$U^{\text{loc}} = \alpha(\rho/\rho_0) + \beta(\rho/\rho_0)^\gamma. \quad (5.25)$$

We now have an additional third parameter, which allows us to fix the compressibility independently of the other quantities. This generalization can be translated back to the nucleon–nucleon potential in a unique way by identifying  $\nu$  in eq. (5.21) with  $\gamma$ . By varying these three parameters we can investigate how different compressibilities, i.e. different equations of state (EOS), influence the observables.

The parameter  $\alpha$  contains contributions from the local two-body potential as well as from the Yukawa potential. In nuclear matter there is no difference between local and nonlocal potentials. We can always expand nonlocal interactions like the Yukawa interaction,

$$\begin{aligned} U_{ij}^{\text{Yuk}} &= t_3 \int d^3r \int d^3r' \frac{e^{-|r-r'|/m}}{|r-r'|/m} \rho_i(r) \rho_j(r') = 4\pi m^3 t_3 \int d^3r \rho_i(r) \rho_j(r) + O(\nabla^2 \rho) \\ &= \frac{4\pi m^3 t_3}{(4\pi L)^{3/2}} e^{(r_{i0}-r_{j0})^2/4L} + O(\nabla^2 \rho). \end{aligned} \quad (5.26)$$

Thus in nuclear matter any combination of  $t_1$ ,  $t_3$  and  $m$  is equivalent as long as we keep

$$a = t_1 - 4\pi m^3 t_3 \quad (5.27)$$

constant. This is not the case with finite nuclei. It turns out that (5.16) in the approximation (5.21) with the values for  $t_1$  and  $t_2$  obtained for the desired nuclear matter properties gives about the right binding

energy for finite nuclei also. Consequently, if we want to employ a Yukawa potential with parameters  $t_3$  and  $m$  we calculate its contribution to the potential energy of particle  $i$ . This energy is then subtracted from the local two-body term by changing the coefficient  $t_1$  to  $t_{1i}$ . It is defined by the relation

$$t_{1i}\tilde{\rho}(\mathbf{r}_{i0}) = t_1\tilde{\rho}(\mathbf{r}_{i0}) - \sum_j U_{ij}^{\text{Yuk}}. \quad (5.28)$$

Thus the total potential energy remains constant independent of the parameters of the Yukawa term we choose. The forces which determine the time evolution, however, depend strongly on the choice of the parameters.

For the actual propagation, as we would like to stress, the explicit two- and three-body interactions (eq. 5.13) are used and not the nuclear matter potentials (eq. 5.25). This is important since the equivalence of both is only true in nuclear matter, not in finite nuclei.

The parameters of the static potential employed are displayed in table 1.

*Momentum dependent interactions.* It has recently been emphasized [13, 32, 33, 35] that nonequilibrium effects can play an important role in a realistic treatment of heavy ion collisions. The most pronounced effect can be expected from the momentum dependence of the nuclear interaction, which leads to an additional repulsion [53] between the nucleons when boosted as in heavy ion collisions. However, as far as multifragmentation is concerned, the influence is small [18].

For the computation of momentum dependent interactions (MDI), we parametrize the momentum dependence of the real part of the optical potential in the following way [13]:

$$U^{\text{MDI}} = t_4 \ln^2(t_5(\mathbf{p}_1 - \mathbf{p}_2)^2 + 1) \delta(\mathbf{r}_1 - \mathbf{r}_2), \quad (5.29)$$

with the parameters  $t_4 = 1.57 \text{ MeV}$ ,  $t_5 = 5 \times 10^{-4} \text{ MeV}^{-2}$ . This term is substituted for the term proportional to  $(\mathbf{p}_1 - \mathbf{p}_2)^2$  in the Skyrme interaction, which is in striking contrast with the data above  $E_{\text{lab}} \geq 150 \text{ MeV/n}$ . The parametrization of the real part of the optical potential together with the data [53] is shown in fig. 7. The present expression for the MDI reproduces the experimental data up to energies  $E \approx 1 \text{ GeV/n}$ .

In order to reproduce the ground state properties of nuclear matter with MDI one has to readjust the parameters  $\alpha$ ,  $\beta$ ,  $\gamma$  of eq. (5.25). In nuclear matter at zero temperature our potential now reads as follows:

$$U \approx \alpha(\rho/\rho_0) + \beta(\rho/\rho_0)^\gamma + \delta \ln^2(\varepsilon(\rho/\rho_0)^{2/3} + 1) \rho/\rho_0, \quad (5.30)$$

where the parameters are given in table 2. With these parameters we obtain for MDI the same compressibilities  $K$  in the ground state as for the static potentials (see table 1). From now on we refer to the soft (hard) EOS plus MDI as SM (HM), respectively.

The equation of state for all four sets of parameters displayed in tables 1 and 2 is shown in fig. 8.

Table 1  
Parameters of the static potentials

$K$ (MeV)	$\alpha$ (MeV)	$\beta$ (MeV)	$\gamma$	EOS
200	-356	303	7/6	S
380	-124	70.5	2	H

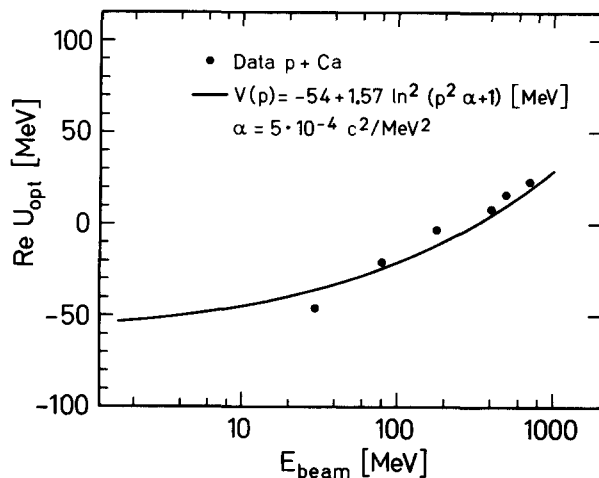


Fig. 7. Real part of the optical potential as compared with experimental data. The line is our parametrization (eq. 5.29), the points are experimental values from ref. [53].

Table 2  
Parameters of the momentum dependent potentials

K (MeV)	$\alpha$ (MeV)	$\beta$ (MeV)	$\gamma$	$\delta$ (MeV)	$\epsilon$	EOS
200	-390	320	1.14	1.57	21.54	SM
380	-130	59	2.09	1.57	21.54	HM

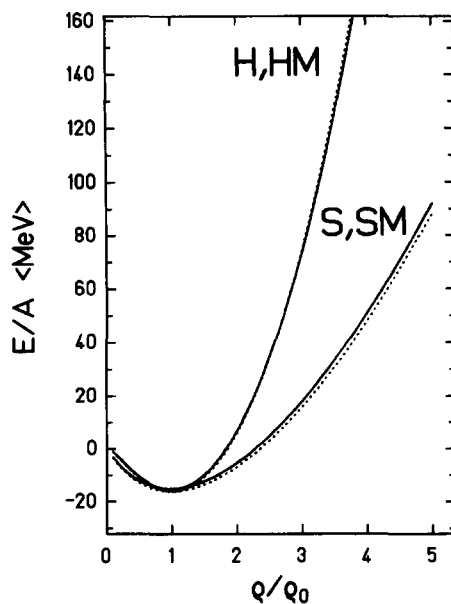


Fig. 8. The equations of state in our calculations. The density dependence of the energy per particle in nuclear matter at temperature  $T=0$  is displayed for the four different sets of parameters shown in tables 1 and 2.

Note that all four equations of state give the same ground state binding energy ( $E/A = -16$  MeV at  $\rho = \rho_0$ ), but differ drastically for higher densities. Here the hard EOS leads to much more compressional energy than the soft EOS at the same density. For infinite nuclear matter at rest the inclusion of the momentum dependent interactions does not change the compressional energy. We see no difference between the cases S and SM or between the cases H and HM. This changes drastically if one considers heavy ion collisions: the additional repulsion due to the initial separation of projectile and target in momentum space shifts the curve for the SM and HM interactions to higher energies.

### 5.3. Collisions

The scattering of nucleons in nuclear matter in the low density expansion should be described in terms of the Brückner  $g$ -matrix (eq. 3.20),

$$g(E) = V + V \frac{Q}{E - e + i\epsilon} g(E), \quad (5.31)$$

where the Pauli operator  $Q$  projects on unoccupied states only and  $e$  is the energy of the intermediate state,  $e = p_1^2/2m + p_2^2/2m + U(p_1) + U(p_2)$ . At high energies the influence of the Pauli blocking is small and the kinetic energy is large compared to the potential  $U$ . Then the  $g$ -matrix becomes identical to the transition matrix which describes the scattering between two free nucleons, and which we discussed in the preceding chapter. We assume for the time being that above  $E_{lab} = 200$  MeV/n we can neglect the Pauli blocking of the intermediate states and include the Pauli blocking of the final state only. Of course it would be highly desirable to have true in-medium corrected scattering amplitudes. At high energies these are only available for an equilibrated environment and amount to a 30% reduction of the free cross section  $\sigma_{free}$  [36, 37]. Recently, however, also an increase of the in-medium cross section compared to the free one has been put forward [38, 39]. Thus presently it is hard to judge the direction of in-medium corrections to the nucleon–nucleon cross section on the basis of nuclear matter calculations. The influence of the Pauli blocking of the intermediate states in a highly nonthermal environment at the beginning of a heavy ion collision has never been investigated in detail. From a simple calculation of the blocked region in momentum space one would estimate that the size of the effect would be less than 30%. For a detailed discussion of these in-medium effects we refer the reader to ref. [17].

For the calculations presented in the next two chapters we neglect the blocking of the intermediate states and the influence of the pion polarization and use the measured free elastic and inelastic nucleon–nucleon scattering cross section. Unfortunately it was recognized only recently that the widely used parametrization of the nucleon–nucleon cross section which is discussed in detail in appendix B of ref. [89] is only a fit to the pp cross section and not a weighted sum of the pp and pn cross sections. Because in the energy regime of interest the pn cross section is (about 30%) larger than the pp cross section, this parametrization underestimates the number of collisions. We use the comparison between calculations employing  $\sigma_{pp}$  and  $\sigma_{pp}$ ,  $\sigma_{pn}$  to estimate the influence of changes in the cross sections. All cross sections were parametrized by Cugnon [66]. The effective cross section, however, is smaller due to the Pauli blocking of the final state.

Table 3 shows the combinations of cross sections and equations of state we employed for the calculations presented in the next two chapters.

Table 3  
Survey of cross sections and equation of states. Note that Pauli blocking in the final state is always applied

Compressibility (MeV)	Velocity dependence	Cross section	Name	Table
200	no	$\sigma_{pp}$	S (SC)	1
380	no	$\sigma_{pp}$	H (HC)	1
200	yes ( $\sim\rho$ )	$\sigma_{pp}$	SM	2
200	no	$\sigma_{pp}, \sigma_{pn}$	SF	1
380	no	$\sigma_{pp}, \sigma_{pn}$	HF	1

For low energy reactions, below  $E_{\text{lab}} = 100$  MeV/n, we employ an isotropic hard core cross section already used in BUU calculations [63, 64] as well as a Brückner  $g$ -matrix approach. This topic will be discussed in section 5.5.

In section 4.3 we have discussed the detailed form of the final state of two scattering nucleons. This form, however, is too complicated for actual calculations. Instead of calculating the final Wigner densities for a given impact parameter, which yields negative values of the Wigner densities in certain phase space regions, we employ an impact parameter averaged transition matrix which yields only positive values. Furthermore we assume that all particles coming closer than  $r = \sqrt{\sigma/\pi}$  scatter with probability 1, whereas those passing at a larger distance do not scatter. This last condition was checked quite extensively by Hartnack [102], who found that other possible prescriptions do not influence the final observables in a way not hidden by statistical fluctuations.

The scattering angles of the single nucleon–nucleon collisions are randomly chosen in such a way that the distribution of the scattering angles of all collisions agrees with the measured or calculated angular distribution for elastic and inelastic collisions.

Inelastic collisions lead to the formation of delta particles, which can be reabsorbed by the inverse reaction. We do not incorporate free ( $s$ -wave) pions here, unlike the VUU approach [64].

#### 5.4. Pauli blocking

Whenever a collision occurs, we check the phase space around the final states of the scattering partners. For simplicity we assume that each nucleon occupies a sphere in coordinate and momentum space. This trick yields the same Pauli blocking ratio as an exact calculation of the overlap of the Gaussians, but is much less time consuming to calculate. We determine which fractions  $P_1$  and  $P_2$  of the final phase spaces for each of the two scattering partners are already occupied by other nucleons. The collision is then blocked with a probability

$$P_{\text{block}} = 1 - [1 - \min(P_1, 1)][1 - \min(P_2, 1)], \quad (5.32)$$

and, correspondingly, is allowed with probability  $(1 - P_{\text{block}})$ . Whenever a collision is blocked, we replace the momenta of the scattering partners by the values they had prior to scattering. Care is taken for nucleons which are close to the surface of the many nucleon system, where the above description includes also portions of phase space which are classically forbidden as a consequence of energy conservation. For a nucleus in its ground state, where all collisions should be blocked, we obtain an averaged blocking probability  $\langle P_{\text{block}} \rangle = 0.96$ . This determines the low energy limit of our theory:

aiming at no more than 25% artificial collisions, i.e. collisions which are due to an insufficient Pauli blocking, we can only admit beam energies at which no more than 84% of the collisions are blocked. Therefore  $E_{\text{lab}} = 20 \text{ MeV/n}$  is at the moment the lower bound of the validity of our approach.

### 5.5. Numerical tests

*Stability.* One basic requirement that the model has to fulfill is the stability of nuclei on a time scale comparable with the time span needed for a nucleus–nucleus collision. High energy collisions ( $E_{\text{lab}} > 500 \text{ MeV/n}$ ) require less than  $80 \text{ fm/c}$  as far as single particle properties are concerned. However, it turns out that in order to investigate the fragmentation process in heavy ion collisions we have to follow the reaction for a considerably longer time. Unstable fragments are formed which have an excitation energy near the particle emission threshold and hence the time for particle emission is quite long, i.e. of the order of a compound nucleus lifetime.

Figure 9 shows how a single nucleon moves in the potential generated by all its fellow nucleons in a gold nucleus. For clarity we also show a circle of the radius of  $r = 1.3A^{1/3}$ . One has to keep in mind that in the QMD approach the surface is a consequence of the strength of the mutual interactions and it is not automatically a constant as a function of time. We see that the nucleon moves quite a distance during  $200 \text{ fm/c}$ . Whenever it comes close to the "surface" it is pulled back by the other nucleons. Thus the nucleons remain confined in a sphere.

Figure 10 shows the time evolution of the root mean square radius of five nuclei ranging in mass from Li to Au.

In each row the time evolution of the radii of 12 differently initialized nuclei is displayed. For the heavy nuclei we see oscillations around the mean value, but no nucleons are emitted. Light nuclei are a little less stable. One or two of the nuclei emit one nucleon in the time span of  $200 \text{ fm/c}$  because the local density approximation is not very good for these light nuclei. Nevertheless, we see that the majority of the nuclei remain stable. As described in section 4.1 we can eliminate the unstable light nuclei.

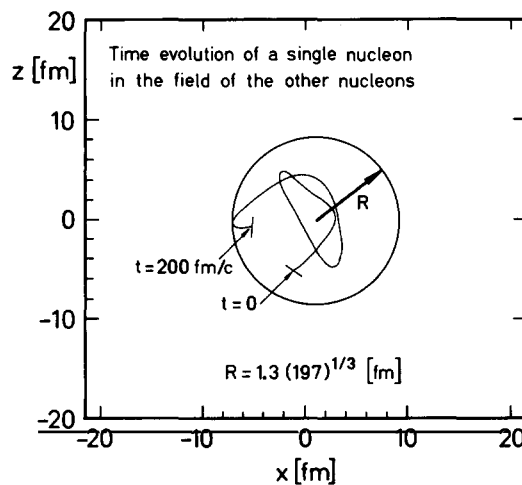


Fig. 9. The trajectory of a single nucleon in the field of 196 others is displayed for a time span of  $200 \text{ fm/c}$ . To visualize the size of the system we show also a sphere of radius  $r = 1.3 \times 197^{1/3}$ .

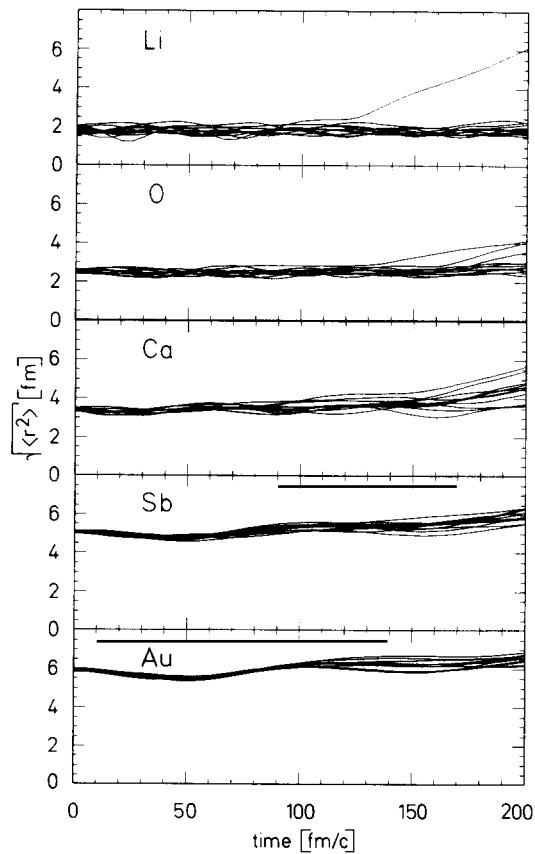


Fig. 10. Root mean square radii of different nuclei as a function of time. For each nucleus we display this radius for 12 different initializations.

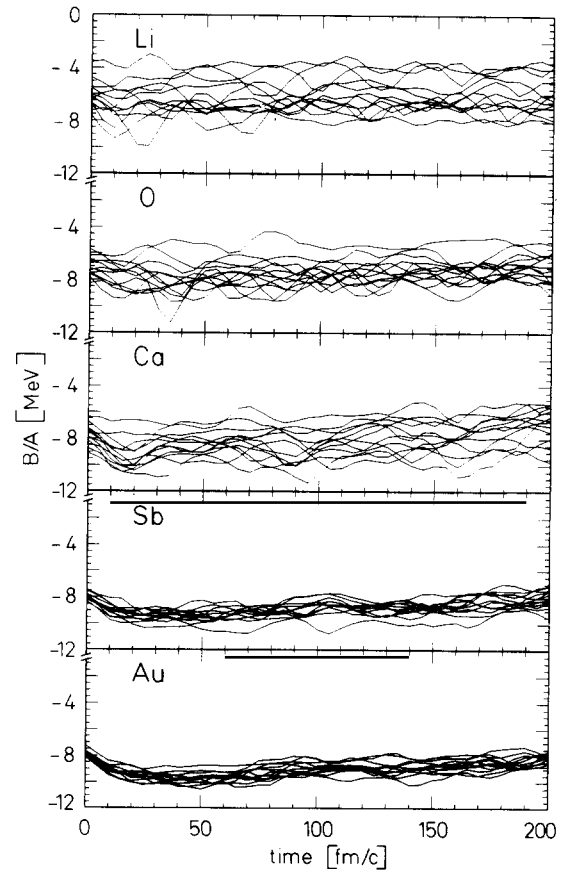


Fig. 11. Binding energy per nucleon as a function of time for the 12 simulations of the different nuclei displayed in fig. 10.

Figure 11 displays the binding energy per nucleon averaged over all nucleons for the same sample of 12 nuclei.

First of all we see that the binding energy fluctuates around a mean value. So we have energy conservation on the average. However, the fluctuations reach 2 MeV/n, a large value compared to the average binding energy of 8 MeV/n. In order to appreciate the size of the fluctuations one has to realize that the potential energy is just the difference between the two large quantities, the attractive two-body part ( $\approx -350$  MeV at  $\rho = \rho_0$ ) and the repulsive three-body part ( $\approx 300$  MeV at  $\rho = \rho_0$ ). Hence a 1 MeV/n fluctuation means that we determine these potentials to an accuracy of one part in  $10^3$ . The light nuclei show more fluctuations than the heavier ones. The many nucleons which have to be initialized in the case of heavy nuclei give a longer series of random numbers. This averages out some of the fluctuations. Thus energy conservation is here much better than in the BUU calculations, where the use of a grid for the determination of the potential energy makes energy conservation quite difficult. Employing a fourth-order Runge-Kutta method for the time evolution the energy fluctuations can be substantially reduced; however, the CPU time then increases by a factor of five.

The least bound configurations in the cases of lithium and oxygen are those which emit particles earliest (fig. 10). Discarding these initial configurations, which have a low binding energy, allows a

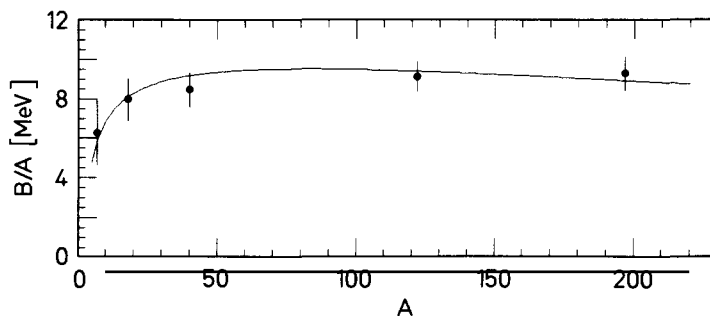


Fig. 12. Average binding energy of the nuclei as a function of the mass number  $A$ . The binding energy is obtained by averaging the binding energy for each individual simulation over the first 100 fm/c. Then we average over the 12 simulations. The values are compared with the Weizsäcker mass formula without symmetry energy.

further reduction in the number of unstable nuclei. This cut can be applied when it is important to keep light nuclei stable for a long time.

In fig. 12 we show the average binding energy per nucleon of our nuclei. These numbers are average values over the first 100 fm/c and over all simulations. For low masses not only the trend but also the absolute values are reproduced. At large masses the binding energy becomes constant and the nuclei are overbound by 1 MeV/n. We do not see a maximum in the binding energy in the region of iron as we did not include the symmetrization energy.

More important than the reproduction of the root mean square radius is the requirement that the nucleus keeps its radial distribution. In fig. 13 we investigate the radial distribution of a gold nucleus in detail. We display the density profiles in timesteps of 30 fm/c for two different Yukawa potentials: In the upper figure we see the distribution with the Yukawa parameters chosen in our calculations. We observe that the nuclear surface is preserved for almost 300 fm/c. To understand the large fluctuations in the interior, one has to recall that there are very few (about four) nucleons in this region. We will see that these fluctuations average out as a function of time. In the lower figure with different Yukawa parameters, we see that the nuclear surface is much less well preserved, although the root mean square radius as well as the nuclear binding energy are very close to those of the upper frame.

If we average the density over the 12 nuclei and over the first 100 fm/c we find a quite smooth density distribution. It is displayed in fig. 14.

Our surface thickness is slightly too large as compared to that extracted from electron scattering experiments; however, the overall features are quite nicely reproduced. Due to the few nucleons present we are not able to avoid fluctuations of the central density. In order to make the density profile as accurate as possible we take care that between 15 and 40 fm/c, when colliding nuclei reach their maximal density and the transverse momentum is built up, the central density of a single nucleus agrees with the values obtained in Hartree-Fock calculations [108]. In these calculations the central density of a static nucleus is around  $0.155 \text{ nucleon/fm}^3$  and thus around 10% lower than the central densities of the BUU simulations. This is probably the reason that in BUU calculations a higher maximal central density is obtained compared with QMD calculations.

*g-matrix approach versus isotropic cross section.* One of the shortcomings of the BUU approach for low energy heavy ion reactions,  $25 \text{ MeV/n} < E_{\text{lab}} < 400 \text{ MeV/n}$ , is the lack of realistic cross sections. At high energies the replacement of the  $g$ -matrix with the transition matrix is a reasonable choice. At low

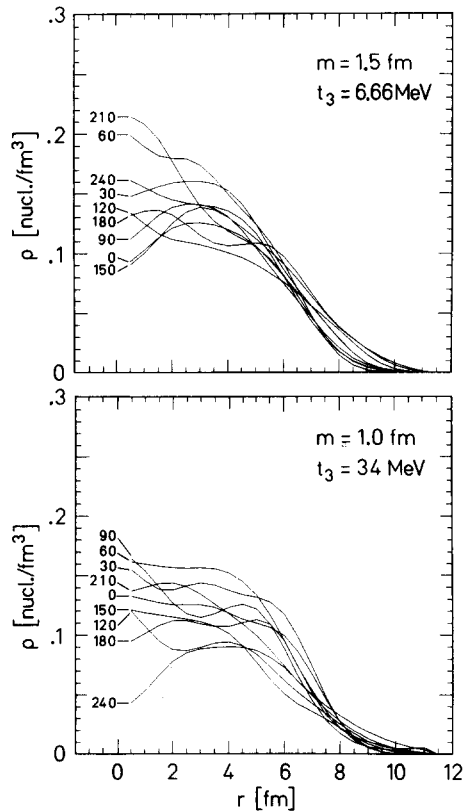


Fig. 13. Radial density distribution for a gold nucleus as a function of time in steps of 30 fm/c. The upper figure shows this distribution for the Yukawa parameters applied in the calculations. The lower figure shows this distribution for a different choice of these parameters in order to demonstrate the dependence of the surface fluctuation on the Yukawa parameters.

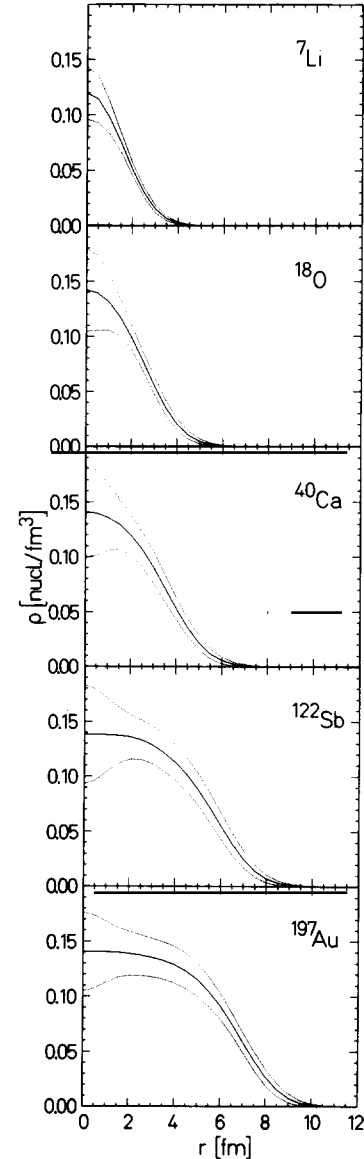


Fig. 14. Radial density distribution of the nuclei. We have averaged the local density over the first 100 fm/c. We display the mean value as well as the standard deviation.

energies the free cross section gets very large, but Pauli blocking in the intermediate steps of the Bethe–Goldstone equation reduces the observed cross section considerably. Due to the lack of any calculation a 40 mb isotropic cross section was employed in the BUU calculations. Its size was inspired by the hard core radius of the nucleon–nucleon potential but never confirmed by calculations.

Recently a nonrelativistic  $g$ -matrix calculation became available [109] which could be employed to

calculate the required cross section as a function of five different parameters (the relative momentum of the collision partners and the Fermi seas, the density of projectile and target at the point of collision and the isospin). We obtain cross sections with a high anisotropy [110] which range between 30 and 200 mb.

Figure 15 shows a comparison of the longitudinal and transverse momentum transfer, the number of emitted nucleons and the number of collisions for two different cross sections. The dots are the results of an isotropic  $\sigma_{\text{eff}} = 40$  mb, the circles those of a calculation where a  $g$ -matrix calculation was employed to calculate the in-medium scattering cross section. The results are displayed for two different reactions, 84 MeV/n C + C and 400 MeV/n Nb + Nb. As far as observables are concerned the differences between the two cross sections are of the order of 15%. Thus these calculations confirm recent results obtained by Bertsch et al. [111], who fitted the absolute value of an isotropic cross section to experimental data and found that  $\sigma = 40$  mb was a good choice. The only major difference is the average number of collisions. This difference can easily be explained: nucleons which escape from the system have the free nucleon-nucleon scattering cross section, which is very large if the scattering partners have a small relative momentum. So most of these additional collisions occur during the later stages of the reaction and hence do not influence the dynamics of the reaction.

It is astonishing that these different cross sections yield the same momentum transfer. However, a closer inspection shows that the key quantity for the dynamics, the average momentum transfer in a nucleon-nucleon collision, is very similar for both cross sections. So we observe that a large cross

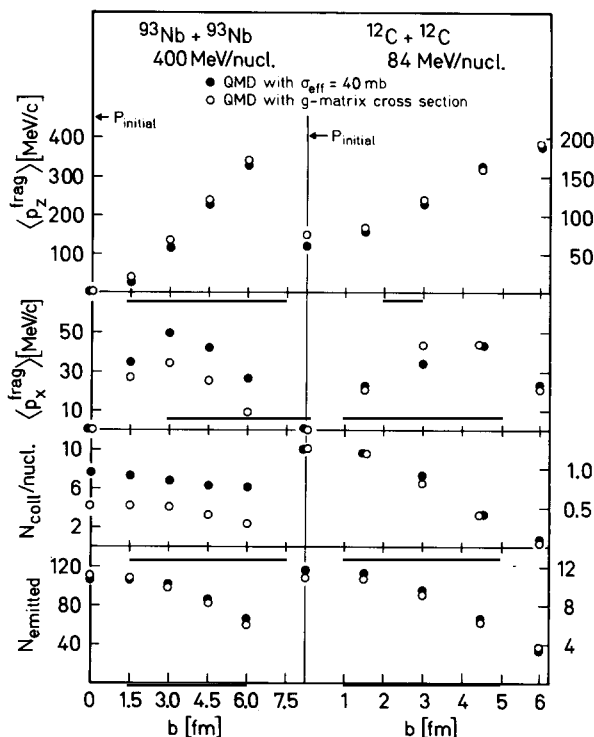


Fig. 15. Comparison of global variables (number of emitted particles, final longitudinal and transverse momentum of all projectile-like fragments and the number of collisions) for two different calculations. The dots mark the results of a calculation using an isotropic 40 mb cross section, the circles are the result of a calculation where a  $g$ -matrix was employed to calculate the scattering cross section.

section which is more forward peaked yields the same result as a smaller more isotropic cross section. The momentum transfer is almost complete only in the case of Nb + Nb for the most central collisions,  $b < 1.5$  fm. We will discuss the longitudinal momentum transfer in more detail in chapter 7.

*Comparison with one-body theories.* How do the results of the  $n$ -body theory differ from those of one-body theories? In fig. 16 we display the time evolution of the density profile of the reaction 84 MeV/n C + C ( $b = 1$  fm) for three different theories [16]: the quantum time dependent Hartree–Fock (TDHF), the classical Vlasov equation and the QMD, in which we have blocked all collisions artificially.

The TDHF and the QMD calculations are displayed in lines of constant densities, where the density changes from line to line by a factor of two. The asymmetry between projectile and target in the QMD calculation is due to the finite number of simulations (100). For the Vlasov calculation we have projected the coordinates of 100 simulations onto the reaction plane. We observe a striking similarity between all three calculations. The longitudinal momentum transfers, as well as the momentum transfers in the transverse direction, are very similar in all three approaches. Only the densities between the two remnants are slightly different. The TDHF calculation finds, in the region around the origin, a density of about  $\rho_0/2^6 = \rho_0/64$ . On this level the fluctuations become important, and furthermore we should not expect agreement between these theories on the one-percent level.

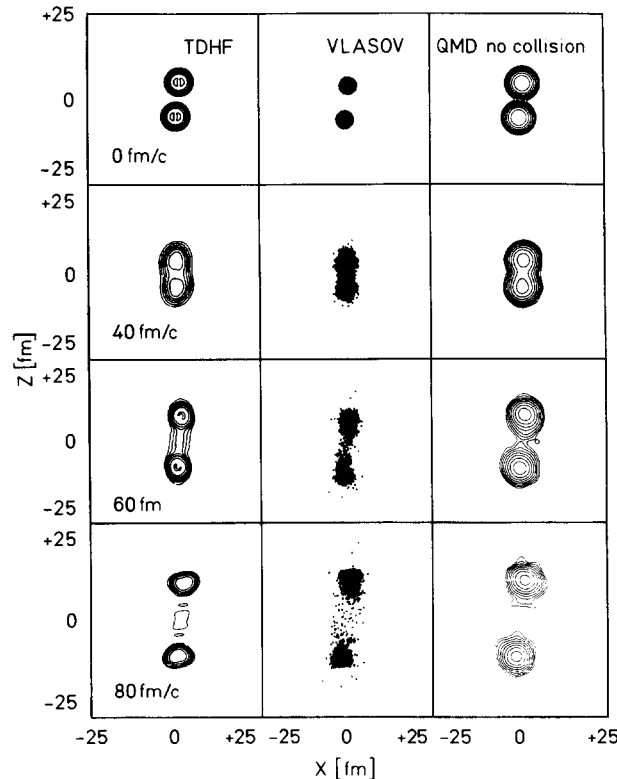


Fig. 16. Comparison of the different mean field calculations of the reaction 84 MeV/n C + C ( $b = 1$  fm) [16]. We display results for the density profile for the TDHF, the Vlasov and the QMD approach for four time steps. The TDHF and the QMD calculations are displayed in lines of constant density which are separated by a factor of 2. For the Vlasov calculation each nucleon of 100 simulations is marked by a circle and the coordinates of all nucleons are projected onto the reaction plane.

Let us recall the different initializations of these theories. The TDHF calculation starts out from a Slater determinant, which is a solution of the static Hartree–Fock equation. The Vlasov equation starts out from randomly drawn positions inside a sphere of radius  $r = 1.12A^{1/3}$  and random momenta between zero and the local Fermi momentum. The QMD starts from a biased choice of positions and momenta as explained in section 4.1. These initializations share the common feature that the density in the interior of the nucleus is almost constant. Since the potentials are most sensitive to the density and not as sensitive to the finer details, we can expect a similar time evolution for a *common* initial configuration in all three approaches. The similarity of the results indicates that finer details of the initial configuration, i.e. the detailed form of the wavefunction of the nucleons inside the nucleus, are of minor importance for the time evolution of the system compared to the average initial density, at the energy considered.

The time evolution changes completely if we include two-body collisions, as done in fig. 17. Here we display the time evolution of BUU and QMD calculations and, for comparison, that of the Vlasov approach (a BUU calculation in which all collisions are blocked). We see a close similarity between those calculations which include collisions, in contrast to the mean field calculation. The lack of two-body collisions results in a strongly forward peaked angular distribution of the few emitted nucleons (about one per nucleus–nucleus collision), which is in sharp contrast to the experimental data. The collision term creates a mid-rapidity source which emits particles almost isotropically. There are two remnants left which contain on the average half of the projectile and target nucleons.

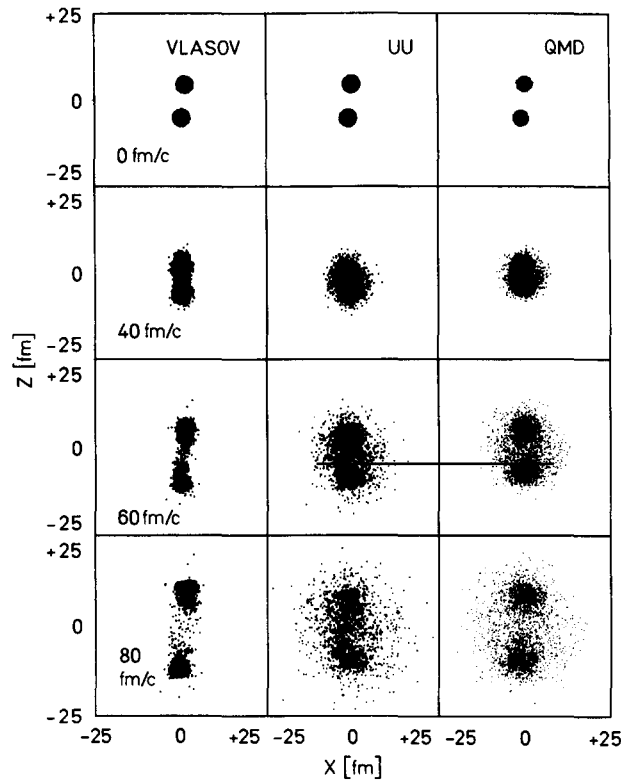


Fig. 17. Comparison between the one-body (BUU) and the  $n$ -body (QMD) theory and, for comparison, the classical mean field theory for the reaction  $84 \text{ MeV/n C} + \text{C}$  ( $b = 1 \text{ fm}$ ) [16]. We display the density profile for four time steps. For each time step 100 simulations are plotted and each nucleon is marked by a square or a circle. The coordinates of all nucleons are projected onto the reaction plane.

A quantitative comparison between BUU and QMD is shown in fig. 18. Here a comparison of different characteristic observables is displayed as a function of the impact parameter. We have averaged over all target and projectile nucleons since the definition of which particles have to be considered as emitted is different in both approaches and would otherwise generate uncertainties. The linear momentum transfer in both approaches is very similar. Even in the most central collisions the linear momentum transfer is far from being complete. At  $b = 1$  fm we still observe a final momentum of  $p_z^{\text{final}} \approx p_z^{\text{initial}}/3$ . The final transverse momentum is also very similar at low impact parameters. At large impact parameters the different surfaces and the finite range of the potential in the QMD as compared with the BUU yield a larger net attractive force. The descriptions used to determine the number of emitted particles also yield a very similar result, which represents a later justification of the method applied in the BUU approach [63]. Only the number of collisions differs between the two approaches. The additional collisions most occur between nucleons in the projectile and target remnants during the later stages of the interaction. For such light nuclei, with  $A \approx 6$ , the prescription of the Pauli blocking is not very satisfying. However, note that these additional collisions do not lead to an artificial emission of nucleons from these light clusters, as can be seen from the number of emitted nucleons. Looking at the observables one can easily see that the additional collisions do not influence the dynamics of the reaction.

An even more extensive comparison between one-body BUU-type calculations and the QMD approach was recently performed [112] at a much higher beam energy (800 MeV/n La + La). As can be seen in fig. 19, all employed theories agree in their prediction of the differential cross section  $E d^3\sigma/dp^3$  for protons.

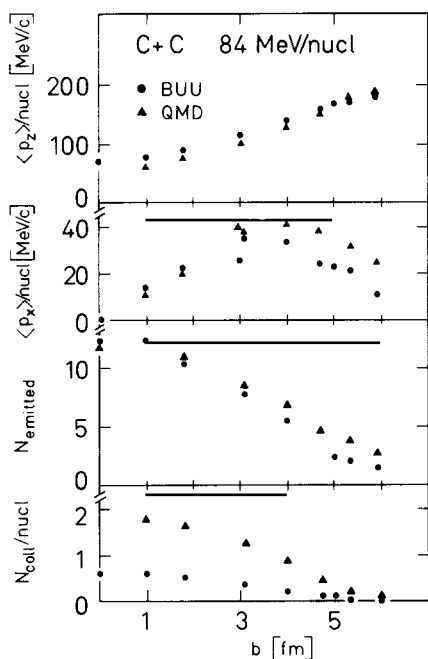


Fig. 18. Comparison of some global variables obtained in the one-body (BUU) and the  $n$ -body (QMD) approach [16]. We display the number of emitted particles, the average final momenta of all target nucleons and the number of collisions for two different calculations.

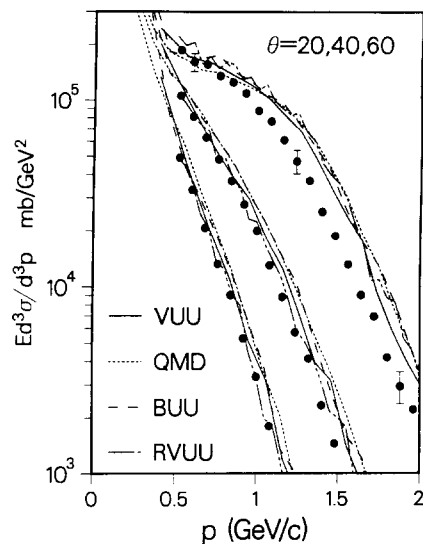


Fig. 19. The differential cross section  $E d^3\sigma/dp^3$  for the reaction 800 MeV/n La + La obtained in the one-body approaches (BUU [32], VUU [64], RVUU [114]) as compared to the  $n$ -body (QMD) approach [11]. We display the results of the four different theories [112] and compare them with data of Hayashi et al. [113].

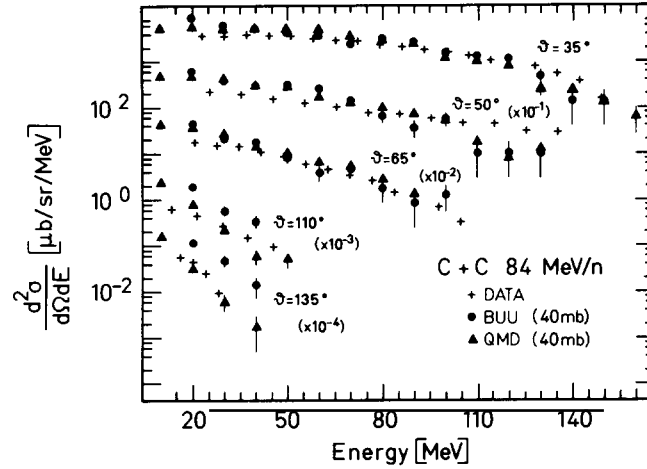


Fig. 20. The double differential cross section  $d\sigma/d\Omega dE$  obtained in the one-body approach (BUU) [63] as compared to the  $n$ -body (QMD) approach [16]. We compare the results with data of Brummund [115].

In view of the vastly different inputs [112] this is an astonishing result, which shows that single particle observables are rather robust against the change of potentials, density profiles and scattering prescriptions. Not only at this high energy but also at 84 MeV/n is the agreement of the QMD approach with the results of the one-body BUU theory and with experiment very good, as can be seen from fig. 20. Here the double differential cross section  $d\sigma/d\Omega dE$  for protons is displayed and compared with data of ref. [115]. At backward angles the BUU calculation suffers from the problem how to determine the target remnant.

We can conclude that the QMD approach reproduces the observables obtained with the BUU approach quite well. In addition, the mean field version produces the same time evolution as the Vlasov and TDHF calculations. The 40 mb isotropic cross section was a good choice, and yields the same results for the investigated observables as the much more refined, but also numerically more expensive,  $g$ -matrix approach. However, if one wants to look into specific exit channels such as subthreshold pion production, the  $g$ -matrix approach should be employed. Having seen that on the one-body level QMD agrees with the one-body theory we can proceed and take advantage of the  $n$ -body nature of the QMD approach.

All calculations presented here with the exception of the reaction 1050 MeV/n Ne + Au were performed with the QMD version 102 [19]. For the Ne reaction an older QMD version (version 100) was employed, which had a different initialization of the nuclei. The older initialization had a slightly higher initial central density and produced a slightly larger transverse momentum. All other observables agree in both versions.

## 6. Multifragmentation

One of the most challenging tasks for an  $n$ -body theory in nuclear physics is the description of the multifragmentation of heavy nuclei. In emulsion experiments, up to seven medium or large mass fragments  $A > 4$  of a gold nucleus have been found. The description of such a process certainly exceeds the limits of any one-body theory.

In section 6.1 we review the basic experimental results as well as the phenomenological and microscopic models which were used up to now to study multifragmentation. We then proceed in section 6.2 to a detailed comparison between the results of our approach and the experimental data. The QMD approach, which is a theory that follows the space–time evolution of the reaction, provides much more information than experiments, which can only measure the momentum space distribution. In section 6.3 we take advantage of this fact and investigate in detail the multifragmentation reaction and, in section 6.4, the cause of fragment formation. What we can learn about the nuclear equation of state from the fragments is presented in section 6.5.

### 6.1. Experimental facts and review of the theories

The first multifragmentation events, or more precisely, medium mass clusters  $5 \leq A \leq 30$ , were observed in high energy proton induced reactions [116]. They were quite unexpected and a straightforward physical explanation of the production mechanism was not at hand. The fragments received the name "deep spallation products", but it has never been proven that they are actually the remnants of a decay chain. The most prominent feature was the power law dependence of the inclusive mass yield [ $\sigma(A) = A^{-\tau}$ ], a functional form which is expected for a system close to the transition between the liquid and vapour phases [116, 117].

The same form of mass yield curve was also found in heavy ion induced reactions [118], where the threshold for the production of the deep spallation products is much lower ( $E_{\text{lab}} \approx 25 \text{ MeV/n}$ ). The similarity triggered the suggestion that the observed shape of the inclusive mass yield curve indeed presents evidence for the occurrence of this phase transition in nuclear collisions [118, 123]. This conjecture raised a lot of opposition. Firstly, the objection was made that it is quite improbable that the system – independently of the impact parameter – exactly hits the critical point. Above and below the critical point the mass yield falls exponentially and much more steeply as a function of  $A$ . The second objection was that most of the observables could be reconciled with the assumption of thermal equilibrium, albeit, with vastly different temperatures. The slope of the fragment momentum distribution was Maxwellian but the slope parameter – which should be the temperature – depends on the fragment mass [116] and is of the order of 15 MeV [116, 119, 120]. The isotopic distribution, which was measured with an admirable accuracy over seven orders of magnitude [121], revealed a temperature of 3 MeV [9, 122]. Finally, whereas the fragments from proton induced reactions showed an isotropic emission pattern, those produced in heavy ion reactions cannot be described by a single thermal source [120].

Further theoretical investigations have demonstrated that the mass yield curve is rather insensitive to the different reaction mechanisms proposed: statistical or thermodynamical models without Coulomb interaction [123–125] or including it [126, 127] describe the observed mass yield equally as well as models in which the system does not come to a global [128] or at least to a local equilibrium prior to fragmentation. The latter class of phenomenological models contains approaches in which the fragmentation is assumed to be similar to the percolation on a finite lattice [129, 130] or to the shattering of glass [131, 132]. For details of these phenomenological models we refer to a recent review [9].

The first dynamical models treated the nucleus–nucleus collision as a two-step process. Firstly an early compression phase which leads to a global thermodynamical equilibrium of the whole system, which can be described completely by two variables: a temperature  $T$  and a density  $\rho$ . This serves as the initial condition for the subsequent expansion phase, which is treated microscopically, either by using the TDHF [133] equations or by applying classical molecular dynamics [73]. The essential result of these

calculations was the observation that fluctuations of the phase space density at the beginning of the expansion are reflected in the distribution of the observed clusters.

Cluster formation was first treated in a model which described the complete time evolution of the reaction by applying a potential model to the final phase space distribution of a Boltzmann–Uehling–Uhlenbeck (BUU) [63] calculation, or by applying a phase space coalescence model to the Vlasov–Uehling–Uhlenbeck (VUU) [64] model. Both approaches aimed at a removal of their contribution to the primordial proton spectra and treated the cluster formation not dynamically but as a final state interaction.

The first attempts to describe the dynamics of the clustering process were performed using modified BUU approaches, although a one-body theory certainly is not a proper tool for the investigation of many body correlations. Here the mean field averages out the correlations and fluctuations among the nucleons in one single nucleus. Consequently, on top of the actual one-body collision dynamics one has to artificially include processes which generate fluctuations. However, because of the one-body dynamics, one cannot follow them in time. Due to this limitation these calculations did not produce results which could be compared either with experiments or with true  $n$ -body theories.

Bauer et al. [134] reduced the nucleon–nucleon cross section by a factor of 100. For compensation, when a collision occurs 198 nucleons in the vicinity of the actual collision partners are scattered as well. Between collisions particles move in the ensemble averaged mean fields. This method has three problems: first of all the result depends on how to select the 198 nucleons out of the total number ( $100A_T + 100A_P$ ) of nucleons present and how to determine the partners in the individual nucleon–nucleon collision. Secondly, the propagation in the mean field washes out part of the fluctuation caused by the collisions, and thirdly the Pauli blocking is not well defined, because the whole neighbourhood of the collision partners in phase space is changed at the same time.

Das Gupta et al. [135] divide the reaction into two steps, an initial stage, where collisions are dominant, and an expansion, where the mean field provides the clustering of the nucleons. The initial stage is described by a high-energy cascade calculation. It generates the input for the subsequent mean field calculation which describes the expansion. If the clusters are made up only by those nucleons whose time evolution is initially dominated by collisions (i.e. "fireball" nucleons), this method will be reasonable. If the clusters are predominantly spectator nucleons, this method will fail, because the first stage of the time evolution of the spectator nucleons is mostly governed by the mean field. As we will see, we find that clusters predominantly contain spectator nucleons.

Recently Beauvais et al. [136] developed an approach similar to QMD, which is based on the local density approach to the potential. They determine the potential at the centre of a Gaussian distribution of nucleons by calculating the local density caused by the other nucleons at that point. This approach is also a true  $n$ -body theory.

## 6.2. Confrontation of the model with data

Although the fragmentation of heavy nuclei is a well established phenomenon, there are only three published experiments known to us in which more than just the inclusive mass yield of the fragmentation products was measured.

(1) The reaction  $\text{Ne} + \text{Au}$  at several beam energies by Warwick et al. [120], where the triple differential cross section  $d^3\sigma/dE d\Omega dZ$ , the associated multiplicity of fast particles and correlations between jets of light fragments and the target rapidity fragment were measured. In this way the strong

azimuthal (anti-)correlation, which was predicted by hydrodynamical [125] models ("bounce off") was observed [120].

(2) The reaction Au + emulsion at 1 GeV/n by Waddington and Freier [137], where all fragments of the gold nucleus were recorded by each individual reaction. The primary goal of this experiment was the search for anomalons. The results, as far as they were of interest for the multifragmentation of the Au nucleus, were recently analyzed [138].

(3) The reaction Au + Au at 200 MeV by Kampert et al. [6], where the fragment multiplicity, the associated multiplicity of fast particles and the fragment flow were recorded.

Calculation of the triple differential cross section  $d^3\sigma/dE d\Omega dZ$  in the QMD approach is beyond the feasibility of present day computers. We therefore have to restrict ourselves to mean values and to the angular distribution  $d\sigma/d\Omega = \Sigma_Z \int dE d^3\sigma/dE d\Omega dZ$ .

We investigated one highly asymmetric reaction, where the participant spectator model [9] has given a quite accurate description of the single particle distribution, as well as a symmetric system, where for central collisions this picture cannot hold. The reactions we have chosen are Ne(1050 MeV/n) + Au and Au(200 MeV/n) + Au. We performed calculations at five different impact parameters ( $b = 1, 3, 5, 7$  and 10 fm). Larger impact parameters do not produce a significant amount of fragments in the most interesting range  $5 \leq A \leq 30$ . For the two most central impact parameters we have calculated 360 events, whereas for the larger impact parameters we restricted ourselves to 180 simulations. One simulation requires around 1 minute CPU time on a Cray 1 computer for the first and 5 minutes for the second reaction.

The reactions were followed for 300 fm/c ( $1 \times 10^{-21}$  s) for Ne + Au and 200 fm/c for Au + Au. The latter reaction is more violent and therefore the final distribution is obtained in a shorter time. Anyway, this is a very long time as compared to the time it takes the neon projectile to cross the target (20 fm/c) and even longer than was required for simulating reactions at 25 MeV/n [63]. As we will see, the mass distribution continuously changes up to this time as a consequence of the long decay time of moderately excited heavy clusters.

Nucleons are considered to be part of a cluster if in the end at least one other nucleon is closer than  $r_{\min} = 3$  fm. No cuts in momentum space are applied. They are not necessary, because after 200 and 300 fm/c, respectively, nucleons with large relative momenta are no longer close together in coordinate space. In addition the Coulomb force helps to separate the clusters.

The cluster distribution is not very sensitive to the value chosen for  $r_{\min}$ . This can be seen from table 4, which shows the exponent  $\tau$  of the mass yield  $\sigma(A) = A^{-\tau}$  for different  $r_{\min}$  and different fragment mass bins for the reaction Ne(1050 MeV/n) + Au.

We start with a survey of both reactions. In fig. 21 we present the time evolution of the reaction Ne + Au in the reaction plane for three different times: 0, 80, 300 fm/c. The arrows are proportional to the momenta of the nucleons.

At 80 fm/c we observe particles escaping from the interaction zone with almost the beam velocity

Table 4  
 $\tau$  parameters for different  $r_{\min}$  and for different fragment mass bins  $A$

$A$	$r_{\min} = 2$ fm	$r_{\min} = 3$ fm	$r_{\min} = 4$ fm
1-10	2.86	3.07	2.99
1-20	2.68	2.82	2.83
1-50	2.33	2.44	2.50

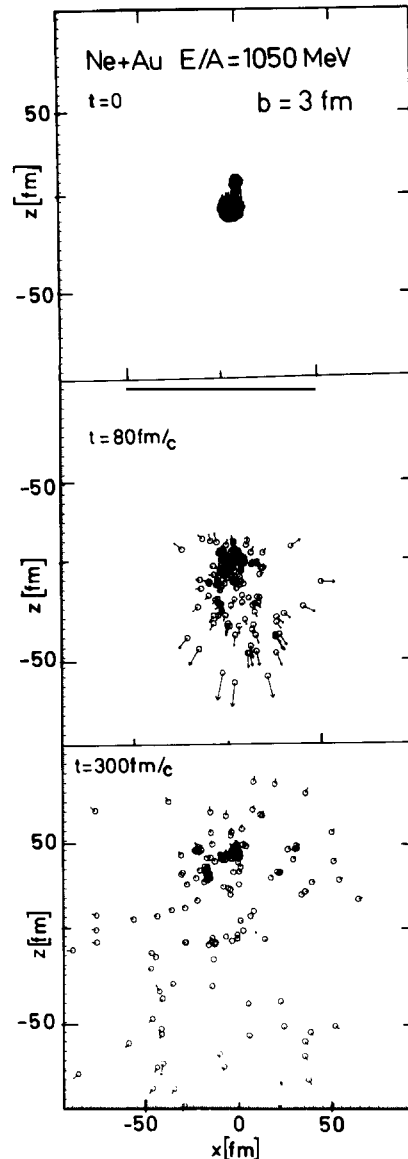


Fig. 21. Survey of the reaction Ne + Au, 1050 MeV/n,  $b = 3$  fm. We display the time evolution of the density distribution in the reaction plane for three different times.

although they have moved through the target. Behind them small clusters and less energetic nucleons are seen. Only a few particles are emitted in the backward direction. At 300 fm/c we observe some clusters which move with roughly the target velocity. They are separated from each other quite clearly. In the forward hemisphere we predominantly see nucleons and very few light clusters.

In fig. 22 we present the same plot (but without arrows) for the time evolution of the symmetric Au + Au reaction for various impact parameters at various time steps.

At central collisions no heavy cluster survives. We see quite a number of small clusters  $5 < A < 30$  which move isotropically out of the reaction zone. The single nucleons also show an almost isotropic

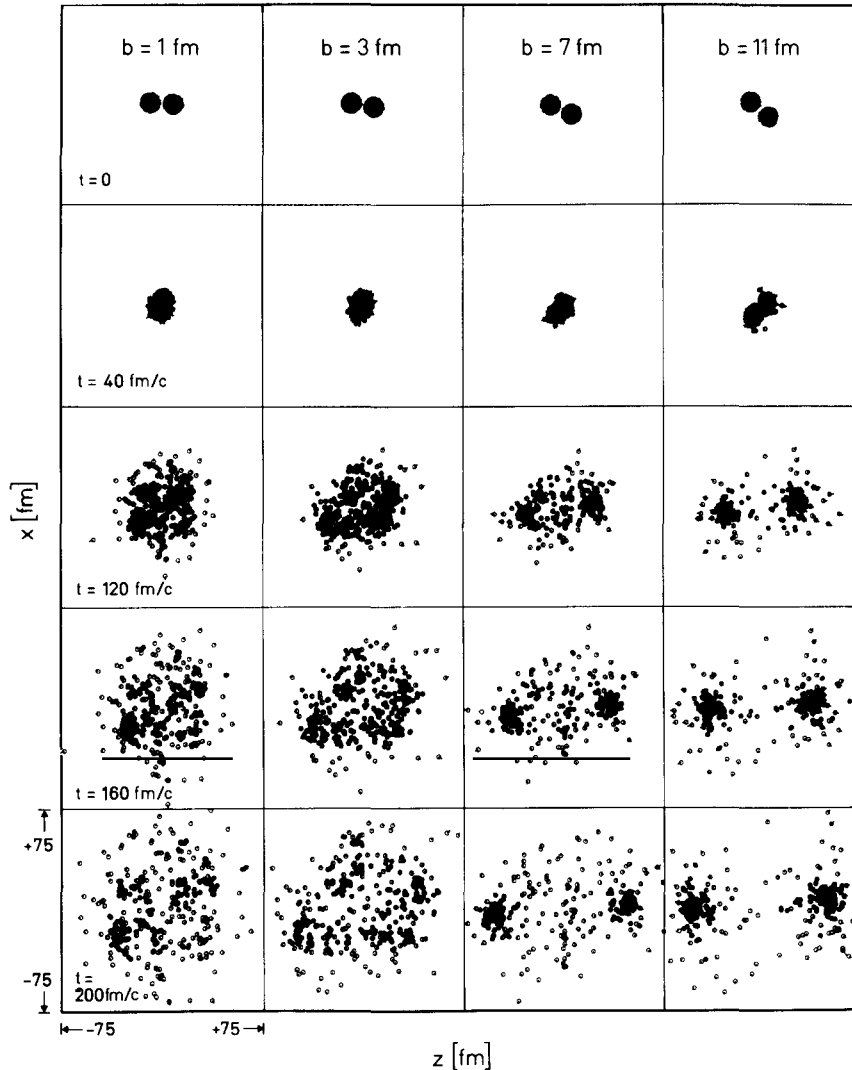


Fig. 22. Survey of the reaction Au + Au, 200 MeV/n, for four different impact parameters (1, 3, 7, 11 fm). We display the time evolution of the density distribution in the reaction plane for five different times.

distribution. The semicentral collision ( $b = 3$  fm) still displays some intermediate mass fragments, but their emission pattern is more elliptic than isotropic. The large axis has an angle of  $45^\circ$  with respect to the beam axis. This is a sign of transverse flow, as we will discuss later. The more peripheral reactions show remnants of projectile and target, which are excited and emit particles in their rest system. These are typical peripheral reactions. At  $b = 7$  fm we still find a small mid-rapidity source, which has disappeared at  $b = 11$  fm.

Figure 23 displays the total mass yield of the reaction Ne(1050 MeV/n) + Au as compared to the experimental data [120]. Both the theoretical and the experimental mass yield fall off with a power law  $A^{-\tau}$ , corresponding to a straight line in our double logarithmic plot. For the value of the constant  $\tau$  we obtain  $\tau = 2.44$  (compare table 4). The form of the mass yield, as well as the value of  $\tau$  ( $2 < \tau < 3$ ), is consistent with the assumption that the mass yield is a signal of a liquid-gas phase transition [117]. The

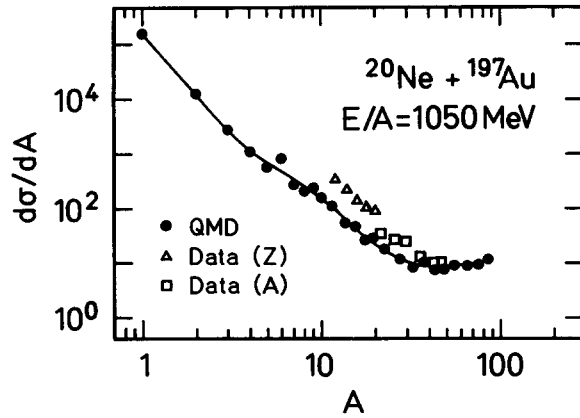


Fig. 23. The inclusive mass yield as compared to the data of ref. [120].

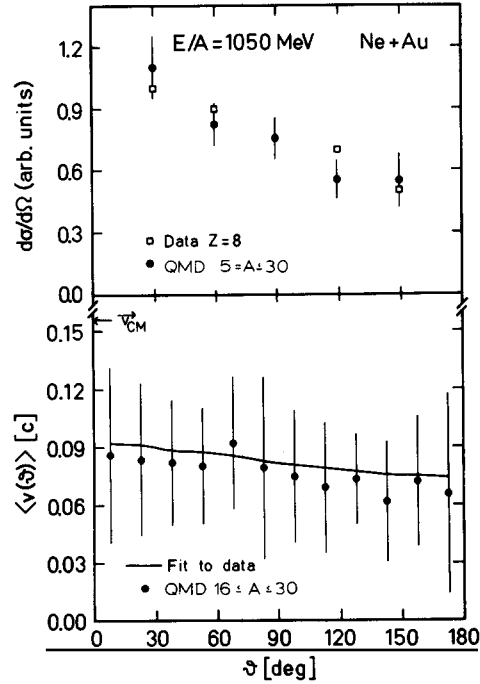


Fig. 24. (Top) Angular distribution and (bottom) average velocity as a function of the emission angle of medium mass fragments. The calculation is compared with data of ref. [120].

calculated slope of the mass yield curve is close to the slope of the experimental data but we underpredict the data by a factor of roughly two to three. The discrepancy is larger at low masses, which are extracted from the experimental  $\sigma(Z)$  under the assumption  $\sigma(A) = 0.5\sigma(Z = A/2)$ , than for those fragments whose masses were directly measured.

This discrepancy is a consequence of the instability of clusters excited with an energy around the particle emission threshold. Whereas – as we have seen – the clusters are stable in their ground state, the higher the excitation, the less correct is our description. Due to an insufficient treatment of the binding energy, weakly bound nucleons escape from the excited fragments and hence lower the average cluster mass. Furthermore, the level density of excited nuclei may be different in our approach compared to the known value. Our medium mass fragments emit one or two nucleons more than real nuclei with the same excitation energy. Only a partial counteraction against this systematic problem is possible. In order to cure this problem completely a quantum description of the final clusters is needed.

The mass yield has a minimum around  $A = 50$  and increases again for higher masses. In this particular experiment the mass yield of heavy fragments was not measured. Experiments with similar projectile–target combinations show a U shape for the mass yield [9], which has a minimum around  $A = A_T/3$  (in the absence of fission).

The upper frame of fig. 24 displays the angular distribution and the lower frame the average fragment velocity as a function of the emission angle for the reaction Ne(1050 MeV/n) + Au in the laboratory system.

Experimentally we see a decrease in the mass yield by a factor of two from forward to backward angles. This is nicely reproduced by the calculation. As we will see in detail later, this strong

dependence rules out an isotropic distribution of fragments in the centre of mass frame. In fig. 24 we observe only a weak dependence of the average fragment velocity on the emission angle. The average velocity is a little larger than half the centre of mass velocity. Hence the linear momentum transfer to the emitting system is far from complete. To determine the experimental average velocity we used the fit function (2.3) and the parameters of table 1 of ref. [132]. Also for the average fragment velocities we obtain agreement with experiment.

The upper frame in fig. 25 displays the number of fast charged particles associated with a fragment of a given size for the reaction Ne(1050 MeV/n) + Au. We applied the experimental cuts (a minimal energy of 25 MeV/n of the fast particles) to our calculation. For medium mass fragments our associated multiplicity is larger than seen experimentally. We should also mention that the experimental value is an extrapolation, because the detectors covered a small part of the total solid angle only. The lower frame in fig. 25 shows the average velocity of fragments as a function of their size in the laboratory system. We see a very high velocity for low mass particles, which gradually decreases for heavier ones. Beyond mass 90 the clusters move backward in the laboratory system! The average momentum transfer to heavy fragments is much smaller than that to the lighter fragments, which clearly shows that the fragments of different masses do not come from a single moving source.

Figure 26 displays the multiplicity distribution of heavy clusters  $Z \geq 3$ . The results of our calculation for ( $b \leq 3$  fm) are compared with data of refs. [137, 138] for Au(1 GeV/n) + emulsion. As already mentioned, in this experiment the charges of all Au fragments were recorded on an event-by-event

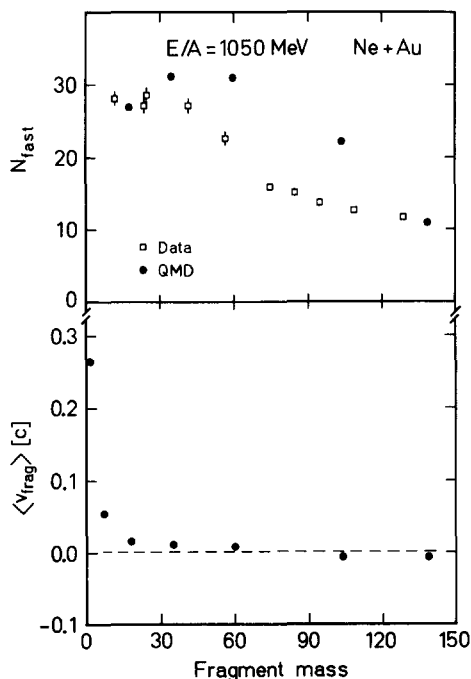


Fig. 25. (Top) Average number of fast particles associated with a heavy fragment and (bottom) the average fragment velocity in the laboratory system, as a function of the fragment mass. The data are from ref. [120].

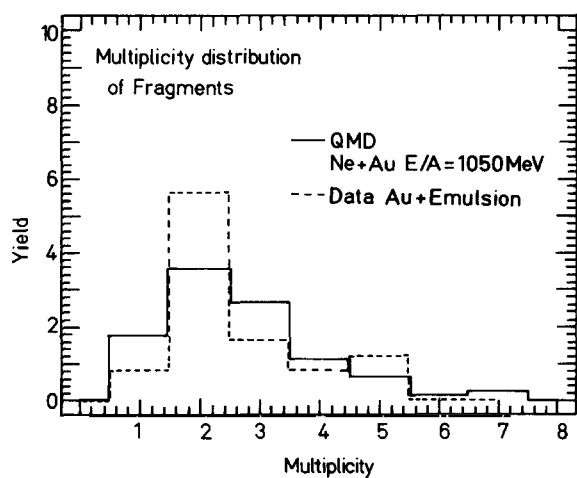


Fig. 26. Multiplicity distribution of heavy clusters  $3 \leq Z \leq 20$ . The results of our calculation ( $b \leq 3$  fm) are compared with data of refs. [137, 138]. To allow a comparison we accepted only those experimental events in which no cluster  $Z \geq 42$  was observed and the number of target tracks was between 5 and 8. By these cuts we want to discard peripheral collisions and those with the heavy emulsion constituents.

basis. To allow for a comparison, we have selected only those experimental events in which no cluster  $Z \geq 42$  was observed and the number of target tracks was between 5 and 8. By these cuts we want to discard peripheral collisions and those with the heavy emulsion constituents. Again we see reasonable agreement with experiment, which indicates that on the average several medium mass fragments are produced.

Not only is the impact parameter averaged multiplicity of medium mass clusters well reproduced in our calculation, but also finer details like the impact parameter dependence of multiplicity. Experimentally the impact parameter cannot be measured. Hence the comparison is done by classifying the experimental and the theoretical events by the associated proton multiplicity. In fig. 27 we compare calculation and experiment [6] for a given multiplicity bin.

Our calculation at  $b = 3$  fm corresponds to the multiplicity bin 4. The multiplicity distribution for that bin was not available. Therefore we compare with the two neighbouring bins. In the Plastic Ball experiment only the Plastic Mall, which has a threshold of 35 MeV/n, can detect medium mass fragments up to  $Z = 10$ . To allow for comparison we applied the Plastic Ball filter SIMDAT [139], which reduces the multiplicity by more than a factor of two. First of all we observe a quite high average multiplicity in central collisions. In these collisions each of the gold nuclei is broken into about five medium mass fragments, of which 2.4 are detected. So we can really talk about multifragmentation. No heavy fragments survive in these collisions.

Figure 28 displays the average transverse momentum in the reaction plane as a function of the rapidity of the particles in the reaction  $\text{Au}(200 \text{ MeV/n}) + \text{Au}$ . The filter SIMDAT [139] was applied to simulate the experimental acceptance. We observe a strong correlation: the larger the rapidity, the larger the average transverse momentum. This collective flow of matter will be discussed later. Again we find good agreement between theory and experiment for all mass bins.

Finally we compare the angular distribution of clusters as seen in the Plastic Ball experiment with our calculation. In fig. 29 we display  $dN/d \cos \theta$  as a function of the laboratory angle  $\theta$  for two types of clusters,  $2 \leq A \leq 4$  and  $5 \leq A$ . We observe reasonable agreement with experiment for both species. The dip around  $10^\circ$  is due to the experimental acceptance hole. The filter, however, does not cut down the cross section as much here. The theoretical angular distribution is forward peaked even in the nucleus-nucleus centre of mass system. Its agreement with experiment presents evidence that the fragmentation is not a thermal process but yields a quite anisotropic angular distribution.

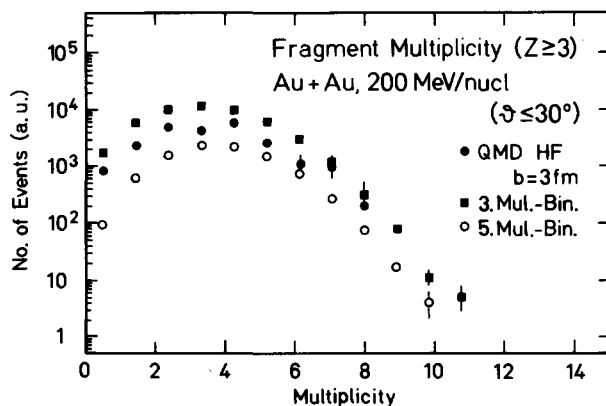


Fig. 27. Multiplicity distribution of medium mass fragments  $5 \leq A \leq 20$  as a function of the associated multiplicity of protons. We compare our calculation for the multiplicity bin 4 with data of ref. [6].

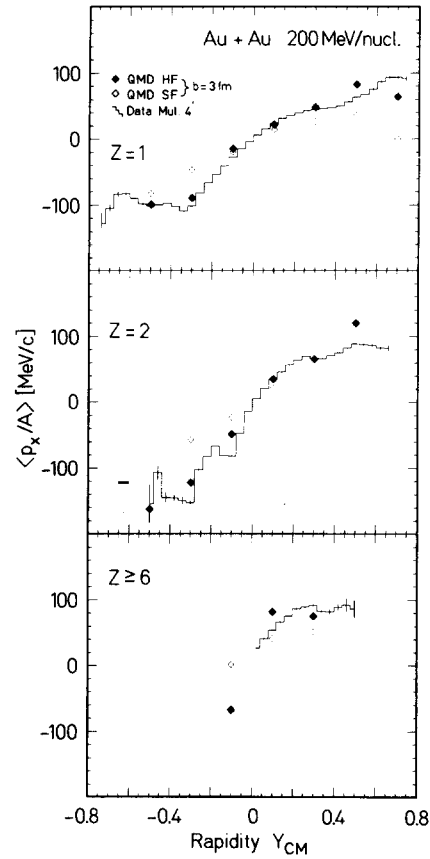


Fig. 28. Comparison of the calculated  $\langle p_x \rangle/A$ - $y$  distribution for different set ups (see table 3) with data from ref. [6]. The theoretical results are acceptance corrected with the Plastic Ball filter SIMDAT [139].

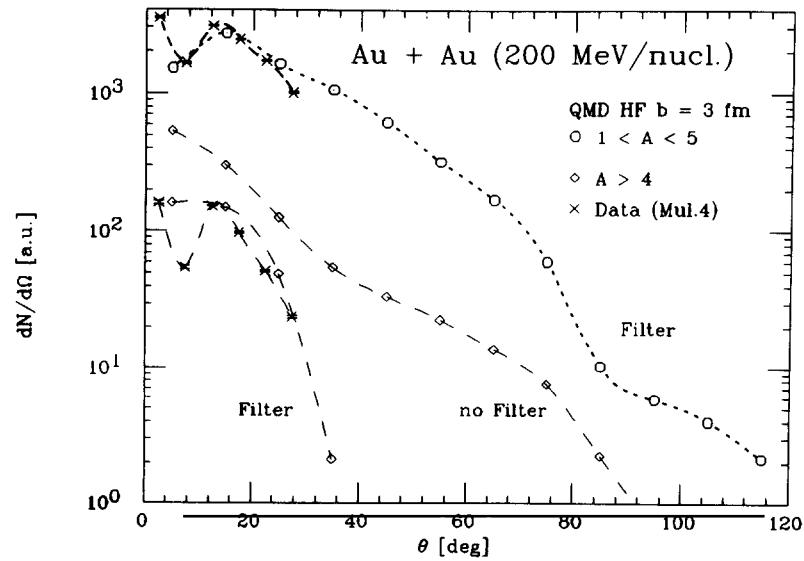


Fig. 29. Angular distribution of two types of clusters as compared with experiment [140] for the reaction 200 MeV/n Au + Au. The theoretical results for  $b = 3$  fm are acceptance corrected with the Plastic Ball filter SIMDAT [139] and compared with data of multiplicity bin 4. For the heavy clusters also the unfiltered distribution is shown.

For the sake of comparison we also display the unfiltered angular distribution for the heavier fragments. We see that the filter does not only cut down the cross section due to energy and angle cuts but also changes the shape of the angular distribution quite seriously. Thus, before one can learn something from the angular distribution a very accurate knowledge of the apparatus and the acceptance is necessary.

### 6.3. Predictions and results of the calculation

*Mass yield.* We now proceed and take advantage of the fact that in simulations more information is available than in an experiment. One additional piece of information is the impact parameter dependence of the observed quantities. In fig. 30 we display the mass yield distribution for our two reactions at different impact parameters.

We see a striking similarity between both reactions, and a clear impact parameter dependence. The mass yield of the reaction Au + Au is almost identical to that of the Ne + Au reaction at a somewhat higher impact parameter. Considering the different beam energy, the vastly different energy available in the nucleus–nucleus centre of mass frame and the different geometry, this is a surprising result, which confirms the insensitivity of the total mass yield on the reaction parameters.

At each impact parameter the mass yield of medium mass clusters is well described by a power law; the slope parameter, however, is vastly different. At the lowest impact parameter no heavy target remnants survive. The gold nucleus is broken into many pieces, none of them heavier than  $A = 80$ . For semicentral collisions we observe a plateau for  $45 < A < 70$ . The most peripheral reactions ( $b = 7$  fm) are not violent enough to destroy the heavy nuclei completely. Here less than half of the projectile volume overlaps geometrically with the target in the case of Ne and we have half overlap in the case of Au. We observe a remnant of the gold nucleus around  $A = 140$ . There are no clusters with masses  $30 \leq A \leq 90$ .

From these observations we can immediately draw several conclusions.

(a) *The power law form of the inclusive mass yield is accidental.* It does not reflect a phase transition – which would require a mass yield independent of the impact parameter – but is merely a

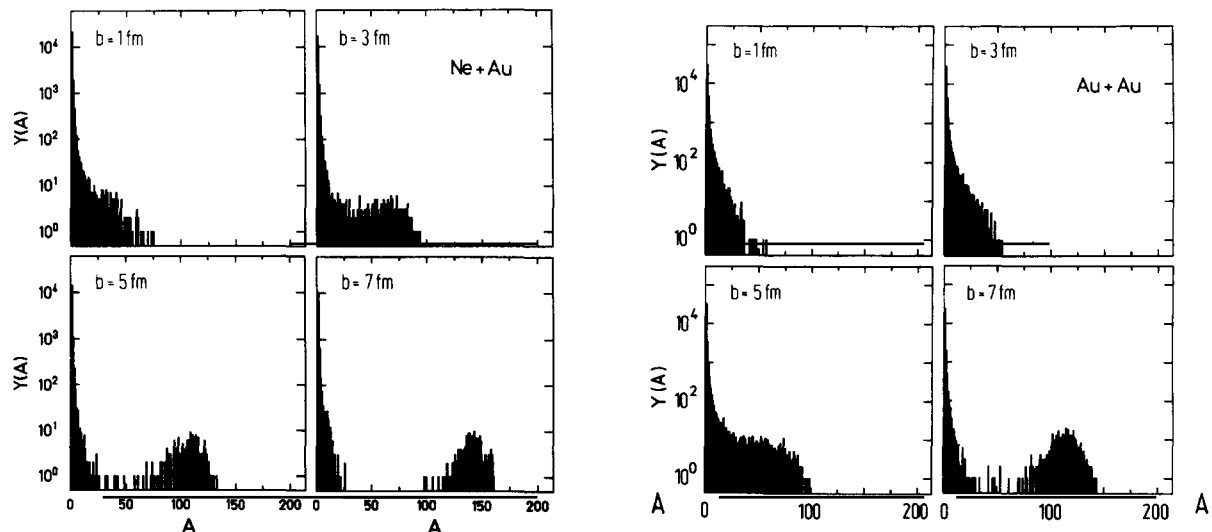


Fig. 30. The mass yield for four different impact parameters,  $b = 1, 3, 5, 7$  fm, for the reactions 1050 MeV/n Ne + Au and 200 MeV/n Au + Au.

parametrization of the sum of different forms of mass yields at different impact parameters. This will be confirmed later when we investigate the momentum space distribution of the fragments.

(b) *The transition from the power law form to a flat and ultimately increasing mass yield at masses around  $A = 45$  reflects the different origin of the clusters.* Fragments larger than  $A = 45$  are target remnants. They are produced when the collision is not violent enough to break up the target completely. Their creation is controlled by the impact parameter. Masses around  $A = 45$  are produced in semi-central collisions by deep spallation. The ultimate increase of the mass yield follows from the increasing probability of peripheral reactions.

(c) *The yield of the heaviest cluster provides a tool to determine the impact parameter of the reaction.* According to the calculation this method is superior in accuracy to the usual method to measure the total multiplicity of light particles.

Figure 31 displays the multiplicity distribution of fragments  $A > 4$  for the four different impact parameters in the reactions Ne + Au and Au + Au. For the Au + Au reaction we also display the multiplicity distribution which would be observed by the Plastic Ball set up.

As expected, the Au + Au reaction yields many more clusters of  $A > 4$  than the Ne + Au reaction. We find up to 16 clusters in one single Au + Au collision! The average values are 9.0 (3.3), 9.2 (2.6), 6.8 (1.7) and 3.5 (2.2) for Au (Ne) + Au at  $b = 1, 3, 5, 7$  fm, respectively. The minimum of the average values in the case of Ne is caused by the survival of projectile-like fragments at the very peripheral reactions.

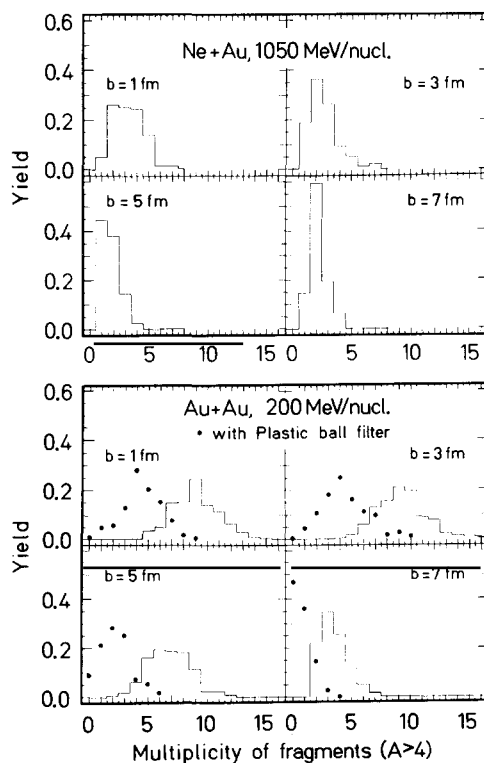


Fig. 31. The multiplicity distribution of fragments heavier than  $A = 4$  for four different impact parameters,  $b = 1, 3, 5, 7$  fm, for the reactions 1050 MeV/n Ne + Au and 200 MeV/n Au + Au.

Another point of interest is how the reaction proceeds in time. Here our conjecture that fragments larger than  $A = 45$  are the end product of a decay chain and that the others have a different origin, can be substantiated. This question is addressed in fig. 32, where we display the number of fragments as a function of time for seven mass intervals, again for both reactions in parallel.

In the case of Ne + Au we selected  $b = 1$  fm, for the Au + Au reaction  $b = 3$  fm. Already in the discussion of fig. 30 we observed that the mass yield is very similar in both these cases. We observe the same similarity for the time evolution as well.

In the case of Ne we see that the mass yield distribution for  $A > 50$  stabilizes not prior to  $300 \text{ fm}/c$  ( $1 \times 10^{-21}$  s), while for  $2 < A < 30$  the distribution is already stable at  $150 \text{ fm}/c$ . In the case of Au the time is a little bit shorter for both bins and we observe a stable distribution at  $200 \text{ fm}/c$ . Nevertheless, this is a very long time for a high energy heavy ion reaction and it is in the range of the lifetime of a compound nucleus. Let us first concentrate on the heavy clusters. At  $t = 50 \text{ fm}/c$  the heavy clusters with a mass larger than 70 are not stable but decay by the subsequent emission of nucleons and light clusters. The decay chain can be seen by the subsequent population and depopulation of the different mass bins. Finally, the end products of the decay chain are mostly in the bin  $31 < A < 50$ . At larger impact parameters we find the decay chain ending at larger masses. So all masses larger than  $A \approx 40$  are end products of the decay chain. Along the evaporation chain the clusters emit neutrons and protons and therefore their number increases and saturates not prior to  $t = 300 \text{ fm}/c$  or  $200 \text{ fm}/c$ , respectively.

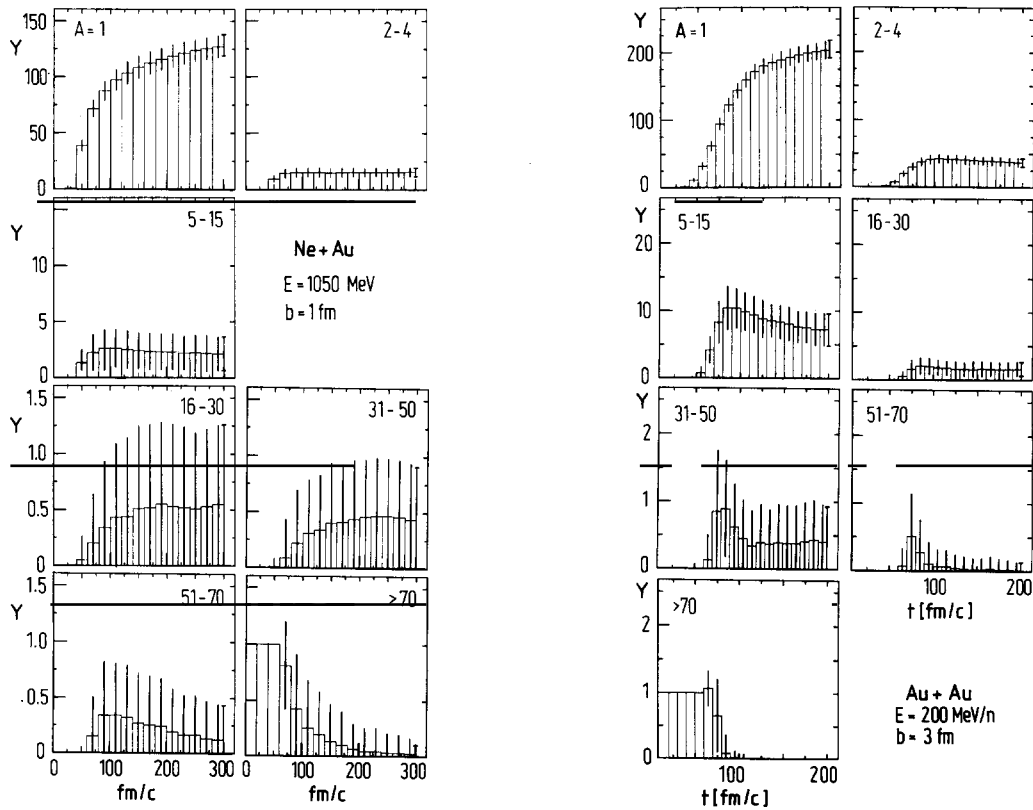


Fig. 32. Time evolution of the fragment number for seven different classes of fragments for the reactions Ne + Au and Au + Au.

The clusters in the range  $2 \leq A \leq 30$  have a completely different history. They are formed at a very early stage of the reaction and are not fed by the decaying remnants, nor do they decay. After 100 fm/c practically all of them are formed. They emerge from the surface region of the combined systems, as we will see, and measure the violence of the reaction, being produced more copiously at small impact parameters than at large ones.

One has to keep in mind that clusters are not counted before all of the cluster nucleons have a minimal distance of 3 fm to all the other nucleons. This is much later than the formation time of the clusters. Which nucleons form a cluster is determined very early in the course of the reaction (at about  $t = 20$  fm/c), as we will see later.

In peripheral reactions we see a different time structure. Here medium mass clusters are produced in a sequential decay of heavy clusters as well. However, in absolute numbers the medium mass events produced in a sequential decay are rare compared to those produced in central collisions. In fig. 33 we show a peripheral event for Au ( $E = 200$  MeV/n,  $b = 7$  fm) + Au in more detail. Fragments with  $A \geq 10$  are depicted from  $t = 0$  (bottom) to  $t = 200$  fm/c (top) in steps of 10 fm/c.

Up to 50 fm/c there is one blob of matter in configuration space which – for this large impact parameter – is still separated in momentum space into a projectile- and a target-like residue [for central collisions ( $b \leq 3$  fm) this is not the case; we then observe almost complete stopping of projectile and

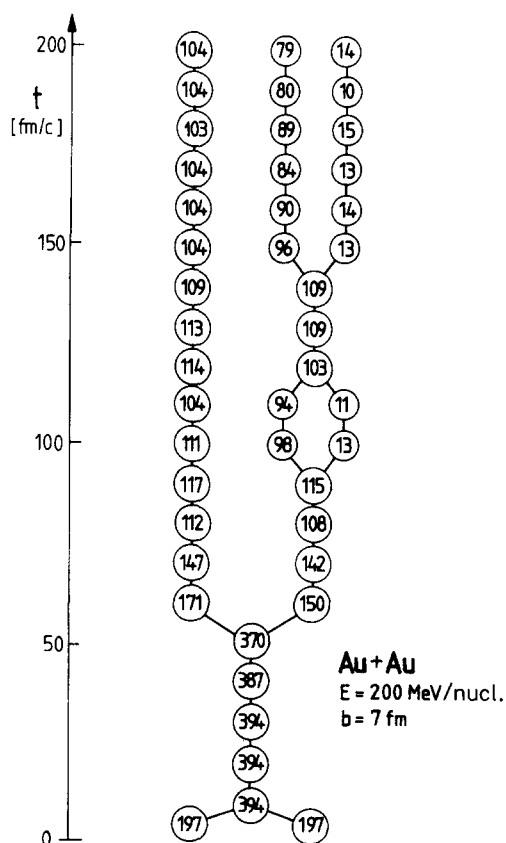


Fig. 33. Time evolution of a single peripheral event 200 MeV/n Au + Au,  $b = 7$  fm. Only clusters with mass  $A > 9$  are displayed.

target in the centre of mass frame]. After 50 fm/c the system breaks up into these two residues. Between 30 and 80 fm/c single nucleons and light fragments ( $A < 10$ ) are emitted. Then a rather stable fragment with  $A \approx 105$  remains in the projectile rapidity regime. In the target regime a second break up is observed, which yields two stable fragments with  $A \approx 80$  and 15. At large impact parameters ( $b = 7$  fm) the intermediate mass fragments are mostly produced in the binary break up of the heavy residues. Recently a similar conclusion was reached experimentally for asymmetric systems [141].

*Correlations between initial and final state.* As we have seen the impact parameter dependence of the mass yield distribution rules out the conclusion that the inclusive data present evidence for a liquid–gas phase transition. In this case the mass yield curve would have to be universal because the system always has to come to the critical temperature.

However, the question remains as to whether equilibrium is reached in the course of the reaction. Some fast projectile nucleons always emerge from the reaction zone prior to equilibration. Hence the energy available for thermalization does not correspond to the total centre of mass energy and may depend on the impact parameter. The different slopes at different impact parameters do not contradict the assumption of complete equilibrium. The crucial test for the assumption of complete global thermalization is to check whether the system loses its memory of the initial configuration. If it equilibrates, we would expect that the final state particles do not carry any information about the initial state, in particular about their initial positions.

The complete recording of the positions and momenta of all particles during the course of the simulation allows us to address this question in a direct way. We can investigate correlations between final and initial states which one would expect for a system which is not completely equilibrated. An obvious candidate for such a correlation is the probability to find a nucleon finally in a cluster as a function of its initial position. Those nucleons which are in the geometrical overlap of projectile and target supposedly have a large probability to suffer violent collisions. The large momentum transfer then suppresses the probability to find other nucleons with small relative momenta which are needed to form a cluster. We study this correlation in fig. 34.

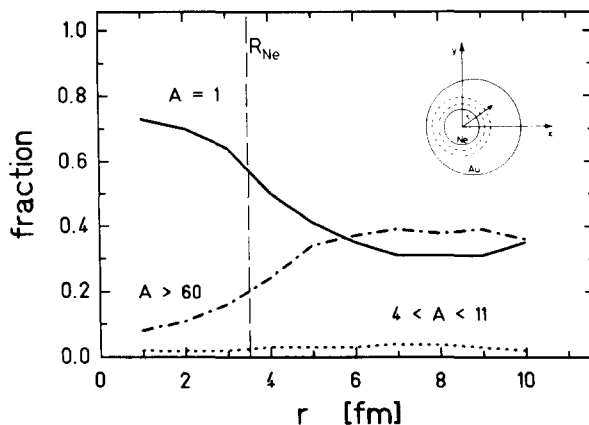


Fig. 34. Correlation between initial and final state of the reaction 1050 MeV/n Ne + Au,  $b = 3$  fm. We display here the fraction  $P(r) = N_i(r) / \sum N_i(r)$ , where  $N_i(r)$  denotes the number of nucleons which are initially located at a distance  $r$  from the impact point and end up finally in a fragment of class  $i$ .

We distinguish three different classes of fragments and investigate the correlation between the initial position of the nucleons and their probability to end up finally (at  $t = 300 \text{ fm}/c$ ) in a cluster. We calculate the distance  $r$  in the plane perpendicular to the beam direction between the initial position of the nucleons and the impact point  $b$  and define the fraction

$$P(r) = N_i(r) / \sum N_i(r). \quad (6.1)$$

$N_i(r)$  is the number of nucleons which are initially located at  $r$  and finally belong to a cluster of class  $i$ . If there were no correlations, this probability should be independent of  $r$ . We see strong correlations for protons and neutrons as well as for heavy clusters. Nucleons in the overlap region between projectile and target have a much higher probability to end up as individual protons and neutrons than to be part of a cluster. Hence clusters mainly consist of spectator matter (those parts of projectile and target which do not overlap). Since the fragments are excited when formed, they have to emit neutrons and protons. Therefore, we observe also protons and neutrons which initially were located quite far from the impact point of the projectile. Medium mass clusters, as we can see, are formed from nucleons all over the place without a significant preference. From the observed correlations we can conclude that in the course of the interaction the system does not reach a global equilibrium as assumed in a number of model calculations [126, 127, 133, 73].

The correlation which we observe could be expected on the basis of the participant-spectator [142] model, in which it is assumed that the geometrically overlapping nucleons  $r < R_{\text{Ne}}$  equilibrate and form a fireball. They are surrounded by cold spectator matter, and there is no communication between the two regions. This model limits the initial position of nucleons which are finally observed as protons or neutrons to  $r < R_{\text{Ne}}$ , whereas those nucleons which are finally contained in clusters are initially at  $r > R_{\text{Ne}}$ . However, we do not find such a clear division, and in addition these models also cannot account for the disappearance of the correlation for the medium mass clusters.

*Momentum space distribution.* In principle the present theory can predict the triple differential cross section  $d^3\sigma/dE d\Omega dA$ . However, due to computational expenditure we restrict ourselves to mean values for the time being.

We start with the laboratory double differential cross section  $d^2\sigma/dy dp_t$ , displayed in fig. 35, for different classes of fragments and two different impact parameters for the reaction Ne + Au.  $Y$  denotes here the rapidity and  $p_t$  the transverse momentum of the particles. The contour lines are separated by a factor of 2.

We see that light fragments have a highly anisotropic emission pattern even in central collisions. There are many fast particles in the forward direction, which are not counterbalanced at backward angles. These particles have a finite emission angle, whose origin will be investigated in the next section. The emission pattern of medium mass clusters is, to 10%, not isotropic, as observed experimentally by Warwick et al. [120], who found that the double differential cross section of medium mass clusters cannot be described by a single thermal source which emits fragments isotropically in its rest system. Comparing  $d^3\sigma/d\Omega dE dZ$  at different laboratory angles one has two possibilities for a definition of the source velocity: (a) either one requires that the slope of the energy distribution (i.e. the "temperature") does not depend on the emission angle in the rest system, or (b) one assumes that the Coulomb peak appears at the same energy in the rest system. If there were an isotropic emission of a single source, both methods would coincide. The experiment shows differences between both methods.

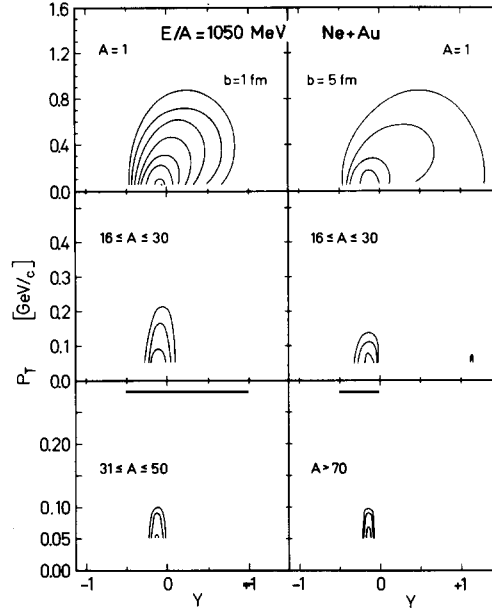


Fig. 35. Contour plot of the double differential cross section  $d^2\sigma/dp_t dy$  for two impact parameters ( $b = 1, 5$  fm) and three different mass intervals for the reaction 1050 MeV/n Ne + Au.

Applying the second method it seems that the fragments gained additional momentum in the beam direction, i.e., show a higher "temperature". This gives rise to an elliptical emission pattern in the rest frame of the source. The heavier clusters, on the contrary, exhibit an isotropic emission pattern in their rest system, which moves with a velocity close to zero in the laboratory system. Note the different scales of the transverse momentum.

Figure 36 presents the rapidity distribution of the different classes of fragments at two impact parameters for Ne + Au and at four impact parameters for the Au + Au reaction. Only for central collisions in the reaction Au + Au are all particles stopped, and do we observe an almost thermal distribution, i.e., a mid-rapidity source appears which emits particles and clusters almost isotropically. Even at small  $b$  ( $b = 3$  fm) we see that the fragments can be attributed to two different sources, although the protons and neutrons will show a rather thermal distribution and mimic a non-existent equilibrium. This is the reason why the inclusive measurement of protons or very small clusters always reveals a thermal distribution. For the very peripheral reaction we see the heavy fragment moving backwards in the laboratory system ( $y_{\text{target}} = 0.33$ ). In the Ne + Au reaction we see that the gold nucleus is not able to stop a 1 GeV/n neon projectile completely. Even in central collisions, where the mean free path is small compared to the diameter of the target, energetic single nucleons and small clusters escape from the interaction zone. Thus even for the single nucleons the fireball picture, i.e. the assumption that the geometrically overlapping projectile and target nucleon form an equilibrated source, does not hold. The spectra are always spoiled by evaporation products of the "cold" spectator matter. For the large impact parameter ( $b = 7$  fm) we clearly see a projectile and a target region. Here also remnants of the projectile survive (and also demonstrate the stability of clusters in our numerical approach).

Finally fig. 37 shows the transverse "temperature", i.e. up to a constant the second moment of the transverse momentum distribution,

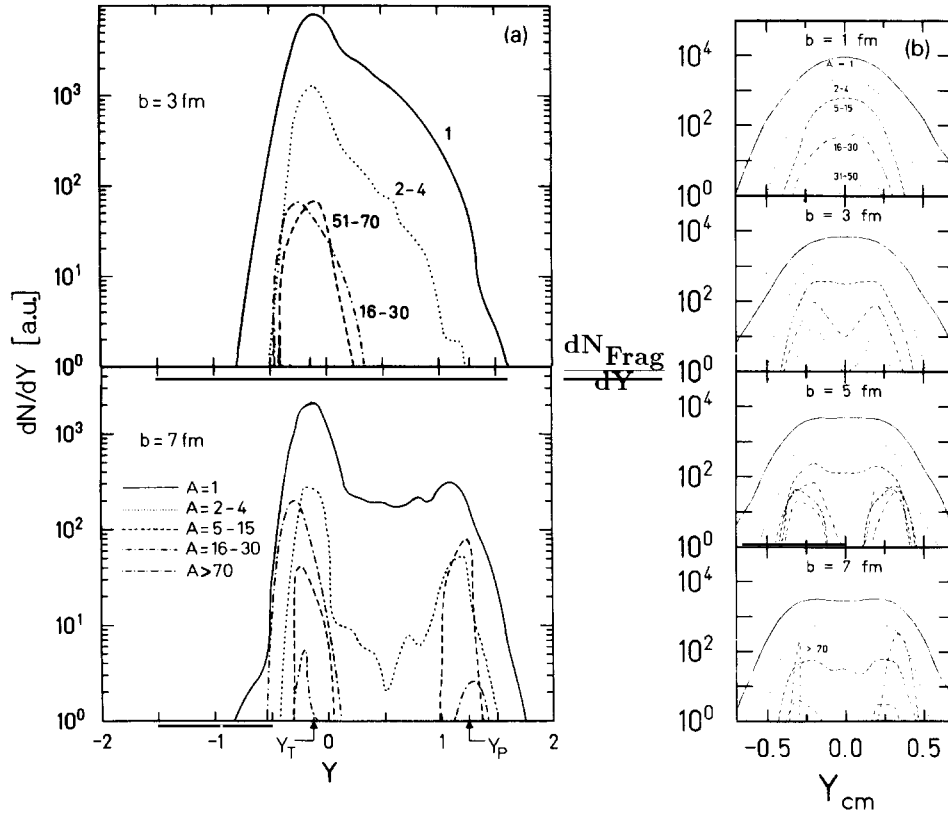


Fig. 36. Rapidity distribution of different mass intervals (a) for  $b = 3, 7$  fm for the reaction  $1050 \text{ MeV/n Ne} + \text{Au}$ , and (b) for  $b = 1, 3, 5, 7$  fm for the reaction  $200 \text{ MeV/n Au} + \text{Au}$  (soft EOS).

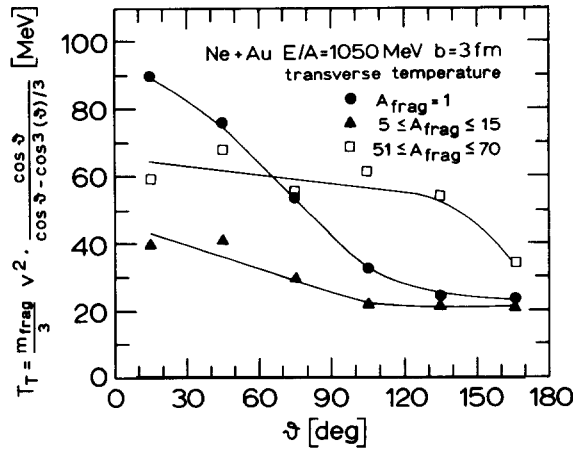


Fig. 37. Transverse "temperature"  $T_T$  of fragments for different mass intervals.

$$T_T = \frac{m}{3} \langle v \rangle^2 \frac{\cos(\theta)}{\cos(\theta) - \cos^3(\theta)/3},$$

for different fragment classes in their rest frame as a function of the emission angle. For a system which is equilibrated longitudinally, this quantity coincides with the apparent temperature, i.e. the slope of the momentum space distribution. Isotropic emission would result in an angle independent  $T_T$ . We see, however, a higher "temperature" for low mass fragments in the forward direction compared to the backward direction. The ratio of the "temperature" of fragments emitted in the forward direction over that of the fragments emitted in the backward direction is between two and six. Only fragments in the largest mass bin, which also has the lowest statistics, can be considered as isotropically emitted. The average  $T_T$  of different clusters are different as well. We observe  $\langle T_T \rangle = 30.1, 27.3, 57.4$  MeV for the mass bins  $A = 1, 5 \leq A \leq 15, 51 \leq A \leq 70$ , respectively. These higher temperatures in the forward direction were also seen experimentally [120] and the values obtained for  $T_T$  by fitting the experimental data are of the same magnitude [132].

From all these observations we conclude that the momentum space distributions of the different cluster classes are greatly different. A single source cannot be identified, apart from the very central Au + Au collision. If one wants to interpret the emission pattern in terms of thermal sources, a continuous source distribution is required.

#### 6.4. What causes fragmentation?

There remains the question of what actually causes the fragment formation. We have seen that clusters are not formed in a globally equilibrated environment. Hence processes other than statistical decay have to be taken into account. We saw that the medium mass clusters are emitted from the system quite early, long before the target evaporation chain ceases. In this section we investigate the details of this process. Since clusters are produced by fluctuations of the system, we have to investigate the cluster formation on an event-by-event basis, looking for the specific environment around a prefragment, i.e., those nucleons which finally form a fragment or are emitted from a fragment, in a given simulation of the reaction.

We start out by examining how the projectile and the target interact at the beginning of the interaction. Figure 38 displays the velocity and the density profile for central collisions 1050 MeV/n Ne + Au from 10 to 20 fm/c and 10 to 35 fm/c, respectively, in steps of 5 fm/c. The velocity profile is shown separately for those nucleons initially belonging to the projectile or the target. Arrows are only plotted if the local density is larger than  $0.1\rho_0$ . In this figure we have averaged over ten events, so fluctuations are reduced, but not completely washed out.

At 10 fm/c the projectile has completely dived into the target. The projectile velocity is much faster than the speed of sound in nuclear matter. Therefore the time scale for the transverse expansion of the projectile is small compared to the time scale for the projectile to traverse the target. The root mean square radius of the projectile nucleons does not increase up to 15 fm/c. The peak compression increases to  $2.1\rho_0$ . While the projectile nucleons travel through the target they experience strong transverse forces due to the strong density gradient at the surface of the projectile. Therefore they pick up transverse velocity and are deflected at finite angles. A shock profile develops, which moves inwards into the projectile nucleus because the outer nucleons have already been carried away by the sideways travelling compression wave. So we see the situation that the projectile causes the emission of clusters with a velocity above the sound velocity, while the source itself decelerates gradually but still has

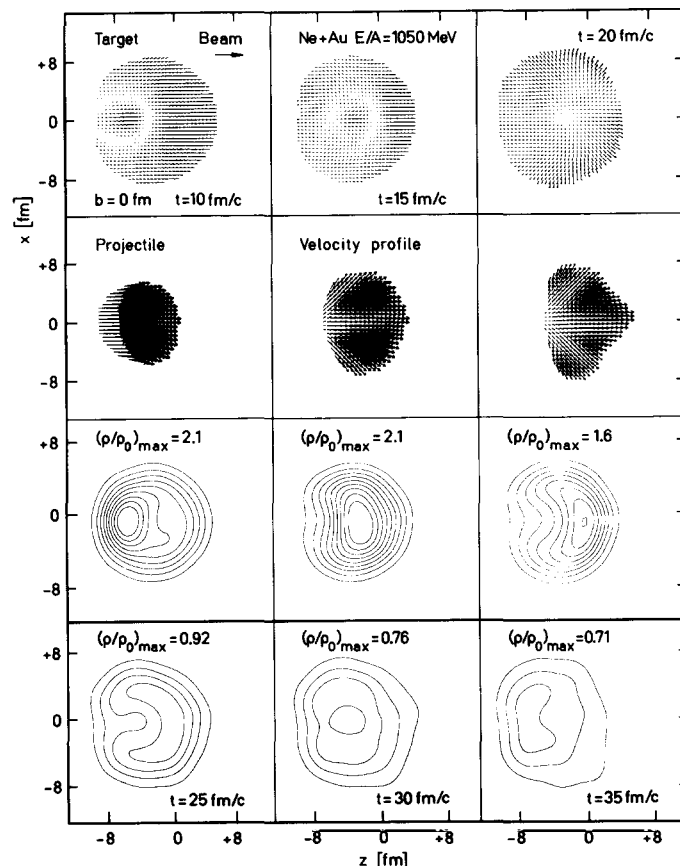


Fig. 38. Velocity (rows 1 and 2) and density profile (rows 3 and 4) for the reaction 1050 MeV/n Ne + Au,  $b = 0$  fm, in the reaction plane at the beginning of the reaction. The velocity profile is separately displayed for projectile and target nucleons. The length and direction of the arrows are proportional to the velocity in the reaction plane. An arrow is only drawn if the projectile or target density is larger than  $0.1\rho_0$ . The contour lines of the density profile are separated by a factor of two, starting with  $\rho/\rho_0 = 0.2$ .

supersonic velocity. In an infinite system this is the situation where a Mach cone would be formed, and indeed the form of the velocity distribution at 20 fm/c resembles such a velocity profile closely. However, one has to keep in mind that we have a system of only 217 particles and therefore we do not obtain a sharp discontinuity in the density as occurs in macroscopic systems. Behind the cone we observe a rarefaction region, which heals, however, because target surface nucleons stream inwards. At 35 fm/c this rarefied region is filled and again has the highest density. Whereas at the beginning projectile and target interpenetrate (the density provides a high Pauli blocking rate), towards the end of the reaction the projectile drags along some target nucleons. At 20 fm/c we see that in the forward direction the target nucleons have the same direction of motion as the projectile nucleons, whereas in the backward direction the target nucleons move collectively with roughly half of the centre of mass momentum. This time evolution of the reaction is similar to that predicted by hydrodynamical calculations [125].

How a prefragment, i.e. an excited fragment which still emits nucleons before being detected, experiences this situation is displayed in fig. 39. The left-hand column shows the time evolution of mean values of different quantities for a large prefragment ( $A = 24$ ). This prefragment emits six nucleons

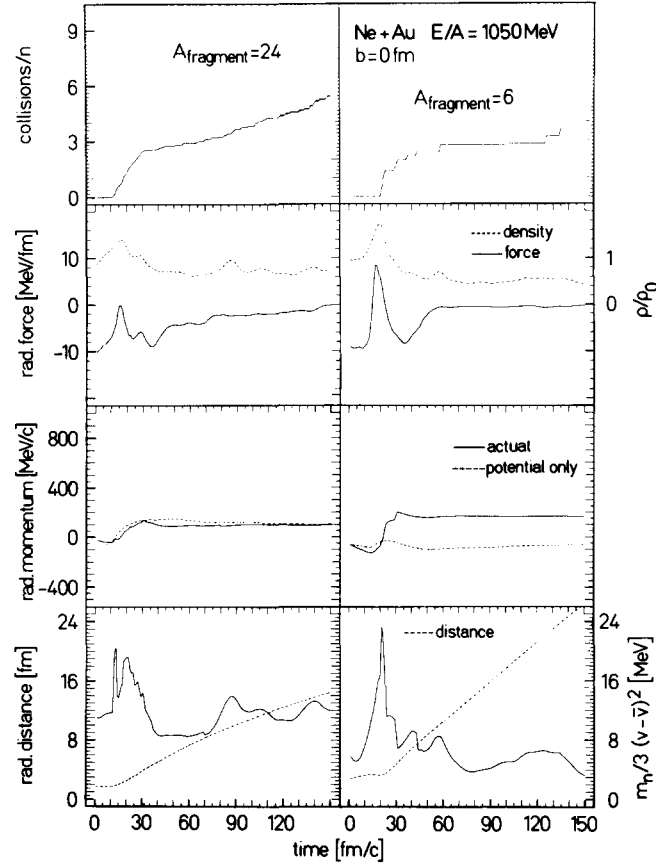


Fig. 39. Time evolution of a single prefragment produced in the reaction 1050 MeV/n Ne + Au,  $b = 0$  fm. The properties of a heavy ( $A = 24$ ) (left) and a light ( $A = 6$ ) (right) prefragment are displayed. We show the average number of collisions, the mean radial force, the density, the mean radial momentum, the mean radial distance from the centre of the target, and the "temperature"  $\Delta = (m/3)\langle v - \langle v \rangle \rangle^2$  as a function of time. The values displayed are averaged over the fragment constituents. For details we refer to the text.

before it is finally (at  $t = 300$  fm/c) registered as a fragment ( $A = 18$ ). The right-hand column shows the analogous quantities for a small fragment ( $A = 6$ ). The upper figure displays the number of collisions per fragment nucleon. Initially, i.e. before the projectile reaches nucleons of the fragment, no collisions occur. Between the arrival of the projectile and the separation of the fragment from the remnant we observe a quite high collision rate. When the fragment is formed there is still excitation energy, which allows further collisions among the fragment nucleons. The next row shows the density

$$\rho = \frac{1}{A_{\text{frag}}} \sum_{j \in A_{\text{frag}}} \sum_{i \in A} \left( \frac{1}{2\pi L} \right)^{3/2} \exp\{-[R_j - R_i(t)]^2/2L\}$$

in units of  $\rho_0$ , and the average radial force

$$F_{\text{rad}} = \frac{1}{A_{\text{frag}}} \sum_{j \in A_{\text{frag}}} \frac{F_j \cdot (\mathbf{r}_j - \mathbf{r}_{\text{cm target}})}{|\mathbf{r}_j - \mathbf{r}_{\text{cm target}}|}.$$

Radial here means with respect to the centre of mass of the target. As already expected from the previous figure we see a strong increase in the density when the projectile matter hits the nucleons which will form the fragment. Initially the collective momentum of those nucleons points inwards. The density, however, causes a strong radial repulsive force, which reverses the direction of the average momentum

$$p_{\text{rad}} = \frac{1}{A_{\text{frag}}} \sum_{j \in A_{\text{frag}}} \frac{\mathbf{P}_j \cdot (\mathbf{r}_j - \mathbf{r}_{\text{cm target}})}{|\mathbf{r}_j - \mathbf{r}_{\text{cm target}}|}.$$

This is displayed in the next row.

So far it seems that collisions are not required at all to cause fragments to break off. This, however, is not true. If the nucleon–nucleon collisions are suppressed, we do not find fragmentation. Collisions have a twofold influence on the fragmentation processes. Firstly, they decelerate the projectile nucleons and hence increase the density in the projectile region. Secondly, they may provide an additional momentum transfer to those nucleons which are going to form a fragment. To check whether the second mechanism is important we compare the actual average radial momentum with that caused by the average radial field only. The latter is determined by

$$p_{\text{rad}}^{\text{field}}(t) = \int_0^t F_{\text{rad}}(t') dt' + p_{\text{rad}}(t=0).$$

The difference between these two reveals the importance of the momentum transfer to the fragment nucleons due to collisions. The results are displayed in the same row. In the case of the large cluster the final momenta are almost identical, whereas the small cluster would not be broken off at all (it still would have an inward directed radial momentum). So the role of collisions in the actual break up process is ambiguous.

The last row displays the time evolution of the internal excitation of the fragment. We define a "temperature"

$$\Delta = \frac{1}{A_{\text{frag}}} \sum_{j \in A_{\text{frag}}} \frac{m}{3} \langle \mathbf{v}_j - \mathbf{v}_{\text{av}} \rangle^2.$$

Keep in mind, however, that this is not a true temperature since it also includes the Fermi momentum. We only see a small increase in the course of the reaction. So the prefragments are only moderately excited and there seems to be no equilibration between the internal degrees of freedom and the translational motion. This is in agreement with recent experiments, which show that the excitation of prefragments corresponds to temperature of 5 MeV, independent of the beam energy [143].

The velocity profile of the same reaction at  $b = 6$  fm is displayed in fig. 40. Here the projectile is slightly deflected, but still drags along some target nucleons. The target becomes slightly excited, and most of the target nucleons retain their initial velocity up to 25 fm/c, where the interaction between projectile and target is over. Only close to the interaction zone do we see a disturbance in the velocity field, which ultimately leads to an excitation of the target. Since particles from this excited zone (hot spot) which travel towards the centre of the target have a higher chance to transfer their momentum to other target nucleons than those travelling towards the surface of the target, we observe a transverse

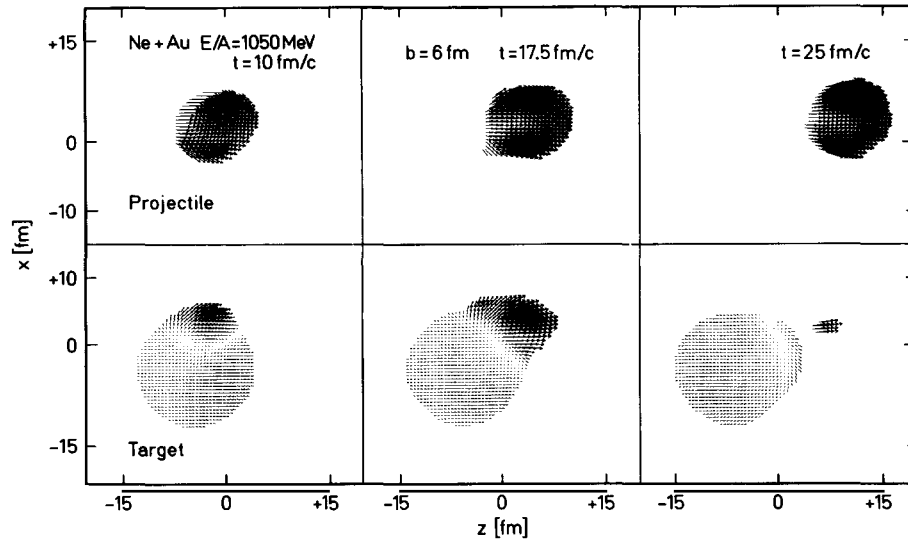


Fig. 40. Velocity profile for  $b = 6$  fm in the  $zx$  plane at the beginning of the reaction,  $t = 10$ – $20$  fm/c, in steps of  $5$  fm/c, separately displayed for projectile and target nucleons. The length and direction of the arrows are proportional to the velocity in the  $zx$  plane.

momentum transfer to the target, which is compensated by the momentum of the emitted single particles in the opposite direction. Hence transverse momentum transfer can also be caused by pure geometry and not only by momentum dependent interactions and compression.

### 6.5. Fragments and the nuclear equation of state

What can we learn from the fragments about the nuclear equation of state? Fragments are, as we have seen, created in the early stage of the reaction. Since the density gradient causes their break off, they should be quite sensitive to the compression achieved in heavy ion collisions and to the transverse momentum transfer. We would further expect that they are also sensitive to the number of nucleon–nucleon collisions. These collisions abruptly change the momentum of the collision partners and lower the probability to find a partner with low relative momentum in order to form a fragment. Figure 41 displays the momentum space distribution of nucleons and light clusters in the reaction plane at the end of the reaction  $Au + Au$ ,  $b = 3$  fm, for two equations of state.

Several simulations are displayed on top of each other. The distribution of unbound nucleons appears to be isotropic, independent of the equation of state and is centred around  $p_x = p_z = 0$ , indicating almost complete stopping. Already clusters with mass  $A = 2$ – $4$ , however, reveal their origin from projectile or target and the  $p_x$  and  $p_z$  distributions peak at finite values (compare fig. 36). But most important, we observe a bounce off, i.e., target- and projectile-like clusters have a finite and opposite  $\langle p_z \rangle$  which depends on the equation of state. The harder the equation of state, the larger is the value of  $\langle |p_z| \rangle$ .  $\langle |p_x| \rangle$  increases with the cluster size. For  $15 < A \leq 30$  the knowledge of  $p_x$  is almost sufficient to identify the clusters as projectile- or target-like.

These findings are expected. Nucleon–nucleon scatterings randomize the momentum distributions. After a large momentum transfer nucleons do not find a partner with low relative momentum and are therefore observed as single nucleons. Clusters consist mostly of nucleons which have not suffered large momentum transfer. Their motion is governed by the density gradients which cause the bounce off. We

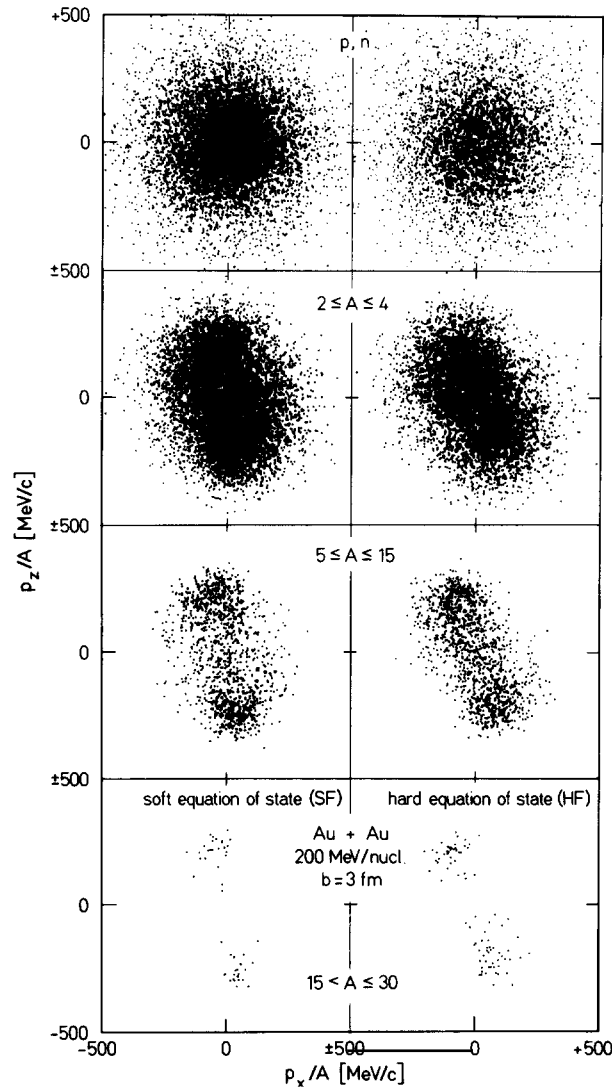


Fig. 41. Survey of the reaction 200 MeV/n Au + Au,  $b = 3$  fm, for two different equations of state (SF, HF). We display the final momenta per nucleon in the reaction plane for a couple of simulations for four different fragment classes.

see that clusters are good candidates for exploring the equation of state. To substantiate these findings we display in fig. 42 the ratio of the transverse momentum in the reaction plane  $p_x$  and the total transverse momentum  $p_{\perp} = (p_x^2 + p_y^2)^{1/2}$  as a function of the rapidity for a stiff and for a soft equation of state in comparison with experimental results [6].

A filter was applied to the theoretical calculations which simulates the acceptance of the Plastic Ball [139]. The calculations are performed at  $b = 3$  fm, where we find the largest  $p_x$ , and compared with the corresponding multiplicity bin. The absolute values of  $p_x/p_{\perp}$  are twice as large for  $A \geq 6$  compared to protons. For all four mass bins we see differences between the different equations of state. As expected they are biggest for the largest clusters. The calculations seem to favour a stiff equation of state.

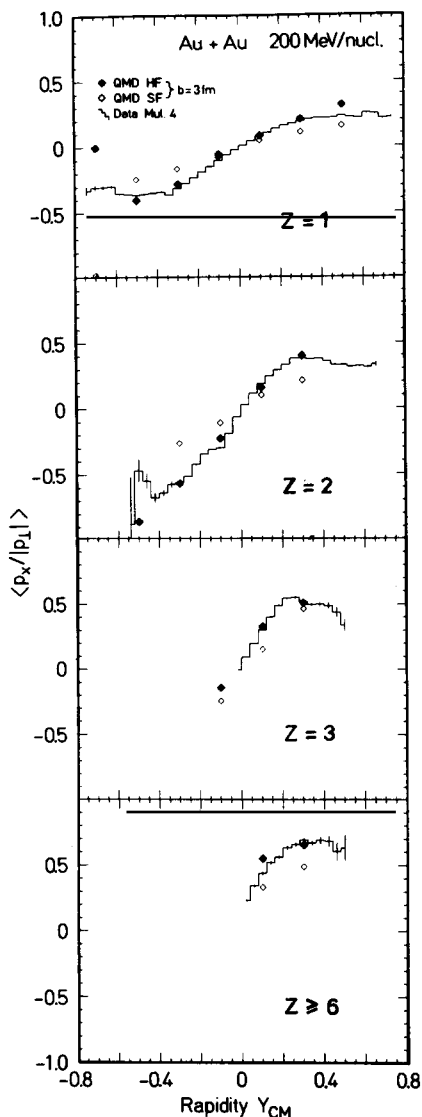


Fig. 42. The transverse momentum per nucleon  $p_x/p_\perp$  as a function of the rapidity. We display calculations for three different charge bins  $Z = 1$  ( $A = 1, 2$ ),  $Z = 2$  ( $A = 3, 4$ ),  $Z = 3$  ( $A = 5, 6, 7$ ),  $Z \geq 6$  ( $12 \leq A \leq 20$ ) and two equations of state (SF, HF) and compare the results with experimental data [6]. A filter is applied to the theoretical calculations which simulates the acceptance of the Plastic Ball [139].

However, before definite conclusions can be drawn, the dependence of  $p_x/p_\perp$  on the other quantities like in-medium cross sections has to be investigated.

Figure 43 shows the mass yield for a stiff and a soft equation of state for the Au(200 MeV/n) + Au reaction at  $b = 3$  fm. As already mentioned we see a power law dependence of the mass yield. There is little difference at low masses. Large mass fragments are more copiously produced if less collisions take place, i.e., when a hard equation of state is employed. The difference is too small, however, to be of practical importance. This confirms once more that the total mass yield is not very sensitive to the dynamics of the reaction.

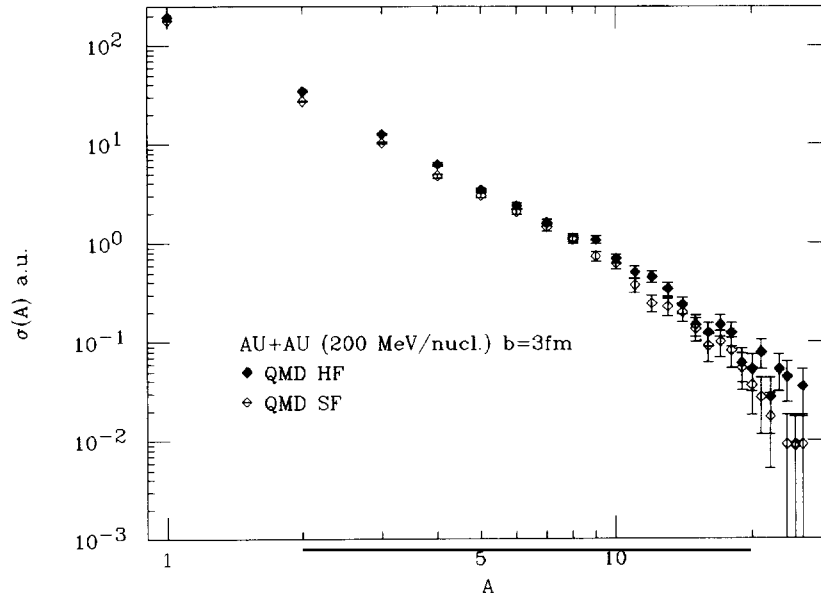


Fig. 43. Mass yield for the reaction 200 MeV/n Au + Au for the soft (SF) and the hard (HF) equation of state at an impact parameter of  $b = 3$  fm.

## 7. Probing the nuclear equation of state

In chapter 2 we discussed that presently the in-medium cross section, as well as the nuclear equation of state, cannot be calculated reliably from the underlying nucleon–nucleon interaction. Furthermore, we have seen that the momentum dependent part of the nucleon–nucleon interaction acts quite differently in nuclear matter and in supernovae, as compared to nucleus–nucleus collisions. In nuclear matter any momentum dependence of the interaction can be expressed as a density dependence since the average relative momentum between the particles is a function of the Fermi energy and hence of the density. In heavy ion collisions the momentum and density dependence of the potential are decoupled. By choosing different beam energies we can probe the potential over a large dynamical range without changing the density substantially. In the energy range of interest,  $100 \text{ MeV/n} < E_{\text{lab}} < 1 \text{ GeV/n}$ , optical model calculations reveal a strong repulsion arising from the momentum dependent interaction. As we have seen in section 2.5, this repulsion can mimic a stiffer equation of state in heavy ion collisions.

Before starting out to pin down the compressional energy in nuclear matter at high density and temperatures, one has to study whether the observables are robust enough so that our lack of complete knowledge of some dependencies does not render any conclusions we might draw obsolete. The essential uncertainties are the momentum dependence of the optical potential at high densities, which may be cast in an effective mass, and the in-medium corrections of the nucleon–nucleon cross section which go beyond the Pauli suppression for the final states.

A first glimpse of the difficulties in determining the nuclear equations of state can be gotten from fig. 44. It shows the maximal density obtained in the reaction Au + Au at  $b = 3$  fm for different beam energies. Although we have chosen one of the heaviest systems available, we observe only a very weak dependence of the maximal density on the projectile energy.

Almost never does the density exceed twice the normal nuclear matter density  $\rho_0$ . This is in strong

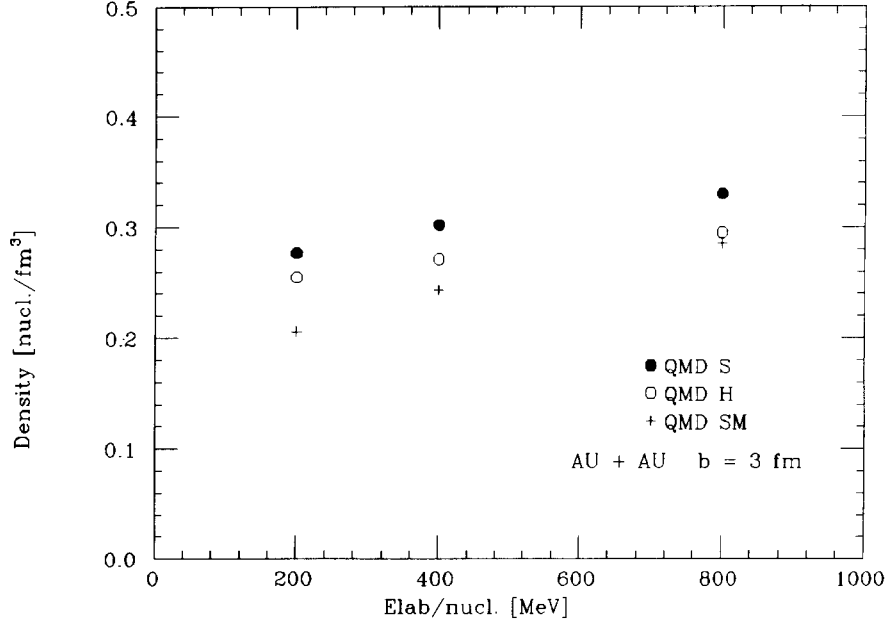


Fig. 44. Maximal central density reached in the reaction Au + Au at  $b = 3$  fm as a function of the beam energy for three different equations of state (see table 3).

contrast to cascade calculations, which lack the compressional energy, and achieve densities up to  $\rho_{\max} = 4\rho_0$ . The values obtained in the QMD model are slightly lower than those obtained in BUU calculations. The situation becomes even worse if we relate the central density to the compressional energy, which can be inferred from fig. 8. We note that the compressional energy is almost identical for S and H. This questions all the suggestions which rely only on different compressional energies obtained from different equations of state. Recalling the vastly different influence of the momentum dependence of the optical potentials at the different beam energies, one can also imagine from this figure the difficulty of separating reliably the momentum dependent part of the optical potential from the density dependent part.

In this section we report on the first steps towards the goal of determining the nuclear equation of state from a comparison between theoretical calculations and experiments. We will see that many parameters have to be measured simultaneously in order to disentangle the effects of the compressibility, the effective mass and the effective cross section on the observables.

### 7.1. Velocity dependence versus compressibility

We first concentrate on the interactions H, S and SM (table 3). We discuss how these reactions proceed in time, and whether SM can yield the same results as H and thus imitate a stiffer equation of state. In fig. 45 we give an overview of different quantities which are relevant for this question. We denote the rows from (a) to (d). All the quantities we display are for the reaction Au + Au,  $b = 3$  fm, at two different beam energies: 200 MeV/n (left) and 800 MeV/n (right).

We start with the transverse momentum

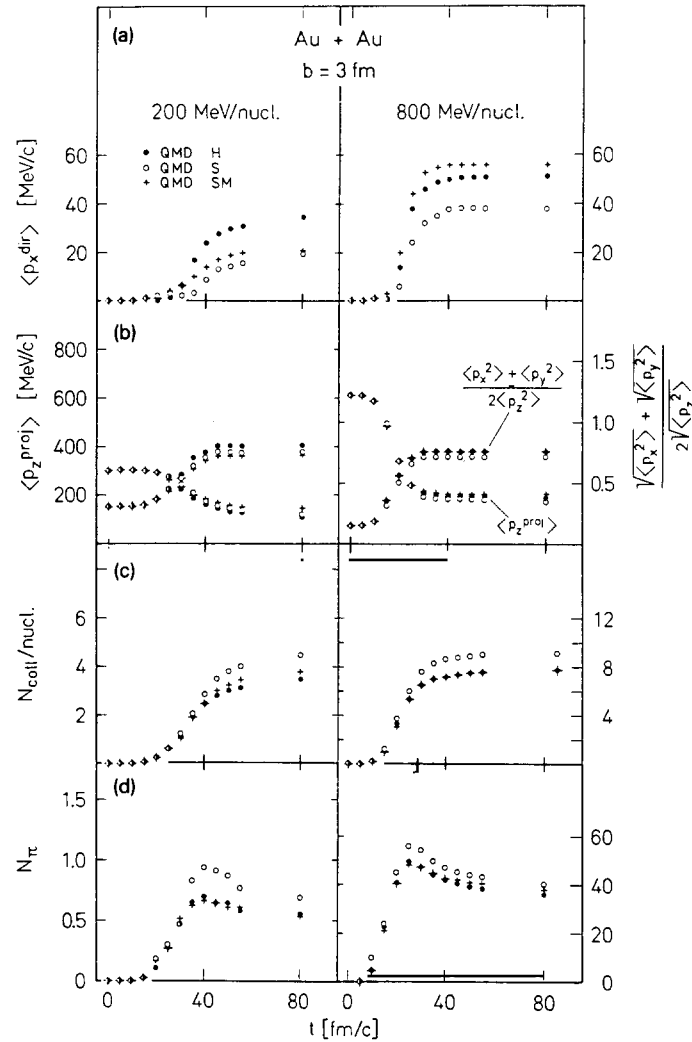


Fig. 45. Time evolution of different observables for the reactions 200 MeV/n and 800 MeV/n Au + Au.

$$\langle p_x^{\text{dir}} \rangle = \frac{1}{A} \sum_{i=1}^A \text{sign}(y(i)) p_x(i), \quad (7.1)$$

where  $y(i)$  is the rapidity of particle  $i$  and  $p_x(i)$  is its transverse momentum in the reaction plane. In earlier years it was common to employ the quantity flow to discuss the transverse momentum transfer. This, however, is not the best choice, since the flow is essentially proportional to the ratio of the longitudinal and the transverse momenta. The excitation function of the average flow angle is almost flat, since with increasing energy both the longitudinal and the transverse momenta increase. The longitudinal momentum reflects the stopping, i.e. the cross section, whereas the transverse momentum is determined by the compression and/or the momentum dependence of the interaction. Since these are two separate physical phenomena, it is better to disentangle both and to discuss the transverse momentum instead of the flow. The transverse momentum in the reaction plane,  $p_x$ , can be obtained by

using the transverse momentum analysis technique [144], which gives a description of how to extract the reaction plane from the experimental data.

The transverse momentum  $\langle p_x^{\text{dir}} \rangle$  is displayed in fig. 45a. We start with the reaction at 200 MeV/n. Initially  $\langle p_x^{\text{dir}} \rangle$  has to be zero. When the nuclei approach each other they feel an attractive potential which – due to the geometry – causes a collective transverse momentum opposite to the impact parameter. As soon as the nuclei overlap, the potential becomes repulsive and accelerates the particles in the transverse direction (figs. 3 and 4). Finally we observe a finite collective flow of the order of some tens of MeV/n. At 200 MeV/n the momentum dependent force is not strong enough to enhance the collective transverse momentum transfer substantially. By contrast, in the reaction at 800 MeV/n the momentum dependent forces enhance the transverse momentum of the soft equation of state by almost 50% so that it exceeds the value expected from a hard equation of state. One has to keep in mind, however, that this conclusion depends strongly on the impact parameter and the mass of the projectile–target combination. The different origin of the transverse flow of SM as compared to S or H can be seen from the time evolution. For SM the transverse flow starts to develop as soon as the projectile and the target overlap and hence before a high density is built up. The transverse momentum of H and S is caused by compression and starts only after we observe a sufficiently high density.

From these results we conclude that the momentum dependence of the nuclear potential can imitate a stiffer equation of state at high beam energies. At  $E_{\text{lab}} = 200$  MeV/n we see little difference between S and SM, but at  $E_{\text{lab}} = 800$  MeV/n the transverse momentum transfer with a soft velocity dependent equation of state exceeds that of a hard equation of state.

Figure 45b shows the longitudinal momentum transfer and the degree of global equilibration. We display the average final longitudinal momentum of all those nucleons which were initially in the projectile. Due to momentum conservation  $\langle p_z^{\text{proj}} \rangle$  equals  $-\langle p_z^{\text{target}} \rangle$ . We observe that the final  $\langle p_z^{\text{proj}} \rangle$  is around 30% of its initial value. Thus there is a considerable longitudinal momentum transfer, but there is no complete stopping. There is also no complete global equilibration, although we display here almost central collisions of a very heavy projectile–target combination. This can be inferred from the quantity  $(\langle p_x^2 \rangle^{1/2} + \langle p_y^2 \rangle^{1/2})/2\langle p_z^2 \rangle^{1/2}$ . If the system is globally equilibrated, this ratio will be 1. The observed ratio is around 0.7 independent of the beam energy and the equation of state. This means that the average kinetic energy in the transverse direction is lower than that in the longitudinal one. Recent investigations have shown that this heavy system does not even become locally equilibrated [145].

The number of collisions which the nucleons suffer is displayed in fig. 45c. Again we observe that SM lies between S and H, as expected from our considerations in section 2.5. The average number of collisions is around 4 for 200 MeV/n and 8–10 for 800 MeV/n. It is remarkable that even this high number of collisions do not equilibrate the system.

The question as to which degree velocity dependent forces can mimic the directed transverse momentum obtained with a much stiffer static equation of state has caused a lot of confusion recently because different calculations yielded quite different results [14, 32, 35]. In some calculations SM yielded much larger  $\langle p_x^{\text{dir}} \rangle$  than H, in other calculations the influence was quite moderate. When comparing the different calculations one has to keep in mind that we expect

(a) a strong mass dependence of this effect; for small masses we observe almost no compression and hence SM should yield a larger  $\langle p_x^{\text{dir}} \rangle$  than H; for large masses the difference should be smaller;

(b) a strong energy dependence; at low beam energy the influence of the velocity dependence should be quite moderate, of course;

(c) that the density dependence of the velocity dependent potential, which cannot be inferred from experiment, influences the result.

Furthermore, even quite different forms of the velocity dependence of the equation of state which yield quite different optical potentials for heavy ion collisions have been used and, last not least, the calculations so far were performed at different impact parameters, which also causes different conclusions. This is certainly a topic that has to be settled in the near future.

## 7.2. Particle production and the equation of state

Pions are produced copiously in high energy heavy ion collisions and are an important source of information on the reaction mechanism. Applying a Cascade calculation, Rosenhauer et al. [146] have shown that the number of pions is directly correlated with the number of hard nucleon–nucleon collisions. Thus the number of pions immediately yields information on the stopping power of nuclear matter.

Experimentally it has been observed that the pion has a nice scaling property. The number of  $\pi^-$  is proportional to the number of participant nucleons, which can be inferred from the observed projectile spectators [147], independent of the mass of the projectile–target combination. We take advantage of this observation and compare our results with those of ref. [147]. In fig. 46 we see the total experimental pion yield as compared with the results of Au + Au reactions at various energies as a function of the mean energy per participant nucleon. We find nice agreement between QMD and experiment. This agreement was also obtained in VUU calculations [64]. Again we see that the results of our  $n$ -body approach coincide with those of the one-body theories as far as single particle properties are concerned.

Some while ago it was proposed [148, 149] to use the particle production as a measure of the compressibility of nuclear matter. This suggestion was triggered by the intra-nuclear cascade results, which always overestimated the number of pions, and was based on the idea that some of the available energy is stored in compressional energy and hence not available for the production of pions. Applying a thermal model, the discrepancy between data and cascade results can be converted to a compressional energy. For a given dependence of the average density at the point of highest compression on the beam energy we can then relate the compressional energy to the compressibility.

More refined calculations [62, 64] did not confirm this suggestion. In fig. 45d we see that for all equations of state almost the same number of pions is obtained. This is a direct consequence of the

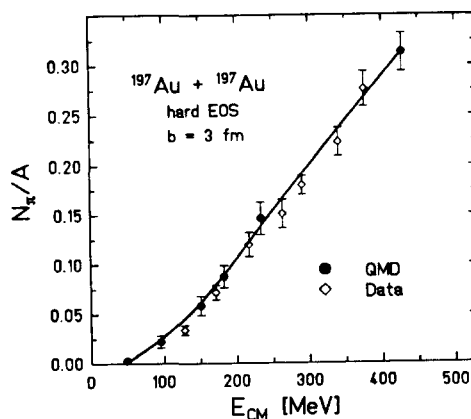


Fig. 46. Number of pions as a function of the energy per participant nucleon as compared with data of ref. [147].

almost identical compressional energy. At 200 MeV/n, the number of produced pions is small and the fluctuations are large. Hence the differences are not statistically significant.

Another possible candidate for testing the equations of state is the  $K^+$  (the  $K^-$  has a higher threshold). For several reasons the  $K^+$  is a [86] more promising particle than the pion:

(1) At the energies of interest kaons can only be produced "subthreshold", i.e., a nucleon–nucleon collision at the same energy is below the production threshold. In nucleus–nucleus collisions the Fermi motion can help to create these particles in a single nucleon–nucleon collision. With increasing impact parameter and hence lower number of collisions it becomes less probable that two nucleons with sufficient relative momentum collide. This concentrates the production at low impact parameters.

(2) The recombination of strange particles has low probability. Hence there is no reabsorption in contrast to the case of the pions.

(3) According to the calculations, the majority of the kaons are produced in a two-step process,  $n + n \rightarrow \Delta$ ,  $\Delta + n \rightarrow n + K^+ + \Lambda$ , because at low energies there are very few nucleons which can provide sufficient energy in a nucleon–nucleon collision. The relative momentum required to produce a  $K^+$  in a  $\Delta + n$  collision is lower due to the larger mass of the  $\Delta$ . This production mechanism favours central collisions because central collisions produce most  $\Delta$ 's and the probability that they interact with another nucleon is high.

There are, however, obstacles to calculating the production of  $K^+$ 's reliably. Firstly, the elementary production cross section  $n + n \rightarrow K^+$  near threshold is not well known. Secondly, the above mentioned two-step process is not established experimentally. It was pointed out recently [86, 150] that some of the uncertainties may cancel if one concentrates on ratios of the cross sections of different symmetric systems and does not aim at a measurement of their absolute values.

Calculations show that kaons are indeed a very good tool to disentangle the momentum dependence of the nucleon–nucleon interaction from the static part. In fig. 47 we show the kaon yield as a function of the impact parameter of the system La + La at 800 MeV/n. For central collisions we see a factor of four between the yield for SM and H and still a factor of two between S and H. The difference between S and H can be understood by inspecting fig. 45. S produces more pions (deltas) and more collisions

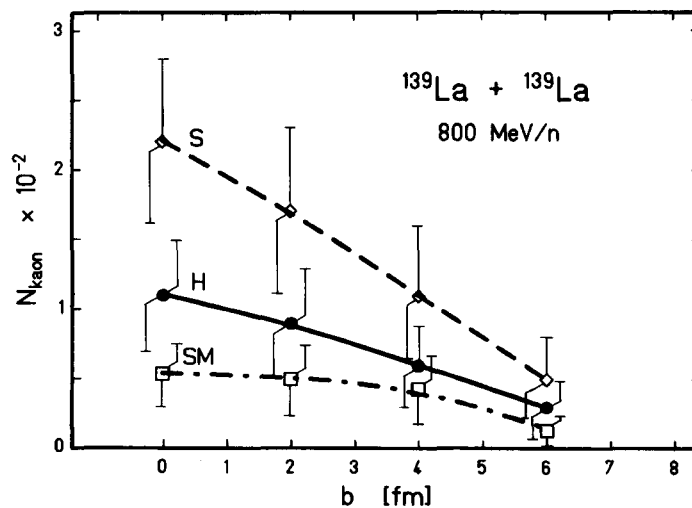


Fig. 47. Production probability of a kaon in the reaction 800 MeV/n La + La for different impact parameters. The error bars display the fluctuation of that number for different simulations.

take place. Both work towards an enhancement of kaon production. Employing velocity dependent forces, the kaon production suffers from the fact that the nucleons which have enough relative momentum to create a  $K^+$  are those which feel the strongest repulsive force, which decelerates them below threshold.

The only other elementary particle one may think of to use for probing the equation of state is the photon. Calculations show that they are sensitive on the 10% level [85, 151] only. This can be understood easily: Each collision in which a proton is involved causes bremsstrahlung. Therefore photons come from everywhere in the collision region and not from the compressed region only. The total production cross sections of composite particles are not sensitive either, as we have seen already in the last chapter.

### 7.3. Can we extract the nuclear equation of state from present data?

The first suggestions on how to measure the nuclear equation of state are rather old [148]. Already in hydrodynamical calculations one observed that the compressional energy is partially released in the transverse direction (bounce off, fig. 4). Thus in the reaction plane projectile and target gain transverse momentum, but in opposite directions. The absolute value of the transverse momentum is related to the equation of state (but unfortunately also to the viscosity [152]). However, there were reasons to hope that a more careful treatment of the collisions between the nucleons, especially during the initial state of the heavy ion reaction, where the approximation of local equilibrium cannot be justified, would allow both effects to be disentangled. First microscopic calculations showed circumstantial evidence for a rather stiff equation of state, but detailed theoretical investigations, as well as the analysis of a large body of experimental data, especially from the Plastic Ball group, rendered this conclusion premature.

In recent years it has been conjectured that other observables should also carry information about the nuclear equation of state. We have discussed in the last section whether produced particles carry information on the nuclear equation of state. In this section we concentrate on proton observables.

Welke et al. [153] presented calculations in the BUU model which showed that the azimuthal distribution of protons with a rapidity larger than  $(y/y_{\text{proj}})_{\text{lab}} > 0.75$  showed a quite strong dependence on the nuclear equation of state. Of course this observable is nothing but a function of the transverse momentum transfer, but it may be a cleaner way of demonstrating the equation of state dependence. If we assume that the particles have a thermal distribution  $f_{\text{th}}$  around the mean  $\langle p_x \rangle$ , we expect for the ratio  $R$  the following dependence:

$$R = \frac{N(\phi = 0^\circ)}{N(\phi = 180^\circ)} = \frac{\int_{-\langle p_x \rangle}^{\infty} f_{\text{th}}(p_x) dp_x}{\int_{-\infty}^{-\langle p_x \rangle} f_{\text{th}}(p_x) dp_x}. \quad (7.2)$$

Thus if  $\langle p_x \rangle$  increases, this ratio increases as well, because the fraction of particles which have a momentum lower than  $-\langle p_x \rangle$  decreases. Only those particles, however, are observed at  $\phi = 180^\circ$ .

This method has two drawbacks. Most particles are at mid-rapidity in these reactions. Hence the effect is caused by a few particles, and consequently the fluctuations are large. Furthermore, in this kinematical regime there are many composite particles (cf. fig. 41), which have to be treated correctly in order to allow a quantitative comparison with the data. But nevertheless, the quoted values of  $R$  for

different equations of state differ by more than a factor of two. Thus – if confirmed by other models – it is certainly a good candidate for a closer inspection.

Another observable which may depend on the equation of state is the collective flow at mid-rapidity perpendicular to the reaction plane, which has recently been observed experimentally [5]. It could be caused by particles whose motion is deflected in the lateral direction through the action of strong density gradients in the course of the reaction. Of course it could also be that particles are emitted preferably perpendicularly to the reaction plane, as, after a nucleon–nucleon collision, there the distance they have to travel in nuclear material is the shortest. In the latter case the equation of state dependence is rather small.

A third conjecture, advanced by Bauer [154], that the quadrupole momentum tensor can be used to determine the nuclear equation of state, did not materialize in actual calculation, neither in the BUU nor in the QMD approach.

In this section we investigate the equation of state dependence of the above mentioned observables in detail. Special emphasis is devoted to the question whether these observables are sufficiently robust in order to reveal information on the equation of state. For this purpose we present calculations with different cross sections (in the limits suggested by nuclear matter calculations) and both with and without a momentum dependent potential. In order to substantiate our calculations we start with a detailed comparison with experiment.

*Transverse momentum transfer.* The quantity  $\langle p_x^{\text{dir}} \rangle$  as defined in eq. (7.1) has been introduced to condense the distribution  $\langle p_x \rangle(y)$  to one number. The value of this variable is displayed in fig. 48 for different beam energies, different projectile target combinations and different theories.

This quantity has much smaller fluctuations than  $\langle p_x \rangle(y)$  for  $y$  near the projectile rapidity. The drawback is, however, that it is dominated by the large number of mid-rapidity particles which do not contribute significantly to  $p_x$ . This quantity also yields much higher values for the BUU calculation as compared to the QMD calculation with the same input parameters. At 800 MeV/n the difference can be as large as a factor of 3. At small beam energies the difference between the calculations is small. Looking at  $\langle p_x^{\text{dir}} \rangle$  for a fixed beam energy as a function of the mass of the scattering partners, we see that at 400 MeV/n a soft velocity dependent equation of state can never imitate the hard equation of state. The opposite is the case at 800 MeV/n, where even for the heaviest system the hard equation produces less  $p_x$  than the soft velocity dependent equation of state. This conclusion, however, depends strongly on the impact parameter. At the lowest energy considered here we see that all calculations with a soft equation of state are below that with the hard equation of state. Thus low energy experiments may be most promising if we want to limit the influence of the velocity dependence of the optical potential. However, even there different cross sections influence the results considerably.

The origin of the difference in  $\langle p_x^{\text{dir}} \rangle$  between the  $n$ -body QMD and the one-body BUU calculation is investigated in detail in fig. 49. There the transverse momentum as a function of the rapidity for 400 MeV/n Nb + Nb at  $b = 3$  fm is plotted for four different computer codes, of which three simulate the BUU equation and one is the solution of the  $n$ -body equation. The BUU [63] and the BUU Welke [35] model have a space fixed grid of length 1 fm (Eulerian method) to determine the local density and hence the potential. The VUU approach [64] measures the density in a comoving sphere of radius  $R$  around the particle under consideration (Lagrangian method). We see a striking similarity of the results of the one-body theories. Together with the results displayed in fig. 19 this shows that the results are independent of the quite different numerical methods employed to solve this complicated equation. The results of the QMD calculations agree with those of the one-body theories at central rapidity but are

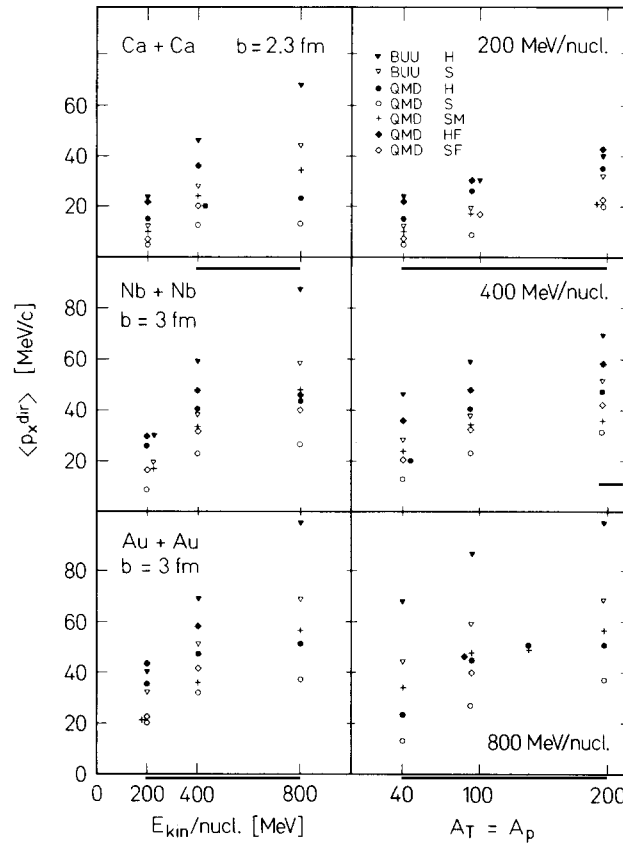


Fig. 48.  $\langle p_x^{\text{dir}} \rangle = A^{-1} \sum_i \text{sign}(y(i)) p_x(i)$  for the different set ups (see table 3), for different beam energies and for different projectile-target combinations at  $b = 3$  fm. BUU refers to results of the Boltzmann-Uehling-Uhlenbeck calculation [63].

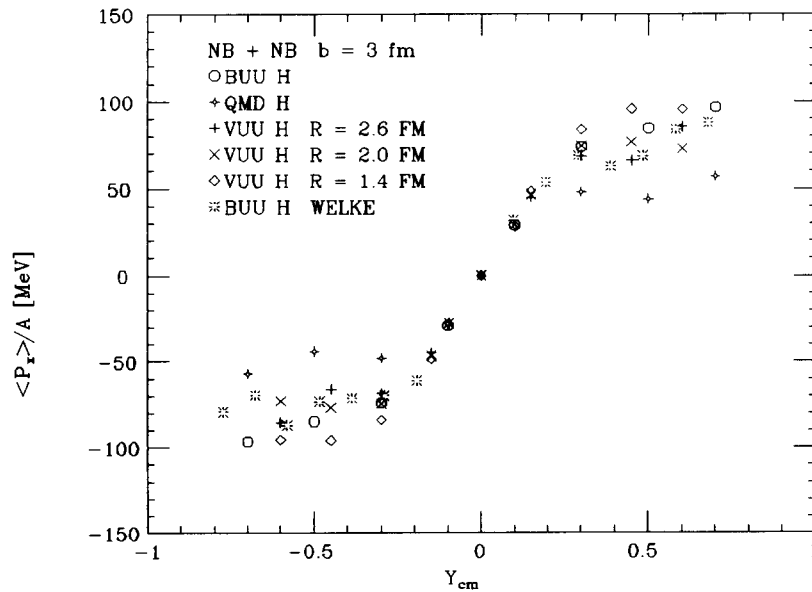


Fig. 49. Average transverse momentum as a function of the centre of mass rapidity for different theories for the reactions 400 MeV/n Nb + Nb,  $b = 3$  fm. We have averaged over all nucleons.

smaller around the beam rapidity. There we observe very few nucleons finally, most of them bound in clusters. We see most of the clusters finally. The reason for this difference is not completely clear so far. It probably depends on two facts:

(a) The unphysical point particles can yield stronger density gradients than the Gaussian Wigner densities, which smear the nucleons over larger space regions. This effect is also indicated by the dependence of the transverse momentum at beam rapidity on the radius of the sphere, in which the local density is determined in the VUU calculation.

(b) In this momentum space region, where many clusters are formed, the fluctuations are most important, which are not treated correctly in the BUU/VUU model.

In fig. 50 we confront the experimental  $\langle p_x(y)/A \rangle$  distribution for the reactions 400 MeV/n Nb + Nb and Au + Au with our calculations. The calculations are performed at  $b = 3$  fm, which yields a proton multiplicity corresponding to the experimental multiplicity bin 4. Therefore, we choose for comparison the data of this multiplicity bin. The first row displays the results of the one-body BUU theory for the reaction. From the theoretical calculation we have ignored all particles which are below the energy threshold of the Plastic Ball. For the sake of comparison we display the results of HC as well (treated with the same filter). Both BUU H and QMD HC (see table 3) employ exactly the same equation of

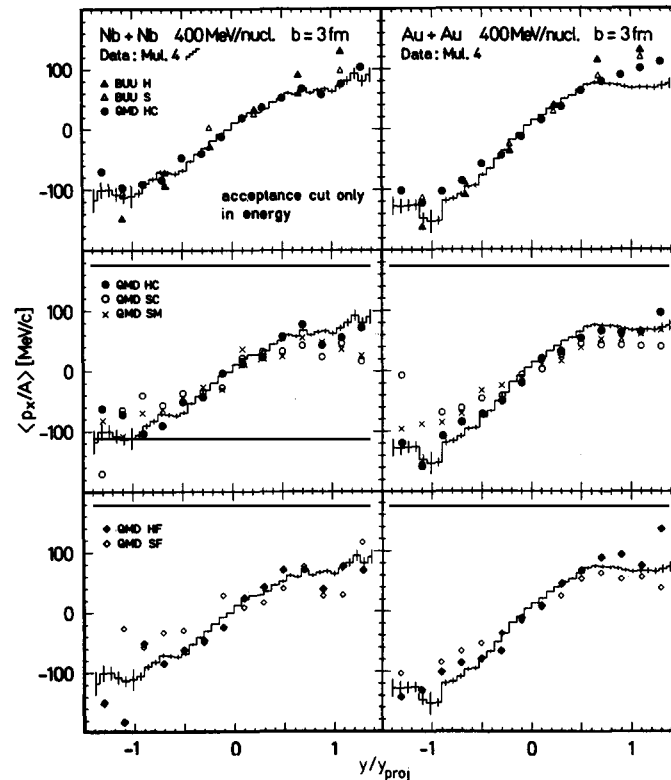


Fig. 50. Transverse momentum transfer as a function of the centre of mass rapidity for different set ups (see table 3) for the reactions 400 MeV/n Nb + Nb and Au + Au as compared to experiments [7]. In the second and the third rows we filtered the theoretical calculation with the Plastic Ball filter SIMDAT [139]. In the first row only an energy and angle cut is applied. BUU refers to results of the Boltzmann-Uehling-Uhlenbeck calculation [63].

state and nucleon–nucleon cross section. Between  $-0.5 < y/y_{\text{proj}} < 0.5$ , where almost all the particles are finally located, the differences between BUU H and QMD HC are small. For larger values of  $y/y_{\text{proj}}$ , however, they become significant. This difference is not yet understood, and – due to the small particle number in this rapidity regime – is hard to investigate. In the QMD calculation we observe high fluctuations of  $\langle p_x/A \rangle$  in this regime. The fluctuations are much smaller in the BUU approach. This may be a hint that the mean field of the BUU calculations acts differently here compared to the nucleon–nucleon potential of the QMD approach. In addition to that, particle identification in the Plastic Ball leads to considerable changes (20%) in  $\langle p_x/A \rangle$  in this rapidity regime, as can be seen from comparing the QMD HC calculations of rows 1 and 2. In rows 2 and 3 we have employed the full Plastic Ball filter SIMDAT [139], which includes, in addition to the threshold, particle misidentification. The momentum dependent equation of state is not able to yield the high  $\langle p_x/A \rangle$  values of a hard equation of state at this energy, but gives results in between those of HC and SC. If we increase the cross section, we produce higher  $\langle p_x/A \rangle$  values. This can be seen from the third row, where protons and neutrons interact with the free np cross section instead of the smaller pp cross section in SC and HC.

From this figure one can conclude that the experimental data are nicely reproduced in the QMD approach, whereas the BUU approach yields values of  $\langle p_x \rangle/A$  which are too large at the beam rapidity. The differences between the different equations of state are of the same order as the differences due to different cross sections or due to the momentum dependence of the potential, and amount to about 20%. Thus from the  $\langle p_x \rangle/A$  distribution alone a firm conclusion on the stiffness of the equation of state cannot be drawn.

The next figure, fig. 51, displays our calculation for 800 MeV/n La + La with H as compared to the data of the streamer chamber group [155]. It seems to be astonishing that the very same data are also well described in the BUU calculations [35] although we have seen (fig. 48) that the average transverse

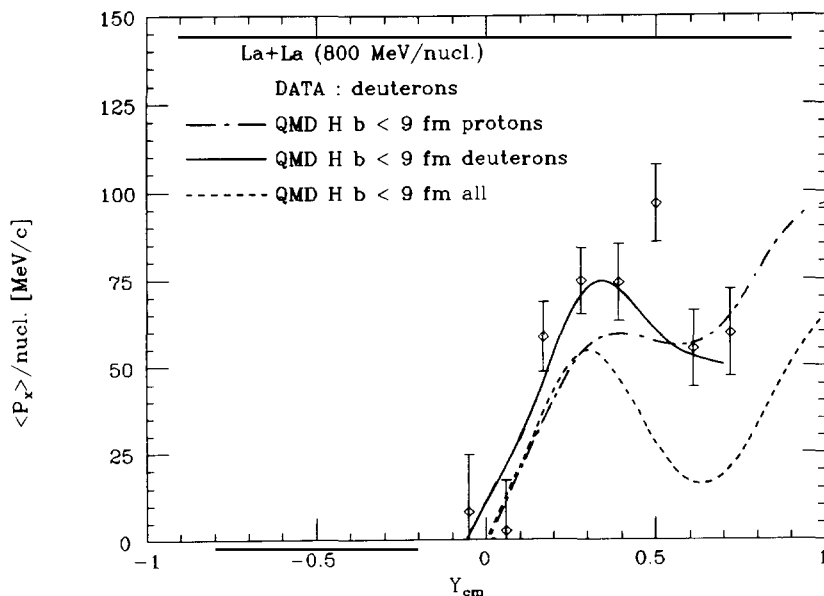


Fig. 51. Average transverse momentum as a function of the centre of mass rapidity for H (see table 3) for the reaction 800 MeV/n La + La as compared to experiment [155]. We display the transverse momentum for protons, deuterons and all nucleons separately.

momentum is larger in BUU calculations as compared with the QMD results. The reason for this – probably accidental – agreement of both theories is a consequence of the fact that in the QMD calculations – as in experiment – we can select the deuterons, whereas in BUU calculations one has to sum over all nucleons because clusters are not defined in these one-body theories. As can be seen in fig. 51, the average transverse momentum of the deuterons is larger than that of the protons, as we have already observed in the 200 MeV/n reaction (fig. 42). More important, however, is the huge difference (about a factor of 2.5) between the average transverse momentum of the deuterons as compared to that obtained by averaging over all nucleons. This large factor is due to large remnants of projectile and target, which do not have a substantial transverse momentum and are present at impact parameters larger than 4 fm. Thus we can conclude that a detailed comparison between experiment and theory requires a separation between singles and different classes of fragments. The maximum of the function  $\langle p_x(y) \rangle$  originates from central collisions. Larger impact parameters decelerate projectile and target less and therefore the deuterons appear at larger  $y$  values.

*Azimuthal distribution.* The next figure, fig. 52, presents our results for the observable proposed by Welke et al. [153]. We display the quantity  $R = N(\phi = 10^\circ)/N(\phi = 170^\circ)$  for particles with

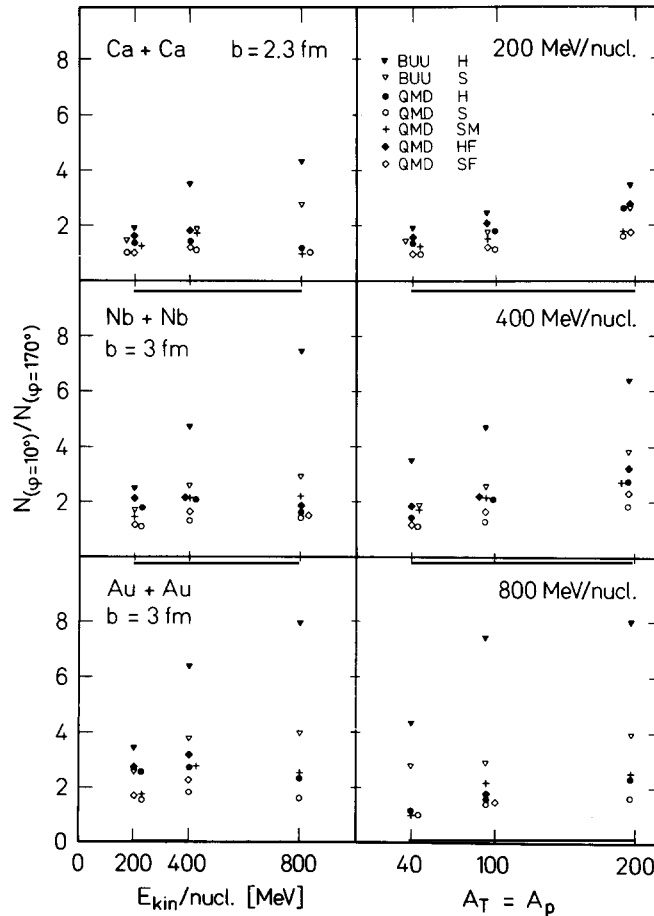


Fig. 52.  $R = N(\phi = 10^\circ)/N(\phi = 170^\circ)$  for  $(y/y_{proj})_{lab} > 0.75$  [153] for different set ups (see table 3), for different beam energies and for different projectile–target combinations at  $b = 3$  fm. BUU refers to results of the Boltzmann–Uehling–Uhlenbeck calculation [63].

$(y/y_{\text{proj}})_{\text{lab}} > 0.75$ . We see that the QMD calculations fall almost on top of each other, independent of the parameters chosen, and independent of energy and projectile–target combination. The BUU results, however, show exactly the behaviour Welke observed: a very strong dependence on the equation of state. Thus this way of plotting  $p_x(y)$  can amplify the differences tremendously. These differences between the BUU and QMD calculations have not been investigated so far. We should mention, however, that the experiments (fig. 50) do not favour the large  $p_x(y)$  values at beam rapidity which are necessary to obtain the large azimuthal anisotropies of the BUU calculation.

*Particle emission perpendicular to the reaction plane.* Already hydrodynamical calculations predicted a preferred emission of mid-rapidity particles perpendicular to the reaction plane ("squeeze out"). Only recently, however, has this prediction been confirmed by experiments of the Plastic Ball group [7]. They found not only that the number of mid-rapidity particles emitted perpendicularly to the reaction plane is larger than that of particles emitted in the reaction plane. Also the average energy of the particles which are emitted out of plane is larger than that of in plane emitted particles. The ratio between in plane and out of plane emission depends on the size of projectile and target as expected for an equation of state dependent effect. However, also shadowing can produce such a result because the distance

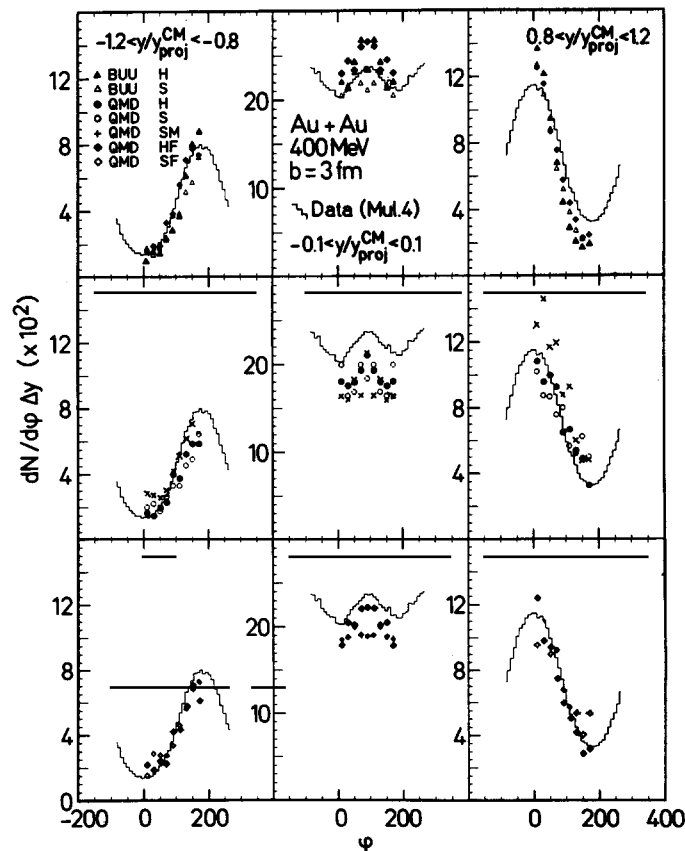


Fig. 53. Azimuthal distribution of protons around projectile, mid- and target rapidity for different set ups (see table 3) as compared to experiment [7]. In the second and the third rows we filtered the theoretical calculation with the Plastic Ball filter SIMDAT [139]. In the first row only an energy and angle cut is applied. BUU refers to results of the Boltzmann–Uehling–Uhlenbeck calculation [63].

particles have to travel in the nuclear medium is longer if they are emitted in the reaction plane as compared to that if they are emitted perpendicularly. If shadowing dominates we would not expect a strong equation of state dependence.

The azimuthal distribution of particles in different kinematical regimes is displayed in fig. 53. Here again the theoretical calculations are acceptance corrected with the Plastic Ball filter SIMDAT [139] and, in the case of the BUU calculations, for the energy threshold. Again we observe for the BUU calculations a quite strong dependence on the equation of state, whereas the dependence of the QMD calculations on the equation of state is quite moderate. In the projectile and target rapidity domain we see only a weak equation of state dependence. More pronounced are the differences at mid-rapidity. However, even here the differences rarely exceed 15% if the variables are calculated in the laboratory system.

The differences become more pronounced, however, if one measures the effect in a system which is rotated by the flow angle into the principal axes system of the momentum flow ellipsoid. The results of our calculation at 400 MeV/n for three different systems as well as the experimental results are presented in fig. 54. The ratio of out of plane and in plane transverse energy increases almost linearly with the mass number of the system, as expected for a collective phenomenon. We observe also a strong dependence of this ratio on the equation of state. The harder the equation of state, the more nucleons are squeezed out. However, a detailed knowledge of the experimental acceptance is necessary in order to find the proper flow angle. (Thus this method relies completely on the experimental acceptance simulation.) Nevertheless, this observable is promising for further investigations due to the relatively large difference between the results for different equations of state and for large systems.

*Rapidity distribution.* The observables we have investigated so far allow no firm conclusion about the equation of state. Thus one has to consider a different strategy: Rather than looking for one variable which immediately allows conclusions about the equation of state, we should investigate a combination of variables. Aiming at those variables which depend strongly on one of the input parameters and less on the others, we may finally be able to reduce the complexity of the problem. One of the possible candidates has already been investigated. The kaon yield showed a very strong dependence on the velocity dependence of the nucleon–nucleon potential, but less dependence on the nucleon–nucleon cross section. The opposite is true for the rapidity distribution of the baryons, as can be seen in fig. 55, where we compare the filtered data [139] with experiment [8].

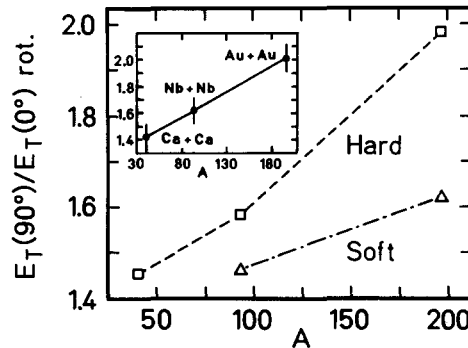


Fig. 54. Projectile and target mass dependence of the out of plane to in plane ratio of the transverse energy for  $X(400 \text{ MeV/n}) + X$  at  $b \approx 0.25b_{\text{max}}$  in the rotated system for a hard and a soft equation of state. The predicted linear mass dependence is also observed by the data measured by the Plastic Ball Group [7], which are presented in the inset.

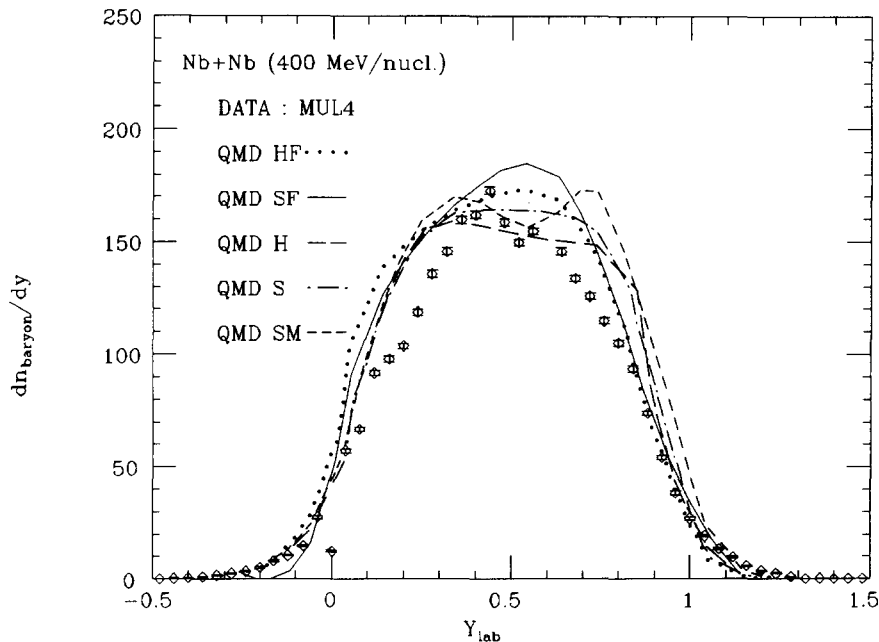


Fig. 55. Rapidity distributions of the baryons for the reaction 400 MeV/n Nb + Nb for different set ups (see table 3) as compared to experiment [8]. We employed the Plastic Ball filter SIMDAT to correct for acceptance [139].

Again the overall agreement between theory and experiment is quite good. We observe that the free cross section leads to a Gaussian form of the rapidity distribution, whereas the reduced cross section causes a plateau, or even a dip, at mid-rapidity, independent of the equation of state. The comparison between calculation and experiment indicates a large cross section. Even the free  $np$  and  $pp$  cross section does not equilibrate the system to a degree which is indicated by the experiment and we can expect that an in-medium enhancement of the free cross section would yield even better agreement.

We also observe here that the differences are of such a magnitude that high precision experiments, together with a good understanding of the acceptance of the detecting devices, are required on the experimental side if one wants to achieve the goal of extracting the nuclear equation of state from experiment. The theory, on the other hand, has to be accurate at least at the 20% level to allow firm conclusions about the equation of state. Both may be within reach in the next decade, when the new SIS accelerator allows high statistics experiments, and also the computations will no longer require unwanted approximations due to increases in the available computer power. However, as we have seen in chapter 4, there remains the problem of how to deal properly with a fermionic system, which has to be solved before the nuclear equation of state can be reliably calculated.

## 8. Conclusions

We have presented a microscopic dynamical  $n$ -body approach to heavy ion collisions which describes the whole time evolution of a nucleus–nucleus collision. We have discussed under which approximations the model can be derived from the Wigner density of the  $n$ -body Schrödinger equation. They include the validity of the impulse approximation and the assumption of independent nucleon–nucleon

collisions. Most of these approximations are reasonably fulfilled under the circumstances we expect for medium and high energy heavy ion collisions. Heavy ion reactions can now be studied theoretically on an event-by-event basis from the initial configuration to the final distribution of nucleons, pions, kaons and fragments in phase space. This is achieved by following the time evolution of the  $n$ -body system, which interacts via mutual two- and three-body potentials and a residual interaction with a Pauli blocked nucleon–nucleon scattering cross section. As far as one-body observables are concerned, we reproduce the results of BUU/VUU and TDHF calculations, except for the transverse momentum transfer.

We find almost complete, to this high degree unexpected, agreement with a large variety of single particle and fragment data. Thus we feel confident that this model allows us, for the first time, to study the formation of fragments in a dynamical model and to make detailed comparisons with experimental data possible by allowing one to separate clusters from single particles. This is a prerequisite for the study of the nuclear equation of state.

We have investigated in detail the formation of fragments and have examined which conclusions about the nuclear equation of state can presently be drawn. As we have seen, heavy ion collisions are presently the only possibility to obtain this desired quantity. The calculations confirm qualitatively the predictions of hydrodynamical calculations, i.e. the squeeze out and the bounce off. Hence the potential is of importance in this energy domain beyond the formation of clusters. Detailed investigations in the QMD model, however, show that different potentials, corresponding to different equations of state in nuclear matter, produce quantitatively almost the same effect.

We present our main results in two sets of conclusions, one for fragment formation and one for the nuclear equation of state.

*Concerning fragment production.*

- (a) The calculation reproduces all investigated observables,
- the fragment yield,
  - the angular distribution of fragments,
  - the associated multiplicity of singles,
  - the mean velocity of fragments,
  - the multiplicity distribution of fragments as a function of the associated multiplicity of fast particles,
  - the average transverse momentum of fragments in the reaction plane.
- (b) Of these observables only the average transverse momentum is, as expected, dependent on the equation of state above the 30% level. On the other hand, this observable is also quite sensitive to the in-medium corrections of the cross section. So both dependences have to be disentangled before this observable can be used to pin down the compressibility of nuclear matter.
- (c) The strong impact parameter dependence of the mass yield curve rules out the conjecture that the power law form of the inclusive mass yield curve provides a signature that the system is close to the critical point of a liquid–gas phase transition. The agreement of the inclusive mass yield distribution with a form expected for a system close to its critical point is purely accidental.
- (d) We observe a strong geometric correlation between the entrance and exit channels of the reaction. Nucleons retain information about their initial position. This rules out the assumption that the system equilibrates globally to some state similar to a compound nucleus. If that were true, any information about the initial state would be lost. Consequently, a thermodynamical single source approach to multifragmentation in heavy ion reactions cannot be considered as adequate.
- (e) Fragments  $2 \leq A \leq 30$  stem from the surface of the system. They separate from the rest system at

a very early time, i.e., when the density is highest. They measure the violence of the reaction, i.e., the number of these clusters strongly decreases as a function of the impact parameter. The medium mass clusters are kicked off from the system as a result of the high density wave and its repulsive force, caused by the interpenetrating projectile.

(f) At later times a compound-nucleus-like remnant is formed, which emits protons and neutrons. The decay chain of these remnants yields fragments with masses down to  $A = 40$ . These heavy clusters can be used to determine the impact parameter of the reaction. This method is superior to the method used up to now to measure the multiplicity of singles.

*Concerning the nuclear equation of state.*

(g) For single nucleons we see a 30% dependence of the average transverse momentum on the equation of state, a much lower value than the factor of two seen for fragments. About the same difference is seen for the different cross sections employed.

(h) The pions are not at all sensitive to the equation of state.

(i) Twice as many kaons are produced with a soft equation of state as compared with a hard one. Including the momentum dependence of the interaction we see a reduction by a factor of four.

(j) Even at almost central collisions ( $b = 3$  fm) a system as heavy as Au + Au does not come to equilibrium. We see fragments emitted from well separated target and projectile sources. The larger the cross section, the closer the system comes to equilibrium. Hence the rapidity distribution can be used as a measure of the in-medium cross section.

(k) As a consequence, the observed transverse momentum depends on the exact knowledge of the cross section. Before we can pin down the stiffness of the nuclear equation of state one has to understand the in-medium correction of the nucleon–nucleon cross section.

To extract the nuclear equation of state from experiments a simultaneous measurement of several variables is necessary. There one should concentrate on those variables, which are sensitive to only one of the unknown inputs. The momentum dependence of the potential can best be investigated by the cross section for kaon production. The ratio  $\sigma_K(A_1 + A_1)/\sigma_K(A_2 + A_2)$  with  $A_1$  being light and  $A_2$  being heavy also gives information on the equation of state. This information should be supplemented by transverse momentum measurements of singles and medium mass clusters. Finally the rapidity distribution of the nucleons has to be measured to reduce the uncertainties of the cross section.

We have reported on the first steps towards the understanding of the equation of state. The calculations performed so far hint at a stiffer equation of state than that obtained in astrophysics. However, a better understanding of the in-medium effects as well as more refined experiments are needed for further progress. Only combined efforts from the experimental and the theoretical side will enable us to pin down the nuclear equation of state by the analysis of heavy ion collisions successfully.

## Acknowledgement

The Quantum Molecular Dynamics approach was initiated while the author enjoyed the hospitality of the Cyclotron Laboratory at the Michigan State University. It is a pleasure to thank H. Stöcker for many discussions in which many facets of the approach were developed. Most of the results presented in this review were obtained in a collaboration between the Universities of Heidelberg and Frankfurt. I would like to thank all members of this collaboration: M. Berenguer, A. Bohnet, W. Greiner, C. Hartnack, J. Jänicke, L. Neise, G. Peilert, A. Rosenhauer and H. Stöcker. The  $g$ -matrix approach was

developed with A. Fässler, R. Linden and N. Ohtsuka from the University of Tübingen. I would also like to thank J. Hüfner for many valuable discussions about the formal aspects of the approach. I am also indebted to the Plastic Ball group for the many discussions about the details of the data and to Dr. Sumbera for the permission to compare the results of our calculation with the yet unpublished angular distribution of fragments. Last, but not least, I would like to thank T. Signal for a careful reading of the manuscript and S. Bartsch as well as M. Steiert for the careful typing of the manuscript.

## References

- [1] R.J. Glauber, in: Lectures in Theoretical physics, eds W.E. Brittin et al., vol. 1 (Interscience, New York, 1959); R.J. Glauber and G. Matthiae, Nucl. Phys. B 21 (1970) 135.
- [2] L.P. Csernai and J.I. Kapusta, Phys. Rep. 131 (1986) 223.
- [3] B. Jakobsson, G. Jönson, B. Lindquist and A. Oskarsson, Z. Phys. A 307 (1982) 293; Nucl. Phys. A 509 (1990) 195; A 488 (1988) 251c.
- [4] H. Stöcker and W. Greiner, Phys. Rep. 137 (1986) 277.
- [5] H.A. Gustafsson et al., Phys. Rev. Lett. 52 (1984) 1590; H.H. Gutbrod, K.H. Kampert, B. Kolb, H. Löhner, B. Ludewigt, A.M. Poskanzer, A. Warwick and H. Wieman, Nucl. Phys. A 447 (1985) 3c; H.A. Gustafsson, H.H. Gutbrod, K.H. Kampert, B. Kolb, H. Löhner, B. Ludewigt, A.M. Poskanzer, H.G. Ritter, H.R. Schmidt and H. Wieman, Phys. Rev. Lett. 57 (1986) 302; H.A. Gustafsson, Mod. Phys. Lett. A 3 (1988) 1323.
- [6] K.H. Kampert, Thesis, Univ. of Münster (1986); K.G.R. Doss et al., Phys. Rev. Lett. 59 (1987) 2720.
- [7] H. Gutbrod et al., Phys. Lett. B 216 (1989) 267; Phys. Rev. C 42 (1990) 640.
- [8] H. Gutbrod et al., Z. Phys. A 337 (1990) 57.
- [9] J. Hüfner, Phys. Rep. 125 (1985) 129.
- [10] B. Day, Rev. Mod. Phys. 39 (1967) 719.
- [11] J. Aichelin and H. Stöcker, Phys. Lett. B 176 (1986) 14.
- [12] A. Rosenhauer, J. Aichelin, H. Stöcker and W. Greiner, J. Physique C 4 (1986) 395.
- [13] J. Aichelin, A. Rosenhauer, G. Peilert, H. Stöcker and W. Greiner, Phys. Rev. Lett. 58 (1987) 1926.
- [14] J. Aichelin et al., Phys. Rev. C 37 (1987) 2451.
- [15] G. Peilert, A. Rosenhauer, J. Aichelin, H. Stöcker and W. Greiner, Mod. Phys. Lett. A 3 (1988) 459; Phys. Rev. C 39 (1989) 1402.
- [16] J. Aichelin, C. Hartnack, A. Bohnet, L. Zhuxia, G. Peilert, H. Stöcker and W. Greiner, Phys. Lett. B 224 (1989) 34.
- [17] A. Rosenhauer, Thesis, Univ. of Frankfurt (1988).
- [18] G. Peilert, Thesis, Univ. of Frankfurt (1988).
- [19] A. Bohnet, Thesis, Univ. of Heidelberg (1988).
- [20] E. Baron, J. Cooperstein and S. Kahana, Nucl. Phys. A 440 (1985) 744; Phys. Rev. Lett. 55 (1985) 126.
- [21] J.P. Blaizot, Phys. Rep. 64 (1980) 171.
- [22] M.M. Sharma et al., Phys. Rev. C 38 (1988) 2562.
- [23] R. Stock, Phys. Rep. 135 (1986) 259.
- [24] D. Keane, S.Y. Chu, S.Y. Fung, Y.M. Liu, L.J. Qiao, G. VanDalen, M. Vient, S. Wang, J.J. Molitoris and H. Stöcker, Phys. Rev. C 37 (1988) 1447; in: Proc. 8th High Energy Heavy Ion Study (LBL, Berkeley, 1987); J.J. Molitoris and H. Stöcker, Phys. Rev. C 32 (1985) 346.
- [25] K. Nomoto and M. Hashimoto, Phys. Rep. 163 (1988) 13.
- [26] S.E. Woosley and T.A. Weaver, Bull. Am. Astron. Soc. 16 (1984) 971.
- [27] W. Hillebrandt, Astron. Astrophys. 110 (1982) L3-6.
- [28] H.A. Bethe and J.R. Wilson, Astrophys. J. 295 (1985) 14.
- [29] N.K. Glendenning, Z. Phys. A 327 (1987) 295.
- [30] E. Baron, H.A. Bethe, G.E. Brown, J. Cooperstein and S. Kahana, Phys. Rev. Lett. 52 (1984) 1590.
- [31] W. Hillebrandt, E. Müller and R. Mönchmeyer, in: Proc. Nato ASI on The Nuclear Equation of State (Peniscola, Spain, 1989).
- [32] C. Gale, G. Bertsch and S. DasGupta, Phys. Rev. C 35 (1987) 1666.
- [33] A.R. Bodmer and C.N. Panos, Phys. Rev. C 15 (1977) 1342; C 22 (1980) 1023; Nucl. Phys. A 356 (1981) 517; A.R. Bodmer, C. Panos and A.D. MacKellar; Phys. Rev. C 22 (1980) 1025.
- [34] B. Schürmann and W. Zwermann, Phys. Lett. B 158 (1985) 366; B. Schürmann, W. Zwermann and R. Malfiet, Phys. Rep. 147 (1987) 1.

- [35] C. Gale, G.M. Welke, M. Prakash, S.J. Lee and S. Das Gupta, *Phys. Rev. C* 41 (1990) 1045.
- [36] B. Ter Haar and R. Malfliet, *Phys. Lett. B* 172 (1986) 10; *Phys. Rep.* 149 (1987) 207.
- [37] J. Cugnon, A. Lejeune and P. Grange, *Phys. Rev. C* 35 (1987) 861;  
J. Cugnon, in: *Proc. Nato ASI on The Nuclear Equation of State* (Peniscola, Spain, 1989).
- [38] G.E. Brown and V. Koch, in: *Proc. 8th High Energy Heavy Ion Study* (LBL, Berkeley, 1987);  
G.F. Bertsch, G.E. Brown, V. Koch and B. Li, *Nucl. Phys. A* 490 (1988) 745;  
G.E. Brown et al., *Nucl. Phys. A* 505 (1989) 823.
- [39] F. De Jong, B. Ter Haar and R. Malfliet, *Phys. Lett. B* 220 (1989) 485.
- [40] H.G. Baumgardt, J.U. Schott, Y. Sakamoto, E. Schopper, H. Stöcker, J. Hofmann, W. Scheid and W. Greiner, *Z. Phys. A* 273 (1975) 359;  
J. Maruhn and W. Greiner, in: *Treatise on Heavy Ion Physics*, ed. A. Bromley (Plenum, New York, 1984).
- [41] J.P. Jeukenne, A. Lejeune and C. Mahaux, *Phys. Rep.* 25 (1976) 83;  
A. Lejeune, P. Grange, M. Martzloff and J. Cugnon, *Nucl. Phys. A* 453 (1986) 189.
- [42] R.V. Reid Jr, *Ann. Phys.* 50 (1968) 411.
- [43] P. Ring and P. Schuck, *The Nuclear Many Body Problem* (Springer, Heidelberg, 1980).
- [44] H. Kümmel, K.H. Lührmann and J.G. Zabolitzky, *Phys. Rep.* 36 (1978) 1;  
H. Kümmel and K.H. Lührmann, *Nucl. Phys. A* 191 (1972) 525; *A* 194 (1973) 225.
- [45] B. Friedman and V.R. Pandharipande, *Nucl. Phys. A* 361 (1981) 502.
- [46] B.D. Serot and J.D. Walecka, in: *Advances in Nuclear Physics*, vol. 16, eds J.W. Negele and E. Vogt (Plenum, New York, 1986).
- [47] C.J. Horowitz and B.D. Serot, *Nucl. Phys. A* 464 (1987) 613.
- [48] R. Brockmann and R. Machleidt, *Phys. Lett. B* 149 (1984) 283.
- [49] J. Boguta and H. Stöcker, *Phys. Lett. B* 120 (1983) 289.
- [50] G.E. Brown, W. Weise, G. Baym and J. Speth, *Comments Nucl. Part. Phys.* 17 (1987) 39;  
G.E. Brown, *Phys. Rep.* 163 (1988) 167.
- [51] T.L. Ainsworth, E. Baron, G.E. Brown, J. Cooperstein and M. Prakash, *Nucl. Phys. A* 464 (1987) 740.
- [52] M. Jaminon, C. Mahaux and P. Rochus, *Nucl. Phys. A* 365 (1981) 371.
- [53] E.D. Cooper, B.C. Clark, R. Kozack, S. Shim, S. Hama, J.I. Johansson, H.S. Sherif, R.L. Mercer and B.D. Serot, *Phys. Rev. C* 36 (1987) 2170.
- [54] R. Cusson, P.G. Reinhard, H. Stöcker, M.R. Strayer and W. Greiner, *Phys. Rev. Lett.* 55 (1985) 2786.
- [55] H. Feldmeier, M. Schönhofen and M. Cubero, GSI preprint 88-63.
- [56] T. Reitz, in: *Proc. XVI Conf. on Gross Properties of Nuclei and Nuclear Excitations* (Hirschegg, 1988).
- [57] L. Wilets, Y. Yariv and R. Chestnut, *Nucl. Phys. A* 301 (1978) 359;  
L. Wilets, E.M. Henley, M. Kraft and A.D. Mackellar, *Nucl. Phys. A* 282 (1977) 341.
- [58] J.J. Molitoris, J.B. Hoffer, H. Kruse and H. Stöcker, *Phys. Rev. Lett.* 53 (1984) 899.
- [59] G. Buchwald et al., *Phys. Rev. Lett.* 52 (1984) 1594, and references therein.
- [60] L.W. Nordheim, *Proc. R. Soc. London A* 119 (1928) 689.
- [61] E.A. Uehling and G.E. Uhlenbeck, *Phys. Rev.* 43 (1933) 552.
- [62] G.F. Bertsch, H. Kruse and S. DasGupta, *Phys. Rev.* 29 (1984) 673.
- [63] J. Aichelin and G. Bertsch, *Phys. Rev. C* 31 (1985) 1730;  
J. Aichelin, *Phys. Rev. C* 33 (1986) 537;  
J. Aichelin and H. Stöcker, *Phys. Lett. B* 163 (1985) 59.
- [64] H. Kruse, B.V. Jacak and H. Stöcker, *Phys. Rev. Lett.* 54 (1985) 289; *Phys. Rev. C* 31 (1985) 1770;  
J.J. Molitoris, J.B. Hoffer, H. Kruse and H. Stöcker, *Phys. Rev. Lett.* 53 (1984) 899;  
H. Kruse, B.V. Jacak and H. Stöcker, *Phys. Rev. Lett.* 54 (1985) 289;  
J.J. Molitoris, H. Stöcker and B.L. Winer, *Phys. Rev. C* 36 (1987) 220.
- [65] C. Gregoire, B. Remaud, F. Sebillé, L. Vinet and Y. Raffray, *Nucl. Phys. A* 465 (1987) 317;  
L. Vinet, C. Gregoire, P. Schuck, B. Remaud and F. Sebillé, *Nucl. Phys. A* 468 (1987) 321.
- [66] J. Cugnon, T. Mizutani and J. Vandermeulen, *Nucl. Phys. A* 352 (1981) 505.
- [67] Y. Yariv and Z. Fraenkel, *Phys. Rev. C* 20 (1979) 2227; *C* 24 (1981) 488.
- [68] I. Tanihata, S. Nagamiya, S. Schnetzer and H. Steiner, *Phys. Lett. B* 100 (1981) 121.
- [69] P. Bonche, S. Koonin and J.W. Negele, *Phys. Rev. C* 13 (1976) 1226.
- [70] R. Cusson and J. Maruhn, *Phys. Rev. Lett.* 36 (1976) 1166;  
K.T.R. Davis, K.R.S. Devi, S.E. Koonin and M.R. Strayer, in: *Heavy Ion Science*, ed. D.A. Bromley (Plenum, New York, 1984), and references therein.
- [71] C.Y. Wong, *Phys. Rev. C* 25 (1982) 1460.
- [72] S. Jones and E. Remler, *Ann. Phys. (NY)* 180 (1987) 152.
- [73] R.J. Lenk and V.R. Pandharipande, *Phys. Rev. C* 34 (1986) 177;  
T.J. Schlagel and V.R. Pandharipande, *Phys. Rev. C* 36 (1987) 192, and references therein.
- [74] T. Wu, *Kinetic Equations of Gases and Plasmas* (Addison Wesley, Reading, MA, 1966).
- [75] C.Y. Wong and H.H.K. Tang, *Phys. Rev. C* 20 (1979) 1419.

- [76] P. Grange, H.A. Weidenmüller and G. Wolschin, *Ann. Phys.* 136 (1981) 190.
- [77] R.F. Snider, *J. Chem. Phys.* 32 (1960) 1051.
- [78] J. Cugnon, *Phys. Rev. C* 22 (1980) 1885.
- [79] G. Bertsch and J. Cugnon, *Phys. Rev. C* 24 (1985) 2514.
- [80] E.A. Remler and A.P. Sathe, *Ann. Phys. (NY)* 91 (1975) 295.
- [81] J. Aichelin, *Nucl. Phys. A* 411 (1983) 474.
- [82] Y.L. Klimovich and D. Kremp, *Physica A* 109 (1981) 517.
- [83] W. Botermans and R. Malfliet, *Phys. Lett. B* 171 (1987) 22.
- [84] J. Aichelin *Phys. Lett. B* 164 (1985) 261;  
W. Bauer, *Phys. Rev. C* 40 (1989) 715.
- [85] T.S. Biro et al., *Nucl. Phys. A* 475 (1987) 579;  
C.M. Ko and J. Aichelin, *Phys. Rev. C* 35 (1987) 1976;  
K. Niita, A.L. de Paoli, W. Bauer, T.S. Biro, W. Cassing and U. Mosel, *Nucl. Phys. A* 482 (1988) 525c;  
T.S. Biro, K. Niita, A.L. de Paoli, W. Bauer, W. Cassing and U. Mosel, *Nucl. Phys. A* 475 (1987) 579;  
W. Bauer, *Phys. Rev. C* 40 (1989) 715.
- [86] J. Aichelin and C.M. Ko, *Phys. Rev. Lett.* 55 (1985) 2661;  
J.Q. Wu and C.M. Ko, *Nucl. Phys. A* 499 (1989) 810.
- [87] J. Aichelin and E. Remler, *Phys. Rev. C* 35 (1987) 1291.
- [88] K. Niita, T.S. Biro, W. Cassing, A.K. de Paoli, U. Mosel and M. Schäfer, *Nucl. Phys. A* 495 (1989) 91c;  
A. De Paoli et al., *Phys. Lett. B* 219 (1989) 194.
- [89] G.F. Bertsch and S. Das Gupta, *Phys. Rep.* 160 (1988) 189.
- [90] G. Welke, R. Malfliet, C. Gregoire, M. Prakash and E. Suraud, *Phys. Rev. C* 40 (1989) 2611.
- [91] W. Cassing, *J. Phys. C* 2 (1987) 185.
- [92] E.P. Wigner, *Phys. Rev.* 40 (1932) 749.
- [93] M. Goldberger and K.M. Watson, *Collision Theory* (Wiley, New York, 1964).
- [94] H. Krimm, A. Klar and H.J. Pirner, *Nucl. Phys. A* 367 (1981) 333.
- [95] M. Thies, *Ann. Phys. (NY)* 123 (1979) 411.
- [96] E. Remler, *Ann. Phys. (NY)* 95 (1975) 455; 119 (1979) 326.
- [97] J. Hüfner, *Ann. Phys. (NY)* 115 (1978) 43.
- [98] G. Chew, *Phys. Rev.* 80 (1950) 196; 85 (1952) 636.
- [99] P. Carruthers and M. Zachariasen, *Rev. Mod. Phys.* 55 (1983) 245.
- [100] G.J. Igo, *Rev. Mod. Phys.* 50 (1978) 523.
- [101] K.M. Watson, *Phys. Rev.* 89 (1953) 575.
- [102] C. Hartnack, Thesis, Univ. of Frankfurt (1989).
- [103] C. Dorso, S. Duarte and J. Randrup, *Phys. Lett. B* 188 (1987) 287.
- [104] Li Zhuxia, H. Stöcker and W. Greiner, preprint UFTP.
- [105] H. Feldmeier, in: *Proc. Nato ASI on The Nuclear Equation of State* (Peniscola, Spain, 1989); *Nucl. Phys. A* 515 (1990) 147; private communication.
- [106] A.K. Kerman and S.E. Koonin, *Ann. Phys. (NY)* 100 (1976) 332.
- [107] J. Aichelin and H. Stöcker, *Phys. Lett. B* 163 (1985) 59.
- [108] D. Vautherin and D.M. Brink, *Phys. Rev. C* 5 (1972) 626.
- [109] N. Ohtsuka, R. Linden, A. Fässler and F.B. Malik, *Nucl. Phys. A* 465 (1987) 550.
- [110] A. Bohnet, N. Ohtsuka, J. Aichelin, R. Linden and A. Fässler, *Nucl. Phys. A* 494 (1989) 349.
- [111] G.F. Bertsch, W.G. Lynch and M.B. Tsang, *Phys. Lett. B* 189 (1987) 384.
- [112] J. Aichelin et al., *Phys. Rev. Lett.* 62 (1989) 1461.
- [113] S. Hayashi et al., *Phys. Rev. C* 38 (1988) 1229.
- [114] C.M. Ko and Q. Li, *Phys. Rev. C* 37 (1988) 2270; C 39 (1989) 849.
- [115] N. Brummund, Thesis, Univ. of Münster.
- [116] R.W. Minich et al., *Phys. Lett. B* 118 (1982) 458;  
J.E. Finn et al., *Phys. Rev. Lett.* 49 (1982) 1321;  
A.S. Hirsch, A. Bujak, J.E. Finn, L.J. Gutay, R.W. Minich, N.T. Porile, R.P. Scharenberg, B.C. Stringfellow and F. Turkot, *Phys. Rev. C* 29 (1984) 508;  
J.A. Gaidos et al., *Phys. Rev. Lett.* 42 (1979) 82.
- [117] M.E. Fisher, *Physics* 3 (1967) 255.
- [118] A.D. Panagiotou, M.W. Curtin and D.K. Scott, *Phys. Rev. C* 31 (1982) 55.
- [119] G. Westfall et al., *Phys. Rev. C* 17 (1978) 1368.
- [120] A.I. Warwick, H.H. Wiemann, H.H. Gutbrod, M.R. Maier, J. Peter, H.G. Ritter, H. Stelzer and F. Weik, *Phys. Rev. C* 27 (1983) 1083;  
A.I. Warwick, private communication.
- [121] G. Westfall et al., *Phys. Rev. Lett.* 43 (1979) 1859.

- [122] X. Campi and J. Hüfner, Phys. Rev. C 24 (1981) 2199.
- [123] G. Fai and J. Randrup, Nucl. Phys. A 404 (1983) 551.
- [124] B.V. Jacak et al., Phys. Rev. Lett. 51 (1983) 1846; Phys. Rev. C 35 (1987) 1751.
- [125] H. Stöcker et al., Nucl. Phys. A 400 (1983) 63c.
- [126] D.H.E. Gross and Ciao-ze Zhang, Phys. Lett. B 161 (1985) 47.
- [127] J.P. Bondorf, R. Donangelo, I.N. Mishustin, C.J. Petrick, H. Schulz and K. Sneppen, Nucl. Phys. A 443 (1985) 347; J.P. Bondorf, R. Donangelo, I.N. Mishustin and H. Schulz, Nucl. Phys. A 444 (1985) 460.
- [128] W.A. Friedman and W.G. Lynch, Phys. Rev. C 28 (1983) 950.
- [129] X. Campi, J. Desbois and E. Lipparini, Phys. Lett. B 142 (1984) 8.
- [130] W. Bauer, D.R. Dean, U. Mosel and U. Post, Phys. Lett. B 150 (1985) 53.
- [131] J. Aichelin and J. Hüfner, Phys. Lett. B 136 (1984) 15.
- [132] J. Aichelin, J. Hüfner and R. Ibarra, Phys. Rev. C 30 (1984) 107.
- [133] B. Strack and J. Knoll, Z. Phys. A 315 (1984) 249; J. Knoll and B. Strack, Phys. Lett. B 149 (1984) 45.
- [134] W. Bauer, G. Bertsch and S. DasGupta, Phys. Rev. Lett. 58 (1987) 863.
- [135] S. Das Gupta, C. Gale, J. Gallego, H.H. Gan and R.D. Ratna Raju, Phys. Rev. C 35 (1987) 556.
- [136] G.E. Beauvais, D.H. Boal and J.C.K. Wong, Phys. Rev. C 35 (1987) 545; D.H. Boal, J.N. Glosli and C. Wicentowich, Phys. Rev. C 40 (1989) 601, and references therein.
- [137] C.J. Waddington and P.S. Freier, Phys. Rev. C 31 (1985) 888.
- [138] J. Aichelin and X. Campi, Phys. Rev. C 34 (1986) 1643.
- [139] A. Poskanzer, Plastic Ball filter SIMDAT, private communication.
- [140] M. Sumner, private communication.
- [141] D.R. Bowman et al., Phys. Lett. B 189 (1987) 282.
- [142] G. Westfall, J. Gosset, P.J. Johanson, A.M. Poskanzer, W.G. Meyer, H.H. Gutbrod, A. Sandoval and R. Stock, Phys. Rev. Lett. 37 (1976) 1202.
- [143] J. Pochodzalla et al., Phys. Rev. C 35 (1987) 1695.
- [144] P. Danielewicz and G. Odyniec, Phys. Lett. B 157 (1985) 146.
- [145] M. Berenguer, Diploma thesis, Frankfurt (1989).
- [146] A. Rosenhauer, J.A. Maruhn, H. Stöcker and W. Greiner, Phys. Lett. B 159 (1985) 239; A. Rosenhauer, H. Stöcker, J.A. Maruhn and W. Greiner, Phys. Rev. C 34 (1986) 185.
- [147] J.W. Harris et al., Phys. Rev. Lett. 58 (1987) 463.
- [148] H. Stöcker, W. Greiner and W. Scheid, Z. Phys. A 286 (1978) 121.
- [149] J.W. Harris et al., Phys. Lett. B 153 (1985) 377.
- [150] B. Schürmann and W. Zwermann, Phys. Lett. B 183 (1987) 31.
- [151] C.M. Ko, private communication.
- [152] G. Peilert et al., in: Proc. 8th High Energy Heavy Ion Study (LBL, Berkeley, 1987); W. Schmidt et al., in: Proc. Nato ASI on The Nuclear Equation of State (Peniscola, Spain, 1989).
- [153] G.M. Welke, M. Prakash, T.T.S. Kuo and S. Das Gupta, Phys. Rev. C 38 (1988) 2101.
- [154] W. Bauer, Phys. Rev. Lett. 61 (1988) 2534.
- [155] P. Danielewicz et al., Phys. Rev. C 38 (1988) 120.

### Note added in proof

After submission of the manuscript we became aware of QMD calculations at very low energies ( $E/N \approx 20$  MeV/n) of a Japanese group [T. Maruyama et al., Phys. Rev. C 42 (1990) 386] and preprints KUNS 1028 and 1033 from Kyoto University.